(毎月1回25日発行) ISSN 0912-9200

urnal of the CERAMIC SOCIETY of
pan,
ernational Edition
.98 May 1990

bers from Nippon Seramikkusu Kyokai Gakujutsu Ronbunshi, Vol.98 No.5 1990

N SERAMIKKUSU KYOKAI GAKUJUTSU RONBUNSHI Vol.98 1990

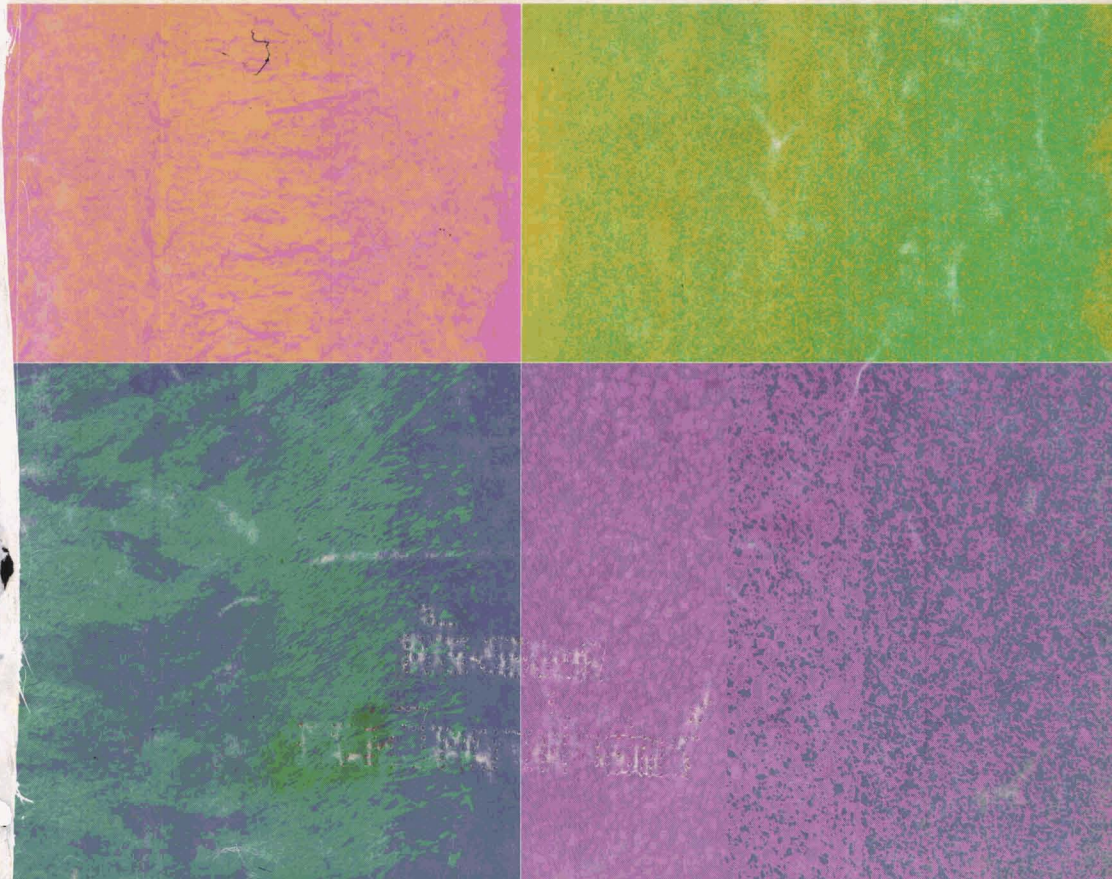

Journal of the CERAMIC SOCIETY of Japan, *International Edition*

Vol.98 No.5
May 1990

Published Monthly by
FUJI TECHNOLOGY PRESS LTD.
7F Daini Bunsei Bldg.
11-7, Toranomon 1-chome
Minato-ku, Tokyo 105, Japan
Tel:(03)-508-0051
Fax:81-3-592-0648

One year subscription
Air Mail ¥200,000

CONTENTS

Papers:

Note:

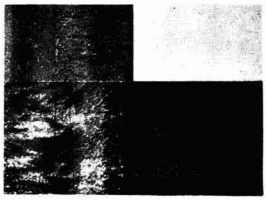

Cover

A concept has been proposed by Japanese scientists to solve the problems of using ceramics as structural materials.

Ceramics are highly heat resistant but have low fracture toughness, while metals have high fracture toughness but less heat resistance. If a new material with the combined advantages of metals and ceramics could be created, it would solve the problems, and thus the concept has been proposed that ceramics and metals should be laminated in layers of atomic order thickness ranging from 100% metal to 100% ceramic. A material with this kind of functional gradient may have the fracture strength of metal combined with the high-temperature resistance of ceramics.

(clockwise from upper left)

1) Cross-sectional surface of SiC-C FGM by SEM
2) Cross-sectional surface of SiC-C FGM by EPMA. (1 & 2: Courtesy of Dr. Hirai and Dr. Sasaki, Institute for Materials Research, Tohoku University)
3) Example of microscopic observation of ZrO2-Ni FGM made by the thin-film lamination method. This sample is a sintered lamination from 100% ceramic to 50% ceramic (Courtesy of Dr. Tamura, NKK)
4) Cross-section photo of C-SiC FGM coated on C/C composite. The composition continuously changes from C to SiC. (Courtesy of Dr. Igarashi and Mr. Kawai, Sumitomo Electric Industries, Ltd.)

Photos taken for "Research on Basic Technologies for Developing Functionally Gradient Materials for Reducing Thermal Stress" supported by the Science & Technology Agency's 1988 Special Coordination Funds for Promoting Science and Technology

Ceramic letter:

Information & Communications

Papers, Letters and Notes

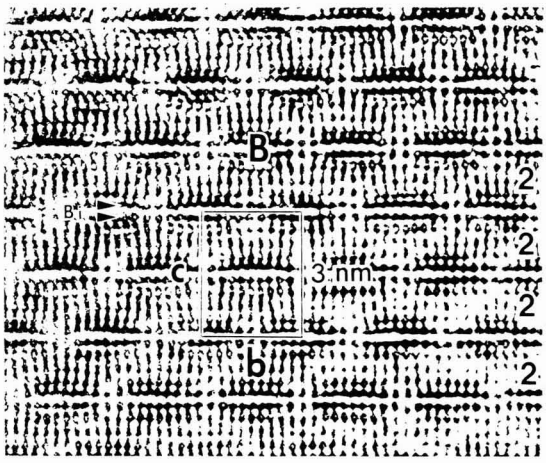

High resolution electron microscope photograph of the modulation doped structure of $Bi_2Sr_2CaCu_2O_y$ (T_c=80K) in the [100] direction. Figures at right side indicate number of copper layers, symbol B indicates bismuth rich region.

Grain Growth during the Sintering of Ultrafine SiC Powders Containing Free Si

Masato Ohkohchi and Yoshinori Ando

Department of Physics, Meijo University, 1-501, Shiogamaguchi, Tenpaku-ku, Nagoya 468, Japan

Ultrafine powders of β-SiC containing 15wt% free Si, which were produced by the gas evaporation method, were pressurelessly sintered. The behavior of SiC crystal growth during the sintering was observed by scanning electron microscopy (SEM). When the sintering was carried out under the condition that the upper side of the sample is free surface, granular crystals only grew up until 2200°C. On the other hand, under another condition that sample surfaces are sandwiched by graphite plates, plate-like crystals began to grow at 1850°C, and these crystals grew remarkably with the increase of the sintering temperature. X-ray diffraction analysis showed that the granular crystals were β-SiC, the same as that of raw powders. Plate-like crystals were α-SiC and the flat surface of the plate was the basal plane, (001). Sintered bodies were not densified when the granular and plate-like crystals remarkably grew. The pressureless sintering of SiC containing free Si at the temperature above the melting point of Si is considered to be liquid phase sintering. The migration of constituent atoms by diffusion becomes easy when free Si existed as liquid phase. Hence the growth of large plate-like crystals could occurred easily at the position existing such liquid phase. Therefore the existence of free Si is not favorable to obtain a dense sintered body.

[Received September 22, 1989; Accepted January 25, 1990]

Key-words: Silicon carbide, Free silicon, graphite-plate, Sintering, Grain growth, Plate-like crystal, Granular crystal

1. Introduction

It is well known that highly densified SiC can be obtained by the pressureless sintering with the aids of boron and carbon.[1] When the ultrafine powders of SiC produced by the gas evaporation method[2] have been used as raw materials for the pressureless sintering, the circumstance was not a little different.[3] A large number of plate-like crystals grew in two extreme cases, namely too much amounts of boron or too little carbon compared with the optimum amounts of sintering aids to obtain the dense sintered body.[3] When such plate-like crystal growth was remarkable at the early stage of the sintering, the density of the sintered body did not reach at high values.

In the case of pressureless sintering of ultrafine SiC powders containing a large amounts of free Si, remarkable grain growth could be observed. Clear-cut concentric circular growth steps also were observed on the crystal surface.[4] Such grain growth heavily prevented the densification of sintered bodies.

In this paper, the behavior of growing SiC crystals during the sintering has been investigated by SEM and X-ray diffraction. The action of free Si during the sintering is discussed from the viewpoint of diffusion.

2. Experimental

2-1. Preparation of SiC Samples

Two kinds of ultrafine SiC powders were produced by the gas evaporation method within different atmosphere.[2] One was the ultrafine SiC powder without free Si, which was produced in an appropriate pressure and flow rate of methane gas. The other was the ultrafine powder containing 50wt% free Si, which was produced in low-pressure gas of helium. The crystal structure of these ultrafine SiC powders was β-SiC, and the average size of them was about 50nm.

Raw powders of SiC containing 15wt% free Si used for the sintering were prepared by mixing the both powders. Boron 1wt% was added as a sintering aid, and mixed by a wet method in a ball mill. After being dried, it was molded to produce pellets (diameter 14mm, thickness 3mm) by uniaxial press. These pellets were pressed isostatically at 300MPa, and they were used as samples in the following sintering.

2-2. Sintering and Characterization

In each time of sintering, two samples were set differently in the sintering furnace. One sample (S1) was just put on a graphite plate, and so the upper side of the sample is free surface. The other sample (S2) was sandwiched by two graphite plates from the upper and lower sides.

Initial sintering was carried out by the following method. After the furnace being evacuated to an order of 2×10^{-3}Pa by an oil diffusion pump, the graphite heater was raised to 1550°C at the rate of 10°C/min. The temperature was kept for one hour, and then cool down slowly in the evacuated furnace. After this initial sintering, the defined position on the surface of the sintered sample was observed by SEM to investigate the phase of the grown grain. Furthermore, the presence of free Si and the crystal structure were examined by X-ray (Cu Kα) diffraction on the same surface.

Subsequently, these samples were set again in the furnace on the same condition as initial sintering, and the temperature was raised to 1550°C at the rate of 10°C/min. Closing the exhausting valve at 1550°C, Ar gas was introduced into the furnace in a flow rate of 5l/min at pressure 1×10^{5}Pa. Within Ar flowing furnace the temperature was raised at the rate of 25°C/min to a fixed value between 1550°C and 2200°C. When the temperature reached to the fixed value,

it was kept one hour. After the sintering, SEM observation and X-ray diffraction carried out at the same surface position of the sample as before. A series of sintering and characterization was repeated at 50°C interval from 1550°C to 2200°C.

In order to compare the phase of grain growth at the surface with that of inside of the sintered body, SEM observation has been done on the fracture surface of the sintered body also. The rate of weight loss was measured from the weight change of the same sample for every sintering at each temperature. The existence of oxygen on the surface and inside of samples were examined by electron probe micro analysis (EPMA).

3. Results

3-1. Sintering of the Sample S1

Figure 1 shows SEM photographs taken at the defined position on the side of upper free surface of the sample S1 sintered at various temperatures. Granular crystals of the order of several microns and fine crystals less than 0.5μm grew at 1550°C. The latter fine crystals disappeared at 1800°C, and the sizes of almost crystals were larger than several microns. Even when the sintering temperature was increased to 2200°C, striking change of granular crystals didn't occur and any growth of plate-like crystals was not observed. Although 15wt% free Si was included in the raw powders, the existence of free Si could not be recognized in the X-ray diffraction pattern from the same surface sintered at 1550°C. Even in the sintering at higher temperature than 1800°C, the grown crystals on the surface remained the same β-SiC (3C) as green body. After sintering at 2200°C, a weak peak of graphite was added.

SEM photographs obtained from the fracture surface of the sintered body at 2200°C are shown in **Fig.2**. Granular crystals similar to ones in Fig.1 were seen on the left side (a), which corresponds to the side of the free surface. Complicate and intertwined plate-like crystals grew on the other right side (b), which side contacted to graphite plate. Being evident from Fig.2, the density of the sintered body was low, because much spaces exist between crystals in most parts of the sintered body.

3-2. Sintering of the Sample S2

The behavior of crystal growth at the same position of the sintered body of the sample S2 for various temperature is seen in **Fig.3**. The similar grain growth to the sample S1 was observed at 1550°C sintering. When the sintering temperature was above 1850°C, plate-like crystals began to grow. The whole surface was covered with the plate-like crystals above 2000°C. The size and the number of the plate-like crystals increased with the increase of sintering temperature. Many holes formed by the combination and absorption existed in the plate-like crystals.

SEM photographs taken at different position from that in Fig.3 of the sample S2 at high magnification are shown in **Fig.4**. Two types of granular crystals, the clear-cut polyhedra (b) and the round-shape (c), are seen in the figure. Polyhedra were formed from the growth of granular crystals (a), which size was in the order of several microns at 1550°C. Round-shape crystals contacted with each other. The plate-like crystal began to grow by combining such round-shape crystals. Such plate-like crystals grew rapidly by coalescing adjacent crystals. However, the clear-cut polyhedra were not absorbed to the plate-like crystals, even when the polyhedra touched with the plate-like crystals.

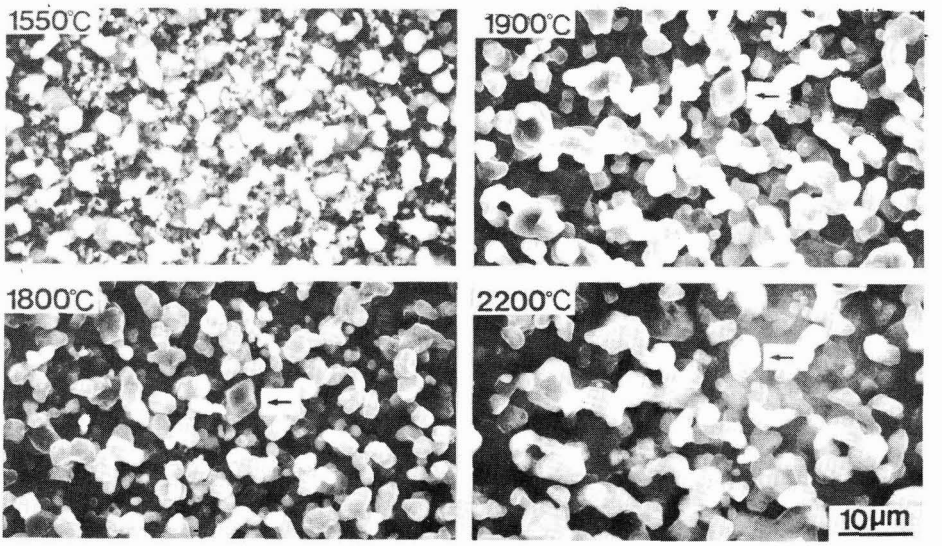

Fig. 1. SEM photographs of the free surface of the sample S1 sintered at each temperature indicated in the figure. The arrow shows the crystal which didn't change the shape up to 2200°C.

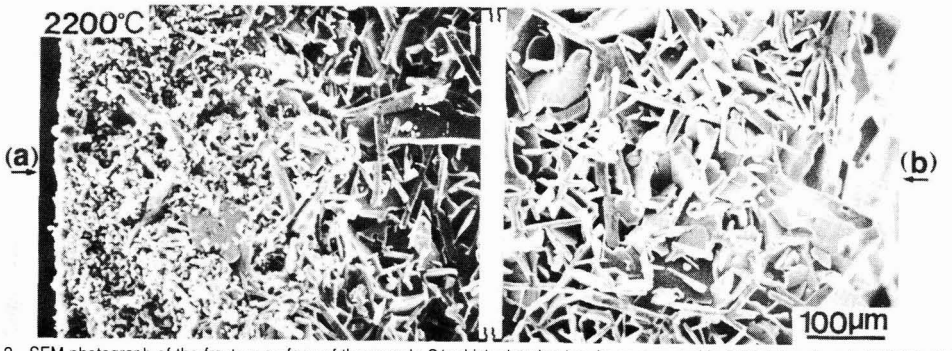

Fig. 2. SEM photograph of the fracture surface of the sample S1 which sintering has been repeated in 50°C interval up to 2200°C. (a) free surface side, (b) side contacting with graphite plate.

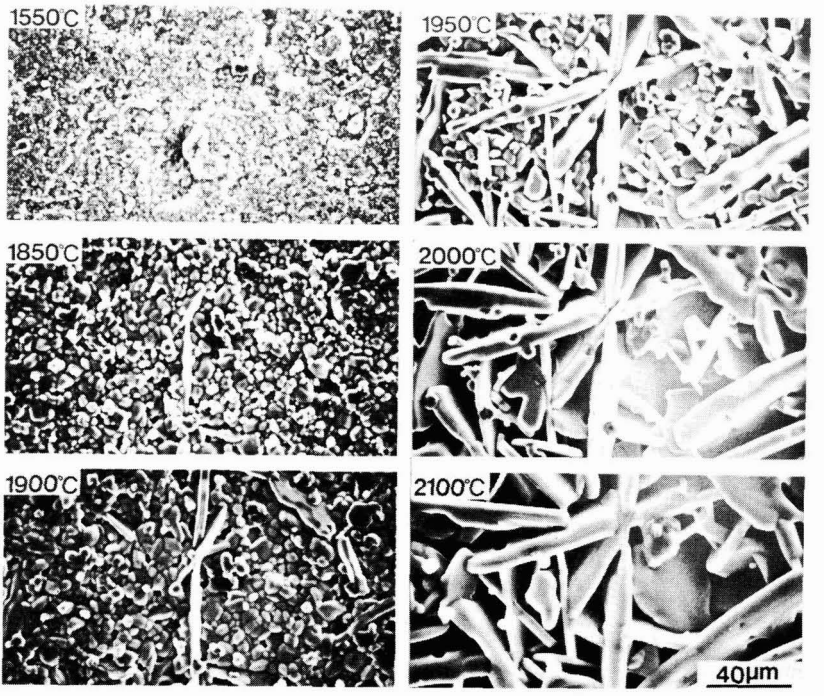

Fig. 3. SEM photographs of the surface of the sample S2 sintered at each temperature.

Growth steps on the plate-like crystal appeared clearly with the increase of the sintering temperature.

Figure 5 shows SEM photographs of the fracture surface near the top surface corresponding to Fig.3. As it is understood from comparison with the photographs at each temperature in Fig.3, the behavior of the growth of plate-like crystals inside the sintered body was similar to the top surface different from the behavior of the sample S1. However, clear-cut polyhedral crystals on the top surface observed in Fig.4 were not seen in the fracture surface. SEM photographs taken at the surface of the same sintered body by the change of the sintering time at 2200°C are shown in **Fig.6**. During the sintering at high temperature of 2200°C, plate-like crystals became thinner and smaller by evaporation with the increase of sintering time. Then, hexagonal growth steps appeared clearly on the partially evaporated surface.

In the X-ray diffraction pattern, the existence of free Si was recognized on the surface up to 1900°C, different from the sample S1. Peaks of α-SiC began to appear at about 1900°C, and clear α-SiC peaks existed at the temperature higher than 1950°C, corresponding to the growth of remarkable plate-like crystals.

By rotating-crystal method of X-ray diffraction, it was confirmed that these plate-like crystals were α-SiC (6H) and the flat surface of the plate was basal plane, (001). In the

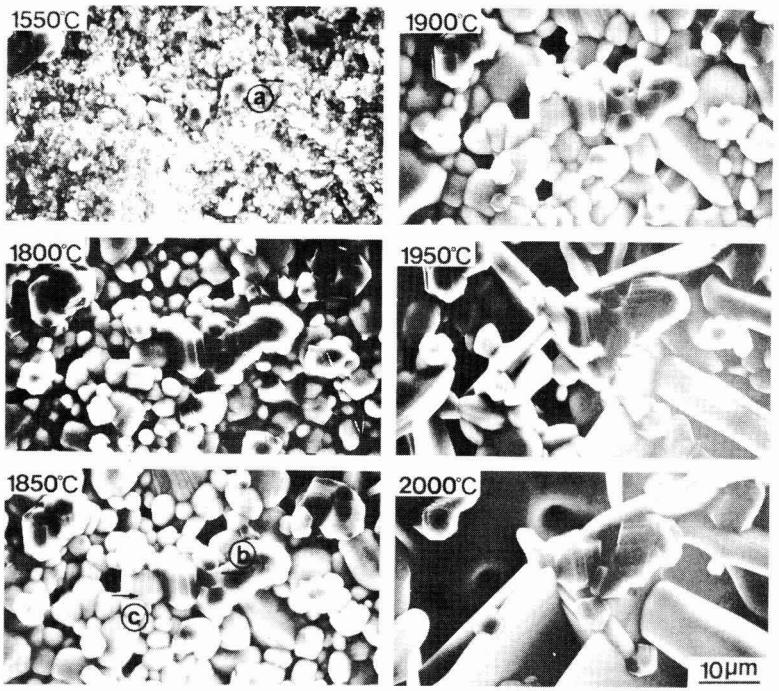

Fig. 4. SEM photographs of the surface of the sample S2 sintered at each temperature. a, b and c show typical three kinds of crystals. a; several microns granular crystal, b; polyhedral crystal, c; round-shape crystal.

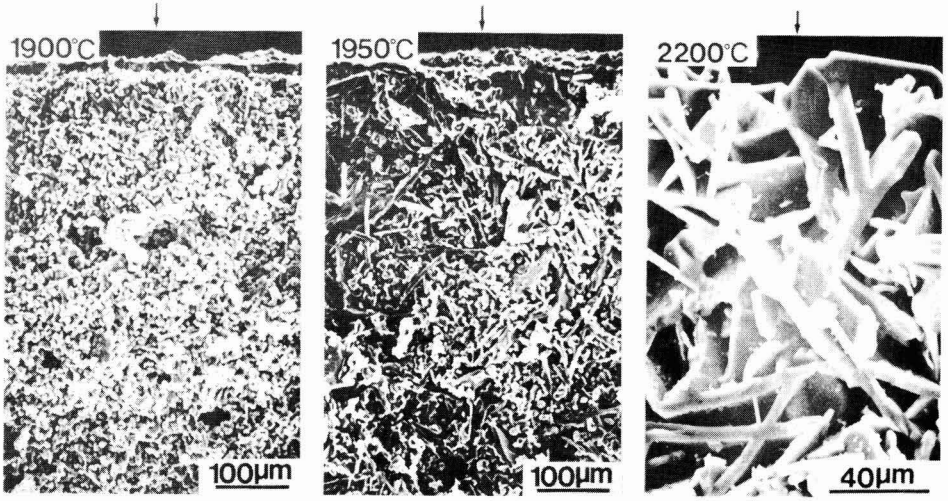

Fig. 5. SEM photographs of the fracture surface near the top surface of the sample S2 sintered at each temperature. Top surface of each sample is shown by the arrows.

powder X-ray diffraction pattern also, the sharp peaks of 6H appeared with the increase of the number of the plate-like crystals.

3-3. Weight Loss Rates of Sintered Bodies

Weight loss rates of sintered bodies at each temperature are shown in **Fig.7**. The weight loss of both samples S1 and S2 up to 1550°C were remarkable. Especially, the weight of S1 decreased as many as 14.5% below 1550°C, but the weight loss was only a little amount at sintering temperature above 1550°C. On the contrary, in the sample S2, the weight loss was increased gradually. In the both samples, weight loss rates had a tendency saturating to about 15% up to 2000°C, and remarkably increased again at 2200°C. Be-

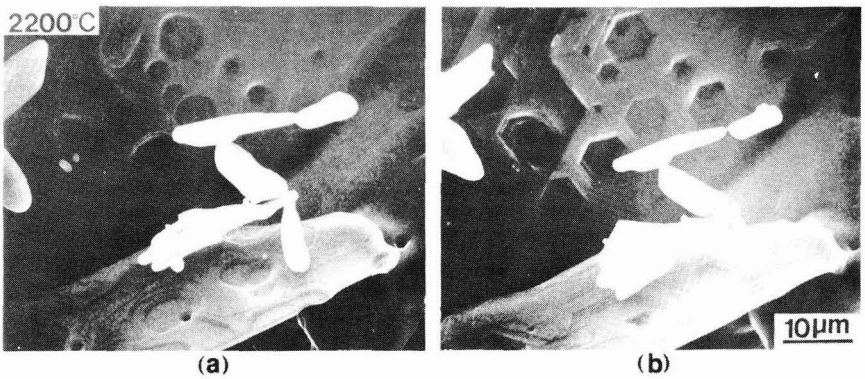

Fig. 6. SEM photographs of the surface of the sample S2 sintered by changing the sintering time at 2200°C. (a) two hours, (b) three hours.

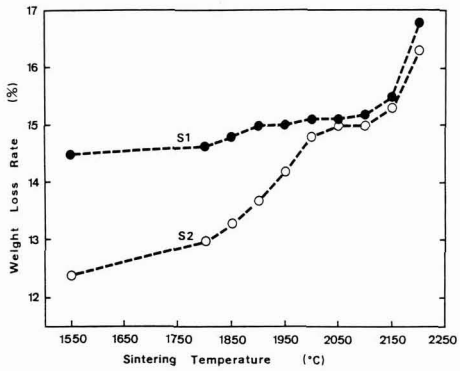

Fig. 7. Weight loss rate of sintered bodies at each sintering temperature.

cause the raw powder contains 15wt% free Si, the saturation value of 15% means that almost parts of free Si in the sample were evaporated up to 2000°C.

4. Discussion

4-1. Effects of the Graphite Plate

In the initial sintering at 1550°C, the evaporation of free Si from the sample S1 was about 2% bigger than that of the sample S2. In the X-ray diffraction pattern, the existence of free Si was not recognized already at 1550°C for the sample S1. On the other hand, the peak of free Si in the sample S2, which was sandwiched by graphite plates, remained up to 1900°C. From these results, it is clear that graphite plates had an effect decreasing evaporation rate of free Si contained in the sample.

Purity of Ar gas used for the sintering atmosphere was 99.999%, but oxygen gas was contained as many as 1ppm in the Ar gas. Furthermore ultrafine powders used as raw material contained about 2wt% SiO_2. It is easily anticipated that the surfaces of the sample were oxidized by these oxygen in the sintering process. This anticipation could be supported from other facts also obtained by EPMA examination, namely the oxygen value was high at the surface than the inside of the sample and that was high in the sample S1 than S2. Because the both surfaces of the sample S2 were in contact with graphite plates, the surfaces were easily deoxidized by the carbon.

4-2. Growth of Granular Crystals

When the samples S1 and S2 were sintered at 1550°C, granular crystals classified into two groups in size grew on the surface of sintered bodies. The size was the order of several microns for one group, and another was less than 0.5μm. At the inside of the both sintered bodies, fine granular crystals only (less than 0.5μm) grew. Hence, it seems that the growth of granular crystals in the order of several microns was caused by the evaporation of free Si from the surface. Because the evaporation rate of free Si was fast in the sample S1 as seen in Fig.7, free Si contained in the raw powder had evaporated already at the initial sintering.

Furthermore contacting area between grain and grain was small as seen in Fig.1, and the oxidation of each grain surface were confirmed by EPMA. In such case the migration of constituent atoms by diffusion through boundary is little. Therefore, in the case of sample S1 the growth of individual grains was observed slightly even in the sintering at higher temperature than the initial sintering. On the other hand, in the sample S2, the evaporation of free Si was progressing slowly up to 2000°C, and the surface of the sample was easily deoxidized by the carbon of graphite plates. Thus the granular crystals of the sample S2 grew to have the clear-cut polyhedral shape.

In the X-ray diffraction pattern taken from the surface of sample S1, where granular crystals grew, the peak of β-SiC only could be recognized. However, in the X-ray image of SEM obtained from the same surface, the existence of boron in the position of granular crystals formed at initial sintering was recognized. There is a possibility that these granular crystals are boron.

4-3. Growth of Plate-like SiC Crystals

At the sintering of SiC ultrafine powders containing free Si, it can be anticipated that liquid phase of Si exists in the sintered bodies when the sintering temperature was higher than the melting point of Si. The migration of constituent atoms by diffusion is easy when the liquid phase existed in

the sample. In the sample S2, the existence of free Si on the surface was recognized by X-ray diffraction up to 1900°C. It means that liquid phase existed on the surface even at 1900°C sintering. It could be recognized that round-shape crystals (c) as seen in Fig.4 grew by the sintering in which liquid phase of Si existed. These round-shape crystals were well in contact with each other, hence the bonding between them was easy. As the results, plate-like crystals began to grow at the position of contacting round-shape crystals at the temperature above 1850°C, and the size of plates became large with the increase of sintering temperature. From these results, we can conclude that plate-like crystals grew at the temperature above 1850°C at which the migration of constituent atoms through boundary by diffusion occurred more easily and actively. When free Si was contained in the raw powder, the migration of constituent atoms became active at the melting point of Si, and the growth of round-shape crystals preferentially occurred at the position which the liquid phase existed in the sample. The round-shape crystals grew to plate-like when sintering temperature reached to 1850°C. Such growth prevented the densification of sintered bodies. Therefore, the existence of free Si in the raw powders is undesirable to produce highly densified bodies of SiC by the pressureless sintering.

SiC began to evaporate at the temperature higher than 2200°C as shown in Fig.7, namely the weight loss rate increased again at 2200°C. Moreover, in the X-ray diffraction pattern, the existence of graphite was recognized from 2200°C sintering. This is considered that SiC was dissociated into Si and graphite, and its Si evaporated remaining graphite on the surface.

5. Conclusions

The following aspects were clarified by the sintering of ultrafine powders of β-SiC containing free Si.

1)The graphite plate that is in contact with the sample surface, functioned in the sintering to retard the evaporation of Si or the oxidation of the sample surface.

2)Granular crystals grew only on the surface of the sample when free Si was evaporating actively.

3)Plate-like crystals began to grow at 1850°C, and the whole surface of sintered bodies was covered by them at the temperature higher than 2000°C.

4)The plate-like crystals were α-SiC (6H) and the flat surface of the plate was basal plane, (001).

5)SiC began to evaporate at 2200°C, and then clear hexagonal steps were formed sometimes on the surface of the plate-like crystal by the evaporation.

6)The pressureless sintering of SiC containing free Si was considered to be liquid phase sintering. Then abnormal grain growth occurred, because the migration of constituent atoms by diffusion became easy. Therefore, the existence of free Si is not favorable to obtain the dense sintered body.

Acknowledgments

The authors wish to thank Dr. A. Isogai of Toyota Central Research & Development Labs., Inc. for his measurement of EPMA and for valuable discussion. They also thank to Prof. H. Iwanaga of Nagasaki University for his help determining the crystal orientation of plate-like crystals.

References:

1) S. Prochazka, "Material Science Research", 9, Plenum Press 421-31 (1975).
2) Y. Ando and M. Ohkohchi, J. Cryst. Growth, 60, 147-49 (1982).
3) M. Ohkohchi and Y. Ando, Yogyo-Kyokai-Shi, 94, 26-34 (1986).
4) Y. Ando and M. Ohkohchi, Yogyo-Kyokai-Shi, 95, 693-96 (1987).

This article appeared in English in Nippon Seramikkusu Kyokai Gakujutsu Ronbunshi (Japanese version), Vol.98, No.5, 1990.

High Strength SiC-Particle/Si_3N_4 Composites

Yoshio Akimune

Scientific Research Laboratory, Central Engineering Laboratories, Nissan Motor Co., Ltd.1, Natsushima-cho, Yokosuka 237, Japan

Adding silicon carbide particles to silicon nitride and subjecting the mixture to hot-isostatic-pressing process after pressureless sintering increases both bending strength and Young's modulus, although fracture toughness remains at almost the same. This is because that the added SiC particles inhibit excess grain growth of β-Si_3N_4 resulting in reducing flaw size for fracture. The SiC particles of less than 0.2μm in diameter are trapped within the β-Si_3N_4 grains through hot-isostatic-process with microcracks which reduce imposed stress resulting in further contribution in high strength. SiC particles, however, do not alter the fracture characteristics for fracture toughness.

[Received October 17, 1989; Accepted January 25, 1990]

Key-words: Silicon nitride, Silicon carbide, Composite, Sintering, Hipping

1. Introduction

Lightweight, high-strength silicon nitride has been used in automobile turbocharger rotors since 1985.[1] Silicon nitride is, however, a naturally brittle material and cracks caused by thermal shock and contact stress can yield catastrophic failure. The fracture toughness and strength of silicon nitride must be improved if it is to be used in gas turbines. Strengthening methods available today include the use of fiber and whisker reinforcement[2-4] and particle dispersion.[4-6] The results of various studies have contributed to improving the mechanical properties of silicon carbide (SiC) /silicon nitride (Si_3N_4) composites.

The mechanical properties of Si_3N_4 have also been improved through microstructural control achieved with a sophisticated sinter-hot-isostatic-pressing process.[7] Naturally, this sintering process is utilized to fabricate ceramic composites with enhanced mechanical properties.[8,9] In the literature,[10] Si-C-N powder precursors obtained by chemical vapor deposition were used to produce a SiC-Si_3N_4 composite, having high strength and high fracture toughness. However, those mixed powders were very fine and required a hot press process.

In the present work, SiC-particle/Si_3N_4 composites were produced by hot-isostatic-pressing (hipping) following pressureless sintering. The mechanical properties and the composite microstructures were then examined using scanning electron microscopy (SEM) and transmission electron microscopy (TEM).

Table 1. Properties of starting powders.

		Si_3N_4 E10 UBE	SiC Beta-SiC IBIDEN
Chemical Composition (wt%)	N	>38.4	--
	O	1.27	0.27
	C	0.3	0.4
	Al	0.05	0.04
	Ca	0.05	---
	Fe	0.1	0.05
Crystal Structure		Alpha-Si_3N_4 > 95%	Beta-SiC
Average Particle Diameter(μm)		0.5	0.26
Specific Density ($x10^3$ Kg/m^3)		3.18	3.21
Specific Surface Area(m^2/g)		10.3	15.1

• Yttria Oxide: Shinetsu Chem. >99.9% ,Average Diameter 0.4μm
• Alumina : Alcoa, A16SG, Average Diameter 0.4μm

2. Experimental Procedure

2-1. Materials

Commercially produced silicon nitride powder+ and SiC particles# (10% by volume) were mixed with 10wt% yttria and 5wt% alumina in a ball mill using ethanol as a solvent. The properties of the powders used are listed in Table 1. After ball milling, the slurry was dried in a rotary evaporator, then sieved to a particle size smaller than 210μm. The mixture of the SiC-particle/Si_3N_4 was then isostatically cold pressed at 400MPa. The compacts were subjected to pressureless sintering at a maximum temperature of 1750°C under 0.1MPa N_2 for 3 hours, and then hot-isostatically pressed (hipped) in a graphite crucible for 1 hour at 1850°C under 100MPa N_2. Pressureless-sintered Si_3N_4 was also produced for comparison using the same process. Fabrication process was illustrated in **Fig.1**.

2-2. Mechanical tesling

The 5 by 6 by 40mm pressureless-sintered and sinter and hipped bars were ground into 4 by 3 by 40mm specimens for bending testing and 4 by 1 by 40mm specimens for measuring the Young's modulus. A four-point bending test (inner span of 10 and outer span of 30mm) at a crosshead speed of 0.5mm/min was used to measure bending strength of 18-20 specimens. The results were analyzed using Weibull statistics.[11] The fracture toughness of 15 measurements was measured by the indentation method,[12] Young's modulus of 5 specimens by resonance, and hardness of 15 measurements by a Vickers indenter with a 300g weight.

3. Results and Discussions

The mechanical properties of three materials; a pressureless-sintered Si_3N_4 (PLS-SN), a pressureless-sintered SiC-

+ UBE Kosan Co., Ltd., E10, 1-12 Akasaka, Tokyo, Japan
# IBIDEN Co., Ltd., Betarandam, 2-1 Kanda, Ohgaki, Japan

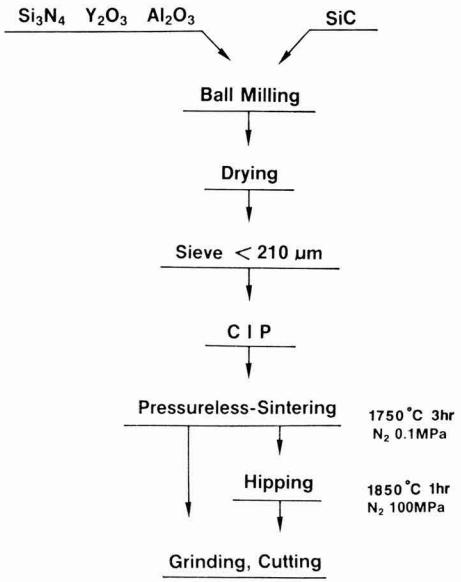

Fig. 1. Fabrication process of pressureless-sintered and sinter and hippped specimens.

particle/Si_3N_4 (PLS-SiC-p/SN) composite, and a sinter and hot-isostatically-pressed SiC-particle/ Si_3N_4 (SH-SiC-p/SN) composite are summarized in **Table 2**. The SH-SiC-p/SN composite exhibited higher density than the PLS-SN and the PLS-SiC-p/SN composite. Comparing PLS-SN and PLS-SiC-p/SN, the addition of SiC particles decreased the sinterability of the composites in pressureless-sintering resulting in lower density due to a porous microstructure. Density was then recovered through the hot isostatically pressing (hipping) process after pressureless-sintering. The SH-SiC-p/SN composite showed the highest Young's modulus because of the SiC addition and its densified microstructure. The decreased hardness value of the SH-SiC-p/SN composite indicated that its deformation resistance was lowered through the hipping process more than that of the PLS-SiC-p/SN composite because of its large β-Si_3N_4 microstructure.

The fracture toughness value (K_{IC}) of SH-SiC-p/SN was slightly higher than that of PLS-SiC-p/SN, which showed the lowest K_{IC} value in this experiment. However, the K_{IC} value of the SH-SiC-p/SN was not higher than other specimens in the literature for small particle added composite.[4] This suggests that the addition of SiC particles may not directly affect the fracture behavior in the SH-SiC-p/SN composite. Nevertheless, the lowered K_{IC} was recovered through the hipping process, since hipping process reduced the pores in a microstructure.[7,8]

On the other hand, a Weibull plot of bending strength (**Fig.2**) shows a considerable improvement due to both SiC-particle addition[4] and sinter and hipping.[8-10] It is considered that SiC-particles inhibit grain growth, as well as densification. Therefore, the PLS-SiC-p/SN exhibits lower strength but a narrower strength scatter due to a more uniform distribution of the largest flaws, which is probably related to porosity than that PLS-SN. Sinter-hot-isostatic-

Table 2. Material properties.

	Pressureless-sintered		Sinter-hipped
	PLS-SN	PLS-SIC-p/SN	SH-SIC-p/SN
Crystal Phase	Beta-SN UK(<5%)	Beta-SN Beta-SIC UK(<5%)	Beta SN Beta-SIC UK(<5%)
Density(g/cm^3)	3.27	3.23	3.29
Young's Modulus(GPa)	289 ±5	298 ±4	303 ±4
Bending Strength(MPa) (4-Point Bending Test)	997 ±176	903 ±105	1226 ±114
Weibull Modulus	7.0	10.4	12.7
K_{IC}(MPa$\sqrt{m}$) (Indentation Method)	5.7 ±0.2	4.6 ±0.1	5.4 ±0.2
Hv (GPa)	16.1 ±0.9	17.3 ±0.9	14.5 ±0.4

±1: Standard Deviation

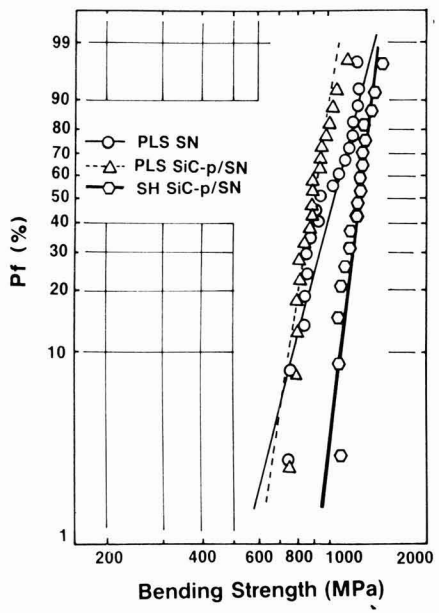

Fig. 2. Weibull plots of bending strength. (PLS: pressureless-sintering, HS: sinter and hipping)

pressing densifies the materials, thereby increasing their strength without significantly altering the microstructural characteristics governing fracture. Thus, a combination of SiC-particle addition and the hipping process yields higher strength as a result of minimizing the critical flaw size for fracture. It is also noted that a larger Weibull modulus indicates that the critical flaw size for fracture tends to converge when SiC particles are added.[2]

Both SEM and TEM were employed to explore the relationship between the mechanical properties and the specimen microstructures. **Figures 3**(A) to (C) are SEM micrographs showing the microstructures of PLS-SN, the PLS-SiC-p/SN composite, and the SH-SiC-p/SN composite. β-Si_3N_4 grains in the SH-material developed better than those in PLS-materials. This alone does not improve fracture toughness, because cracks do not seem to interact with SiC-particles and fracture is actually dominated by the microstructural characteristics rather than the SiC particles.

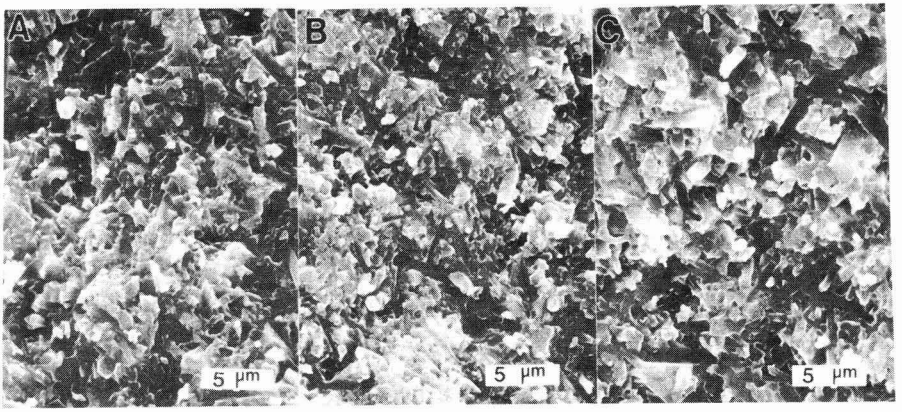

Fig. 3. SEM micrographs showing microstructural characteristics of three materials. (A)Pressureless-sintered Si_3N_4, (B)Pressureless-sintered SiC-p/Si_3N_4, (C)Sinter and hipped SiC-p/Si_3N_4.

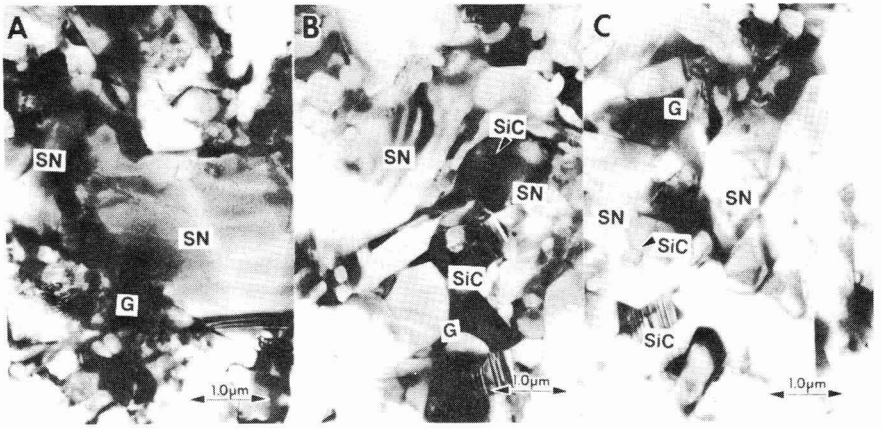

Fig. 4. TEM micrographs of three specimens showing β-Si_3N_4 grains(SN) and SiC-particles (SiC and arrow) with glassy layer(G). (A)Pressureless-sintered Si_3N_4, (B)Pressureless-sintered SiC-p/Si_3N_4, (C)Sinter and hipped SiC-p/Si_3N_4.

The TEM micrographs show the microstructural characteristics of three types of materials. **Figure 4**(A) shows the microstructure of PLS-SN, its partially developed β-Si_3N_4 grains are of scattered sizes and are distributed within a glassy phase. The PLS-SiC-p/SN composite (Fig.4(B)) exhibited similar microstructure to the PLS-SN with SiC grains (under 0.1μm of diameter) trapped in beta-SN grains and distributed within the glassy phase. It is also suggested that carbon contamination from SiC particle (see Table 1) influences the grain growth of β-Si_3N_4 grains.[13] Figure 4(C) shows a microstructure where some of the SiC particles smaller than 0.2μm[10] are trapped in the beta-Si_3N_4 grains, which also developed, and others are distributed along the grain boundaries.

From these observations, it can be deduced that a SH-SiC-p/SN composite having a microstructure with β-Si_3N_4 grains provides high bending strength.[10] Such a microstructure, however, does not yield either high hardness or fracture toughness values. The microstructure of the SH-SiC-p/SN composite is shown in **Fig.5**. Similar to the results in Fig.3(C), SiC particles are trapped within the grain boundary glassy phase and the β-SN grains. As cracks extending from SiC were detected in the β-Si_3N_4 grain by TEM, a grain boundary phase may have been presented considering the difference in thermal expansion coefficient

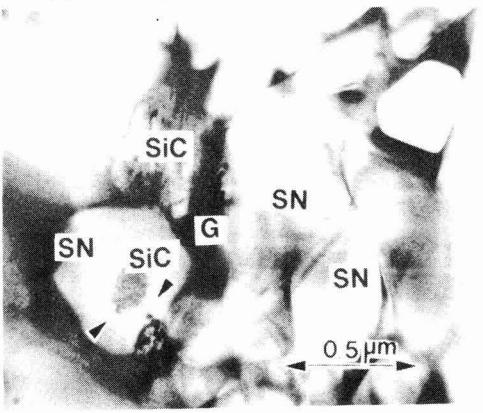

Fig. 5. TEM micrograph of the sinter-HIPped SiC-p/SN exhibiting SiC particles in the b-SN grains. (beta-SN grains(SN) and SiC-particles(SiC) with glassy layer(G), crack(arrow)).

between SiC and Si_3N_4 as suggested by Li and Bradt[14] and Hsueh et al.[15] This microstructure may reduce the imposed stress resulting in yielding further contribution to high strength. The lowered hardness also explained with the microcracks in the SH-SiC/Si_2N_4 composites. The high strength of SH-SiC-p/SN composite is thought that inhibition of excess grain growth and reduction of imposed stress by microcracking.

4. Summary and Conclusions

In the present study, a pressureless-sintered SN, a pressureless-sintered SiC-p/SN composite, and a sinter-hot-isostatic pressed SiC-p/SN composite were produced. Investigation of their mechanical properties showed that a combination of SiC-particle addition and sinter and hipping yields dense compacts, which have a higher bending strength and Young's modulus, although fracture toughness remains at almost the same level. This is because that the added SiC particles inhibit excess grain growth of β-Si_3N_4 resulting in reducing flaw size for fracture. Fine SiC particles of less than 0.2μm in diameter are trapped within the β-Si_3N_4 grains through hot-isostatic-process with microcracks which reduce imposed stress resulting in further contribution in high strength. SiC particles do not alter the fracture characteristics resulting in almost the same K_{IC}.

References:

1) M. Taguchi, Advanced Ceramic Materials, 3 [4], 754-762 (1987).
2) K. Ueno, and Y. Toibana, Yogyo-Kyokaishi, 91[11] 491-97 (1983) (in Japanese).
3) D. Shalek, J.J. Petrovic, G.F. Hurley, and F.D. Gac, Am. Ceram. Soc. Bull., 65[2] 351-56 (1986).
4) S.T. Buljan, J.G. Baldoni, and M.L. Hukabee, Am. Ceram. Soc. Bull., 66[2] 347-52 (1987).
5) F.F. Lange, J. Am. Ceram. Soc., 56[10] 518-22 (1973).
6) D.J. Green, Comm. Am. Ceram. Soc., 66[1] c4-c5 (1983).
7) H. Yen, H. Fang and K. Teng, Ceramic Eng. Sci. Proc., 9[9-10] pp.1337-40 (1988).
8) P. Greil, G. Petzow, and H. Tanaka, Ceram. Int., 13, 19-25 (1987).
9) K.G. Nickel, M.J. Hoffmann, P. Greil, and G. Petzow, Advanced Ceram. Mat., 3[6] 557-62 (1988).
10) K. Niihara, G. Hirano, A. Nakahira, A. Izaki, and T. Kawakami, pp.100-104, in the Proceedings of High Temp. Mat. Div. Meeting of Japan Ceramic Soc., Tokyo, Japan (1988).
11) W. Weibull, J. Appl. Mech., 18, 293-97 (1951).
12) B.R. Lawn and E.R. Fuller, J. Mater, Sci., 10, 2016 (1975).
13) M. Mitomo, N. Yang, K. Kishi and Y. Bando, J. Mat. Sci., 23, 3413-19 (1988).
14) Z. Li and R.C. Bradt, J. Am. Ceram. Soc., 72[1] 70-77 (1989).
15) C.H. Hsueh, P.F. Becher and P. Angeline, J. Am. Ceram. Soc., 71[11] 929-33 (1988).

This article appeared in English in Nippon Seramikkusu Kyokai Gakujutsu Ronbunshi (Japanese version), Vol.98, No.5, 1990.

Analyses of Microstructure and Sintering Mechanism of Si_3N_4-Bonded SiC Ceramics

Yoshiyuki Yasutomi, Masahisa Sobue, S. Shinozaki* and J. Hangas*

Hitachi Research Laboratory, Hitachi, Ltd., 832-2, Horiguchi, Katsuta-shi, Ibaraki 312, Japan
*Scientific Research Laboratories, Ford Motor Company, Dearborn, Michigan 48121, U.S.A.

The sintering mechanism of Si_3N_4-bonded SiC ceramics produced by sintering compacts of powder mixtures of SiC and Si in a nitrogen atmosphere is discussed based on the microstructural analyses by scanning electron microscopy (SEM) and transmission electron microscopy (TEM).

SEM observations showed that amorphous whiskers and fine Si_3N_4 grains grew on the SiC particles surfaces at the initial stage of sintering, and that amorphous whiskers disappeared to form fine Si_3N_4 grains when heated to the final sintering temperature of 1350°C.

TEM observations showed that Si_3N_4 grains grew epitaxially on the SiC lattice and no foreign elements such as oxygen were detected at the SiC-Si_3N_4 interface, and that grain growth of Si_3N_4 seems to be suppressed by the presence of oxygen.

[Received September 14, 1989; Accepted January 25, 1990]

Key-words: Silicon nitride bonded silicon carbide, Reaction-bonding, Near-net-shape, No-shrinkage, Epitaxial growth, SEM, TEM, EELS

1. Introduction

The authors have been studying near net-shape ceramics which have very small sintering-induced shrinkage, with the objective of developing a manufacturing process for structural ceramic parts which need no post-treatment. One of the results is the development of a Si_3N_4-bonded SiC ceramic which has a sintering-induced shrinkage of 0.13% and bending strength of 350MPa.[1,2]

Ceramic strength depends, in general, on grain size and shape, grain boundary structures, and size and quantity of pores. The major factors in Si_3N_4-bonded SiC composites are the mode of the SiC-Si_3N_4 bonding and interfacial structures. Some researchers have discussed the microstructures of Si_3N_4-SiC composites for the grain boundaries of those prepared by hot pressing, or from polycarbosilane.[3,4] However, there are few studies on reaction-sintered Si_3N_4-SiC composites.[5] In this study, the microstructure of Si_3N_4-bonded ceramic materials was analyzed by a scanning electron microscope (SEM), transmission electron microscope (TEM) and electron energy-loss spectrometer (EELS, capable of analyzing light elements, such as C, N and O), in order to investigate the sintering mechanisms.

2. Experimental Procedure

2-1. Sample Preparation

Figure 1 illustrates the production process of Si_3N_4-bonded SiC, and **Fig.2** shows the SEM photographs of the starting powders used in this study. The metallic Si powder consisted of microparticles with a broad size distribution and average size of 0.9μm, and the SiC powder was of the α morphology, crushed to an average size of 16μm.

The Si and SiC powders were mixed (60/40 by weight) together with Si_3N_4 balls for 24h in the presence of methanol in a pot mill. The mixture was dried at room temperature, and mixed with a polyethylene-base thermoplastic resin as the organic binder under pressure for 5h by a kneader. It was then cooled, and crushed by a crusher to 10 meshes or less. About 50g of the crushed particles were press-formed under 98MPa in a die heated to 140°C, into a piece of diameter 40mm and thickness 10mm. The green body thus prepared was heat-treated in an Ar gas atmosphere in a dewaxer oven to remove the resinous matter, and then sintered in a graphite induction heater in nitrogen gas containing 5ppm or less of oxygen. The heater was kept at 0.88MPa with nitrogen gas, after having been evacuated to 5.1mPa (5×10^{-4} Torr) by an oil-diffusion pump.

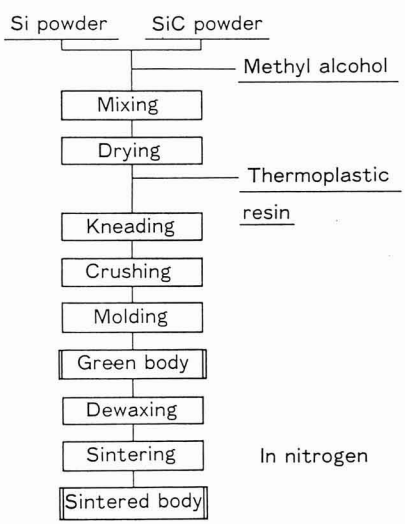

Fig. 1. Production process of Si3N4-bonded SiC ceramics.

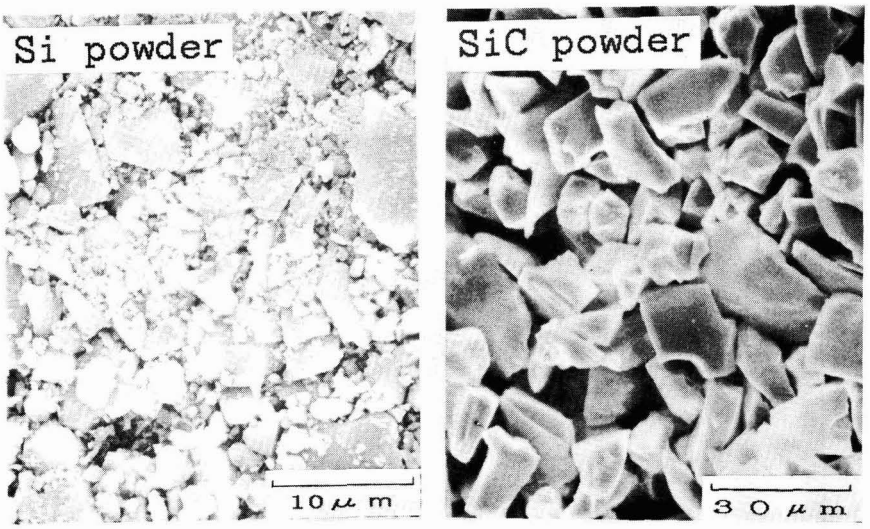

Fig. 2. Scanning electron micrographs of Si and SiC powders.

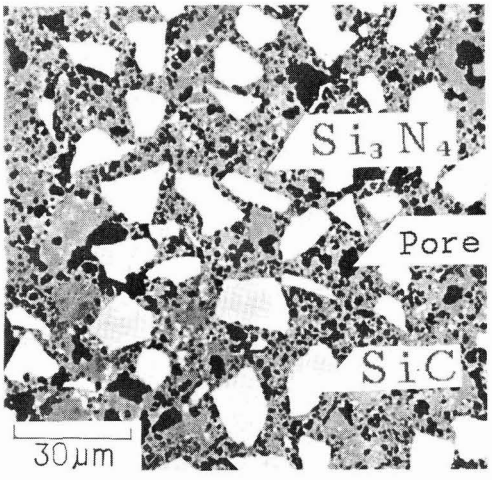

Fig. 3. Optical micrograph of polished surface of sintered body.

Two types of specimens were prepared for the SEM and TEM analyses; one was incompletely heat-treated at 1100°C for 5h, and the other was more fully treated at 1350°C for 5h.

2-2. Analytical Procedure

The fracture face of each sample was analyzed, after having been deposited with carbon, by a high-resolution SEM (Hitachi's S-900) for the grain boundaries.

In addition, the sample was ground to a thin plate and carbon was deposited for the TEM analysis. The microstructure was examined by 3 microscopes (Hitachi H-800 (200kV), Siemens' 102EM (125kV) and JOEL 2000FX (200kV)). The 2000FX microscope was equipped with an electron energy-loss spectrometer (Gatan EELS).

Table 1. Properties of Si_3N_4-bonded SiC ceramics.

Item	Measurement Condition	Value
Dimensional change in sintering stage (%)	Green body →Sintered body	0.13
Density (Mg/m^3)	RT	2.81
Crystal structure of sintered body (%)	X-ray diffractometry	α-SiC : 33 α-Si_3N_4 : 50 β-Si_3N_4 : 17
Volume fraction of pore(%)	RT	12
Thermal expansion coefficient($°C^{-1}$)	RT−900°C	2.9×10^{-6}
Thermal diffusivity (m^2/s)	Laser flash method	9.77×10^{-6}
Bending strength (Max.) (MPa)	RT 1200°C	350 350
Weibull modulus	Least squares method	13.8
Young's modulus (GPa)	Supersonic wave method	172
Poisson's ratio		0.20
Vickers hardness (MPa)	Hv (50kg/30s)	9330
Oxidation weight gain (kg/m^2)	1200°C 100h in air	5.2×10^{-4}

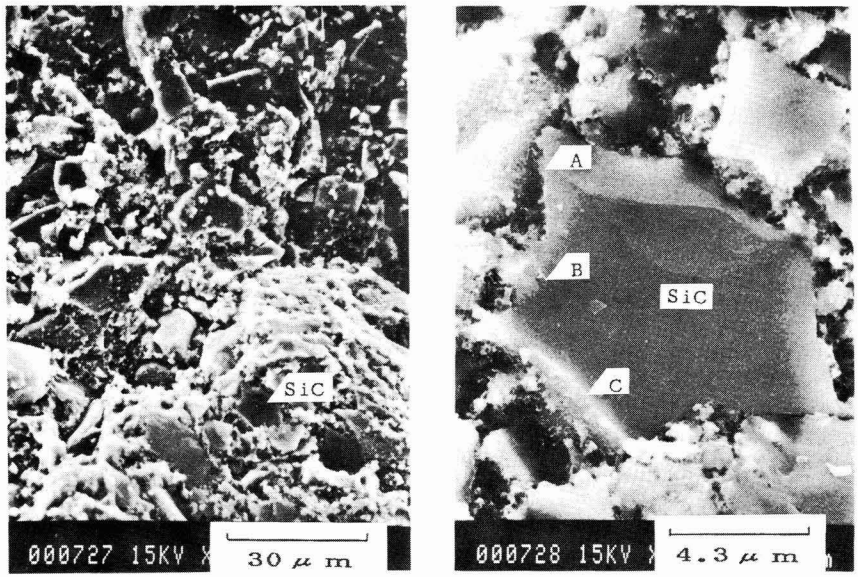

Fig. 4. Scanning electron micrographs of fracture surface of partially sintered body (at 1100°C for 5 hours).

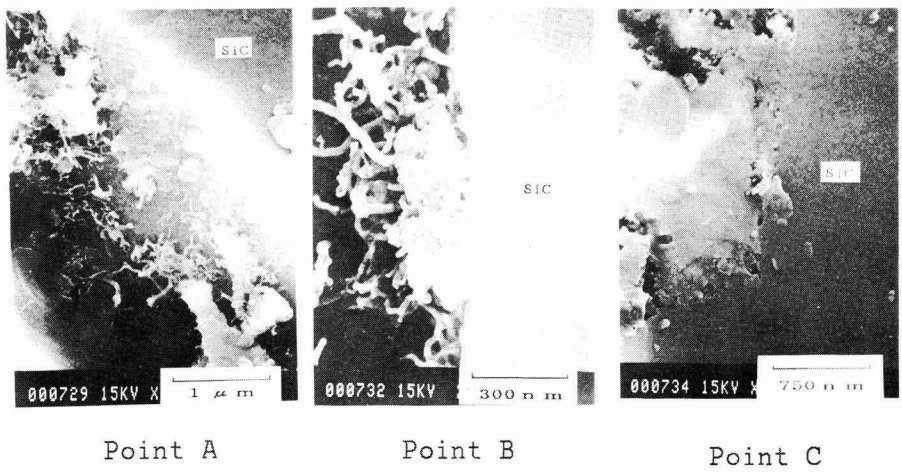

Fig. 5. Higher magnification images taken at A, B and C marked in Fig.4.

3. Results and Discussion

3-1. Nitride Formation over α-SiC Particles

Figure 3 shows an optical micrograph of the Si_3N_4-bonded SiC sample prepared at the final temperature of 1350°C, and **Table 1** shows its properties. Referring to Fig.3, the large, white grains are of α-SiC, the black portions represent pores and the other portion is Si_3N_4. The pores were small, about 20μm or less, and distributed relatively uniformly. This may account for its high bending strength for a high porosity of about 12%.

The sintering process discussed here is based on the nitridation of Si, in which Si_3N_4 particles are deposited and grow on the SiC particle surfaces. The growth process of the reaction products on the α-SiC particles were followed by a high-resolution SEM. The results are presented in Figs.4 through 7.

Figures 4 and **5** show the microstructures of the fracture faces, where the sample was sintered at 1100°C for 5h, and withdrawn from the oven in the middle of the sintering process. The A, B and C portions on the micrograph in Fig.4 were magnified as shown in Fig.5. The magnified A and B portions indicate that whisker-like reaction products were grown and deposited on the α-SiC particle surfaces in the initial stage of sintering. Referring to the C portion, the

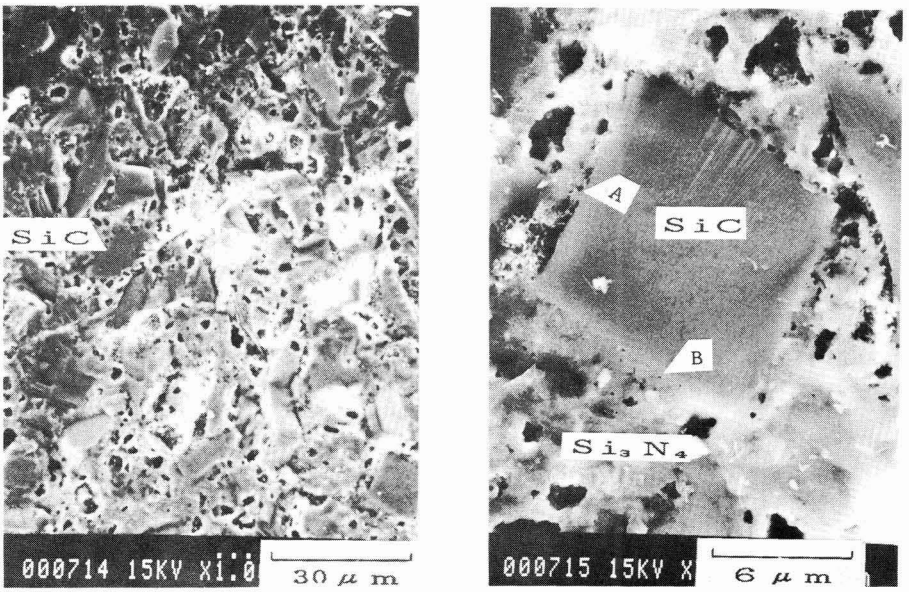

Fig. 6. Scanning electron micrographs of fracture surface of sintered body (at 1350°C for 5 hours).

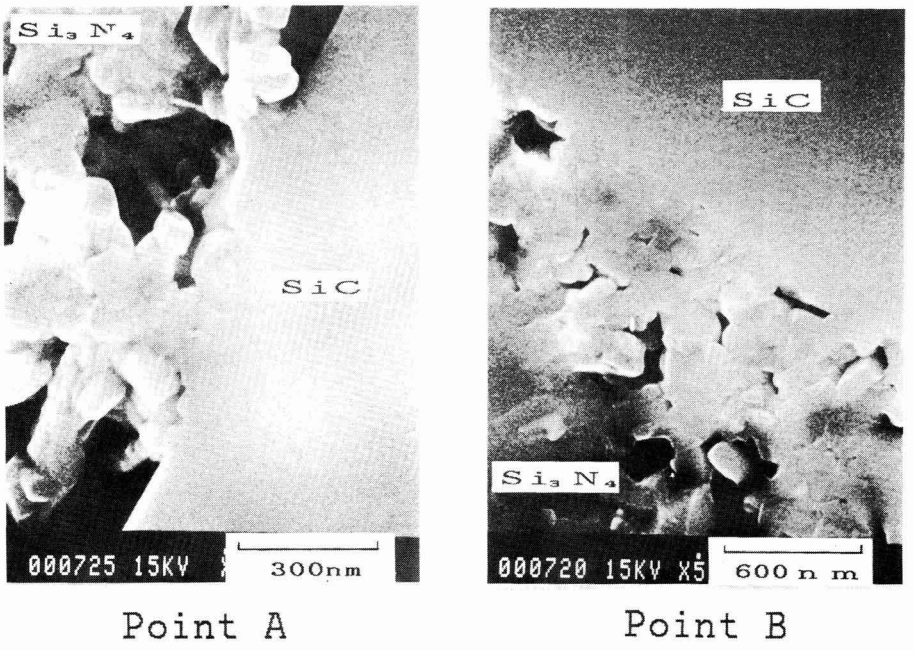

Fig. 7. Higher magnification images taken at A and B marked in Fig.6.

micrograins of Si_3N_4 were partly grown on the α-SiC particle surfaces.

Figures 6 and **7** show the conditions in the vicinity of the SiC-Si_3N_4 interfaces on the fracture faces, where the sample was sintered at the final temperature of 1350°C. The A and B portions on the micrograph in Fig.6 were magnified as shown in Fig.7. The whisker-like reaction products, shown in Fig.5, were eventually transformed into the micrograins of Si_3N_4 to fill the pores.

Next, the whisker-like reaction products shown in Fig.5 were analyzed. **Figure 8** shows the results of the TEM, electron diffraction and windowless dispersive spectroscopic (EDS) analysis. The arrowed portion in the TEM photograph was amorphous, and Si and O or Si, O and N

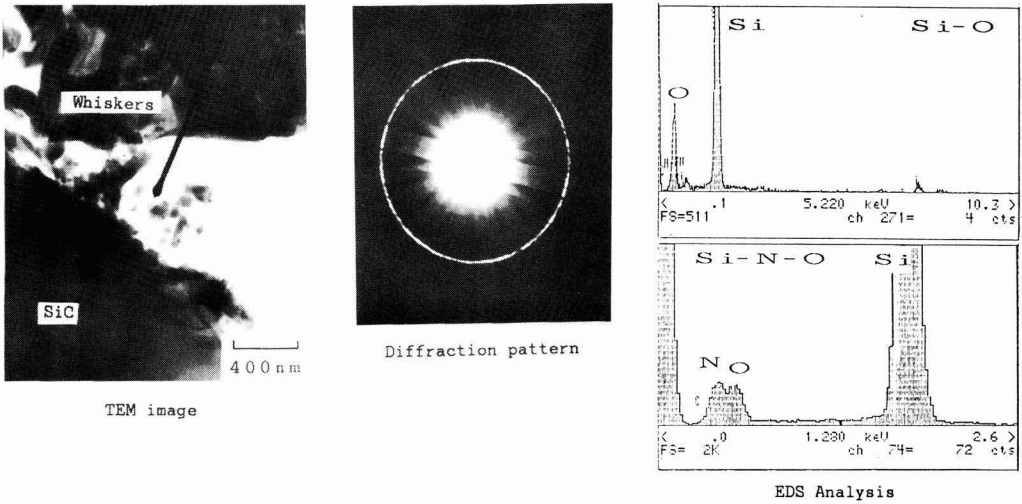

Fig. 8. Typical field transmission electron microscopy, microdiffraction pattern and windowless electron dispersive spectroscopy showing amorphous whiskers on the SiC particle in a partially sintered body (at 1100°C for 5 hours).

were present in that portion, as revealed by electron diffractometry and EDS analysis, respectively. These results indicated that the whiskers found in the sample nitrided at 1100°C for 5h were of Si-O-N bonds. These amorphous whiskers resulted conceivably from the reactions of oxygen in the atmosphere, Si and the oxide film over the SiC particles. The electron diffractiometry confirmed that the Si_3N_4 grains were partly formed in places, as shown in Fig.5 (the SEM photograph at point C).

3-2. Crystalline Structures at the Interfaces between α-SiC and Si_3N_4 Particles

This section discusses the results of the sample treated at the final temperature of 1350°C. Figure 9 shows the TEM image and **Fig.10** the EELS results for the portion in the vicinity of the grain boundaries. The measured region of the EELS analysis ranged from 5 to 10nm. The results shown in Fig.9 indicated that the β-Si_3N_4 grains grew epitaxially in line with the α-SiC grains on which they were deposited at an angle of about 25°. The EELS results (Fig.10) showed no oxygen peak in the grain boundaries, by which it was confirmed that the amorphous Si-O and Si-O-N whisker-like features formed during the initial stage of nitridation were not left over the SiC grain surfaces, and there was no oxide in the interfaces between α-SiC and Si_3N_4. The absence of oxide may account for the strength of the composite sample kept intact at high temperature.

It was observed, as shown in Fig.9, that the Si_3N_4 grains grew at a definite angle (about 25°) with the lattices in the α-SiC grains when these lattices were almost perpendicular to the interfaces. Next, the visual fields in which the lattices in the α-SiC grains ran in parallel to the Si_3N_4-bonded faces were examined, to investigate how the Si_3N_4 grains grew in this case. **Figure 10** shows the TEM photograph of such a portion, indicating that the α-Si_3N_4 grains grew in a similar manner in the portion where the lattices in the α-SiC grains were in parallel to the Si_3N_4-bonded faces. It was also

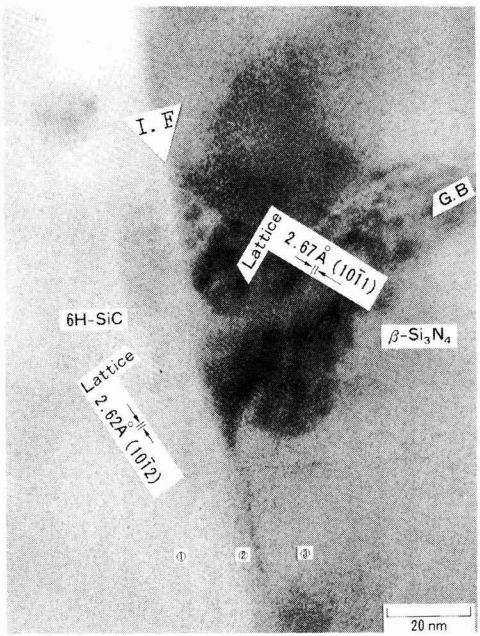

Fig. 9. High resolution TEM image showing interface of SiC and Si_3N_4 in fully sintered body (at 1350°C for 5 hours).

observed that the α-Si_3N_4 grew in different directions in line with the dislocations in the α-SiC grains, which was evidence that growth of the Si_3N_4 grains was restricted by the SiC lattices.

Figure 12 shows the micro-diffraction patterns and analytical results of the interfacial area between α-SiC and Si_3N_4.[6,7] The diffraction patterns indicated that there was no reaction product other than 6H-SiC and α-Si_3N_4, and that

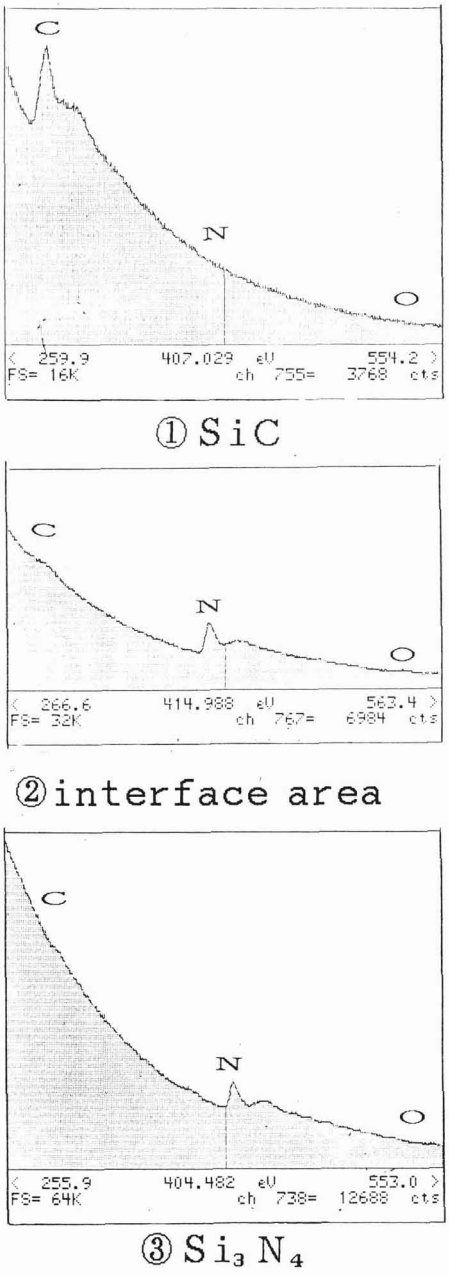

Fig. 10. Electron energy-loss spectroscopy of the vicinity of SiC/Si3N4 interface (symbols 1, 2 and 3 indicate measuring points marked in Fig.9).

6H-SiC and the hexagonal structure of α-Si_3N_4 overlapped each other at a definite angle of about 12°. Extensive study of these diffraction patterns may allow the discovery of bonding regularities.

3-3. Effects of Oxygen on Si_3N_4 Grains

Detailed investigation of the Si_3N_4 particles formed by the nitridation of Si particles revealed that there were oxygen-rich and oxygen-free portions, and they differed in Si_3N_4 grain size from each other. **Figures 13 and 14** present the TEM and EELS results for the Si_3N_4 grains. Figure 13 shows that the oxygen-rich grain was much smaller than the oxygen-free one. The EELS results, shown in Fig.14, indicate the presence of oxygen, though the crystalline structures of each grain were not clarified, because the grains were so small (50nm or less) that their electron diffraction images overlapped each other. The oxygen presumably came from the amorphous Si-O and Si-O-N bonds formed during the initial stage of nitridation (discussed in section 3-1), and left between the Si_3N_4 particles in the form of the SiO_2 or Si_2N_2 grains, to control growth of the Si_3N_4 grains.

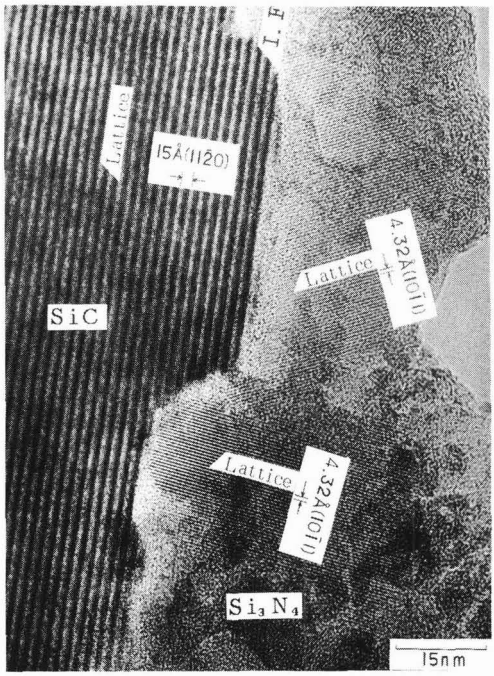

Fig. 11. High resolution TEM image showing 6H-SiC lattice parallel to interface.

Figure 15 shows the triple point of the Si_3N_4 grains at the point where no oxygen was found; no impurity was present in the grain boundaries and the crystal lattices were uniformly lined. The upper two grains had no Moiré fringes and were uniform in the direction of growth, while some Moiré fringes were observed in the lower right grain boundary region, due to a slippage of the direction by several degrees. As a whole, however, these three grains grew in the same direction.

Figure 16 presents the high-resolution TEM image of the position where no oxygen was detected and the lattices of the Si_3N_4 grains ran parallel to the grain boundary, showing that these grains were uniform in growth direction.

It is possible to postulate, based on the above results, that the direction in which Si_3N_4 grains grow on the SiC particles affects the growth direction of the other Si_3N_4 grains nearby.

Thus it may be concluded that the Si_3N_4 grains formed by the nitridation of SiC grow faster and are more com-

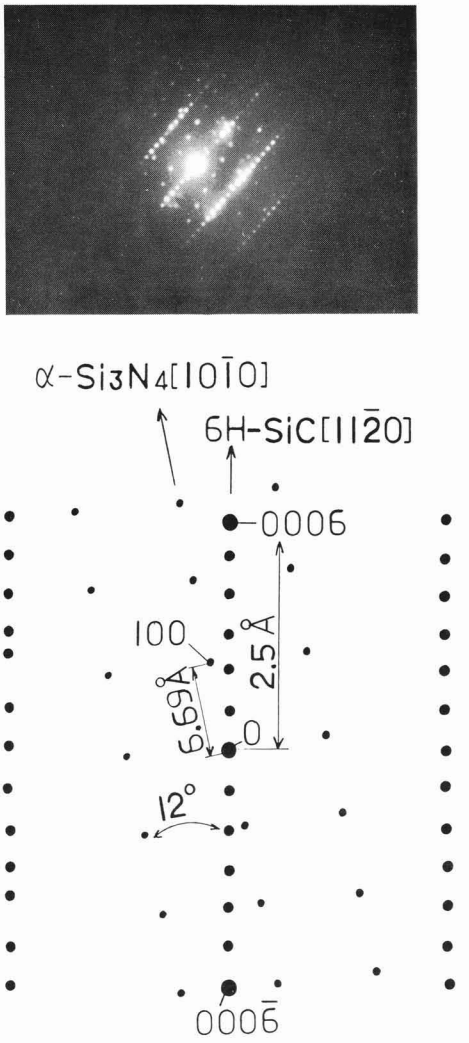

Fig. 12. Analysis of micro-diffraction pattern of the interface area of SiC and Si_3N_4.

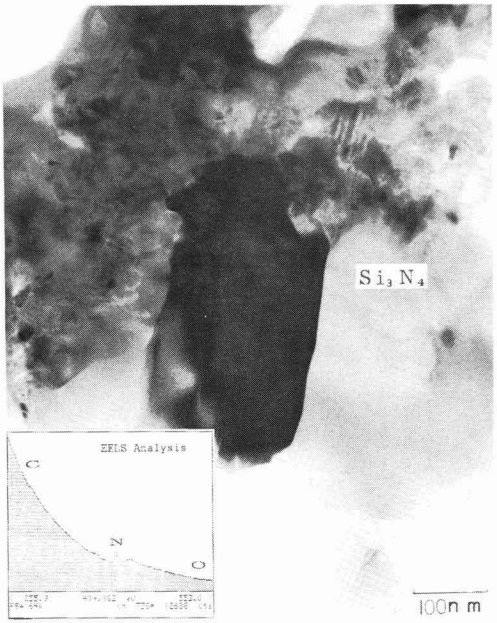

Fig. 13. Transmission electron microscopy and electron energy-loss spectroscopy showing no trace of oxygen in the Si_3N_4 crystals in fully sintered body.

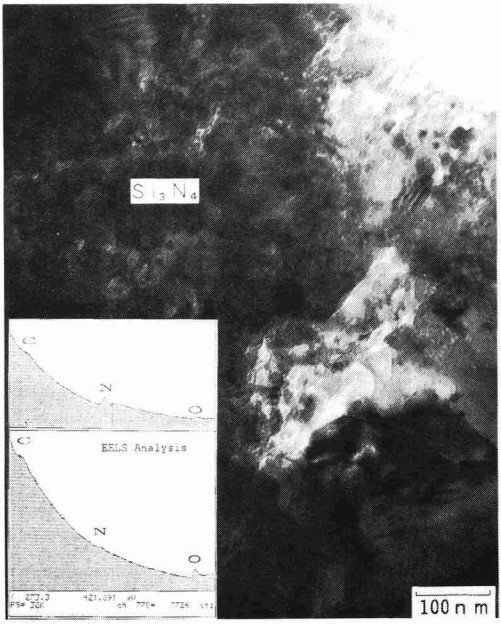

Fig. 14. Transmission electron microscopy and electron energy-loss spectroscopy showing the presence of oxygen in the Si_3N_4 region in fully sintered body.

by the nitridation of SiC grow faster and are more compatible with other Si_3N_4 grains when they are free of oxygen, and that decreasing the oxygen content of the starting material increases the bonding strength between the Si_3N_4 grains.

3-4. Sintering Model

As discussed in section 3-1, the amorphous Si-O and Si-O-N bonds formed in the whiskers in the initial stage of the sintering process are considered to result from the reduction of the oxide films over the starting particles caused by the residual carbon present in the dewaxed binder and an excessive quantity of carbon present in the SiC particles, and from nitridation by nitrogen from the atmosphere. It was already confirmed that the dewaxed sample contained 1.2wt% of free carbon and 1.4wt% of oxygen, while the nitrogen atmosphere gas contained 5ppm or less of oxygen.

The overall process is considered to consist of the following reactions, where Am stands for the amorphous state:

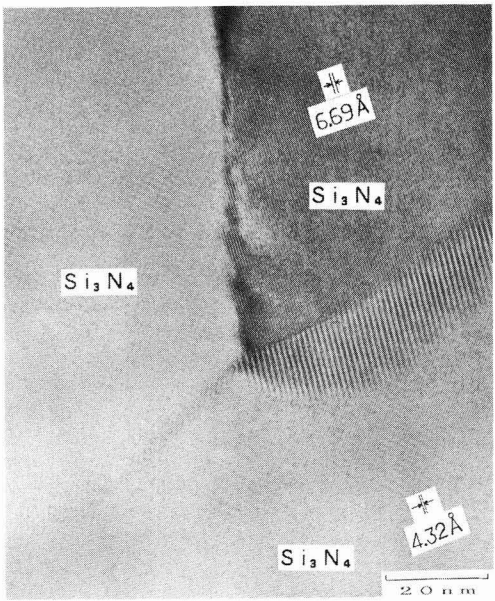

Fig. 15. High resolution TEM image showing triple grain junction of Si_3N_4 crystals in fully sintered body.

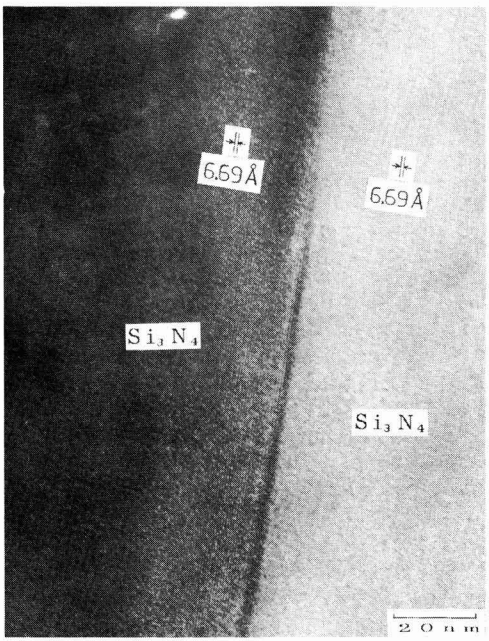

Fig. 16. High resolution TEM image showing Si_3N_4 lattice parallel to its grain boundary.

$$Si(s) + O_2(g) \rightarrow SiO_2(s) \quad \ldots\ldots (1)$$

$$2C(s) + O_2(g) \rightarrow 2CO(g) \quad \ldots\ldots (2)$$

$$SiO_2(s) + CO(g) \rightarrow SiO(g \text{ or } Am) + CO_2(g) \ldots (3)$$

$$3SiO(g \text{ or } Am) + 2N_2(g) + 3CO(g) \rightarrow Si_3N_4(s) + 3CO_2(g) \quad \ldots\ldots (4)$$

or

$$2SiO(g \text{ or } Am) + N_2(g) \rightarrow 2SiNO(Am) \quad \ldots\ldots (5)$$

$$6SiNO(Am) + N_2(g) + 6CO(g) \rightarrow 2Si_3N_4(s) + 6CO_2(g) \quad \ldots\ldots (6)$$

Thus, the SiO_2 film is generally formed on Si and SiC particle surfaces by the oxidation of Si. On the other hand, carbon in the graphite portion of the sintering vessel and residual carbon in the binder react with traces of oxygen present in the nitrogen atmosphere gas to form CO(2). SiO_2 is reduced by CO gas into SiO gas or the amorphous Si-O bond (3), which reacts, as the sintering process proceeds, with N_2 and CO to form Si_3N_4(4), or with N_2 to form the amorphous Si-N-O bond (5). The amorphous Si-O-N bond further reacts with N_2 and CO to form Si_3N_4. The amorphous SiO and Si-N-O bonds, though they exist as intermediates, are eventually converted into Si_3N_4.

The grain size of reaction-sintered Si_3N_4 is generally very small, 1μm or less.[8] The Si_3N_4 grains prepared in this study were also small, mostly 0.5μm or less in size. They were much smaller than, and did not much correspond in shape to, the starting Si particles, suggesting that Si_3N_4 might be formed from Si via the vapor-phase process. The very small shrinkage (about 0.1%) of the sinter, in spite of the significant volumetric expansion (23%) associated with the nitridation of Si, will support the theory that Si particles packed to a high density are not directly expanded in volume by the nitridation, but Si_3N_4 is formed by the nitridation of gaseous Si or SiO. It is therefore considered that the microstructures of the sinters prepared in this study are represented by Si_3N_4 deposited through a CVD-like process on the α-SiC particles, and that the α-SiC and Si_3N_4 particles are bonded to each other at a relatively high bonding strength via the interfaces characterized by the uniformly configured lattices, as shown in Figs.9 and 11.

Next, the reaction process is discussed thermodynamically. Consider the conditions under which decomposition of SiO_2 proceeds purely thermally:

$$SiO_2(s) \rightarrow Si(s) + O_2(g)$$

$$\Delta G^\circ = 215{,}600 - 41.5T \text{ (cal/mol)}$$

ΔG° = 148,246 (cal/mol) at T = 1623K (1350°C).Based on the Henry standard assuming the unity activity of Si,[9] $\Delta G^\circ/RT = 46$, and $\exp(G^\circ/RT) = 10^{-20}$ atm. Therefore, $\exp(-\Delta G^\circ/RT) = 10^{-20}atmPO_2$ is the necessary condition. In other words, an oxygen partial pressure of 10^{-20}atm or less within the green body is necessary to sustain thermal decomposition of SiO_2. Such a high vacuum could not be realized in the sintering process considered in this study.

It is however necessary to take into account the effects of C and CO. The residual carbon in the dewaxed green body reacts with oxygen present in the nitrogen atmosphere gas to form CO. The ΔG° values at 1673K (1400°C) were

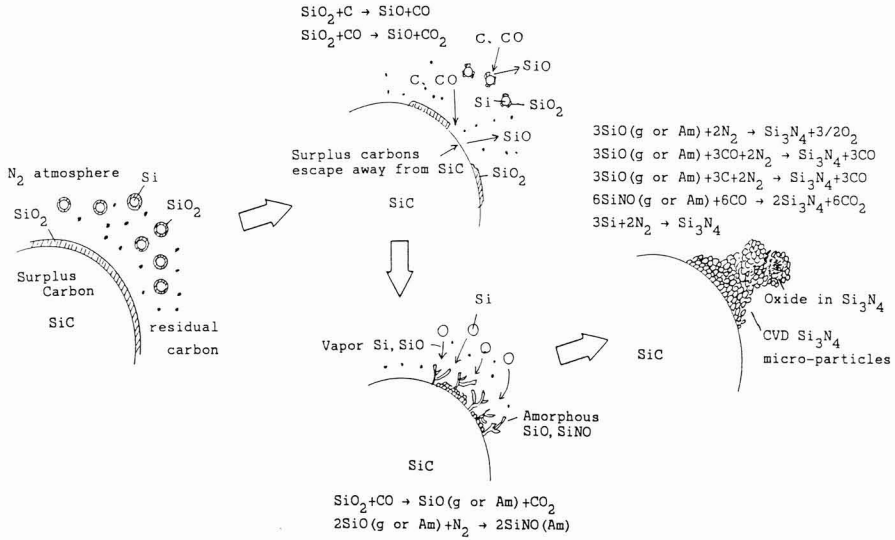

Fig. 17. Sintering model of Si_3N_4-bonded SiC ceramics.

found for the reactions of SiO_2 with C or CO:[10]

$$SiO_2(s) + C(s) \rightarrow SiO(g) + CO(g)$$

$$\Delta G^\circ_{1673} = 12{,}015 \text{ (cal/mol)}$$

$$SiO_2(s) + CO(g) \rightarrow SiO(g) + CO_2(g)$$

$$\Delta G^\circ_{1673} = 24{,}461 \text{ (cal/mol)}$$

The $\exp(-\Delta G^\circ/RT)$ values are 36.6 and 1,568 (atm), respectively. Thus, the conditions necessary to sustain the reactions are:

$$\exp(-\Delta G^\circ/RT) = 36.6 \text{ (atm)} > P_{SiO(g)} \cdot P_{CO(g)}, \text{ and}$$

$$\exp(-\Delta G^\circ/RT) = 1{,}568 \text{ (atm)} > P_{SiO(g)} \cdot P_{CO2(s)}] / P_{CO(g)}.$$

SiO(g) formed by the above reactions reacts with $N_2(g)$ in the atmosphere to form Si_3N_4 by the following reactions:

$$3SiO(g) + 3CO(g) + 2N_2(g) \rightarrow Si_3N_4(s) + 3CO_2(g)$$

$$\Delta G^\circ_{1673} = 11{,}856 \text{ (cal/mol)}$$

$$\exp(-\Delta G^\circ/RT) = 35.4 \text{ (atm)}$$

$$> P_{CO2}{}^3(g)/[P_{SiO}{}^3(g) \cdot PMVCO^3(g) \cdot P_{N2}{}^2(g)], \text{ or}$$

$$3SiO(g) + 3C(s) + 2N_2(g) \rightarrow Si_3N_4(s) + 3CO(g)$$

$$\Delta G^\circ_{1673} = -23{,}403 \text{ (cal/mol)}$$

$$\exp(-\Delta G^\circ/RT) = 8.76 \times 10^{-4} \text{(atm)}$$

$$> P_{CO}{}^3(g)/[P_{SiO}{}^3(g) 83 P_{N2}{}^2(g)]$$

These reactions are possible, judging from their $\exp(-\Delta G^\circ/RT)$ values.[11]

Thus, the major phenomena involved in the overall nitridation process are the reaction of SiO_2 with C or CO, or the formation of SiO by the decomposition of SiO_2, and the reaction of SiO with N_2 to form Si_3N_4.

Figure 17 summarizes the results, to propose the reaction models.

It is necessary to extend the study scope to the quantitative analysis of the effects of free carbon and oxygen, to understand the reaction rate of each step and the factors that determine the reaction rate.

4. Conclusions

Si_3N_4-bonded SiC ceramic samples with a sintering-induced shrinkage of 0.13% and bending strength of 350MPa were analyzed by scanning and transmission electron microscopes, to investigate the sintering mechanisms and grain boundary structures.

1) In the production process of Si_3N_4-bonded SiC, whisker-like features with an amorphous Si-O or Si-O-N bond are formed, in addition to the Si_3N_4 grains, on the SiC particles during the initial stage of sintering.

2) Heating the sample to the final sintering temperature of 1350°C causes the microcrystalline Si_3N_4 grains to grow epitaxially in the vapor phase over the SiC particles, with the amorphous whisker-like features formed during the initial stage vanishing.

3) No oxygen inclusion is found in the interfaces between the SiC grains and the epitaxially grown Si_3N_4 micrograins.

4) The Si_3N_4 grains formed from Si are larger and more compatible with each other when they are free of oxygen. The grain growth tends to be controlled in the section which

contains a large quantity of oxygen.

5) The thermodynamic discussion indicates that the SiO_2 films on the starting particles react with C or CO into SiO gas, which reacts with nitrogen to form Si_3N_4.

6) The small sintering-induced shrinkage may be accounted for by the vapor-phase growth of the Si_3N_4 grains which are deposited on the SiC particles.

7) The increased strength results conceivably from good compatibility between the Si_3N_4 and SiC grains which are directly bonded to each other, and microcrystalline Si_3N_4 grains.

Acknowledgments

The authors thank Dr. W. Dolon of Ford's Scientific Research Laboratory, and Messrs. Y. Ueki and M. Goto of Hitachi Technological Research Center for their cooperation.

References:

1) Y. Yasutomi, H. Kita, H. Nakamura and M. Sobue, Development of High-Strength Si_3N_4-Bonded SiC Ceramics, J. Ceram. Soc. Japan, 96, 783-88 (1988).

2) Y. Yasutomi, M. Sobue and T. Miyoshi, Development of High Strength Si_3N_4 Bonded SiC Engineering Ceramics: to be published in the Proceedings of The First International SAMPE Symposium, Society for the Advancement of Material and Process Engineering, Japan, 1989.

3) Y. Ikuhara, H. Ueno and H. Yoshinaga: Mechanical Properties of Newly Developed Si_3N_4-SiC Composite Material with Relatively High Flexibility, Yogyo-Kyokai-Shi, 93, 409-17 (1985).

4) T. Kandori, S. Kobayashi, S. Wada and O. Kamigaito, SiC Whisker Reinforced Si_3N_4 Composites, J. Mater. Sci., 1356-58 (1987).

5) A. Lightfoot, B.W. Sheldom, J.H. Fint and J.S. Haggerty, Nitriding Kinetics of Si-SiC Powder Mixtures as Simulations of Reaction Bonded Si_3N_4-SiC Composites: to be published in the Proceeding of the 13th Annual Conference on Composites and Advanced Ceramics, Engineering Ceramics Division Meeting, American Ceramic Society, Cocoa Beach, 1989.

6) P.B. Hirsh, A. Howie, R.B. Nicholson, D.W. Pashley and M.J. Whelan, Electron Microscopy of Thin Crystals, Appendix 4, Butterworths (1965).

7) A.H. Heuer, G.A. Fryburg, L.U. Ogbuji, T.E. Michell and S. Shinozaki, ba Transformation in Polycrystalline SiC: I, Microstructural Aspects, J.Am. Ceram. Soc., 61, 9-10, 406-12 (1978).

8) S. Shinozaki and M.E. Milberg, Electron Microscopy Study of the Effect of Iron in Reaction-Sintered Silicon Nitride, J.Am. Ceram. Soc., 64, 7, 382-85 (1981).

9) Barrow, Physical Chemistry, Vol.2, Chap.21, Tokyo Kagaku Dojin (1976).

10) S. Zhang, and W.R. Canon, Preparation of Silicon Nitride from Silica, J. Am. Ceram. Soc., 67, 10, 691-95 (1984).

11) H. Wada and M.J. Wang, Ceramic Whiskers Synthesis and Phase Stability in the Si-C-N-O System, The Proceeding of the International Conference on Whisker and Fiber-Toughened Ceramics, ASM Int., 63-72 (1988).

This article is a full translation of the article which appeared in Nippon Seramikkusu Kyokai Gakujutsu Ronbunshi (Japanese version), Vol.98, No.5, 1990.

Sintering Behavior of TiB_2 with Cr_3C_2 Additive

Junichi Matsushita,*+ Hideo Nagashima,*, and Hajime Saito*,***

*STK Ceramics Laboratory Corp, 1-11 Tsukisan, Minato-ku, Nagoya 455, Japan
**R&D Center, Toshiba Ceramics Co., Ltd., 30 Soya, Hadano 257, Japan
***Toyota Technological Institute, 2-12-1 Hisakata, Tempaku-ku, Nagoya 468, Japan
+Now with Toshiba Ceramics Co., Ltd., 1 Minamifuji, Ogakie-cho, Kariya 448, Japan

The effect of Cr_3C_2 additive was investigated on the sintering process of TiB_2. The 5 to 7.5wt% of Cr_3C_2 well functioned to improve the relative density, the bending strength and Vickers hardness. According to the X-ray diffraction data, TiC and CrB were formed at the grain boundaries of TiB_2. Also, the solid solution between TiB_2 and Cr_3C_2 was recognized. The SEM observation supported that a liquid phase was significantly concerned in the sintering of TiB_2. The sintering behavior of TiB_2 was discussed on the microstructural and compositional viewpoints.

[Received September 21, 1989; Accepted December 11, 1989]

Key-words: TiB_2, Cr_3C_2, Pressureless sintering, Densification, Microstructure, Solid solution

1. Introduction

Because of its high melting point, high hardness and good electrical conductivity, TiB_2 has potential uses for cutting tools, heat resistant material and abrasion resistant material.

Among the reports on the sintering of TiB_2 published in recent years, Watanabe et al.[1] found that sintered body of TiB_2 having high density and high strength was obtained by adding CoB or TaB_2 to TiB_2 and hot press sintering, and Nishiyama et al.[2] reported that the addition of Ni-Zr alloy was effective for the densification of TiB_2 sintered bodies.

The authors have carried out a series of studies aimed at the pressureless sintering of TiB_2, and reported[3] that the addition of Cr_3C_2 to TiB_2 promoted the densification of sintered TiB_2. However, the function of Cr_3C_2 in the densification process of TiB_2-Cr_3C_2 system ceramics could not be clarified. In our present paper, we report the results of further detailed investigations on the effect of added Cr_3C_2 in TiB_2 sintering and discuss the mechanism of densification.

2. Experimental Procedure

The starting materials were TiB_2 powders produced by Cerac Co. and Cr_3C_2 powders produced by Soekawa Rikagaku Co., the average particle sizes and chemical compositions of which are given in **Table 1**. The data were supplied by the manufacturers. The particle sizes of the powders were measured using an automatic particle size analyzer (Micro-truck size analyzer, Leeds & Northrup Co.), and the results are shown in **Fig.1**. The particle size of TiB_2 powder was centered at around 5μm and that of Cr_3C_2 at around 18μm. The oxygen and carbon contents in the powders were measured using an oxygen and carbon analyzer (Leco Co.) and the results are given in **Table 2**.

The powders were blended in the required ratio and wet-mixed in ethanol for 24hr using a plastic container and nylon balls. After drying, the mixture was formed with a press under 30MPa, and finally formed in the required shape under CIP at 300MPa. The green bodies were packed in a carbon container, which was placed in an electric furnace of the resistance heating type (carbon heating elements), and the green bodies were sintered at 1900°C for 1hr under an argon atmosphere. The heating rate was 15°C/min. After sintering, the sintered bodies were furnace-cooled under

Table 1. Average particle and chemical composition of raw materials.

Material	Average particle size (μm)	Composition (wt%)
TiB_2	2.65	B:30.50, Al:0.1, Fe:0.2
		Mg:0.30, Cr:0.001, Si:0.3
		Ca:0.01
Cr_3C_2	7.5	Cr:86.2, Fe:0.07, Si:0.008
		Total carbon:13.1
		Free carbon:0.2

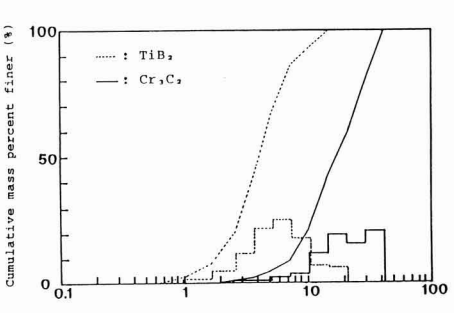

Fig.1. particle size distribution of raw materials.

Table 2. Total oxygen and carbon contents of raw materials.

Material	Total oxygen(wt%)	Total carbon(wt%)
TiB_2	0.9	0.6
Cr_3C_2	0.2	—

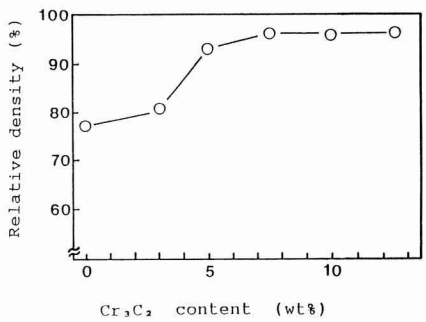

Fig. 2. Relative density as a function of Cr_3C_2 content.

argon.

The density, bending strength and Vickers hardness of the sintered bodies were measured by the same methods as in our previous study.[3)]

The crystalline phases in the sintered bodies were identified by powder X-ray diffraction, with samples prepared by crushing the sintered body. A powder X-ray diffraction apparatus (model 11RA, Nippon Denshi Co.) was used with CuKα radiation (filter: Ni). For the X-ray analysis of the sample surface, a model JCMA 733 (Nippon Denshi Co.) was used to observe the microstructures, an optical microscope (model 104, Nikon Co.) and a scanning electron microscope (model S530, Hitachi Corp.) were used.

3. Experimental Results

3-1. Effect of Cr_3C_2 Addition on Density, Bending Strength, and Vickers Hardness of Sintered TiB_2

Using the sintered bodies obtained by adding Cr_3C_2 to TiB_2 and sintering at 1900°C for 1hr, we investigated the relationship between Cr_3C_2 content and the relative density, bending strength and Vickers hardness of the sintered body.[3)] The results are shown in **Figs.2** to **4.** As seen in Fig.2, when the Cr_3C_2 content is higher than 5wt%, the relative density based on the density of sintered TiB_2 without Cr_3C_2 addition increased to more than 95%. This result indicated that a sintered body of TiB_2 of high density could be obtained by the addition of Cr_3C_2. As seen in Figs.3 and 4, both bending strength and Vickers hardness had the maximum values when Cr_3C_2 content was in the range of 5 to 7.5wt%. These results indicate that both properties could be remarkably improved in comparison to those of sintered TiB_2 without Cr_3C_2. With an increase of Cr_3C_2 content beyond the maximum value range, however, both the bending strength and Vickers hardness tended to decrease in spite of the continued increase of density.

3-2. Phase Change During Sintering

Cr_3C_2 was added to TiB_2 at 7.5wt% and fired at 1100°, 1300° and 1900°C. Powder X-ray diffraction patterns were obtained for these samples, as shown in **Fig.5**. In the case of the sample fired at 1100°C, only the diffraction peaks for TiB_2 and Cr_3C_2, both starting materials, were detected. In the case of the sample fired at 1300°C, the diffraction peaks for Cr_3C_2 disappeared, and those for CrB and TiC, although broad, appeared, in addition to those for TiB_2. In the case of the sample fired at 1900°C, sharp diffraction peaks for CrB and TiC were found, in addition to those for TiB_2.

The results above suggest that CrB and TiC formed in the TiB_2 matrix formed a liquid phase and significantly accelerated the intergranular diffusion of TiB_2, promoting the sintering and densification of TiB_2. These results will be discussed in detail later.

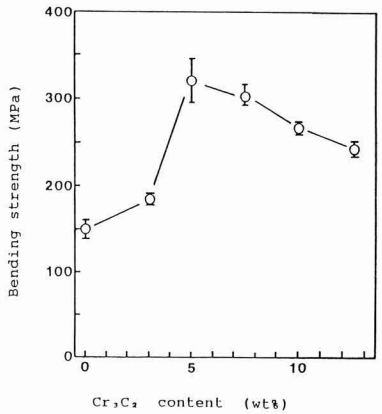

Fig.3. Bending strength as a function of Cr_3C_2 content.

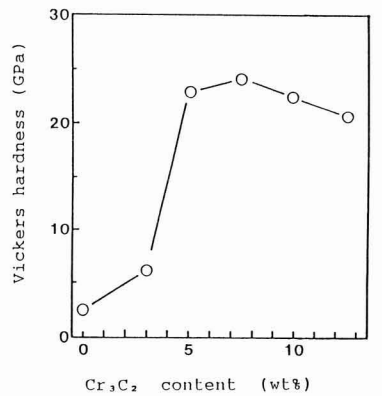

Fig.4. Veckers hardness as a function of Cr_3C_2 content.

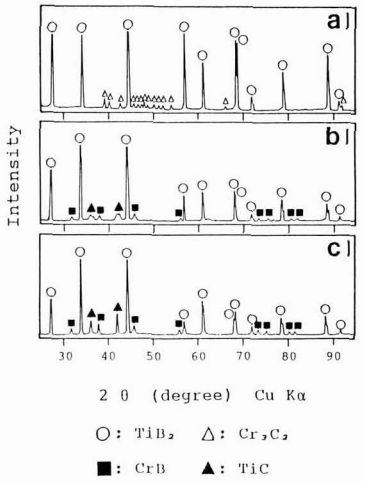

Fig.5. X-ray diffraction pattenns for (a) TiB_2-7.5wt% Cr_3C_2 material sintered at 1100°C, (b) TiB_2-7.5wt% Cr_3C_2 material sintered at 1300°C and (c) TiB_2-7. 5wt% Cr_3C_2 material sintered at 1900°C.

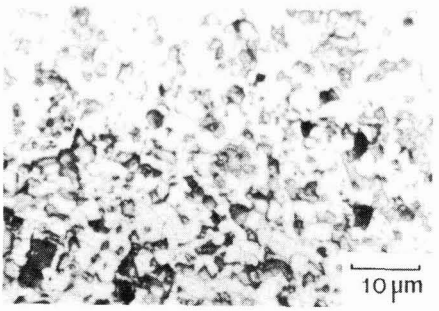

Fig.6. Microphotograph of polished surface of TiB_2-7.5wt% Cr_3C_2 composite sintered at 1900°C after etching chemically by HNO_3 liquids.

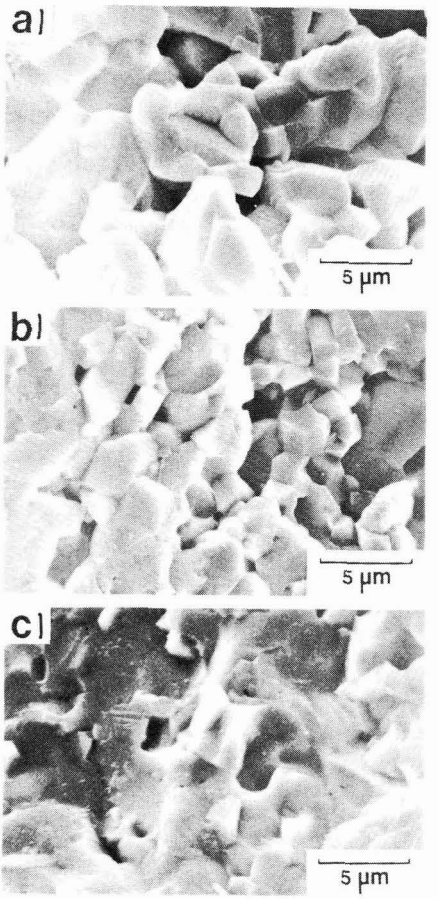

Fig.7. Scammomg e;ectron micrographs of fracture surface of (a) TiB_2-100wt%, (b) TiB_2-5wt% Cr_3C_2 and (c) TiB_2-10wt% Cr_3C_2 composites sintered at 1900°C.

4. Discussion

4-1. Mechanical Properties and Microstructure

A sintered body of TiB_2 with a Cr_3C_2 content of 5wt% sintered at 1900°C was surface etched with HNO_3 and observed with an optical microscope. The photograph in Fig.6 clearly shows that no remarkable grain growth of the TiB_2 grains of 2 to 3μm size with rounded shapes has occurred, and the grain sizes are distributed in a narrow size range.

Three sintered bodies of TiB_2 were prepared, one was TiB_2 without Cr_3C_2 content and sintered at 1900°C, and the other two were TiB_2 with Cr_3C_2 contents of 5 and 10wt% and sintered at 1900°C. The fracture surfaces of the sintered bodies were observed using a scanning electron microscope (SEM). The photographs obtained are shown in **Fig.7**. It can be seen that the sample was fractured predominantly at the grain boundary in the case of the sintered body of TiB_2 without Cr_3C_2 content, but the sample was fractured inside the grains in the case of the sintered body of TiB_2 with a Cr_3C_2 content of 10wt%.

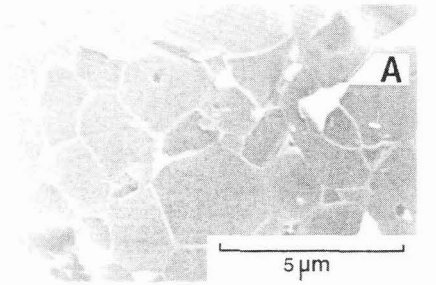

Fig.8. Scanning electron micrograph of polished surface of TiB_2-5wt% Cr_3C_2 composite sintered at 1900°C after etching chemically by HNO_3 liquids.

Figure 8 shows a SEM image of the microstructure on the surface etched with HNO_3 of the sintered body of TiB_2 with a Cr_3C_2 content of 5wt%. Clearly the TiB_2 grains are surrounded by continuous grain boundary phase, so they have not grown much. Additionally, a different phase indi-

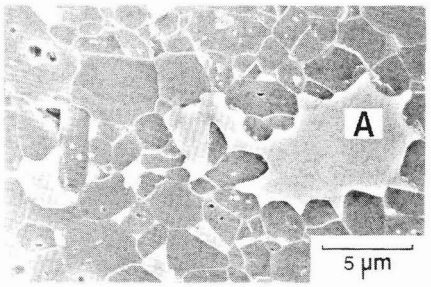

Fig.9. Scanning electron micrograph of polished surface of TiB_2-10wt% CrC_2 composite sintered at 1900°C after etching chemically by HNO_3 liquids.

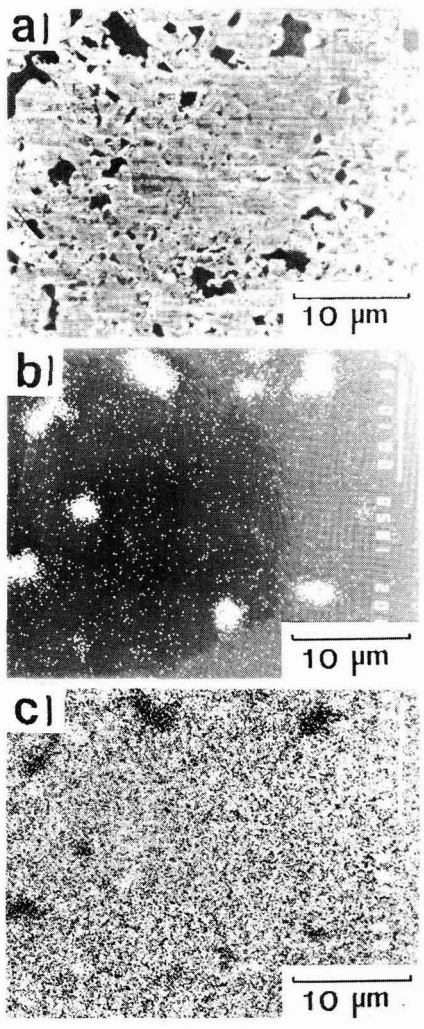

Fig.10. Scanning electron micrograph and X-ray image micrographs of TiB_2-7.5wt% Cr_3C_2 composite sintered at 1900°C. (a) Microstructure, (b) The distribution of Cr element and (c) The distribution of Ti element.

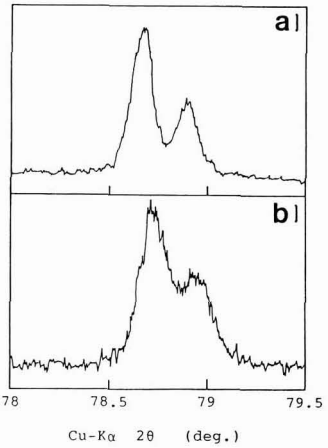

Fig.11. X-ray diffraction patterns of TiB_2(201). (a) TiB_2-7.5wt% Cr_3C_2 raw material and (b) TiB_2-7.5wt% Cr_3C_2 composite sintered at 1900°C.

cated by area A in the figure was formed in the neighborhood of the TiB_2 grains, which is assumed to be a precipitated phase. This new phase increased in quantity with an increase in Cr_3C_2 content, and in the case of the sintered body of TiB_2 with Cr_3C_2 content of 10wt%, this precipitated phase was observed in a fairly large quantity, including areas of remarkably large size as shown in area A in **Fig.9**. These phenomena suggest the presence of a liquid phase in the grain boundary of TiB_2.

As previously observed in Figs.2 to 4, the addition of Cr_3C_2 to TiB_2 of more than 5wt% increased the density of sintered TiB_2, but more than 7.5wt% tended to decrease the bending strength and the Vickers hardness of sintered TiB_2.

Presumably the cause of such behavior is that precipitated phase formed around the TiB_2 grain increased remarkably in quantity with the increase of Cr_3C_2 content, and the increased amount of precipitated phase decreased the bending strength and the Vickers hardness of the sintered body of TiB_2.

Figure 10 shows the results of X-ray surface analysis of the sintered TiB_2 body with Cr_3C_2 content of 7.5wt%. From Figs.10 (a) to (c), this precipitated phase was proved to contain a large quantity of Cr.

Figure 11 shows X-ray diffraction peaks for TiB_2 on the (201) plane. It is seen that the diffraction peaks of the sintered body of TiB_2 with Cr_3C_2 added have shifted towards higher angles from the position for the TiB_2 starting powder. We assume that the unit lattice of the TiB_2 crystal in the sample contracted due to the solid solution of Cr into TiB_2, so the diffraction peaks for TiB_2 shifted towards higher angles.

Judging from the behavior discussed above, we can estimate the formation of the Cr solid solution in TiB_2.

4-2. Sintering Behavior and Densification

As mentioned in section 4-1, we assume TiB_2 with Cr_3C_2 added was densified due to the generation of a liquid phase in the TiB_2 matrix, that is, TiB_2 grains in matrix were surrounded by this liquid phase and Ti and B atoms dissolved

into this liquid phase, resulting in acceleration of diffusion among TiB_2 grains. We further assume that CrB and TiC were formed through this liquid phase to form a mixed phase in the grain boundary phase, and a part of this mixed phase formed a solid solution with TiB_2.

Therefore, a sintered body of TiB_2 having increased density, high strength and high hardness can be obtained by the addition of Cr_3C_2 to TiB_2.

5. Conclusions

The authors investigated the sintering behavior of TiB_2 with Cr_3C_2 added, and obtained the following results.

1) Then TiB_2 with Cr_3C_2 added was sintered, TiB_2 and Cr_3C_2 reacted to produce CrB and TiC phases, which formed a liquid phase which promoted the sintering of TiB_2, resulting in densification of the sintered body TiB_2.

2) Some of the added Cr_3C_2 reacted with TiB_2, forming a solid solution.

3) The grain boundary phase and the precipitated phase in the sintered body of TiB_2 with Cr_3C_2 consisted of a mixture of CrB and TiC.

4) The increased amount and the grain growth of the precipitated phase caused a reduction in the bending strength and Vickers hardness.

References:

1) T. Watanabe and S. Kouno, Am. Ceram. Soc. Bull., 61, 970-973 (1982).
2) K. Nishiyama and S. Umekawa, Powders and Powder Metallurgy Institute Spring Time Proceedings (in Japanese), 74-75 (1985).
3) J. Matsushita, H. Nagashima and H. Saito, Ceramics Ronbun-shi, 98, 355-359 (1990).

This article is a full translation of the article which appeared in Nippon Seramikkusu Kyokai Gakujutsu Ronbunshi (Japanese version), Vol.98, No.5, 1990.

Optimum Synthetic Conditions of Ammonium Aluminum Carbonate Hydroxide (AACH) as Starting Material for Fine α-Alumina Powders

Koichi Hayashi, Seiji Toyoda*, Kunihiko Nakashima and Ken-ji Morinaga****

R&D Division, TOTO Ltd, .2-1-1, Nakashima, Kokurakita-ku, Kitakyushu-shi, Fukuoka 802, Japan
*Graduate School, Kyushu University, 6-1, Kasugakoen, Kasuga, Fukuoka 816, Japan
**Dept. of Materials Science and Technology, Graduate School of Engineering Sciences, Kyushu University, 6-1, Kasugakoen, Kasuga, Fukuoka 816, Japan

Ammonium aluminum carbonate hydroxide (AACH) as starting material to obtain α-alumina fine powders was synthesized between aqueous solutions of ammonium hydrogen carbonate (AHC) and ammonium alum (AA). The effects of pH of the AHC aqueous solution and reaction temperature on the formation of AACH were discussed. Three products, amorphous aluminum hydroxide, pseudoboehmite (=low crystalline boehmite) and AACH were formed depending on pH. AACH was mainly formed in alkaline aqueous solutions. The optimum synthetic condition of AACH was discussed in terms of the relation between pH and concentration of species calculated by the master variable technique of ionic equilibrium in AHC and AA aqueous solutions. NH_4^+, $AlO(OH)_2^-$ and HCO_3^- species were necessary to form AACH. Crystallite size of AACH decreased with increasing concentrations of ionic species, $[NH_4^+]\cdot[AlO(OH)_2^-]\cdot[HCO_3^-]$ and decreasing reaction temperature. Homogeneous, spherical α-alumina particles with a particle size of 0.2μm were obtained by firing at 1050°C for 6hr from the AACH with a crystallite size of 50 synthesized at a pH of 10.0 at 5°C.

[Received September 29, 1989; Accepted January 25, 1990]

Key-words: Ammonium aluminum carbonate hydroxide (AACH), Synthesis, pH, Master variable technique, Crystallite size, α-alumina

1. Introduction

Alumina used in transparent ceramics and single crystals for laser elements has high purity and fine, uniform particles.[1,2] Alumina for such purposes has been produced by a variety of processes, including the thermal decomposition of ammonium alum, hydrolysis of organic metals, ethylene chlorohydrin process, underwater spark discharge, thermal decomposition of ammonium aluminum carbonates, and a modified Bayer process.[3] All these processes fire the starting salt to produce α-alumina. Kato suggested that the sinterability of α-alumina is greatly determined by the chemical composition of the starting salt,[4] and it is accepted that the thermal decomposition of ammonium carbonate gives, in general, α-alumina with the highest sinterability. The authors studied a process for producing artificial, polycrystalline ruby, finding that the best starting material among those studied was a solid solution of fine α-alumina powder containing 1.2wt% of Cr_2O_3, prepared by the thermal decomposition of an ammonium carbonate. The thermal decomposition of ammonium carbonate is a process in which aqueous solutions of ammonium hydrogen carbonate (NH_4HCO_3) and ammonium alum ($NH_4Al(SO_4)_2$) are reacted to form ammonium aluminum carbonate hydroxide ($NH_3AlO(OH)HCO_3$), which is thermally decomposed to form α-alumina.[6] The important process conditions are the pH of the reactant solutions, the ionic species present in these solutions, and their concentrations.[7] However, these were not discussed sufficiently to clarify the optimum conditions. In this study, the authors investigated the effects of pH of the reactant solution and reaction temperature on the formation of ammonium aluminum carbonate hydroxide, with the objective of producing fine, uniformly shaped α-alumina particles, and discuss the effects of the ionic species present in the reactant solution, and the effects of the process conditions on the transformation temperature of α-alumina.

2. Experimental Procedure

2-1. Preparation of Ammonium Aluminum Carbonate Hydroxide

The starting materials for the synthesis of ammonium aluminum carbonate hydroxide, $NH_4AlO(OH)HCO_3$, (AACH) were ammonium hydrogen carbonate (NH_4HCO_3, Wako Junyaku, first grade), and ammonium alum ($NH_4Al(SO_4)_2\cdot12H_2O$, Wako Junyaku, special grade).

AACH was prepared by adding an aqueous solution of ammonium alum (0.1mol/l) dropwise to an aqueous solution of ammonium hydrogen carbonate (1.5mol/l).[6] The aqueous solutions of ammonium hydrogen carbonate and ammonium alum are referred to as aqueous AHC and AA solutions. The aqueous AHC solution was kept in a pH range from 7.0 to 12.0 with HCl (1mol/l) and NH_4OH (4mol/l), and the reaction temperature was 5 to 60°C. The concentrations of the aqueous AHC and AA solutions were chosen because of the optimum AHC/AA ratio of 10 to 15mol/mol for the formation of α-alumina of good sinterability, proposed by Kato et al.,[8] and also to keep them below the solubilities at 5°C.

Preparation of AACH: 100ml of the aqueous AHC solu-

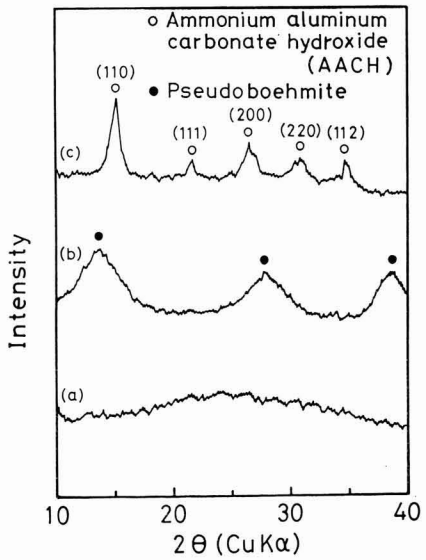

Fig. 1. X-ray diffraction patterns of products, (a): amorphous product, (b): pseudoboehmite (=low crystalline boehmite), (c): ammonium aluminum carbonate hydroxide (AACH).

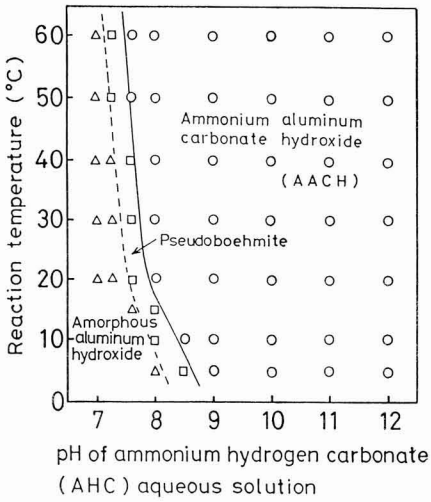

Fig. 2. Formation region of amorphous aluminum hydroxide, pseudoboehmite (=low crystalline boehmite) and ammonium aluminum carbonate hydroxide (AACH) of as a function of reaction temperature and the pH of AHC aqueous solution.

tion at a given pH was put into a beaker at a given temperature, and 100ml of the aqueous AA solution was added at 8.2ml/min, with stirring by a magnetic stirrer, to form the precipitate. The precipitate, after standing for 30min, was suction filtered, washed with ammonia water kept at the same pH as that of the aqueous AHC solution, and dried for 24h under a vacuum at room temperature.

The dried powder was analyzed by X-ray diffractometry (Philips, PW1730 diffractometer), to identify the products. The grain size of the AACH powder at the (110) face was determined using the Scherrer equation.[9] It was also analyzed by a scanning electron microscope (SEM, Hitachi, S-800) to observe the grain shapes.

2-2. Preparation of α-Al_2O_3 by Thermal Decomposition of AACH

AACH powders prepared under various conditions were fired for 6h at given temperature levels (1000°, 1050°, 1100° and 1150°C), to investigate the transformation temperature of α-Al_2O_3 in the formation of α-Al_2O_3 by the thermal decomposition of AACH. Each sample was heated at 200°C/h up to 1000°C, and at 100°C/h thereafter. The heat-treated samples were analyzed by X-ray diffractometry to identify the products, and those completely transformed into α-Al_2O_3 were analyzed by SEM, to observe the particle shapes.

3. Results

3-1. Preparation of AACH

The product of the reaction between the aqueous AHC and AA solutions was either an amorphous product, or low-crystalline boehmite (pseudo-boehmite)[10] or ammonium aluminum carbonate hydroxide (AACH).[6] The amorphous product resulted when the aqueous AHC solution was nearly neutral, irrespective of reaction temperature.The aqueous AA solution was at pH 3, containing, so long as it remained acidic, hexa-aquoaluminum ions ($[Al(H_2O)_6]^{3+}$], referred to as Al^{3+}, as discussed later. It is considered that Al^{3+} forms aluminum hydroxide ($Al(OH)_3$), when its aqueous solution is nearly neutral, i.e., when an aqueous AA solution is added dropwise to a neutral aqueous AHC solution,[11] from which it was decided that the amorphous product was amorphous aluminum hydroxide. **Figure 2** shows the regions of formation of amorphous aluminum hydroxide, pseudo-boehmite and AACH as a function of the pH of the reactant solution (7.0 to 12.0) and reaction temperature (5 to 60°C), indicating that increasing temperature accelerated the formation of AACH when the AHC solution was at a pH in a range from 7.6 to 8.5 and that AACH was formed at any temperature used in this study (5 to 60°C) when the AHC solution was at a pH of 9 or higher.

Figure 3 shows an SEM photograph of the AACH powder prepared from an aqueous AHC solution at pH 10 and 5°C reaction temperature, as an example of AACH powders. It consisted of fine particles of about 0.2μm in size. The AACH powders were quite similar to each other in particle size and shape, irrespective of the conditions (pH of the aqueous AHC solution and reaction temperature) under which they were prepared.

3-2. Preparation of α-Al_2O_3 by Thermal Decomposition of AACH

Table 1 shows the temperatures at which the AACH samples prepared under various conditions were trans-

formed completely into the α-Al_2O_3 phase, when heated at given temperatures for 6h. It was found that, at a reaction temperature of 20°C using an aqueous AHC solution at pH 10.0, AACH was transformed completely into the α phase at the lowest temperature of 1050°C. It was also found that with an aqueous AHC solution pH 10 and reaction temperature of 60°C, the transformation temperature at which AACH was transformed into the α phase tended to increase to 1100°C. **Figure 4** shows the SEM photographs of the α-Al_2O_3 samples prepared by sintering the AACH powder under the conditions given in Table 1. The heat treatment temperature and holding time were the same as those given in Table 1 as conditions under which each AACH sample was transformed completely into α-Al_2O_3. The results indicated that, of the samples prepared at various pH of the aqueous AHC solution and a constant reaction temperature of 20°C (Figs. 4(a), (c), and (e)), the α-Al_2O_3 sample which had the smallest particle size was that synthesized by firing

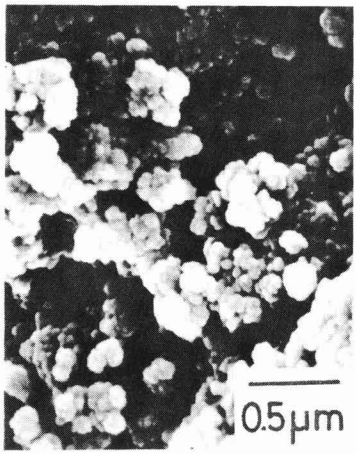

Fig. 3. SEM photograph of AACH powder synthesized at a pH of 10.0 at 5°C.

Table 1.a-alumina transformation temperature of synthesized AACH powders.

Synthetic conditions of ammonium aluminum carbonate hydroxide (AACH)		α-alumina transformation temperature (°C) x6h.
pH of ammonium hydrogen carbonate (AHC) aqueous solution	Reaction temperature (°C)	
8.1	20	1100
10.0	5	1050
10.0	20	1050
10.0	60	1100
12.0	20	1100

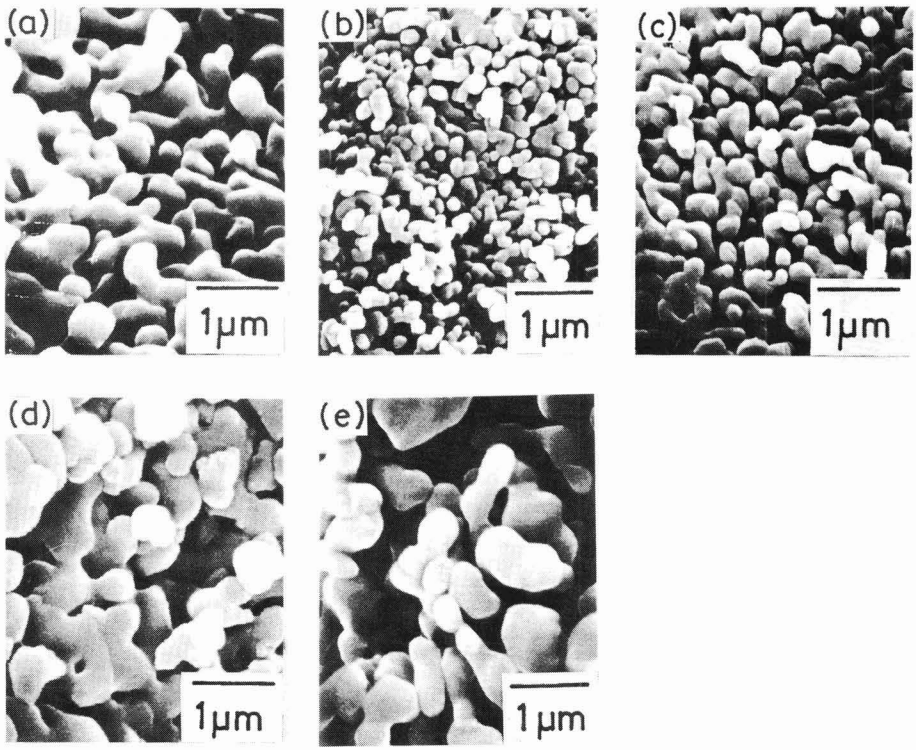

Fig. 4. SEM photographs of a-Al_2O_3 powders obtained by firing from synthesized ammonium aluminum carbonate hydroxide (AACH) powders. The pH of ammonium hydrogen carbonate (AHC) aqueous solution, reaction temperature: (a) 8.1, 20°C (b) 10.0, 5°C, (c) 10.0, 20°C, (d) 10.0, 60°C and (e) 12.0, 20°C.

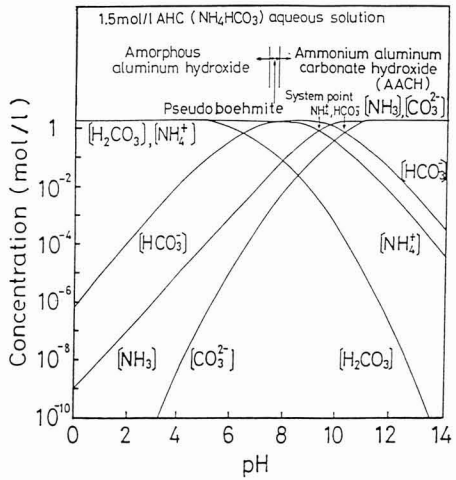

Fig. 5. Relationship between pH and concentration of species calculated by the master variable technique of ionic equilibrium in 1.5mol/l AHC aqueous solution.

the AACH sample, prepared at pH 10.0, at 1050°C for 6h (Fig. 4(c)). It was also found that, of the samples prepared at various reaction temperatures and a constant pH level of 10.0 (Figs. 4(b), (c) and (d)), the one with the largest particle size was that synthesized by firing the AACH sample prepared at 60°C at 1100°C for 6h, and the particles were bonded to each other (Fig. 4(e)). In conclusion, the α-Al_2O_3 sample with the smallest particles (about 0.2μm) uniformly shaped and not connected to each other was that from the AACH sample prepared from the aqueous AHC solution at pH 10.0 and reaction temperature of 5°C, which was fired at 1050°C for 6h.

4. Discussion

As discussed in Section 3.1, increasing temperature accelerated the formation of AACH when the AHC solution was at a pH in a range from 7.6 to 8.5 and AACH was formed at any temperature used in this study (5 to 60°C) when the aqueous AHC solution was at a pH of 9 or higher. In view of these results, the AACH formation conditions are discussed using the master variable technique for ionic equilibrium in an aqueous solution.[12] When the aqueous AHC solution reacts with the aqueous AA solution to form AACH, dissociation of AHC or AA depends on the pH level of the reactant solution,[7] and the pH level is selected as the master variable. It is necessary to understand the relationship between concentration of the chemical species present in the aqueous AHC solution and pH level of the solution, in order to establish the master variable diagram for the ionic equilibrium in the aqueous AHC solution. It is assumed that AHC is dissociated into NH_4^+ and HCO_3^- in an aqueous solution, and the following equilibria will exist at 25°C in the aqueous AHC solution[13]:

$$NH_4^+ \leftrightarrow NH_3 + H^+$$

$$K = [NH_3]\cdot[H^+]/[NH_4^+] = 10^{-9.24}\ (mol/l) \quad \ldots\ldots (1)$$

$$H_2CO_3 \leftrightarrow H^+ + HCO_3^-$$
$$K = [H^+]\cdot[HCO_3^-]/[HMV2CO_3] = 10^{-6.35}\ (mol/l) \quad \ldots (2)$$

$$HCO_3 \leftrightarrow H^+ + CO_3^{2-}$$
$$K = [H^+]\cdot[CO_3^{2-}]/[HCO_3^-] = 10^{-10.33}\ (mol/l) \ldots (3)$$

$$H_2O \leftrightarrow H^+ + OH^-$$
$$K = [H^+]\cdot[OH^-] = 10^{14}\ (mol^2/l^2) \quad \ldots\ldots\ldots (4)$$

where, [ ] represents the concentration of each chemical species. Knowing that the concentration of the aqueous AHC solution used in this study is 1.5mol/l, the following equations will be the mass balance conditions:

$$[NH_4^+] + [NH_3] = 1.5\ (mol/l) \quad \ldots\ldots (5)$$

$$[H_2CO_3] + [HCO_3^-] + [CO_3^{2-}] = 1.5\ (mol/l) \ldots (6)$$

Figure 5 presents the master variable diagram of the ionic equilibrium in the aqueous AHC solution for the concentrations of the chemical species of $[NH_3]$, $[NH_4^+]$, $[H_2CO_3]$, $[HCO_3^-]$ and $[CO_3^{2-}]$ at each pH level.

Figure 6 presents the master variable diagram for the ionic equilibrium in the aqueous AA solution, where only Al^{3+}, $Al(OH)_3$ and $AlO(OH)_2^-$ are selected as the variables controlling the formation of AACH. This diagram was drawn in the same manner as that for the aqueous AHC solution, shown in Fig. 5. It is assumed that AA is dissociated into NH_4^+, Al^{3+} and SO_4^{2-}, and the equations (7) and (8), in addition to (4), hold for the equilibrium constants[14]:

$$Al(OH)_3 \leftrightarrow Al^{3+} + 3OH^-$$
$$K = [Al^{3+}]\cdot[OH^-]^3 = 10^{-32.3}\ (mol^4/l^4) \quad \ldots\ldots (7)$$

$$Al(OH)_3 \leftrightarrow H^+ + AlO(OH)_2^-$$

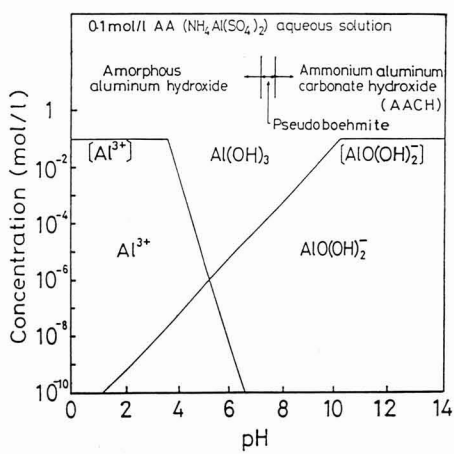

Fig. 6. Relationship between pH and concentration of species calculated by the master variable technique of ionic equilibrium in 0.1mol/l AA aqueous solution.

$$K = [H+]\cdot[AlO(OH)_2^-] = 10^{-11.2}\ (mol^2/l^2) \quad \ldots . (8)$$

Knowing that the concentration of the aqueous AA solution used in this study is 1.5mol/l, the following equations will be the mass balance:

$$[Al^{3+}] \leq 0.1\ (mol/) \quad \ldots . (9)$$

$$[AlO(OH)_2^-] \leq 0.1\ (mol/l) \quad \ldots . (10)$$

The AACH formation conditions are discussed based on the master variable diagrams for the ionic equilibrium in the aqueous AHC and AA solutions, and the dependence of the amorphous aluminum hydroxide, pseudo-boehmite and AACH formation regions on the pH level of the reactant solution.

The master variable diagram, shown in Fig. 5, indicates that the region in which AACH is formed is in the vicinity of the system points of NH_4^+ and HCO_3^-.Kato et al. also observed that dawsonite ($NaAlO(OH)HCO_3$) with the same crystal structure as AACH is formed in the presence of HCO_3^-.[15] It is also noted that pseudoboehmite was formed near pH 7.0, in spite of the presence of a much larger quantity of HCO_3^- than near pH 12.0, which also indicates that NH_4^+ and HCO_3^- ions are necessary for the formation of AACH.

It was also observed, as shown in Fig. 6, that addition of an aqueous AA solution at pH 3 dropwise to an aqueous AHC solution at a pH near 7.0 transformed Al^{3+}, present in the AHC solution, into $Al(OH)_3$. This was accompanied by the formation of amorphous aluminum hydroxide, as discussed in Section 3-1. Furthermore, the concentration of the aluminate ion ($AlO(OH)_2^-$) in the aqueous solution increased as the pH level increased.Kwon et al. reported that $AlO(OH)_2^-$ is present in the solution in which pseudoboehmite is formed. It was also observed in this study that pseudoboehmite was formed in the solution at pH 7.6, when $AlO(OH)_2^-$ was considered to be present in the solution. The quantity of $AlO(OH)_2^-$ increased further in the AACH formation region, indicating that $AlO(OH)_2^-$ was also necessary for the formation of AACH.

Kato et al. proposed the following reactions for the formation of AACH and boehmite:

$$8NH_4HCO_3 + (NH_4)_2Al_2(SO_4)_4 \rightarrow 2NH_4AlO(OH)HCO_3 + 4(NH_4)_2SO_4 + 6CO_2 + 2H_2O \quad \ldots . (11)$$

$$6NH_4HCO_3 + (NH_4)_2Al_2(SO_4)_4 \rightarrow 2AlO(OH) + 4(NH_4)_2SO_4 + 6CO_2 + 2H_2O \quad \ldots . (12)$$

These equations suggest the effects of the reactant solution on the formation of AACH,[6] but do not suggest explicitly the effects of pH level of the reactant solution or the ionic species involved in the reactions. For AACH to be formed, the ionic species of NH_4^+, HCO_3^- and $AlO(OH)_2^-$ must be present in the reactant solution, as indicated by the master variable diagrams for the ionic equilibrium in the aqueous AHC and AA solutions, shown in Figs. 5 and 6. It is also necessary to take into account the effects of OH^-, because AACH was found to be formed in an alkaline AHC solution, as shown in Fig. 2.

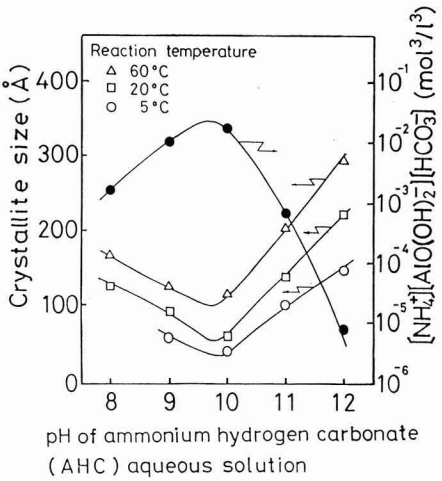

Fig. 7. Change of crystallite size of synthesized AACH and $[NH_4^+]\cdot[AlO(OH)_2^-][HCO_3^-]$ calculated by the master variable technique of ionic equilibrium in AHC and AA aqueous solutions as a function of pH of AHC aqueous solution.

These discussions have led to the proposal of the following equations for the formation of AACH and pseudoboehmite:

$$NH_4^+ + AlO(OH)_2^- + HCO_3^- \rightarrow NH_4AlO(OH)HCO_3 + OH^- \quad \ldots . (13)$$

$$AlO(OH)_2^- \rightarrow AlO(OH) + OH^- \quad \ldots . (14)$$

These equations show that AACH is formed by the reactions of $AlO(OH)_2^-$, NH_4^+ and HCO_3^-, and pseudoboehmite is formed by releasing OH^- from $AlO(OH)_2^-$.

Next, the effects of AACH (ammonium aluminum carbonate hydroxide) formation conditions on the crystallinity of AACH are discussed. **Figure 7** shows the effects of the pH of aqueous ammonium hydrogen carbonate (AHC) solution on the AACH crystallite size, and on the product of NH_4^+, $AlO(OH)_2^-$ and HCO_3^- concentrations estimated by the master variable diagrams shown in Figs. 5 and 6. As shown, the maximum concentration product of the ions necessary for AACH formation and minimum crystallite size were at the same pH level; thus, the aqueous AHC solution prepared at pH 10.0 and temperature 5°C gave the minimum AACH crystallite size of about 50.

It is considered that AACH, deposited during the precipitation reactions, increased in supersolubility in the reactant solution, as the concentration product of NH_4^+, $AlO(OH)_2^-$ and HCO_3^- necessary for the formation of AACH increased. It is also considered that the supersolubility increased as the reaction temperature decreased at the same pH level, as the solubility of a solid generally. Therefore, as the AACH solution increased in supersolubility, AACH decreased in

crystallite size, resulting from the accelerated formation of the fine nuclei.

Table 1 suggests that ammonium aluminum carbonate hydroxide (AACH) of smaller crystallites was transformed into α-Al_2O_3 at a lower temperature. AACH of finer crystallites, having a larger number of asymmetric structure positions within the grains, is considered to be transformed into α-Al_2O_3 at a lower temperature, because of a larger number of decomposition nuclei for the thermal decomposition process.[15]

Thus, the thermal decomposition of AACH under the optimum conditions formed fine α-Al_2O_3 grains of about 0.2μm in size.

5. Conclusions

Ammonium aluminum carbonate hydroxide (AACH), prepared by reacting aqueous solutions of ammonium hydrogen carbonate (AHC) and ammonium alum (AA), was thermally decomposed to form fine α-Al_2O_3 particles, in order to identify optimum pH level of the AHC solution and reaction temperature for the formation of AACH.

1) The aqueous AHC solution, when reacted with the aqueous AA solution, produced amorphous aluminum hydroxide, pseudoboehmite or AACH, depending on the pH level of the reactant solution. AACH was mainly formed when the AHC solution was alkaline.

2) The conditions under which AACH was formed by the reactions between AHC and AA were discussed using the master variable technique[12] for the ionic equilibrium in the aqueous solution. The master variable diagrams for the AHC and AA solutions indicated that the NH_4^+, HCO_3^- and $AlO(OH)_2^-$ ionic species were necessary for the formation of AACH. The new reaction equations were proposed for the formation of AACH, taking OH^- ion into account, knowing that AACH was mainly formed when the AHC solution was alkaline. The $AlO(OH)_2^-$, NH_4^+ and HCO_3^- ions were considered to be involved in the formation of AACH.

3) Increasing the concentration product of $AlO(OH)_2^-$, NH_4^+ and HCO_3^-, the essential ionic species for the formation of AACH, or the reaction temperature, accelerated the formation of fine crystalline nuclei, as a result of increased supersolubility of the reactant solution, and hence the formation of fine crystallites of AACH.

References:

1) Oda and S. Shibusawa, FC REPORT, 4, 17-22 (1986).
2) S. Horikiri, ibid., 3, 9-17 (1985).
3) M. Hama and H. Umezaki, Kagaku Sosetsu, 48, 173-78 (1985).
4) S. Kato, Seramikkusu, 11, 1101-08 (1976).
5) H. Hayashi and K. Morinaga, Seramikkusu-Gakujutsu-Ronbun-shi, 97, 868-71 (1989).
6) S. Kato, T. Iga, S. Hatano and Y. Izawa, Yogyo-Kyokai-shi, 84, 215-20 (1976).
7) Y. Ozaki, "Handbook of New Ceramic Powders." Science Forum, (1983), pp.79-87.
8) S. Kato, T. Iga, S. Hatano and Y. Izawa, Yogyo-Kyokai-shi, 84, 255-58 (1976), and 104-12 (1964).
9) H. Eguchi and H. Arai, Shokubai, 28, 218-23 (1986).
10) K. Funaki and Y. Shimizu, Denki Kagaku, 28, 302-12 (1960).
11) S. Takagi, "Qualitative Analytical Chemistry." vol. 2, Nanko-do.
12) A.J. Bard, "Ionic Equilibriums in Solution." translated by Y. Matsuda and K. Ogura, Kagaku Dojin, (1980) pp. 113-42.
13) Handbook of Chemistry vol. 2." edited by Chemical Society of Japan, Maruzen, (1984) pp.338.
14) T. Mizutani, Seramikkusu, 16, 774-80 (1981).
15) S.W. Kwon, B.H. Kim and H. Ishikawa, Kogyo Kagaku, 74, 2411-15 (1971).
16) H. Hashimoto, Kagaku Sosetsu, 9, 290-36 (1975).

This article is a full translation of the article which appeared in Nippon Seramikkusu Kyokai Gakujutsu Ronbunshi (Japanese version), Vol.98, No.5, 1990.

Synthesis of Li_2O-Fe_2O_3-Bi_2O_3 System Amorphous Ferrite and Properties

Toshio Tsuchiya and Mitsuyoshi Nakamura*

Department of Materials Science and Engineering, Faculty of Industrial Science and Technology, Science University of Tokyo, 2641, Yamazaki, Noda-shi, Chiba 278, Japan

*Department of Chemical Industry, Faculty of Science and Technology, Science University of Tokyo 2641, Yamazaki, Noda-shi, Chiba 278, Japan

Ferromagnetic amorphous oxides were prepared by rapidly quenching the molten antiferromagnetic ferrite $BiFeO_3$ containing lithium oxide. The composition range giving an amorphous phase in the system of Bi_2O_3-Li_2O-Fe_2O_3 was found to contain more than 30 mol% Bi_2O_3. Composition within this range which gave X-ray amorphous phase on quenching were confirmed to be amorphous by X-ray diffraction analysis. Especially, the crystallization temperature of the composition $20Li_2O \cdot 30Bi_2O_3 \cdot 50Fe_2O_3$ was observed to be 430, 580 and 730°C by differential thermal analysis. The saturation magnetization and coercive force of this amorphous oxide were about 13 emu/g at 15kOe and about 100Oe at room temperature, respectively. The thermomagnetic curve showed irreversible change and the curve was slanted near the Curie point. Extrapolation gave the Curie temperature at 563°C. 57Fe Mössbauer absorption spectra indicated that the amorphous phase is composed of two phases paramagnetic and ferromagnetic having small particles. X-ray photo electron spectroscopy spectra showed that Fe^{3+} ions exist in both states of 6-coordinate site and 4-coordinate plus 6-coordinate sites.

[Received October 8, 1989; Accepted January 25, 1990]

Key-words: Rapidly quenching, Crystallization temperature, Saturation magnetization, Coercive force, Curie temperature, Mössbauer absorption spectra

1. Introduction

A number of study results on magnetic amorphous oxide materials have been reported for the past 10 years or so. The magnetic amorphous oxides so far prepared experimentally were paramagnetic or antiferromagnetic. Gyorgy et al.[1] experimentally prepared amorphous thin band with a twin roller by heating and melting $Y_3Fe_5O_{12}$ to 1700-1850°C in the air. The product was antiferromagnetic. Lavill[2] prepared magnetic amorphous $BaO \cdot Fe_2O_3 \cdot B_2O_3$ system, which was paramagnetic at room temperature. Sugimoto et al.3) prepared ferromagnetic substances by melting and rapidly quenching ferromagnetic or ferromagnetic oxide crystals, especially spinel type crystals ($CoFe_2O_4$, $CuFe_2O_4$) to which phosphorous pentaoxide was added as a vitrification accelerator. The resulting amorphous samples had a magnetization value of several emu/g at room temperature, which was far lower than that of spinel-type ferrite of the parent material. The reason for this was thought to be that the saturation magnification and Curie temperature of the glass obtained by quenching molten ferromagnetic oxide crystals are often consideravely reduced due to the disintegration of regular atomic arrangement.

On the other hand, Suzuki et al.[4,5], noting that the antiferromagnetic order of magnetic moment is not always stable in amorphous conditions, attempted to vitrify antiferromagnetic oxides for producing ferromagnetic substances by the following method. Bismuth ferrite ($BiFeO_3$), which is antiferromagnetic in the crystalline state, and zinc ferrite ($Zn\ Fe_2O_4$) were mixed, melted, and rapidly quenched. The resulting ferromagnetic amorphous ferrite had a saturation magnetization of about 17emu/g and a Curie temperature of about 450K at room temperature. Ichinose et al.[6,7,8], from the same viewpoint as Suzuki et al., obtained amorphous ferrites with a saturation magnetization of about 13emu/g at room temperature by rapidly quenching the molten mixture of antiferromagnetic $BiFeO_3$ and various kinds of Ca ferrites ($CaFe_2O_4$, $CaFe_4O_7$, $CaFe_2O_5$) by means of a twin roller.

The bismuth-base amorphous ferrites studied previously are based on antiferromagnetic ferrites only. In the present study, the effect of magnetization due to the fluctuation of antiferromagnetic spin and magnetization due to ferromagnetic oxides was investigated on antiferromagnetic bismuth ferrite containing ferromagnetic lithium ferrite. It was found that, in synthesizing molten materials, the melting point was lower and the amorphous phase range was wider than that of solid solution of other spinel-type ferromagnetic oxides. The synthesis method was like the conventional method for synthesizing amorphous ferrites. Bismuth ferrite containing lithium, which is antiferromagnetic in the crystalline state, was synthesized by adding lithium to antiferromagnetic $BiFeO_3$ to give a single-phase sintered body. The synthesis of amorphous ferrite was attempted by melting the sintered body and then quickly quenching the molten material with a twin roller. To obtain a sintered body with homogeneous composition, the sol-gel method, which can be easily used for multi-composition systems, was used instead of the conventional solid-phase reaction method. The synthesis conditions of the amorphous ferrite thus obtained and its magnetic properties were investigated.These samples were internally analyzed by Mössbauer spectroscopy and photoelectron spectroscopy, and the presence of iron ions

was investigated.

2. Experiment

2-1. Synthesis of Samples

The composition of $xLi_2O\cdot(100-x-y)\,Fe_2O_3\cdot yBi_2O_3$ (x:0-40, y:50-30) was investigated. A twin roller unit (roller diameter, 70mm. Material, 18-8 stainless steel. Revolutions per minute, about 3000rpm.) was used for synthesizing amorphous samples.

The starting materials of iron (II) nitrate ($Fe(NO_3)_3\cdot 9H_2O$), lithium nitrate ($LiNO_3$), and bismuth oxide (Bi_2O_3) were taken according to the above composition. The samples were prepared by the sol-gel method. The nitrate of Fe and Li was weighed, and ethylene glycol and water were added as solvents. This was then heated and stirred at 60°C for 2 hours to produce a uniform solution. The solution was dried at 80°C for 4 hours, at 230°C for 6 hours, and at 350°C for 12 hours, and then allowed to cool in an oven. The dried powder to which bismuth oxide was then added, was ground into 37μm or smaller size in a mortar. The ground powder was heated to the specified temperature at a rate of 2.5°C/min and heat-treated for 24 hours. Drying and heat treatment were carried out in the air. The sintered body thus produced was ground again, melted at 1200 to 1300°C in the air, and flowed onto the twin roller to synthesize the sample.

The quenched sample was a very brittle film with a width of 5-15mm, a length of 15-50mm, and a thickness of 50μm. The physical properties of sample were measured after it was powdered to 75μm or finer.

2-2. Analysis

An X-ray diffraction unit CN2013 (Cu, Kα) supplied by Rigaku Corporation was used for the identification of phase and setting of conditions for synthesizing sintered bodies. The differential thermo-balance TG-DTA, 8078G2 supplied by Rigaku Corporation was used for measuring crystallization temperatures. The measurement was made at a rate of 5°C/min from room temperature. The magnetic properties of coercive force (Hc) from hysteresis loop at room temperature, saturation magnetization (σs), and residual magnetization (σr) were measured by using the sample vibration type magnetization measuring instrument BHV-55 supplied by Riken Electronics Co., Ltd. Curie points were measured in a vacuum of 10^{-5}torr at a rate of 4°C/min by installing a heating attachment. In all cases, the comparison method was used with the Ni standard sample. Temperatures were measured by using a platinal thermocouple.

The surface and inside of the film sample were analyzed using the photoelectron spectrometer ESCA, JPS-90SX supplied by JEOL Ltd. The Mössbauer absorption spectra were measured by the conventional transmission method using the Mössbauer effect measuring unit AME50 supplied by Israel Elsinton Co., Ltd. ^{57}Co (25mCi) was used as the γ-ray source, and pure iron was used as the standard sample.

3. Experimental Results and Discussion

3-1. Synthesis of Samples

The iron materials used were iron nitrate, iron chloride, iron oxalate, and iron oxide. The lithium materials used were lithium nitrate, lithium chloride, and lithium carbonate. The bismuth materials used were bismuth nitrate and bismuth oxide. The iron nitrate and iron chloride dissolved well in the solvent (ethylene glycol), while the iron oxalate did not. All of the lithium materials dissolved. The bismuth nitrate dissolved well in the solvent, but yellow precipitation of bismuth oxide readily occurred due to oxidation of nitric acid ions during stir by heating. To prevent the system from being heterogeneous, bismuth oxide was used; it was mixed with the dried materials of lithium and iron, and then fired. For chlorides, the analysis of sintered bodies showed residual chlorine, and the deposits of γ-ferrite and α-lithium ferrite were found on the rapidly quenched samples. Therefore, nitrates were used for both iron and lithium. Besides the sol-gel method, the solid-phase reaction method was used for obtaining sintered bodies by mixing iron oxide, lithium carbonate, and bismuth oxide.

Figure 1 shows the X-ray diffraction patterns of sintered bodies that have been heat-treated in the system of $20Li_2O\cdot 30Bi_2O_3$. The iron-lithium mixture dried at 350°C had no definite analysis peaks. The dried product, to which bismuth oxide was added, was heat-treated at increasing temperature. When heat-treated at 600°C, crystals of bismuth-iron complex oxide β-ferrite, and bismuth oxide were precipitated. At 750°C a single phase of bismuth ferrite was precipitated. At higher heat treatment temperatures, the crystals were partially melted and cooled gradually in the

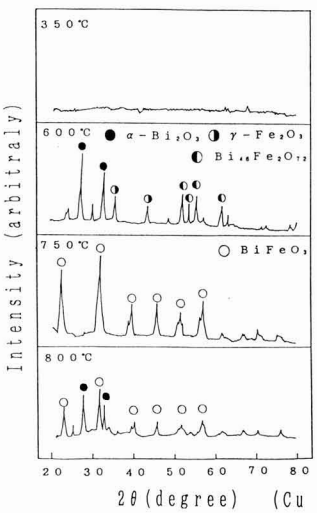

Fig. 1. X-ray diffraction pattern in the system of $20Li_2O\cdot 30Bi_2O_3\cdot 50Fe_2O_3$. Sintering temperature: 750°C.

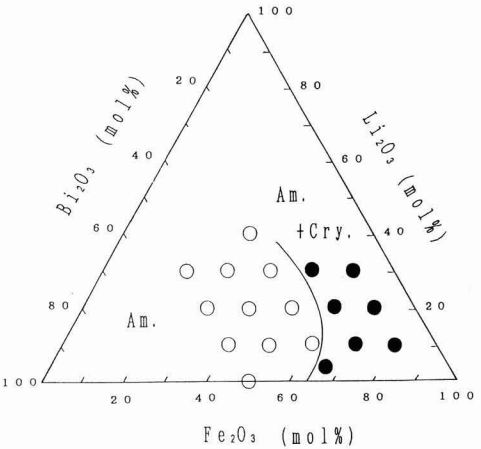

Fig. 2. Amorphous formation range in the system of Li_2O-Bi_2O_3-Fe_2O_3.

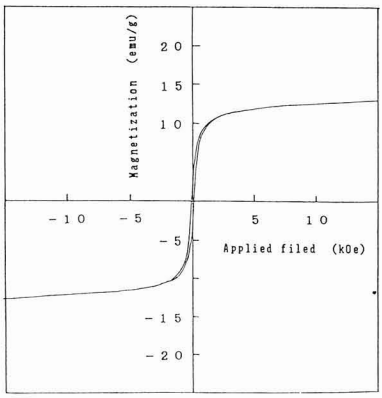

Fig. 3. Magnetic hysteresis loop of amorphous $20Li_2O$ $30Bi_2O_3$·$50Fe_2O_3$ at room temperature.

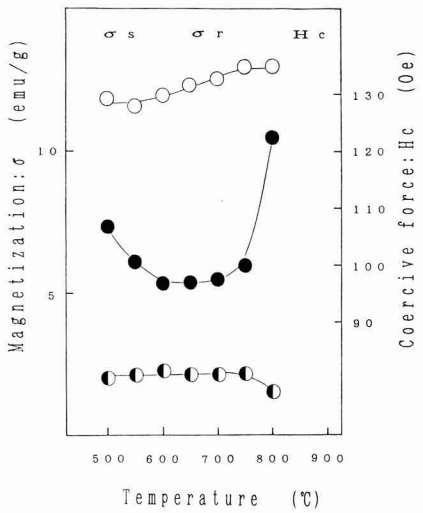

Fig. 4. Magnetic properties of amorphous $20Li_2O$ $30Bi_2O_3$·$50Fe_2O_3$ specimen at room temperature.

oven, precipitating a-bismuth oxide crystals. With reference to the above results, the sintered bodies were prepared at 750°C so that a single phase product was yielded, and then the sintered bodies were melted.

3-2. Amorphous Formation Range

Figure 2 shows the amorphous formation range determined under the firing condition established in 3-1. Amorphous substances were obtained in the range of Fe_2O_3, 30-60mol.%; Bi_2O_3, 30-50mol%; and Li_2O, 0-50mol%. Outside this range, the mixed phase of amorphous substances and crystals was obtained. The crystals precipitated were β-ferrite, α-lithium ferrite, and α-bismuth oxide. When the product of a similar composition range was prepared by the solid-phase reaction method using iron oxide, lithium carbonate, and bismuth oxide, crystals of β-ferrite were precipitated, and the amorphous formation range was narrowed at a content of iron oxide above 50mol%. The reason for this was considered to be that nonuniform reaction in the solid-phase reaction method left part of the iron oxide unreacted, which changed into β-ferrite.

3-3. Magnetic Properties

Figure 3 shows the magnetic hysteresis loop of the quenched sample in the system of amorphous $20Li_2O$ ·$50Fe_2O_3$ at room temperature. The saturation magnetization (σs), residual magnetization (σr), and coercive force (Hc) in an applied field of 15KOe were 12.8emu/g, 2.63emu/g, and 101Oe, respectively.

Figure 4 shows the magnetic properties of the unmelted sintered body in the system of amorphous $20Li_2O$·-$30Bi_2O_3$·$50FeO_3$ as a function of firing temperature. The value of saturation magnetization increased with an increase in firing temperature of the pretreated sintered body. The magnetism-generating mechanism is not always stable when antiferromagnetic spin arrangement is amorphous, which results in ferromagnetic behavior. At lower firing temperatures, different crystalline phases exist, which form a non-magnetic phase. The increase in firing temperature provides single phase bismuth ferrite, which increases the spin involving the generation of magnetism, thereby increasing the value of magnetization. The residual magnetism was almost constant as the temperature increased. The coercive force decreased at temperatures up to 700°C, and then increased at higher temperatures.

One of the reasons why the coercive force changes with the heat-treating temperature of sintered bodies may be the ease of movement of the domain wall. In this system, non-magnetic crystals like bismuth oxide exist when unmelted sintered bodies are fired at a low temperature. In the sample obtained by melting these mixed crystals and quenching them, different phases based on non-magnetic crystals exist and serve to pin the domain wall movement, with an increase in coercive force being observed. When the sample is pretreated at a high temperature too, an increase in coer-

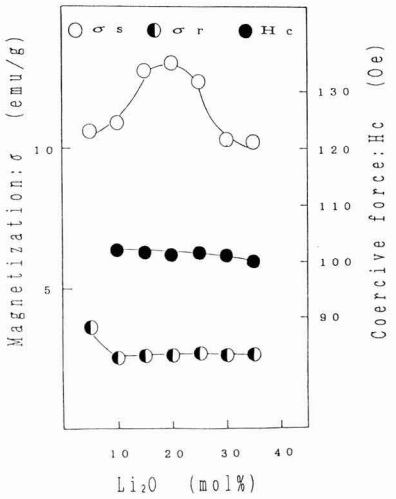

Fig. 5. Magnetic properties in the system of amorphous $xLi_2O\cdot(70-x)Fe_2O_3\cdot30Bi_2O_3$ at room temperature.

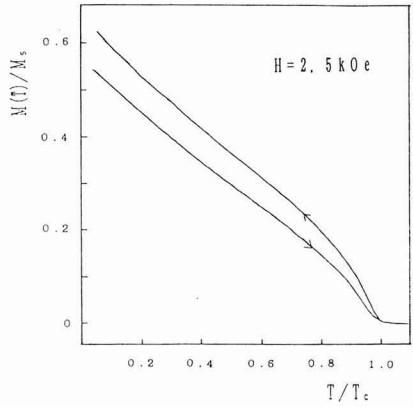

Fig. 6. Thermomagnetic curve of amorphous $20Li_2O\cdot30Bi_2O_3\cdot50Fe_2O_3$ specimen in the applied magnetic field of 2.5kOe.

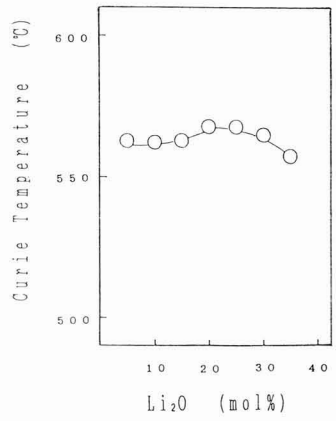

Fig. 7. Curie temperature in the system of amorphous $xLi_2O\cdot(70-x)Fe_2O_3\cdot30Bi_2O_3$.

cive force is observed for the same reason. When the coercive force Hc is the minimum, this amorphous substance has a multi-magnetic domain structure, and the magnetization occurs mainly due to the domain wall movement.

Figure 5 shows the magnetic properties as a function of lithium content. The residual magnetization σr and coercive force Hc were almost unchanged. Magnetization in an amorphous substance is governed by the domain wall movement, and this property is unchanged regardless of the Li_2O content. The saturation magnetization σs has a maximum value at a lithium content of 20mol%. The reason for this is probably the existence of a majority quantity of amorphous phase exhibiting magnetization. With a smaller proportion of lithium, less iron reacts with lithium to form spinel cluster, and excess iron ions exist as a paramagnetic phase.

Figure 6 shows the thermomagnetic curve of amorphous ferrite in the system of $20Li_2O\cdot30Bi_2O_3\cdot50Fe_2O_3$. An accurate Curie point was not determined from these results, because the magnetization decreased ferromagnetically and the curve was slanted near the Curie point. The Curie point was therefore estimated to be 563°C by extrapolation. It is characteristic of amorphous substances to have a slanted thermomagnetic curve, and this is because of their ferromagnetic behavior. When the sample was cooled at a rate of 4°C/min in the same magnetic field, it did not show irreversible change, and the value of magnetization rather increased. This is probably because, since the amorphous substance exists inherently in the metastable state, it is thermally unstable and part of the amorphous phase is changed into γ-ferrite, magnetite and so on by heating. The appearance of these ferromagnetic substances provided this effect in addition to the normal characteristics of amorphous ferrite.

Figure 7 shows the Curie temperature as a function of Li_2O content. The Curie temperature does not show significant change with Li_2O content. The change in Curie temperature is similar to the change in saturation magnetization with Li_2O content; the Curie temperature reaches the maximum at a Li_2O content of 20mol% and then decreases with increasing Li_2O content. The Curie temperature is lower than that of α-lithium ferrite or magnetite, and the thermomagnetic curve does not change stepwise. This suggests that the magnetization is not directly caused by these ferromagnetic crystals.

3-4. Mössbauer Absorption Spectra

Figure 8 shows the ^{57}Fe Mössbauer absorption spectra of amorphous ferrite in the system of $20Li_2O\cdot30Bi_2O_3\cdot50Fe_2OV3$ at room temperature. As the results of Mössbauer absorption spectrometry of calcium-base amorphous ferrite, it has been reported that the amorphous phase is divided into paramagnetic and ferromagnetic phases, and the paramagnetic phase shows two peaks due to quadrupole splitting, while the ferromagnetic phase shows six peaks due to magnetic splitting.[6] In the present study, therefore, it was thought that the central peak splitting into two was the

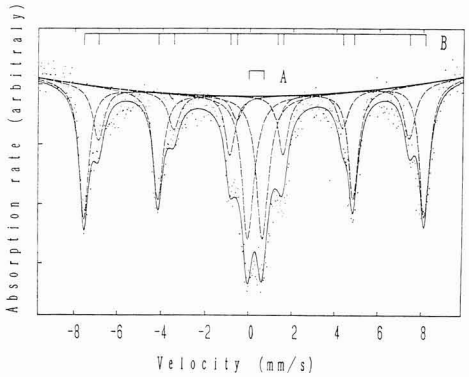

Fig. 8. ^{57}Fe Mössbauer absorption spectra of amorphous $20Li_2O{\cdot}30Bi_2O_3{\cdot}50Fe_2O_3$ specimen at room temperature.

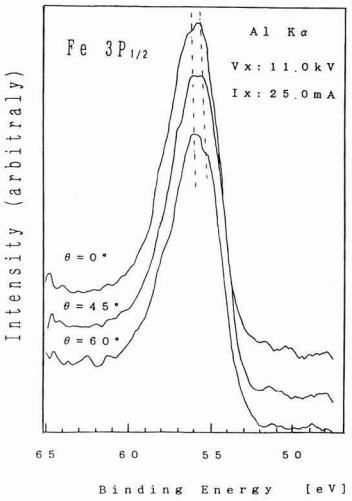

Fig. 9. XPS spectra of amorphous $20Li_2O{\cdot}30Bi_2O_3{\cdot}50Fe_2O_3$.

peak of the paramagnetic phase due to quadrupole splitting (Phase A), and the other peaks were the peaks of the ferromagnetic phase due to magnetic splitting (Phase B). Symmetric positioning of peaks means that quadrupole magnetic splitting does not occur and that paramagnetic and ferromagnetic phases exist independently.[9] Both phases have a wide line width. The half-value width of these phases are 0.66mm/s and 0.55mm/s, respectively, which are high values peculiar to amorphous oxides. This means a high internal distortion.[10] The isomer shifts of these two phases are 0.29mm/s and 0.33mm/s, respectively, which means that Fe ions exist in the form of Fe^{3+}. The peaks of the two kinds occur in a ratio of about A:B=4:5 when a Lorentz-type function is used, which means that about half of the amorphous phase exists as ferromagnetic phase.

In phase A, the value of quadrupole splitting is 0.66mm/s, which is lower than that of calcium-base or zinc-base amorphous substance. This is because the electric field gradient is smaller, resulting in less polarization.

In phase B, the magnitude of internal magnetic field is 483(±46)kOe. Such a wide distribution of internal magnetic field suggests that the sample is an amorphous substance and the arrangement of atoms is nonuniform. The existence of a shoulder of another spectrum or 1 and 2 spectra in phase B means the existence of two kinds of ferromagnetic phases. When the intensity ratio of the peak area for each separated peak is determined by assuming a Lorentz-type absorption curve on Lines 1-6, B_1:B_2=5:2 is obtained. The wide spectrum width suggests that the sites of iron ions have a wide distribution. Assuming that the magnetic moment of B_1 and B_2 phases is arranged magnetically, the value of magnetization at room temperature can be calculated as follows:

$$\sigma_{RT} \approx (\text{Number of Fe atoms in 1g}) \times (\text{proportion of ferromagnetic phase}) \times (\text{ratio of } B_1 \text{ to } B_2) \times 5 \times \mu_B = 7.98 \times 10^{20} \times 0.555 \times 0.714 \times 5 \times 9.27 \times 10^{-21} \approx 14.7 \text{ (emu/g)}$$

where μ_B: Bohr magneton.

Although the above result is σ_{RT}=14.7emu/g, the value of saturation magnetization at room temperature is lower than the above value, being 12.8emu/g. At room temperature, the spins do not always arrange regularly because of thermal energy. In addition, it is not thought that they arrange fully ferrimagnetically because of amorphous condition. Also, since the Bohr magneton is a theoretical value in terms of one free atom, the interaction with other atoms is neglected. Considering these factors, the calculated value agrees nearly with the measured value.

3-5. Photoelectron Spectroscopy

Figure 9 shows the photoelectron spectroscopy spectra of amorphous ferrite $20Li_2O{\cdot}30Bi_2O_3{\cdot}50Fe_2O_3$ obtained in this experiment. The figure shows the photoelectron spectra of 3P electron, $Fe3P_{1/2}$, directly affected by 3d electron with magnetic moment.

Before the measurement was made, the specimen was etched with argon gas and carbon on its surface was removed. The parameter θ is the inclination of the specimen with respect to the photoelectron detector. θ=60° indicates the spectrum on the specimen surface, while θ=0° indicates that within the specimen. Each peak is split into two; the magnitude of splitting is about 0.6eV. The peak shifts to the low-energy side as the measurement point approaches the surface. This means that the binding of iron ions to oxygen is weak on the surface layer unlike within the specimen. Comparing the photoelectron spectra of a quenched sample of lithium-base bismuth ferrite with those of bismuth ferrite, the peak of lithium-base bismuth ferrite was split into two, while split peaks were not observed on the spectra of simple bismuth ferrite. The photoelectron spectra of $Fe_3P_{1/2}$ of corundum-type α-iron oxide and inverse-spinel-type nickel ferrite have an energy difference of about 0.6eV. Fe^{3+} ions exist in the state of the 6-coordinate site in α-iron oxide, and the 4-coordinate plus 6-coordinate sites in nickel ferrite. These measurement results suggest the existence of two

coordinate sites of iron ions. That is, the peak at the higher energy side indicates the peak of Fe^{3+} at the 6-coordinate site, while the peak at the lower energy side indicates the peak of Fe^{3+} at the 4-coordinate plus 6-coordinate sites.

For the peaks split into two, it is thought that many Fe^{3+} ions at the 6-coordinate site exist at $\theta=60^{\circ}$ (surface layer), and as θ approaches 0°, the peak intensity is reversed, with many Fe^{3+} ions at the 4-coordinate plus 6-coordinate sites existing in the amorphous ferrite.

4. Conclusion

Amorphous ferrites in the system of $Li_2O \cdot Fe_2O_3 \cdot Bi_2O_3$ were prepared by the sol-gel method. The composition range giving an amorphous phase in this system was found to be Fe_2O_3:30-60mol%, Li_2O: 0-50mol%, and Bi_2O_3:30-50mol%. Especially in the composition of $20Li_2O \cdot 30Bi_2O_3 \cdot 50Fe2O_3$, the saturation magnetization and coercive force were 12.8emu/g and 101Oe (applied field: 15kOe) at room temperature, respectively, and ferromagnetic behavior was observed at a Curie temperature of about 563°C. The crystallization temperature of this composition was 430°C, 580°C, and 730°C, and the precipitation of α-lithium ferrite and γ-ferrite due to crystallization was observed. ^{57}Fe Mössbauer absorption spectra and photoelectron spectroscopy spectra indicated that most Fe ions exist as Fe^{3+} ions. This amorphous ferrite consisted of phase A of paramagnetic phase and phase B of ferromagnetic phase. In each of these phases, Fe^{3+} ions existed in the states of both the 6-coordinate site and the 4-coordinate plus 6-coordinate sites. Supposing that the B_1 and B_2 phases behave ferromagnetically in phase B, and assuming a simple ferromagnetic model, the calculated value of saturation magnetization agrees nearly with the measured value.

References:

1) E.W. Gyorgy, K. Nassau, M. Eibschutz, J.V. Waszczak, C.A. Wang and J.C. Shelton, J. Appl. Phys. 50, 2883-86 (1979).
2) H. Laville and J.C. Bernier, J. Mat. Sci., 15, 73-81 (1980).
3) M. Sugimoto and N. Hiratsuka, J. Mag. Magn. Mat., 31-34, 1533-34, (1983).
4) N. Ota, M. Okubo, S. Matsuda and K. Suzuki, J. Mag. Magn. Mat., 54-57, 293-94, (1986).
5) K. Suzuki and A. Matsumoto, Jpn. J. Applied Physics. 56-5, 596-600, (1987).
6) S. Nakamura and N. Ichinose, Journal of the Ceramic Society of Japan, 96, 5, 590-94, (1988).
7) S. Nakamura and N. Ichinose, The Ceramic Society of Japan 1987 Annual Proceedings, 1027-28, (1987).
8) S. Nakamura and N. Ichinose, The Ceramic Society of Japan 7th Electronic Material Seminar Proceeding, 64-65 (1987).
9) M. Katada and H. Sano, Metal Surface Technology, 37, No.3, 94-10, 2, (1986).
10) M. Sugimoto, T. Takahashi, K. Noya, N. Hiratsuka and Y. Soeno, Journal of Japan Applied Magnetics Institute, 9, No.2, 167-172, (1985).

This article is a full translation of the article which appeared in Nippon Seramikkusu Kyokai Gakujutsu Ronbunshi (Japanese version), Vol.98, No.5, 1990.

Effect of Microstructure on Cyclic Fatigue Properties of Al_2O_3 Ceramics and Al_2O_3 Composites

Hidehiro Kamiya, Manabu Takatsu, Kanji Ohya*,Masashi Ando and Akiyoshi Hattori

Nagoya Institute of Technology , Gokiso-cho, Showa-ku, Nagoya 466, Japan
*R/D NTK Technical Ceramics Div. of NGK Spark Plug Co., Ltd. , Takatsuji-cho, Mizuho-ku, Nagoya 467, Japan

The cyclic fatigue properties of three kinds of toughened Al_2O_3 composites added with SiC whisker, TiC and partially stabilized ZrO_2 particles were compared with results of four kinds of Al_2O_3 ceramics with different purities. The effects of stress amplitude and initial crack size on fatigue properties were investigated by using polished and pre-cracked samples. Furthermore, the accelerated phenomena on initiation and propagation velocities of fatigue crack under cyclic loading condition were quantitatively assessed by the estimation method using an experimental relation based on subcritical crack growth velocity and static fatigue data.

As results, in the case of polished sample, the accelerated effect on fatigue that 99.99% and 99% Al_2O_3 ceramics typically showed were restrained in Al_2O_3 composites. The cyclic fatigue properties of Al_2O_3 composites used in this paper can be successfully estimated under wider condition of stress application from the data on static fatigue than the case of Al_2O_3 ceramics. On the condition that a sample was pre-cracked by Knoop indenter, Al_2O_3 composites hindered the accelerated effect on fatigue crack propagation under cyclic loading as well. Especially, the cyclic fatigue data of pre-cracked ZrO_2/Al_2O_3 composite agreed well with the estimated value from static fatigue properties.

Key-words: Cyclic fatigue, SiC whisker Al_2O_3 composite, TiC/Al_2O_3 composite, ZrO_2/Al_2O_3 composite, Al_2O_3, Ceramics

1. Introduction

A variety of composite materials in which microparticles or whiskers are dispersed in SiC, Si_3N_4, Al_2O_3 and other ceramic materials have been extensively studied, in an attempt to improve mechanical properties, such as toughness and strength, of the matrix materials.[1-4] These composites are assessed, for the most part, by their fracture toughness and strength, and, to a much lesser extent, by their cyclic fatigue properties and resistance to thermal shocks, which are important properties in assessing them as commercial structural materials. It is of particular importance to understand their cyclic fatigue properties, because it is anticipated that cyclic loading may cause the dispersed materials to become the fracture origins for the fatigue-induced cracks. The composite materials may have improved fracture toughness, which, however, is not necessarily accompanied by improved strength,[1] and it is necessary to assess the mechanical properties of the composite sinters from various aspects.

In this study, the authors have carried out cyclic fatigue tests at 550Hz for 3 types of composites of alumina dispersed with SiC whiskers, partially stabilized ZrO_2 particles and TiC particles, and 4 types of alumina ceramics of varying purity. These dispersed materials are known for their effects of greatly improving strength and toughness of alumina. In the tests, stress amplitude was varied to investigate the effects of load stress conditions on the fatigue properties. Furthermore, the properties of mirror-polished samples were compared with those of the samples pre-cracked by a Knoop indenter, to investigate the effects of the initial crack size. The test results were analyzed by the empirical equation for the crack propagation speed, proposed previously,[5] in an attempt to quantitatively assess cyclic fatigue behavior of composite ceramic materials.

2. Experimental Procedure

2-1. Experimental Apparatus and Procedure

The bimorph type experimental apparatus with a piezoelectric material as the driving source was used for the cyclic fatigue tests, in which cyclic stresses were applied to the ceramic test sample via a 3-point bending jig, attached to the free end of a metallic cantilever which was vibrated by a voltage alternating at a frequency equivalent to the resonance frequency of the system applied to the piezoelectric ceramic plates provided on the upper and lower sides of the cantilever. The apparatus is described in detail elsewhere.[6] The load stress frequency was set at 550Hz, and the wave form was almost sinusoidal. The load stress ratio R, i.e., the ratio of the maximum stress σ_{max} to the minimum stress σ_{min}, was varied from 0.1 to 1.0 at several points; the former stress ratio represented the almost perfect pulsating condition, while the latter was in the static fatigue region. Those samples which were not fractured when exposed to cyclic stresses for 10^5sec or more were withdrawn from the test system, and their bending strength was measured.

2-2. Mechanical Properties of Fatigue-Tested Samples

Of the 3 types of the composite Al_2O_3 ceramics samples, those reinforced with SiC whiskers and TiC particles were hot-pressed sinters containing the reinforcing materials at 30vol%.The ZrO_2/Al_2O_3 type was sintered without pressure, and contained the reinforcing material at 40vol%,

Table 1.Mechanical properties of Al_2O_3 ceramics and Al_2O_3 ceramics and Al_2O_3 composite.

(a) Al_2O_3 ceranics

Al_2O_3 content [%]	density ρ [g/cm^3]	Vicker's hardness H_v [GPa]	fracture toughness K_{Ic} [MNm$^{-3/2}$]	bending strength S_f [MPa]	Weibull's modulus m [-]
99.99	3.96	17.8	2.7	474	6.5
99	3.93	16.0	3.3	375	16.2
97	3.69	12.2	2.8	317	10.9
92	3.49	10.1	2.7	325	13.3

(b) Al_2O_3 composites

additive name	density ρ [g/cm^3]	Vicker's hardness H_v [GPa]	fracture toughness K_{Ic} [MNm$^{-3/2}$]	Young's modulus E [GPa]	bending strength S_f [MPa]	Weibull's modulus m [-]
SiC(w)	3.74	21.9	7.0	428	871	8.1
TiC(p)	4.25	18.2	5.4	429	631	5.8
ZrO_2(p)	4.68	14.9	4.7	305	748	7.3

where ZrO_2 was partially stabilized with 3mol% of Y_2O_3 (HSY-3.0, Dai-ichi Kigenso) and Al_2O_3 as the matrix was 99.99% pure (TM-D, Taimei Kagaku). Four types of Al_2O_3 ceramics of varying purity were also tested, for comparison; two were 99.6% pure (Al 160SG, Showa Keikinzoku) and 99.99% pure (TM-D, Taimei Kagaku) Al_2O_3 powders CIP-formed and pressurelessly sintered at 1550° and 1350°C, respectively, while the other 2 types were 97% and 92% pure commercial sinters. The 99.6% and 99.99% pure Al_2O_3 powders were those used as the matrices of the composite materials.EDAX analysis was used to identify the impurities in these test samples, and Mg and Si were found in the grain boundaries.

Each sample was cut into 3×4×50mm, rod-shape specimens, which were chamfered and mirror-polished. These were for the 3-point bending tests (span, 30mm. Cross-head speed 1.6μm/s), Vickers hardness tests under a load of 98N, and measurements of critical stress intensity factor. **Table 1** shows the hardness test results, and **Fig.1**(a) the bending strength distributions. As the purity of sintered Al_2O_3 increased, its strength and hardness increased, but its fracture toughness and strength distribution tended to be degraded. Combination of Al_2O_3 with the reinforcing agent had the effect of increasing hardness and fracture toughness, but degraded strength distribution.

Cyclic fatigue tests were also conducted for some of the precracked specimens, i.e., the mirror-polished specimens which were precracked by a Knoop indenter under varying loads, in order to investigate the effects of the initial crack size on the mechanical properties. Figure 1(b) shows the relationship between the tensile stress at a time of fracture and Knoop indented load for the bending-tested specimens. The TiC/Al_2O_3 sample was more degraded in strength by precracking than were the 99% pure Al_2O_3 and ZrO_2/Al_2O_3 samples, to a level equivalent to that of the 99% pure Al_2O_3 sample. It was actually observed that the TiC/Al_2O_3 sample, though mirror-polished, was degraded in strength, when fractured from the surface flaws, and the data of those specimens having surface flaws on the fracture surfaces were eliminated from the discussions.

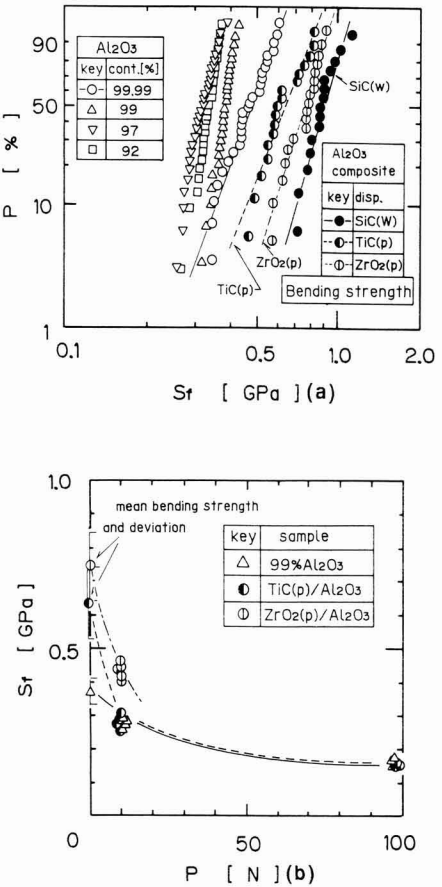

Fig. 1. (a) Weibull's distribution of bending strength on toughened Al_2O_3 composites used SiC whisker, TiC and ZrO_2 particles and different purity Al_2O_3 ceramics. (b) Dependence of Knoop indented load on bending fracture stress for pre-cracked samples.

3. Results

3-1. Cyclic Fatigue Test Results of Mirror-Polished Samples

Figure 2 shows the cyclic fatigue test results of the sintered Al_2O_3 samples of varying purities, for comparison, in which the maximum loading stress (σ_{max}) is plotted against fatigue failure life t_f, i.e., the time span extending from the initiation of loading to fracture of the specimens, with loading stress ratio (R) as a parameter. The data and the ranges described on the axis of ordinates represent the averaged bending strength values and the range of their standard deviations, determined beforehand. The data marked with the left-directing arrows, at around 1sec, represent those of the specimens which were fractured immediately after the load was increased to near the set level. Those marked with the right-directing arrows, on the other hand, represent those data of the samples which were not

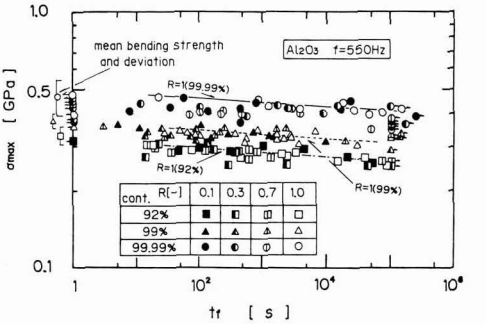

Fig. 2. Effect of stress ratio (R) on relation between maximum loading stress and fatigue failure life of polished different-purity Al_2O_3 ceramics.

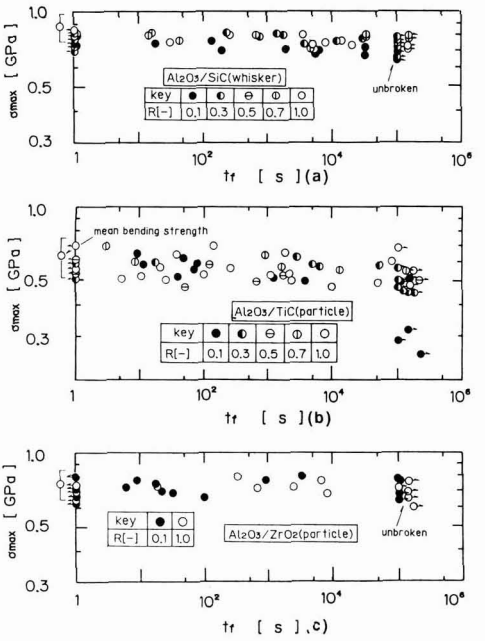

Fig. 3. Effect of stress ratio (R) on relation between maximum loading stress and fatigue failure life of polished Al_2O_3 composites.
(a) SiC whisker-toughened Al_2O_3, (b) TiC-toughened Al_2O_3, (c) ZrO_2-toughened Al_2O_3.

fractured for a time span extending to around 10^5sec. The straight lines represent the σ_{max}–t_f relationships of those samples tested at R=1. These lines had almost the same slope, and the higher-purity sample of higher average bending strength tended to have higher maximum loading stress. As for the effects of stress loading conditions, the data of the 99% and 92% pure Al_2O_3 samples subjected to varying R ratios were distributed around the line representing the relationship at R=1. Those of the 99.99% pure Al_2O_3 sample tested at an R ratio other than unity, on the other hand, were distributed almost totally below the line of R=1, indicating that the composite sample, because its σ_{max}–t_f relationship was represented by the single straight line, was independent of the R ratios, unlike that of the 99.99% pure Al_2O_3 sample where the fatigue life was determined by the cyclic fatigue rather than the static fatigue. Thus, combining Al_2O_3 with the reinforcing agent decelerated the progress of cyclic fatigue; it should be noted that the 99.99% pure Al_2O_3 served as the matrix of the ZrO_2/Al_2O_3 system. It is therefore considered that the polished composite samples have better pulsating cyclic fatigue characteristics than the single phase samples. The precracked samples were also investigated in a similar manner.

3-2. Cyclic Fatigue Test Results of Samples Precracked by a Knoop Indenter

Figure 3 shows the σ_{max}–t_f relationships for the 3 different composite samples of Al_2O_3 reinforced with (a) SiC whiskers, (b) TiC particles, and (c) ZrO_2 particles. Each sample had higher σ_{max} values than the Al_2O_3 samples of varying purities, because of the high average bending strength. The slope of the straight line was smaller, indicating the possibility that the fatigue limit of each composite sample is closer to bending strength than those of the single-phase Al_2O_3 samples.

No significant effect of loading stress amplitude was observed with each Knoop test.

Figure 4 shows the results of the 99% pure Al_2O_3 sample for comparison, in which the maximum loading stress (σ_{max}) is plotted against fatigue failure life t_f for the specimens precracked by a Knoop indenter under three different loads, 0, 9.8 and 98N (the sample subjected to no load was the as-polished one). The solid and broken straight lines represent the relationships of the specimens tested at

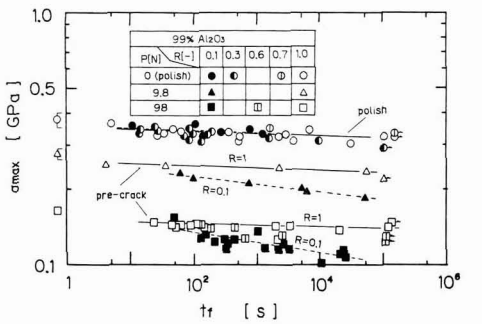

Fig. 4. Effect of Knoop indented load on relation between maximum loading stress and fatigue failure life of 99% Al_2O_3 ceramics.

R = 1 and 0.1, respectively. The data and the ranges described on the axis of ordinates again represent the averaged bending strength values and their standard deviations, determined beforehand. The as-polished sample had almost the same σ_{max}–t_f relationships under the static and cyclic fatigue conditions. For those precracked under a load of 9.8 or 98N, on the other hand, the specimens were fractured at lower maximum loading stresses under the cyclic fatigue conditions than under the static fatigue conditions. It is also noted that the cyclic fatigue conditions gave a

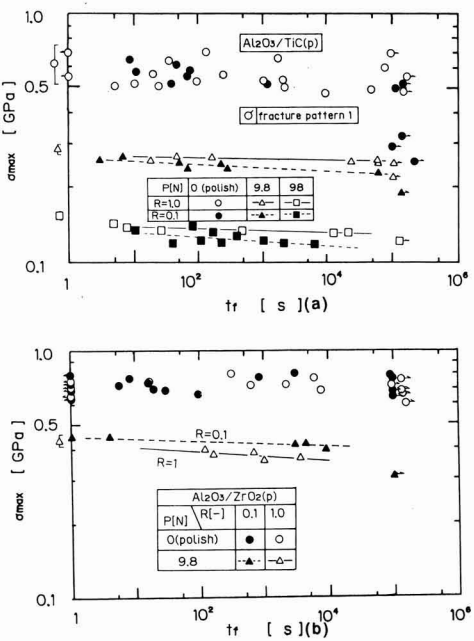

Fig. 5. Relation between maximum loading stress and fatigue failure life of pre-cracked Al_2O_3 composite used Knoop indenter.
(a)TiC-toughened Al_2O_3 (b) ZrO_2-toughened Al_2O_3.

larger slope of the straight line. No effects of different indented loads of 9.8 and 98N was observed with respect to the straight line slope. The slope, however, tended to increase as R ratio decreased, by which was meant that the n-value was affected by the R level more than the initial crack size, under the condition ranges adopted in this study. The authors have also observed that the precracked Si_3N_4 samples were fatigued faster under cyclic loads than the as-polished ones.[6] The comparison of results of the as-polished Al_2O_3 and Si_3N_4 samples[7,8] with those of the precracked ones[9,10] indicates that the latter samples are fatigued notably faster than the former.

Figure 5 shows the results the similar tests for the Al_2O_3 samples dispersed with (a) TiC particles, and (b) ZrO_2 particles, to demonstrate the effects of reinforcement. The TiC-reinforced sample had a σ_{max}–t_f relationship similar to that of the single-phase Al_2O_3 sample. Furthermore, the relationship of the precracked sample was similar to that of the 99% pure Al_2O_3 sample, because the strength of the former sample decreased to that of the latter sample under the cyclic or static fatigue conditions. It is also noted that the broken straight line representing the σ_{max}–t_f relationship of the precracked sample under the cyclic fatigue conditions at R = 0.1 had a more moderate slope than that of the 99% pure Al_2O_3 sample under the same conditions, also indicating the effects of the reinforcement for controlling progress of the fatigue of the precracked sample under the cyclic loads.

Figure 5 (b) shows the σ_{max}–t_f relationships of the ZrO_2-reinforced Al_2O_3, where the broken line representing the relationship under the cyclic fatigue conditions is above the solid line representing that under the static fatigue conditions. Such a phenomenon is interesting in that it is peculiar to the ZrO_2 system, and was not observed with other precracked ceramic materials, including sintered Si_3N_4.

The results obtained in this study have confirmed, though qualitatively, that reinforcement with the other materials effectively improves the cyclic fatigue characteristics of sintered Al_2O_3 under the pulsating loads, both for the as-polished and precracked samples. It is difficult, however, to quantitatively assess the effects of the reinforcement through the conventional method, because of the greatly fluctuating fatigue failure life results, in particular those of the as-polished samples. Therefore, a quantitative assessment was attempted using the correlation $V = AK_I^n$,[11] where V is the crack propagation speed (V = da/dt) in the subcritical crack growth (hereinafter referred to as SCG) discussed previously,[5] K_I is stress intensity factor, and A and n are constants.

4. Discussion

The fatigue characteristics of ceramic materials under cyclic loads may be represented by the following formula, which is obtained by integrating the correlation developed for the Subcritical Crack Growth (SCG)[11]:

$$\log(\sigma_{max}/S_f) = -\log(g^{-1}\cdot t_f)/(n+1) + B \quad \ldots\ldots (1)$$

where, g^{-1} is the term related to load stress waveform, given by equation (2),[6] and B is regarded as a constant. S_f is the bending strength of each fatigue-tested sample, estimated by the method discussed previously.[5]

$$g^{-1} = \int_0^{\lambda} \{\sigma(t)/\sigma_{max}\}^n/\lambda dt. \quad \ldots\ldots (2)$$

where, λ is one cycle time of the load stress waveform.

Assuming that the constants n and A are constant, irrespective of load stress conditions, the fatigue behavior under cyclic loads may be estimated, using equation (1), from the actual results under static loads, the conditions which are represented by the simplest form of R = 1. It has been confirmed that the above assumption is applicable to some materials, such as relatively low-purity Al_2O_3, which are subjected to a load stress of an R ratio close to unity.[11] In this study, the authors investigated whether or not the above assumption was applicable to the composite and high-purity Al_2O_3 samples at widely varying R ratios under the pulsating load stresses.

The fatigue results of the 4 types of Al_2O_3 samples were analyzed using equations (1) and (2) and the method discussed previously,[5] to estimate the constants n and B values and bending strength S_f. The results are shown in **Fig. 6** for (a) 99.99%, (b) 99%, (c)97%, and (d) 92% pure Al_2O_3, where σ_{max}/S_f is plotted against $t_f \cdot g^{-1}$. The axis of ordinates gives the value of the left side of equation (1), while the axis of abscissas gives the first term of the right side of

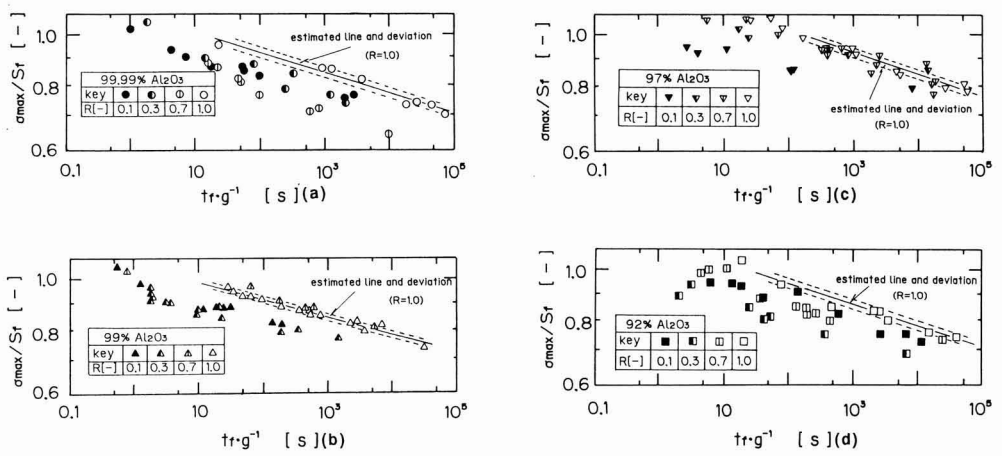

Fig. 6. Analysis of cyclic fatigue properties on polished different-purity Al_2O_3 ceramics by estimated method based on experimental equation (1) of subcritical crack growth.
(a) 99.99% Al_2O_3 ceramics (b) 99% ceramics Al_2O_3, (c) 97% Al_2O_3 ceramics (d) 92% Al_2O_3 ceramics.

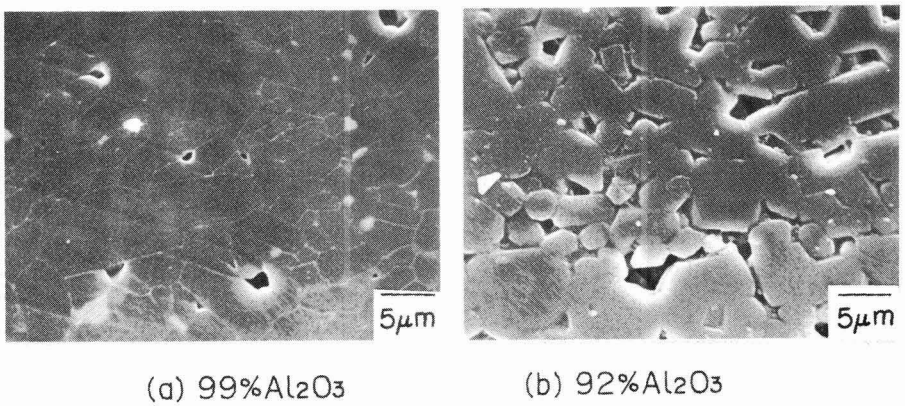

Fig. 7. Examples of microstructure on Al_2O_3 ceramics.
(a) 99% Al_2O_3 ceramics (b) 92% Al_2O_3 ceramics.

equation (1). The straight line in each figure represents the σ_{max}/ S_f–$t_f \cdot g^{-1}$ relationship, and the broken lines the range of the standard deviation. The results obtained under cyclic fatigue conditions will be distributed around the straight line, so long as the n and A values are constant.

In the case of the 99.99% pure Al_2O_3 sample (Fig. 6 (a)), the data obtained at below R = 1, even those obtained at R = 0.7, are shifted to the left side of the straight line for R = 1, by which is meant that assumption of n and A values being constant will overestimate the fatigue failure life. As the purity of the Al_2O_3 sample decreases, the data obtained at a smaller than unit R level approaches the straight line. It is particularly interesting to note that all the data of the 97% pure Al_2O_3 sample, except those obtained at R = 0.1 (almost complete pulsating conditions), are well represented by the single straight line, as shown in Fig. 6 (c). The data of the 92% pure Al_2O_3 sample obtained at a smaller than unit R level, however, are significantly apart from the straight line (Fig. 6 (d)), like those of the 99.99% pure Al_2O_3 sample, shown in Fig. 6 (a).

One explanation for the deviation of the cyclic fatigue results from the straight line obtained by the static fatigue results, and the accelerated fatigue under the cyclic stress loads is that the non-linear fracture at the crack ends which prevents the cracks from being completely closed when the load pressing the sample is removed, even though it has been pulsating, and the stress generated as a result of the contact of the cracks at both ends, accelerate propagation of the cracks, as discussed by Reece.[12] In addition, Kawakubo considers the above effects to be more notable when the cracks meander more, and states that the cyclic fatigue results are in relatively good agreement with the results estimated using equation (1), when the grains are sufficiently large to cause the intragrain fracture or the glassy phase in the grain boundaries to be sufficiently thick, because cracks in such a system will make a straighter path.

In an attempt to compare the results of the 4 types of as-polished Al_2O_3 samples with each other, their structures were observed by a scanning electron microscope. The results are shown in **Fig. 7**, for the (a) 99% pure and (b)

Table 2.Mean grain size of Al_2O_3 ceramics.

Al_2O_3 content [%]	99.99	99	97	92
crystal size d [μm]	1.2	4.8	3.7	4.7

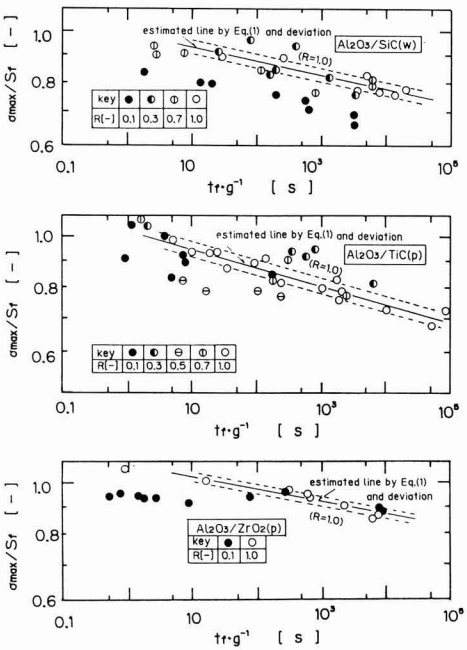

Fig. 8. Analysis of cyclic fatigue properties on polished Al_2O_3 composite by estimated method based on experimental equation (1) of subcritical crack growth.
(a) SiC whisker-toughened Al_2O_3 (b) TiC-toughened Al_2O_3 (c) ZrO_2-toughened Al_2O_3.

92% pure Al_2O_3 samples. Each sample was mirror-polished and thermally etched at 1300°C for 20min prior to the analysis. **Table 2** gives the mean grain size of each sample, determined by the SEM analysis. The grain boundaries of the 92% pure Al_2O_3 sample (Fig. 7 (b)) were thicker than those of the 99% pure sample, and became more porous by thermal etching. The 99.99% pure Al_2O_3 sample had a smaller grain size (1.2μm) than the others, whose grain sizes were about 4μm. Next, their ceramic structures are compared with each other. All the 99% pure Al_2O_3 specimens, having a smaller grain size and thinner grain boundary than the other samples, were fatigued faster than estimated under the cyclic load conditions at any R level tested, which is in agreement with Kawakubo's hypothesis.[13] As purity decreased to 99% and 97%, which was accompanied by the increased grain size and thickness of the grain boundaries, the data were represented by the single straight line in an increasingly wider range. However, the 92% pure Al_2O_3 sample, having the thickest grain boundaries, was fatigued faster than estimated, like the 99.99% pure sample. In the case of the as-polished samples, the microscopic cracks coming from the fracture origins, such as the impurity phases, precede crack propagation. It is considered that, in a low-purity system, cyclic load stresses may increase concentration of the impurity phases sufficiently to generate a stress at the interface with the alumina phase, to accelerate formation of the cracks. Increasing purity decreases quantity of the microcrack origins, with the result that the data are represented by the single straight line under a wider range of load stress conditions. At the same time, the cracks tended to be deflected more as purity increased, causing them to propagate faster.

Figure 8 presents the σ_{max}/S_f–$t_f \cdot g^{-1}$ relationships for Al_2O_3 reinforced with (a) SiC whiskers, (b) TiC particles and (c) ZrO_2 particles, where the meanings of the solid and broken straight lines are the same as those shown in Fig. 6. All the data of the SiC-reinforced composite sample, except those obtained at R = 0.1 (almost complete pulsating conditions), are well represented by the single straight line, drawn for the data obtained at R = 1. All the data of the TiC- and ZrO_2-reinforced samples, including those obtained at R = 0.1, are represented relatively well by the respective straight line.

Figure 9 compares the results of the single Al_2O_3 phase samples with those of the composite samples, in which the n value (a) and the $t_g \cdot g^{-1}$ value at 0.9 σ_{max}/S_f (b) are plotted against load stress ratio. The data for each R level, shown in Figs. 6 and 8, were processed by the least squares method to draw a straight line, the slope of which was used to estimate the n value. The $t_f \cdot g^{-1}$ value on the axis of ordinates in Fig. 9 (b) is dimensionless, reduced by the $t_f \cdot g^{-1}$ value at R = 1. As it nears unity, the data will move on towards the straight line, and as it parts from unity downwards, the fatigue-acceleration effects by the cyclic load stresses become more conspicuous. As shown in Fig. 9 (a), the n values of the composite samples are generally higher than those of the single Al_2O_3 samples; in particular,

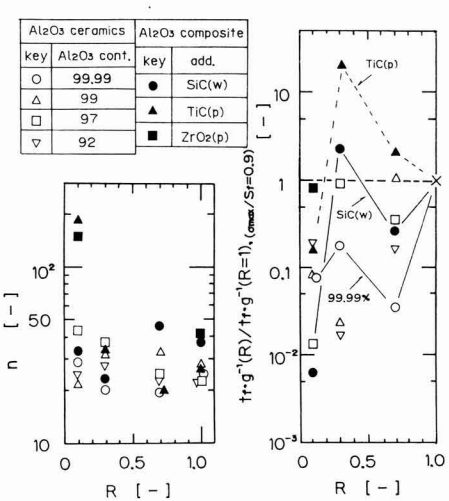

Fig. 9. Estimated value of parameter n in Eq. (1) and $t_f g^{-1}$ at σ_{max}/S_f=0.9 to analyze cyclic fatigue data in Figs. 6, 8.
(a) parameter n (b) $t_f \cdot g^{-1}$ at σ_{max}/S_f=0.9

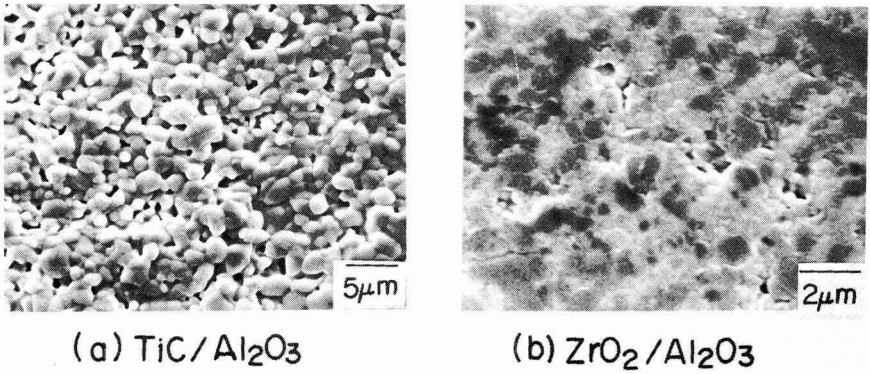

Fig. 10. Examples of microstructure on Al_2O_3 composite. (a) TiC (p)/Al_2O_3 (b) ZrO_2/Al_2O_3.

those of the TiC- and ZrO_2-reinforced samples are notably higher than the others at R = 1 (almost complete pulsating conditions). However, no significant effects of the R level are observed on the n values of the samples, except the above. In other words, the slope of the straight line representing the stress-life relationship is generally constant, irrespective of the load stress conditions. It is therefore possible to estimate to what extent the fatigue under cyclic stress conditions deviates from that under static stress conditions by comparing the reduced $t_f \cdot g^{-1}$ values shown in Fig. 9 (b). Taking the data of the 99.99% pure Al_2O_3 sample as an example, the life tends to be shorter than estimated when it is subjected to cyclic stresses at R The actually observed lives of the composite samples, on the other hand, are fairly close to those estimated, except that of the SiC-reinforced sample subjected to cyclic stresses at R = 0.1. The matrices of the composite materials prepared in this study were 99.99% and 99% pure Al_2O_3, whose cyclic fatigue results were not generally represented by the estimated straight lines. They were more resistant to cyclic load stresses, when combined with the reinforcing agents, and their lives were predicted by equation (1) under wider cyclic load stress conditions.

Several mechanisms have been proposed to account for the improved mechanical properties of composite materials; blocking, meandering and branching of the cracks by the dispersed particles,[14,15] or pulling-out of the cracks by whiskers.[16] Assuming that the dispersed particles cause the cracks to meander more, dispersion of these particles should accelerate fatigue of the composite materials, in accordance with the Kawakubo model.[13] The acceleration effects were more notably observed in the composite dispersed with SiC whiskers than those dispersed with the particles under the almost completely pulsating conditions. The fatigue of the whisker-dispersed composite might be partly accounted for by the crack meandering effects. However, it was observed that fatigue acceleration was controlled in the particle-dispersed systems. The structures of the composite materials reinforced with TiC and ZrO_2 particles were observed, in order to investigate the above phenomena. The results are shown in **Fig. 10** (a) and (b). The dark portions of both photographs represent Al_2O_3. These results show that both

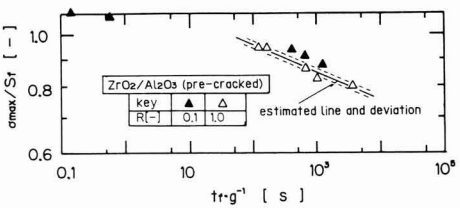

Fig. 11. Analysis of cyclic fatigue properties on pre-cracked ZrO_2/Al_2O_3 composite used Knoop indenter by estimated method based on experimental equation (1) of subcritical crack growth.

composites were of microstructures consisting of particles with average sizes of 1μm or less. It is difficult to explain the controlled fatigue acceleration of the particle-reinforced composites by a model which assumes that the cracks tend to move straight, because the crack propagation will be hindered greatly by the dispersed TiC or ZrO_2 particles known for high hardness or toughness. Fatigue acceleration under cyclic load stresses, therefore, is controlled by other mechanisms, such as relaxation of non-linear fractures and prevention of fatigue-causing crack formation by the dispersed phase. Lastly, the results of the precracked materials are discussed. Fatigue acceleration under cyclic load stresses is more notably expressed in the samples precracked by a Knoop indenter, and equation (1) is apparently useless for the analysis of the results of the single phase Al_2O_3 samples. It is however expected that the equation is useful for the analysis of the results of the ZrO_2/Al_2O_3 sample, because its stress-life relationship is shifted to the longer-life side from the relationship under static load conditions. **Figure 11** shows the σ_{max}/S_f $t_f \cdot g^{-1}$ relationship of the precracked ZrO_2/Al_2O_3, which indicates that the data obtained under cyclic load stress conditions (R = 0.1) are in good agreement with those obtained under static load stress conditions (R = 1). It has been thus confirmed that crack propagation is not accelerated under cyclic load stress conditions in the ZrO_2/Al_2O_3 composite system, whether it is precracked or

not. The controlled formation or propagation of the fatigue-causing cracks should be elucidated in the future.

4. Conclusions

Three types of Al_2O_3 composite samples and 4 types of single phase Al_2O_3 ceramics samples of different purities were subjected to pulsating load stress conditions of varying stress amplitudes, to investigate their fatigue behavior. The as-polished and precracked samples were tested, and pulsating frequency was set at 550Hz.

1) The relationship between maximum load stress and fatigue failure life was established for each sample type. No significant effect of stress load ratio (R) was observed on the fatigue behavior of each as-polished sample, whether it was reinforced or not. The analysis of the fatigue-acceleration effects under cyclic load stress conditions, using the empirical Subcritical Crack Growth (SCG) correlation, revealed that the effects appeared differently in the single Al_2O_3 samples, depending on their purities and characteristic structures, whereas they were effectively controlled in any of the composite samples.

2) The cyclic load stresses notably accelerated propagation of the cracks in the precracked, single Al_2O_3 samples. These effects, however, were substantially controlled in the composite samples dispersed with TiC or ZrO_2 particles, more conspicuously in the latter sample, where the fatigue behavior of the as-polished and precracked samples were well represented by the empirical SCG correlation. (Part of the results were presented to the 27th Ceramic Science Basic Seminar, held in Tokyo in January, 1989)

References:

1) N. Claussen, J. Steeb and R.F. Pabst, Am. Ceram. Soc. Bull., 56, 559-62 (1977).
2) R.P. Wahi and B. Ilschner, J. Mat. Sci., 15, 875-85 (1980).
3) H. Niihara and A. Nakahira, The Ceramic Society of Japan 1988 Annual Proceedings, p. 169 (1988).
4) P.F. Becher and G.C. Wei, ibid., 63, C-267-69 (1984).
5) M. Takatsu, H. Kamiya, H. Ohya, Y. Ogura and T. Kinoshita, J. Ceram. Soc. Jpn., 96, 990-96 (1988).
6) H. Ohya, M. Takatsu, H. Kamiya and A. Hattori, The Ceramic Society of Japan 1988 Annual Proceedings, Tokai Branch (1988).
7) T. Yamada, T. Hoshiide and H. Furuya, Zairyo, 33, 28-33 (1984).
8) M. Masuda, T. Soma M. Matsui and I. Oda, J. Ceram. Soc. Jpn., 96, 277-83 (1988).
9) T. Kawakubo and K. Komeya, J. Am. Ceram. Soc., 70, 400-405 (1987).
10) Y. Yamauchi, K. Sakai, M. Oto, T. Ohtsukasa, W. Kanematsu and M. Ito, Report of the Government Industrial Research Institute, Nagoya, 35, 325-31 (1986).
11) A.G. Evans and E.R. Fuller, Met. Trans., 5, 27-33 (1974).
12) M.J. Reece, F. Guin and M.F.R. Sammur, J. Am. Ceram. Soc., 72, 348-52 (1989).
13) T. Kawakubo, Doctoral Thesis, Tokyo Institute of Technology (1988).
14) K.T. Faber and A.G. Evans, Acta. Metall, 31, 565-76 (1983).
15) F.F. Lange, Phill. Mag., 22, 982-92 (1970).
16) A. Kelly, Roy. Soc. Lon. A, 319, 95-116 (1970).

This article is a full translation of the article which appeared in Nippon Seramikkusu Kyokai Gakujutsu Ronbunshi (Japanese version), Vol.98, No.5, 1990.

Effect of Pd on Crystallization in TeO_X-Pd Thin Films for Optical Recording

Kunio Kimura

Electrochemical Materials Research Laboratory, Matsushita Electric Industrial Co., Ltd.
3-15, Yagumo-Nakamachi Moriguchi-shi, Osaka 570, Japan

TeO_X-Pd thin films were studied for optical recording. $Te_{48}Pd_{24}O_{28}$ in the system TeO_X-Pd had a high crystallization temperature and showed a large difference in transmittance between the amorphous and crystalline states. The crystallization of $Te_{48}Pd_{24}O_{28}$ thin film took place stepwise in 4 stages at 150, 270, 326, and 365°C. The activation energies for the crystallization were 4.17, 2.84, 5.39, and 1.79eV, respectively. The crystallization which plays a key role in the optical memory by laser irradiation was shown to be the first stage crystallization. The threshold laser power for crystallization was 9mW for 50ns irradiation. The $Te_{48}Pd_{24}O_{28}$ thin films were found to be good optical memory materials of the so called "write-once" type showing high speed response and high stability.

[Received November 14, 1989; Accepted January 25, 1990]

Key-words: Optical recording materials, TeO_X-Pd films, PdTe, Crystalline, Amorphous, Crystallization, Activation energy

1. Introduction

It has been known that chalcogenide containing Te, Se and S forms amorphous or crystalline states according to the conditions of cooling after heating. This principle is applied to phase-change optical discs, which are receiving considerable interest as the next generation of memory in which information is both written and erased optically.

The author previously reported a study in which TeO_X as a matrix with various elements added to it was used as an optical memory material of the "write-once" type, with a short period of time for completion of crystallization after recording.[1] It was found that the addition of Ge Sn or Pd to TeO_X greatly reduced the time to complete the crystallization to 300ns, whereas the pure TeO_X films require about 30s for completion of crystallization. The TeO_X containing Pd, above all, shows high stability and can be used as a practical optical recording material. The author also reported that for the TeO_X containing Au, which is a noble metal in the group of Pd, the time taken for completion of crystallization depends upon the content of Au, being at least above 66ms, which is longer than the time for the TeO_X-Pd system.[2]

The authors further investigated the crystallization process of the TeO_X-Pd system and found the crystallization state produces by laser irradiation similar to that obtained by static heating at 270°C, which was caused by the precipitation of PdTe crystals accompanied by no grain growth.[3]

The present report, dealing with TeO_X-Pd thin films used as an optical recording material of "write-once" type, discusses the composition best suitable for optical discs, closely analyzes the crystallization process by using differential scanning calorimetry (DSC) and X-ray diffraction and discusses the possibility of practical use of this material for optical discs on the basis of the above results.

2. Experimental Method

TeO_X-Pd was deposited on substrates by controlling the individual deposition rates from the evaporation source of TeO_2, Te and Pd using a multi-electron-beam evaporating apparatus. The composition of the deposits was analyzed by fluorescent X-ray spectroscopy (Rigaku Corporation System-3370). The crystallization temperature of each composition was measured on a specimen of 100nm thin film deposited onto a quartz substrate (9mm dia. 0.5mm) by using a measuring instrument that monitored the change in transmittance during temperature rise at a heating rate of 100°C/min. Crystallization temperature was defined as the temperature at which the transmittance begins to decrease.

The specimens used for measurement by differential scanning calorimetry DSC (Rigaku Corporation DSC-1230) were prepared by depositing thin film of about 800μm on a glass substrate, stripping it with a spatula, and powdering. The specimens used for identification of crystalline phase produced after heating were prepared by depositing thin film of about 100μm on a fused-silica substrate 0.5mm thick and 8mm in diameter under the same depositing condition as that for DSC. The specimens were heated at these temperature for 5 minutes in an argon gas atmosphere. The precipitated crystalline phases were identified by using X-ray diffraction (Rigaku Corporation RU-200B).

The crystallization rate was evaluated by measuring the reflectivity of thin film with an instrument that provided the measurements of laser irradiation and reflectivity, while varying the pulse width and power of laser irradiation. The thin film used for the evaluation had a thickness of 100nm.

An accelerated test of disc life was carried out by evaluating the bit-error-rate (BER) using a disc drive before and after putting the disc into a thermohygrostat. The evaluation was based on the mean value of information written on 100 tracks. The temperature and humidity were increased and decreased at rates of 10°C/h and 10%RH/h, to prevent deformation of the disc due to thermal shock caused by insertion into the thermohygrostat, cracking of the

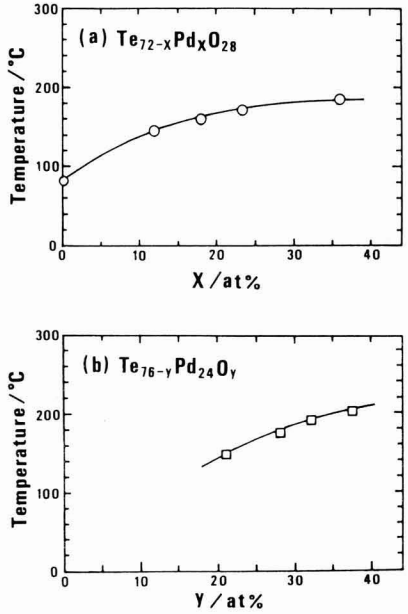

Fig. 1. Crystallization temperature in TeO_x-Pd thin films with annealing.
Composition: (a) $Te_{72-x}Pd_xO_{28}$, and, (b) $Te_{76-y}Pd_{24}O_y$.

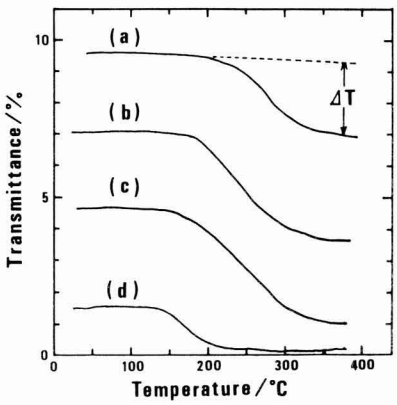

Fig. 2. Transmittance changes in TeO_x-Pd thin films with annealing.
Composition: (a) $Te_{39}Pd_{24}O_{37}$, (b) $Te_{44}Pd_{24}O_{32}$, (c) $Te_{48}Pd_{24}O_{28}$, and (d) $Te_{55}Pd_{24}O_{21}$.

thin film and condensation due to water vapor.

3. Results and Discussion

The optical change of TeO_x-Pd materials is caused by the increase in refractive index and extinction coefficient due to crystallization of amorphous PdTe. Although this transition is reported to be completed in less than 300ns,[4] the crystallization process has not been clarified.

One of the important considerations in using a phase-change type of optical disc is thermal stability. This feature depends upon the temperature of transition from amorphous to crystalline phase (crystallization temperature). Higher crystallization temperature provides better thermal stability, but suffers from decreased recording sensitivity. **Figure 1** shows the relationship between crystallization temperature and composition for TeO_x-Pd thin films. Figure 1(a) shows the relationship between crystallization temperature and x concentration for $Te_{72-x}Pd_xO_{28}$, in which the oxygen content is fixed (TeO_2 content is fixed). It indicates that the crystallization temperature increases with increasing x concentration. Figure 1(b) shows the relationship between crystallization temperature and oxygen content (i.e., TeO_2 content) y for $Te_{76-y}Pd_{24}O_y$. The crystallization temperature, depending heavily on the oxygen content, increases with increasing TeO_2 content.

Figure 2 shows the transmittance change due to heating for various compositions with the Pd content fixed. As seen from this figure, the difference in transmittance T before and after heating decreases with an increase in oxygen content and therefore an optical change of the disc before and after recording cannot be expected. The curve (d) at first seems to show a small T since the absolute value of transmittance before heating is low, however, thickening of recording film provides a value of T as high as those of curves (b) and (c).

From the above results, the composition of $Te_{48}Pd_{24}O_{28}$ was regarded as the optimal composition, with a high crystallization temperature and a large optical change caused by heating. The studies described below were carried out on this composition.

It is known that the crystallization of amorphous substances like glass consists of two processes, nucleus formation and crystal growth, and that thermal changes cannot be detected in the process of nucleus formation. Thermal changes can be detected by thermal analysis only when crystal growth occurs. Therefore, thermal analysis is able to provide information on crystal growth. Assuming that the crystal growth rate obeys the first-order-reaction, the activation energy of crystallization of amorphous substances is determined by Kissinger's equation.[5]

$$\ln(\alpha/T_x^2) = -Ea/K_B \cdot T_x + C \quad \ldots\ldots\ldots (1)$$

where α is the heating rate in differential thermal analysis (DTA) or differential scanning calorimetry (DSC), T_x is exothermic peak temperature, Ea is activation energy, K_B is the Boltzmann constant, and C is a constant. When plotting is performed according to equation (1) by varying the heating rate in DSC, the slope gives the activation energy.

Figure 3 shows the DSC measurement for $Te_{48}Pd_{24}O_{28}$ films. The measurement was made at heating rates of 5°C/min, 10°C/min, and 20°C/min. Four exothermic peaks due to crystallization were observed at each heating temperature. This fact indicates that the crystallization of $Te_{48}Pd_{24}O_{28}$ occurs stepwise, not continuously. The third peak observed at 320 to 330°C is especially high, showing great thermal change, as compared with other

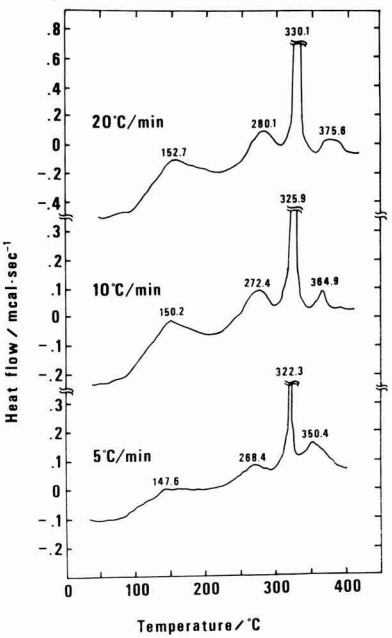

Fig. 3. DSC curves of $Te_{48}Pd_{24}O_{28}$ films at a heating rate of 5°C/min, 10°C/min and 20°C/min.

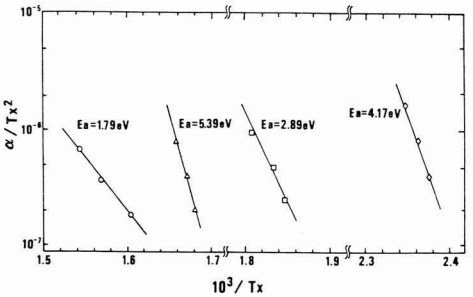

Fig. 4. Kissinger plots of the exothermic peaks in DSC curves of the $Te_{48}Pd_{24}O_{28}$ films.

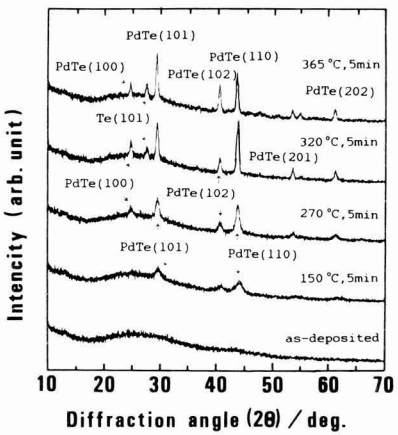

Fig. 5. X-ray diffraction patterns (CuKα) of $Te_{48}Pd_{24}O_{28}$ films as-deposited and annealed at different temperatures.

peaks.

Figure 4 shows the Kissinger plot of exothermic peaks based on equation (1). The activation energy corresponding to each peak was 4.17, 2.84, 5.39, and 1.79eV in order of increasing temperature. It was found from the result that high activation energy of crystallization appears at the first and third peaks.

A high value of Ea shows that the crystallization temperature changes little even when the heating rate is changed. This means that the crystallization occurs too rapidly to depend on heating rate. Considering the characteristics of discs, the crystallization rate is high if the crystallization occurs by getting sufficient energy from laser irradiation or heating. At a temperature somewhat lower than the crystallization temperature, high stability may be expected since a high value of Ea provides a very low reaction rate. Considering the results of the present experiment from this viewpoint, if this crystallization state, in which the value of activation energy is high at the first and third peaks, can be obtained by actual laser irradiation, the $Te_{48}Pd_{24}O_{28}$ films have a possibility of being a recording material with a rapid crystallization speed and high stability.

Figure 5 shows the X-ray diffraction patterns of $Te_{48}Pd_{24}O_{28}$ films as deposited and annealed at 150, 270, 320 and 365°C for 5 minutes. The annealing temperature was set to a temperature corresponding to the exothermic peak given by DSC measurement. The figure indicates that the as-deposited film shows a halo pattern peculiar to amorphous phase, while the film annealed at 150°C or above shows the precipitation of crystalline phase. On the sample annealed at 150°C, the crystalline phase of PdTe is observed. The exothermic peak found near 150°C in DSC seems to be due to the precipitation of this crystal. On the sample annealed at 320°C, Te crystal is observed in addition to the growth of peaks found on samples annealed up to 270°C. The result of DSC indicates that the exothermic peak at 320°C is far sharper than other peaks. Therefore, this peak may be due to the precipitation of Te crystal. On the samples annealed at 270°C and 365°C, the precipitation of crystalline phase other than PdTe and Te described above is not observed. The reason for the generation of exothermic peaks at 270°C and 365°C is unknown at present, though the short annealing time of 5 minutes for samples used for X-ray diffraction and the precipitation of crystalline phase that cannot be identified by X-ray diffraction may be possible reasons.

The fact that the crystalline phase precipitated by 8mW laser irradiation (wavelength: 830nm) by using $Te_{48}Pd_{24}O_{28}$ films is PdTe has been reported,[3] though the precipitation of Te crystalline phase has not been confirmed. A possible reason for this fact may be that the temperature of heating by laser irradiation is below 270°C. However, the temperature obtained by 8mW laser irradiation should not be below 270°C, as indicated in a report of another researcher.[6] Static heating and heating of the nanosecond

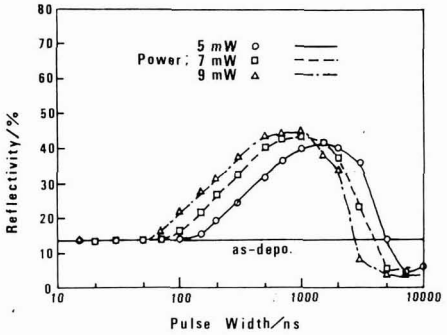

Fig. 6. Threshold crystallization laser pulse duration in $Te_{48}Pd_{24}O_{28}$ films.

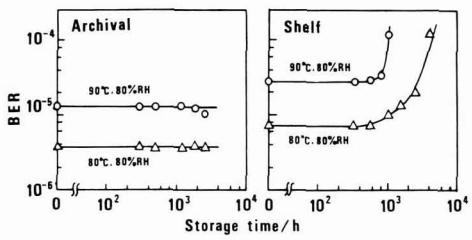

Fig. 7. Acceleration life test results of archival and shelf BER as a function of storage time.

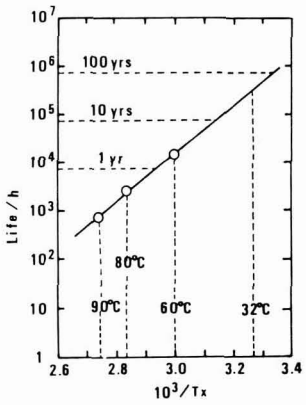

Fig. 8. Estimation of room temperature life based on shelf BER at different temperatures.

order by laser irradiation, though having the same ultimate temperature, are not equivalent in terms of time. With laser irradiation, since the material, though melted once, is soon cooled, the migration of atoms is limited, so that the crystallization does not occur completely. Although the actual temperature increases considerably after laser irradiation, the crystallization occurs to nearly the same extent as with material heated statically at a temperature below 270°C.

As described above, the optical change of $Te_{48}Pd_{24}O_{28}$ films is due to the precipitation of PdTe crystal from the amorphous state. From this viewpoint, it is concluded that though four stages are found in crystallization of $Te_{48}Pd_{24}O_{28}$ films, the crystallization obtained by annealing at temperature below 270°C causes actual optical changes, and that the required activation energy is 4.17eV. This high value makes crystallization rate high, and thus it is likely that it will provide high stability optical recording materials.

Figure 6 shows the threshold crystallization laser pulse duration for $Te_{48}Pd_{24}O_{28}$ films. In the figure, the abscissae represent the laser irradiation pulse width and the ordinates the reflectivity after irradiation. The increase in reflectivity resulting from crystallization occurs at a pulse width of 100ns for 5mW irradiation power, and at 50ns for 9mW power; that is, the figure indicates that the crystallization is caused by a very short duration of laser irradiation. The reflectivity was increased 30% or more as compared with that of the as-deposited sample. When the pulse width is above 2000ns, a decrease in reflectivity was observed. This decrease resulted from the destruction of film caused by too strong irradiation power.

Figure 7 shows the acceleration life test results of archival and shelf BER for $Te_{48}Pd_{24}O_{28}$ films as a function of storage time. The ordinates in the figure represent BER. A small and unchanged value of BER means that the film has high stability as a recording disc. "Archival" in the figure shows the test results obtained by reproducing the initially recorded signals after a certain period of time, while "Shelf" shows the test results obtained by writing data after storage. As seen from the figure, the BER in the archival test was unchanged even after 1000 hours at 90°C and 80%RH. In the shelf test, the BER greatly increased after 1000 hours, which means the deterioration of the disc. This is probably because the crystallization gradually proceeds in the amorphous area during the acceleration tests at 80°C and 90°C since the crystallization temperature of $Te_{48}Pd_{24}O_{28}$ films is about 150°C, making impossible the retention of difference in reflectivity between the non-recording (amorphous) and recording (crystalline) areas. The reason for unchanged BER in the archival test is probably because the difference in reflectivity between the amorphous (non-recording) and crystalline (recording) areas is retained since the crystallization proceeds further in crystalline area as the crystallization proceeds in the amorphous area than with the shelf test.

As described above, the reliability of $Te_{48}Pd_{24}O_{28}$ films is evaluated by the shelf test. **Figure 8** shows the estimation of room temperature life based on shelf BER at different temperature. In this figure, the disc life is taken as the value in which the BER increases one order of magnitude after storage at 80%RH and 90, 80, and 60°C. The extrapolation estimates the life at 32°C to be 10 years or longer. This result indicates that $Te_{48}Pd_{24}O_{28}$ films are more reliable than other Te films[7] and Te-based alloys[8] reported previously.

The above results mean that the fast crystallization and high reliability of $Te_{48}Pd_{24}O_{28}$ films may result from high

activation energy for crystallization.

4. Conclusion

TeO_x-Pd thin films were studied for optical recording. $Te_{48}Pd_{24}O_{28}$ in the system TeO_x-Pd was the most suitable because it had a high crystallization temperature and showed a large difference in transmittance before and after heating, DSC measurement and X-ray diffraction revealed that the crystallization of $Te_{48}Pd_{24}O_{28}$ thin films took place stepwise in four stages. The activation energy for crystallization in each stage was 4.17, 2.84, 5.39, and 1.79eV. The actual activation energy for crystallization seems to be 4.17eV because the crystal found in $Te_{48}Pd_{24}O_{28}$ films recorded on the disc was PdTe precipitated by the first-stage crystallization.

The laser irradiation pulse duration required for crystallization was investigated from the viewpoint of practical use. The result proved that the crystallization was caused by irradiation of a pulse width of 50ns or greater for 9mW power. The study of reliability indicated that the film had a life of 10 years or longer at 32°C. These results were discussed by relating them to the fact that $Te_{48}Pd_{24}O_{28}$ films had high activation energy for the first-stage crystallization.

Acknowledgment

I would like to thank Prof. T. Minami at the Applied Chemistry Faculty, Engineering Department, University of Osaka Prefecture, for his guidance and advice in this study. I would also like to thank E. Ohno at the Information Equipment Institute of Matsushita Electric Industrial Co., Ltd. for his help in DSC measurement and T. Kurumizawa at Matsushita Techno Research Co., Ltd. for his help in X-ray diffraction measurement.

References:

1) K. Kimura: "Optical Recording Materials Based on TeO_x Films", Jpn. J. Appl. Phys., 28 [5], 810-813 (1989).
2) K. Kimura and E. Ohno, "Effect of Au Addition on Crystallization of TeO_x-Au Thin Films", J. Ceram. Soci. Jpn, 98[2], 193-97 (1990)
3) K. Kimura and E. Ohno, "Crystallization of TeO_x-Pd Films for Optical Recording Materials", Jpn. J. Appl. Phy., 28[11], 2223-26 (1989).
4) T. Ohta, K. Kotera, K. Kimura, N. Akahira and M. Takenaga: "New Write-once Media Based on Te-TeO_2 for Optical Disk" Proc. SPIE vol. 695 2-9 (1986).
5) S. Sakka, "Science of Amorphous Glass", Uchida Rokakuho, Tokyo (1985), p. 258.
6) R. Akutagawa, S. Aso, H. Takekawa, H. Kodama and T. Ohta, "Phase-changing Type Optical Discs (4) Thermal Simulation", Text Book for 48th Applied Physics Symposium, 18 P-ZP-14, 736 (1987).
7) D.Y. Lou, G.M. Blom and G.C. Kenny: "Bit Oriented Optical Storage with Thin Tellurium Films" J. Vac. Sci. Technol., 18[1], 78-86 (1981).
8) G.M. Blom and D.Y. Lou: "Archival Life of Tellurium-Based Materials for Optical Recording", J. Electrochem. Soc.: Solid-State Science and Technology, 131[1], 146-151 (1984).

This article is a full translation of the article which appeared in Nippon Seramikkusu Kyokai Gakujutsu Ronbunshi (Japanese version), Vol.98, No.5, 1990.

Preparation of Porous Li_2SnO_3 for Blanket Material of Fusion Reactor and Its Tritium Release Behavior

Michio Inagaki, Shigeo Nakai, Takayuki Terai* and Yoichi Takahashi*

Materials Science, Toyohashi University of Technology, Tempaku-cho, Toyohashi 440, Japan

*Department of Nuclear Engineering, Faculty of Engineering, University of Tokyo,Hongo, Bunkyo-ku, Tokyo 113, Japan

As a candidate for solid blanket material of fusion reactor, porous particles of lithium stannate Li_2SnO_3 were prepared by the decomposition of lithium hexahydroxystannate $Li_2Sn(OH)_6$ at a relatively low temperature of 600°C. Sintering of these porous particles at 1000°C resulted in blocks with bulk densities as low as about 50% theoretical. Densification of the block was found to be accelerated by either grinding of the starting powder or addition of Li_2O. The present process has advantages of low temperature synthesis of lithium compounds, and small size and high porosity of primary particles.

Release of tritium generated by neutron irradiation and stored in the block occurred up to 600°C, a much lower temperature than with Li_2O. This result is reasonably explained as due to the small size of primary particles of Li_2SnO_3 and also due to the high porosity of the sintered block.

[Received November 15, 1989; Accepted January 25, 1990]

Key-words: Fusion reactor, Blanket material, Li_2SnO_3, Sintering, Porous material, Tritium release

1. Introduction

It is generally considered that nuclear fusion is essential as a future energy source. At present, the reaction between deuterium and tritium (D-T reaction)

$$^2D + ^3T \rightarrow ^4He + ^1n$$

is being investigated for nuclear fusion. The tritium used for the D-T reaction is considered to be formed by the following reactions

$$^6Li + ^1n \rightarrow ^4He + ^3T$$

$$^7Li + ^1n \rightarrow ^4He + ^3T + ^1n$$

by irradiating neutrons n produced by the D-T reaction onto the blanket containing lithium installed around the fusion reactor core. The blanket materials for feeding tritium are broadly divided into two groups: liquid feeder materials represented by liquid lithium, lithium lead alloys and Li_2BeF_4 molten salt, and ceramic solid feeder materials represented by Li_2O. The advantages and disadvantages of these materials have been pointed out in different articles.[1)]

For solid blanket materials, Li_2O, $LiAlO_2$, Li_5AlO_4, Li_2SiO_3, Li_4SiO_4, and Li_2ZrO_3 have been studied.[2-4)] These solid blanket materials have the advantages of higher chemical stability and higher working temperature than those of liquid blanket materials, while they have the disadvantage that the presence of neutron multipliers is required since the lithium content is not so high, except for Li_2O. In the preparation process of these materials (for example, the preparation of Li_2O by thermal decomposition of Li_2CO_3 or the reaction of Li_2O with other metal oxides), there are some problems: very active lithium compounds are produced and corrode the vessel, and lithium easily sublimes at high temperatures, creating a high risk of change in composition. Lithium compounds generally have high corrosive and moisture absorption properties, and also have accelerated grain growth at high temperatures, leading to easy sintering and densification. Such characteristics interfere with the conditions required for tritium feeder blanket materials where tritium produced inside the blanket must diffuse out to its surface.

To solve such problems of the preparation process and lithium compounds, the coprecipitation of various complex oxides and preparation by the alkoxide process have been tried, and also the control of grain structure by the spray drying method has been carried out.

In fusion reactors, the recovery efficiency of tritium from the blanket is so important as to greatly govern the system integrity. Therefore, the basic process in which tritium produced in solid blanket crystals transfers into the sweep gas has been studied theoretically and experimentally.[1)] The elementary process of transfer is divided into six processes as follows:

1) Diffusion within the primary particles.

2) Release on the surface of the primary particles.

3) Permeation and diffusion along the interface of primary particles.

4) Release on the surface of secondary particles.

5) Permeation and diffusion in the pores between secondary particles.

6) Mass transfer in the gas boundary film.

The processes (1) and (2) depend on the primary particles' size and crystallinity, the processes (3) and (4) on the properties of the sintered body such as density, grain size, and pore size, and the process (5) on the bulk properties of the blanket such as density. This means that the blanket for fusion reactors should be studied thoroughly to investigate the texture of the sintered blocks as well as the composition and the crystalline structure of the compound.

We previously proved that Li_2SnO_3 powder, in which fine primary particles of about 0.2μm are aggregated to produce highly porous secondary particles, can be prepared by thermal decomposition at a low temperature of about

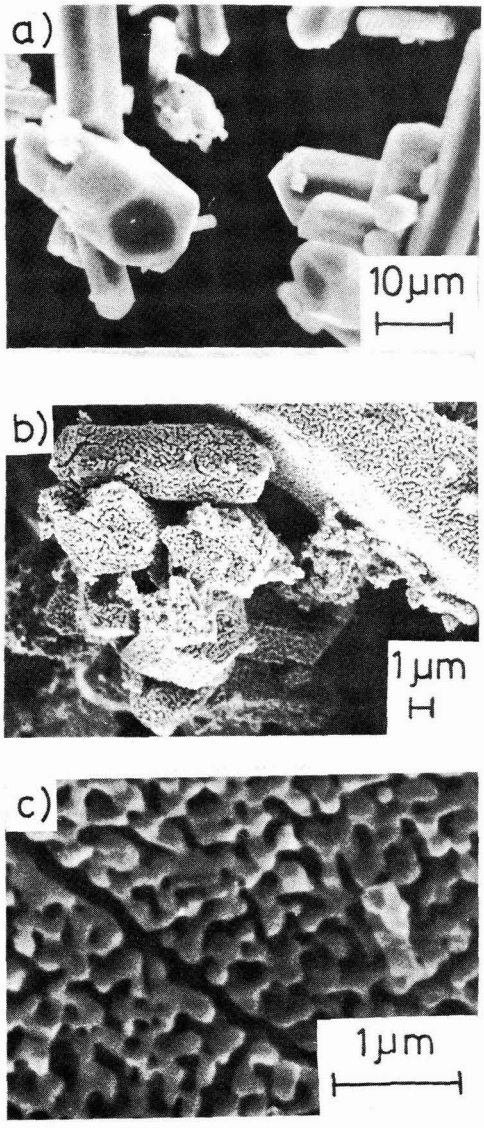

Fig. 1. SEM micrographs.
a) $Li_2Sn(OH)_6$ precipitated ,b) and c) Li_2SnO_3 heated at 800°C for 4 hrs.

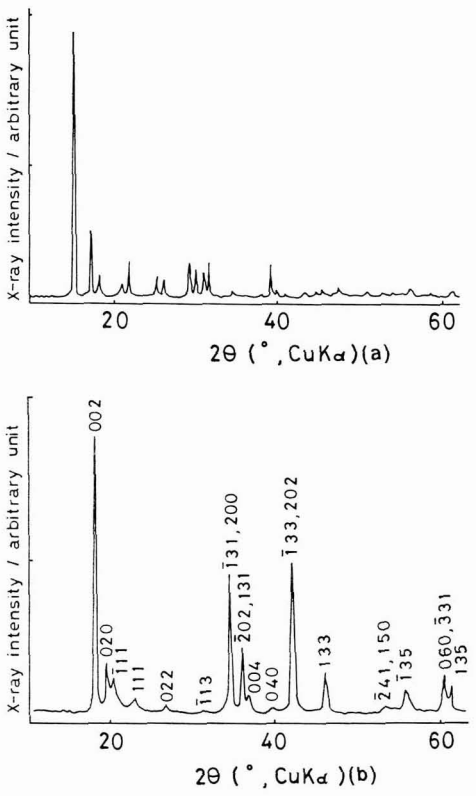

Fig. 2. X-ray powder patterns.
a) as-precipitated $Li_2Sn(OH)_6$,
b) Li_2SnO_3 heated at 800°C for 4 hrs.

400°C after precipitating lithium as a complex hydroxide with tin, thus avoiding formation and sublimation of active lithium oxides, and that Li_2SnO_3 powder is difficult to sinter even at 1000°C. The basic physical properties of Li_2SnO_3 were not known. Its behavior under neutron irradiation has also not been investigated. However, Li_2SnO_3 can be regarded as a candidate for blanket material because of its advantages of a simple manufacturing process suitable for high volume production, low sinterability at high temperatures, retention of porosity, and low moisture absorption properties.

In the present study, the preparation of porous Li_2SnO_3 including the compacting pressure in sintering, the effect of grinding before pressing and the effect of added Li_2O on sintering, was investigated. Also, the release behavior of tritium was investigated by determining the tritium released by gradually heating porous Li_2SnO_3 powder to a high temperature after forming tritium by neutron irradiation of the powder.

2. Experimental Method, Results and Discussion

2-1. Preparation of $LiSn(OH)_6$ Complex Hydroxide Powder

As described in the previous report,[11] the complex hydroxide $Li_2Sn(OH)_6$ is precipitated by gradually adding 1M $SnCl_4$ aqueous solution to 2M LiOH aqueous solution and standing at room temperature. The precipitated $Li_2Sn(OH)_6$ mainly consists of hexagonal column-shaped particles about 10μm thick and about 40μm long as shown in Fig.1a. The X-ray powder patterns of this powder have not been indexed and its structure is unknown. As shown in **Fig.2a**, however, each diffraction peak is very sharp, showing high crystallinity. The correspondence of this powder pattern to $Li_2Sn(OH)_6$ can be inferred by the fact

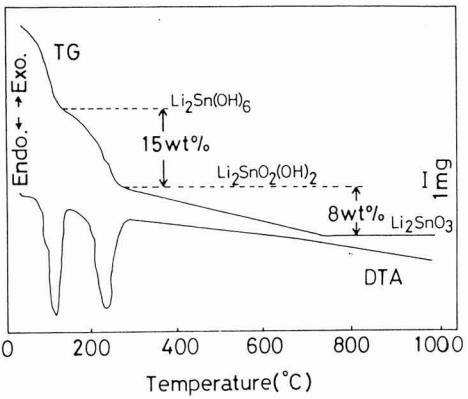

Fig. 3. DTA-TG curves of the precipitate $Li_2Sn(OH)_6$.

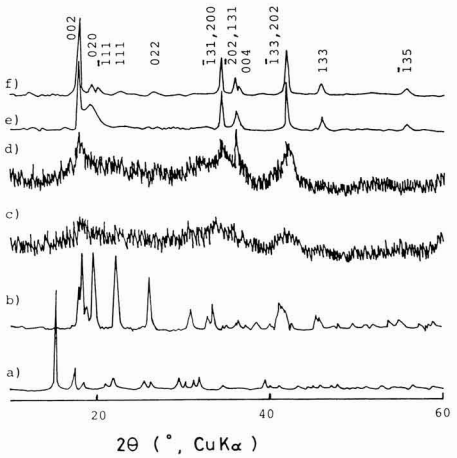

Fig. 4. X-ray powder patterns.
a) as-precipitated, b) heated at 160°C for 4 hrs.,
c) at 160°C for 11 days, d) at 240°C for 15 days
e) at 600°C for 2 days, f) at 800°C for 4 hrs.

that after decomposition of the powder at a high temperature the resultant powder had the pattern of single-phase Li_2SnO_3.

To obtain $Li_2Sn(OH)_6$ complex hydroxide, aqueous LiOH may be added dropwise to aqueous $SnCl_4$. However, this process is unsuitable for obtaining single-phase complex hydroxide since $Sn(OH)_4$ is often present in the precipitate. This is because the addition of a small amount of LiOH to weakly acidic $SnCl_4$ water solution increases the pH value of the solution, resulting in rapid precipitation of $Sn(OH)_4$. The coexistence of $Sn(OH)_4$ also occurred when $SnCl_4$ solution was rapidly added to strongly alkaline LiOH solution, or when the agitation was insufficient. For this reason, the $SnCl_4$ solution was diluted and dropped gradually (for example, at a rate of 0.4ml/min) as described above. Since the addition of $SnCl_4$ solution decreased the pH value of the mother liquor, the addition of $SnCl_4$ solution was stopped at pH11.5. The precipitate was filtered, washed with distilled water, and dried at 80°C. The yield of complex hydroxide was about 60% based on added Sn.

Such a low yield of Li_2SnO_3 was considered to be due to the high solubility in water. Therefore, the LiOH and $SnCl_4$ solutions were mixed and the mother liquor was added dropwise to a large amount of methanol to precipitate $Li_2Sn(OH)_6$. In this case, the yield increased to nearly 90%. However, the process using methanol was not employed in the experiments described below in this report for simplicity of operation.

The previous report[12] showed that metal stannate complex hydroxide $MSn(OH)_6$ precipitates when a bivalent metal ion M^{2+} (for example, Mg or Co) is added dropwise. The feature of this process is the formation of oxide powder as fine particles by direct thermal decomposition of the complex hydroxide at relatively low temperatures. The process is called the complex precipitation process.

2-2. Thermal Decomposition and High Porosity of Li_2SnO_3

Heating of $Li_2Sn(OH)_6$ powder at 800°C for 4 hours yields highly crystalline single-phase Li_2SnO_3 powder. This powder consists of secondary particles formed by the aggregation of primary particles of about 0.2μm with pores of nearly the same size lying between the particles, as shown in Figs.1b and 1c. The secondary particles are hexagonal columns as with the starting hydroxide powder and are nearly the same size as the starting powder particles. The X-ray powder patterns (Fig.2b) agree exactly with those already reported for Li_2SnO_3.[13] This means that single-phase Li_2SnO_3 was obtained. The lattice constants determined for this sample were as follows:

a = 0.5308nm, b = 0.9185nm, c =1.0022nm,
β = 100.28°

These constants agree with the values in reference.[13]

The thermal decomposition process of Li_2SnO_3 is given as DTA-TG curves in Fig.3. Up to 120°C, a sudden weight loss and the accompanying high endothermic peak were observed. These were considered to be due to the elimination of absorbed water since the weight loss ratio and the shape of the endothermic peak were different from sample to sample. In Fig.3, for example, the endothermic curve in this temperature range seems to have two peaks. On the curves for other samples, however, these two peaks were not so clear.

A large weight loss and a high endothermic peak were found in the temperature range from 120° to 260°C, and another weight loss in the wide temperature range up to 700°C; so the thermal decomposition proceeds in two stages.The weight loss percentage in each stage was 15 and 8wt%, respectively.For $Li_2Sn(OH)_6$ to decompose into Li_2SnO_3, three molecules of water must be released. Considering that the elimination of one molecule of water causes a weight loss of 7.5wt%, two molecules of water are released to form $Li_2SnO_2(OH)_2$ in the first stage of thermal decomposition, and the remaining one molecule of water is released to form Li_2SnO_3 in the second stage.

The structure change in this decomposition process was followed by measuring the X-ray powder patterns of samples heated at various temperatures up to 800°C for

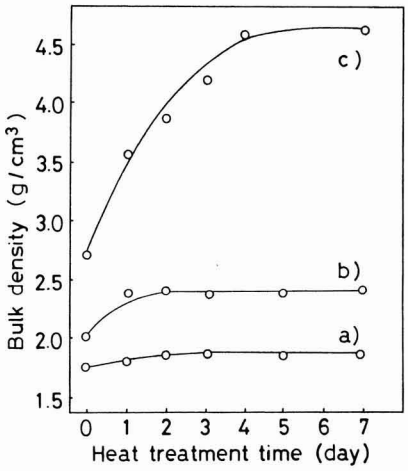

Fig. 5. Changes of bulk density of Li_2SnO_3 with heat treatment time.
a) specimen compressed under 20 MPa,
b) specimen compressed under 100 MPa,
c) specimen prepared from ground powder bycompessing under 200 MPa.

various times. The typical X-ray powder patterns are shown in **Fig.4.**

The sample heated at 160°C in the first stage of decomposition for 4 hours shows sharp diffraction peaks (Fig.4b), showing high crystallinity. This pattern, however, differs from that of the sample obtained immediately after precipitation (Fig.4a). This suggests a change in the structure of the hydroxide. As the heating time was increased at this temperature, the diffraction pattern gradually became broad. After 11 days, no diffraction peak was found, so the structure had become amorphous (Fig.4c). At 240°C, close to the end of the first stage in DTA, this structural change naturally occurred earlier; heating for only one day made the structure amorphous. After 15 days, the broad diffraction peaks were detected (Fig.4d), and the diffraction angles for these lines agreed roughly with those for Li_2SnO_3 (Fig.4f) obtained by heating at a substantially high temperature. Therefore, crystallization is considered to begin in the second stage of thermal decomposition. The sample heated at 600°C in the second stage of thermal composition for 2 days showed fairly sharp diffraction peaks, which means that crystallization proceeded. As seen in Fig.4e, however, 020 and 111 diffraction peaks were still broad. Because the thermal decomposition had not been completed, the crystallization of this sample was not so complete as compared with the sample heated for 4 hours at 800°C.

As a result of SEM observation of the heated samples, no porosity was found as shown in Figs.1b and 1c in the sample heated at 600°C for 2 days. In contrast, at 800°C characteristic pores were clearly observed after 4 hours heating. It is therefore considered that pores are formed when the thermal decomposition has ended and crystallization is proceeding. The mean pore diameter was 0.18μm as measured by mercury porosimetry for the sample heated at 800°C for 4 hours. This value agrees well with the results of SEM observation. The surface area of the sample measured by porosimetry was $6.4m^2/g$, and the specific surface area measured by the BET method was $5.2m^2/g$. These values nearly agree with the specific surface area of $4.2m^2/g$ calculated by assuming a true sphere of 0.2μm. All pores in this Li_2SnO_3 powder were considered to be open pores.

2-3. Sintering of Li_2SnO_3 Powder

The sintering properties of the Li_2SnO_3 powder were evaluated. The powder was prepared by thermal decomposition at 800°C for 4 hours and had a characteristic porous structure. About 0.4g of porous particles heated at 800°C and of powder ground in an agate mortar after being heated were used. The sample was compressed into pellets 20 or 13mm in diameter and 1 to 3mm thick under various pressures, and heated at 1000°C. The bulk density of the pellet was measured daily. The results are shown in Fig.5. For the sample heated for 7 days in which the bulk density was maximum the fractured surface was observed by SEM. Typical SEM photographs are shown in **Fig.6.**

The sample prepared by pressing Li_2SnO_3 powder that had not been ground had a bulk density as low as $2g/cm^3$ immediately after being compressed. The bulk density did not increase even when heating at 1000°C was repeated, and only reached $2.5g/cm^3$, which was about 50% of the theoretical Li_2SnO_3 density of $4.98g/cm^3$. Even for such a low density, the effect of compressing pressure was noticed; the sample compressed at a higher pressure had a higher density immediately after being compressed, and heating at 1000°C achieved a relatively higher bulk density.

For these compressed samples, the porosity of the starting powders was retained as shown in Figs.6a and 6b. For the specimen heated at 1000°C for 7 days with the maximum bulk density, the primary particles grew from 0.2μm of the starting powder to about 1μm, and minute pores remained between the primary particles.

For the specimen ground before being compressed, the density was high immediately after compression, and heating caused rapid densification. The result shown in Fig.5 was the most remarkable example, in which the relative density increased to about 93%, and considerable sintering occurred. The SEM photographs of the fractured surfaces (Figs.6c and 6d) indicate that the individual particle surfaces consist of distinct crystal faces and almost no pores were found between them. The photographs also indicate that the size of the primary particles was almost unchanged as compared with those obtained by heating of the unground specimen, but the surface conditions had greatly changed.

Although a large effect on sintering due to grinding was noticed, it is difficult to quantitatively evaluate the effect of grinding on the starting powder, and reproducibility was not very high. Therefore, unground porous powder was compressed after Li_2O was added, and heated at 800°C for 20 hours to measure the bulk density and observe the fractured surface by SEM. As a result, it was found that the addition of a small amount of Li_2O greatly accelerated the crystallization of primary particles and densification of the compressed block. For a specimen to which 5wt% Li_2O was added, for example, the relative density increased to 77%,

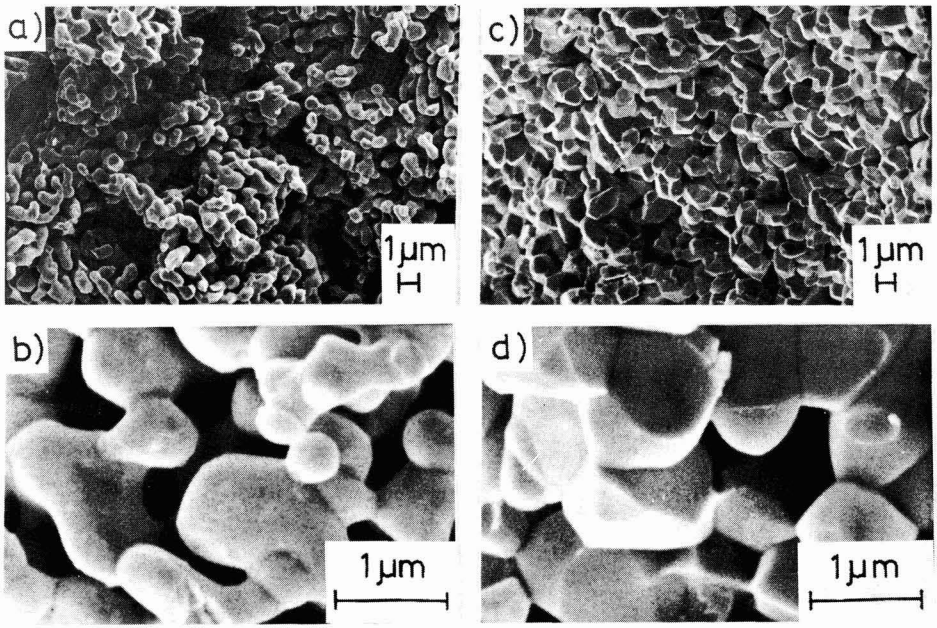

Fig. 6. SEM micrographs. a, b)specimen compressed under 20 MPa and heated at 1000°C for 7 days, c, d)specimen compressed under 200 MPa and heated at 1000°C for 7 days.

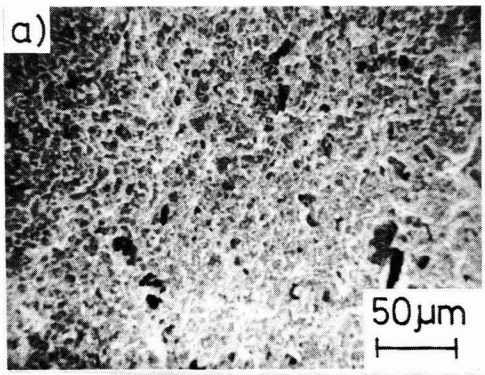

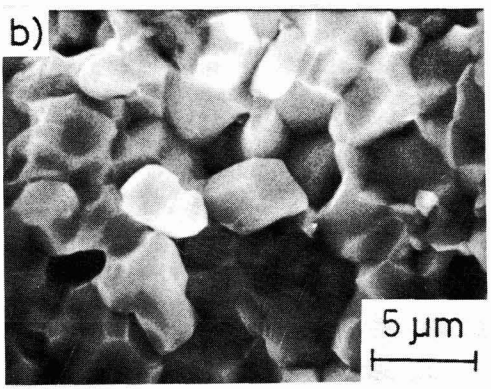

Fig. 7. SEM micrographs of Li_2SnO_3 sintered at 800°C for 2 days by adding 5% Li_2O.

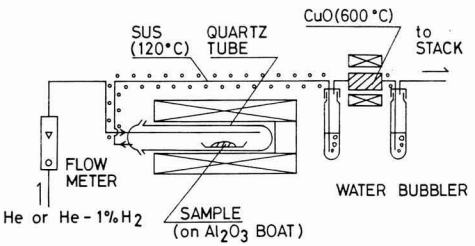

Fig. 8. Experimental set-up for recovery of tritium released from the Li_2SnO_3 block at different temperatures.

and primary particles surrounded by distinct crystal faces, as shown in **Fig.7**, were observed on the fractured surface, and large particles with abnormal growth were found in some areas when the specimen was heated at 800°C for 20 hours. The addition of more LiO_2 increased the size of primary particles, but did not always increase the relative density of the compressed block. This is probably because of partial evaporation of Li_2O. In these cases the platinum foil on which the compressed block was placed was corroded.

2-4. Tritium Release

Neutron irradiation was carried out on Li_2SnO_3 powder obtained by heating $Li_2Sn(OH)_6$ at 800°C for 4 hours, so that the release behavior of the tritium formed could be investigated.

0.12g Li_2SnO_3 powder was vacuum-encapsulated in a quartz ampoule. Tritium of about 37kBq was formed by

Table 1. Chemical forms of released tritium.

Sample	Sweep gas	Water-soluble component (%)	Water-insoluble component (%)	Temp.
Li_2SnO_3-1	He	98.8	1.2	
Li_2SnO_3-2	He	98.5	1.5	R.T.
Li_2SnO_3-3	He + 1%H_2	95.8	4.2	1000 °C
Li_2SnO_3-4	He + 1%H_2	96.0	4.0	
Li_2O (Ref. 5)	release to vacuum	98.2	1.8	R.T. 600 °C

neutron irradiation at the thermal neutron irradiation aperture ($10^8 n_{th}/cm^2$ sec) of the fast neutron reactor "Yayoi", at the Nuclear Engineering Research Laboratory, Faculty of Engineering, University of Tokyo. The irradiated sample was placed on an alumina boat positioned in a quartz sample holder in a glove box with an Ar atmosphere. The experimental equipment was set up as shown in **Fig.8**. He or He + 1%H_2 (100cm^3/min) was used as a sweep gas. Tritium released by heating of the specimen was transferred to the tritium recovery system. The released and transferred tritium was recovered as a water-soluble component (mainly HTO) and water-insoluble component (mainly HT) with two water bubbler traps between which copper oxide was installed. At the end of the experiment, the concentration was measured with a liquid scintillation counter. Heating during the experiment was carried out stepwise at 100°C intervals from room temperature to 1000°C. Each temperature was held for 40 minutes, during which the released tritium was recovered with the water bubbler (the water bubbler was changed at each interval). The integrity of the experimental equipment against tritium release was checked by performing a release behavior test for a Li_2CO_3 sample subjected to neutron irradiation, and by comparing the result with the value in reference.[14] **Table 1** lists the chemical forms of tritium released in this experiment. The chemical form of tritium released when He is used as a sweep gas contains a water-soluble component of above 98%. This result is similar to the experimental result of tritium release from Li_2O into a vacuum.[5] The addition of 1% H_2 gas to the sweep gas decreases the content of water-soluble component.

Figure 9 shows the tritium release profiles obtained by this experiment. In this figure, the normalized values of the amount released at each holding temperature in relation to the total release amount were plotted as a function of holding temperature. Eleven percent of the water-insoluble tritium component was released at room temperature. This is due to the fact that tritium (27 MeV) produced by the nuclear reaction was adsorbed again on the sample surface after evolution from the sample particle to the gas phase.

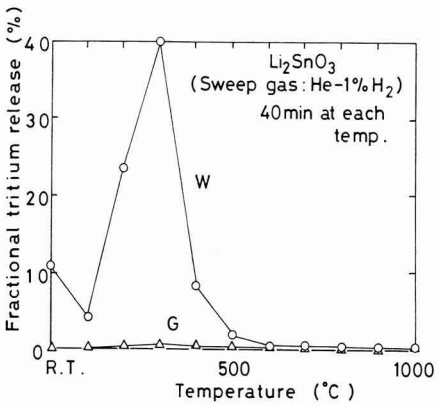

Fig. 9. Tritium release profiles from the Li_2SnO_3 block in the forms of water-soluble(W) and water-insoluble(G) components.

The amount of tritium released from the sample increased at about 300°C. Almost all the tritium was released up to 600°C. This result indicates that Li_2SnO_3 has a tritium release peak at a temperature equal to or lower than that for Li_2O, which is promising for a solid feeder material. This is due to the small primary particles and high porosity of the sintered blocks of Li_2SnO_3. We are planning to determine the diffusion coefficient of tritium in the crystal grains and at the grain boundaries, and the rate constant for the release from the surface.

Acknowledgments:

This study was partially supported by Grant-in-Aid for Fusion Research by the Ministry of Education; Science and Culture of Japan, (No.62055015).

References:

1) C.E. Johnson and G.W. Hollenberg, J. Nucl. Mater., 122 & 123, 871-881 (1984); P. Groner and W. Seifritz, ibid, 133 & 134, 176-180 (1985); Y. Liu, M.C. Billone, A.K. Fisher, S.W. Tam, R.G. Clemmer

and G.W. Hollenberg, Fusion Technol., 8, 1970-1984 (1985); C.E. Johnson, K.R. Kummer, and E. Roth, J. Nucl. Mater., 115-157, 188-201 (1988).
2) H.A. Lehman and H. Hesselbarth, Z. anorg. allg. Chem., 315, 14-18 (1962).
3) R. Scholder, D. Raede and H. Schwarz, ibid., 364, 113-126 (1977).
4) R. Hoppe and R.M. Braun, ibid., 433, 181-188 (1977).
5) H. Kudo and K. Okuno, J. Inorg. Nucl. Chem., 40, 363-367 (1978).
6) K. Kinoshita, J.W. Sim and J.P. Ackerman, Mater. Res. Bull., 13, 445-455 (1978).
7) D. Vollath, H. Wedemeyer and E. Guenther, J. Nucl. Mater., 133-4, 221-225 (1985).
8) S. Hirano, T. Hayashi and T. Kageyama, J. Am. Ceram. Soc., 70, 171-174 (1987).
9) A. Watanabe, Y. Takeuchi and G. Saeki, ibid., 70, 268-269 (1987).
10) S. Tanaka, Nuclear Fusion Research, 56, 318-340 (1986).
11) M. Inagaki, S. Nakai and T. Ikeda, J. Nucl. Mater., 160, 224-228 (1988).
12) M. Inagaki, S. Okada and M. Sakai, 1981, 1517-1521 (1981).
13) JCPDS files No.31-761.
14) K.E. Collins and C.H. Collins, J. Inorg. Nucl. Chem., 39, 745-748 (1977).

This article is a full translation of the article which appeared in Nippon Seramikkusu Kyokai Gakujutsu Ronbunshi (Japanese version), Vol.98, No.5, 1990.

Changes in Infrared Spectra and Lattice Constants of Fluorine Micas with Al-Substitution

Kunio Kitajima, Tatsuya Inada[+] and Nobuo Takusagawa

Department of Chemistry and Materials Engineering, Faculty of Engineering, Shinshu University , 500, Wakasato, Nagano 380, Japan
[+]Now with Ohmachi Factory, Showa Denko Co., Ltd. 6850, Ohmachi, Ohmachi 398, Japan

Series of Al-substituted fluorine micas, $KMg_{2+x}Li_{1-x}(Al_xSi_{4-x-y}Ge_yO_{10})F_2$ and $KMg_{2+x}Li_{1-x}(Al_xGe_{4-x-y}Si_yO_{10})F_2$; x=0.0 to 1.0, y=0, 1, 2, 3, were synthesized and variations of infrared spectra and lattice constants with Al-substitution were studied and compared to those with Ga-substitution reported previously. The infrared spectra of the synthesized micas varied sensitively with composition. Continuous changes in lattice constants with increasing Al-contents proved that there were complete series of solid solutions between the end member micas. Lattice constants a and b increased almost linearly with increasing Al-content in all series. However, $c\cdot\sin\beta$ (basal spacing) remained almost unchanged or slightly increased in the case of Al-for-Si substitution while it decreased linearly in the case of Al-for-Ge substitution. These complicated changes of cell dimensions were explained in terms of the tetrahedral rotation angle α, the octahedral flattening angle ψ, and the change in interlayer conformation. Linear relationships between $c\cdot\sin\beta$ and average radius of tetrahedral cation were obtained for Al- and Ga- micas having an x-value of 1.0 and for micas having x-value of 0.0, respectively, showing that the cell dimension and structural deformation depend essentially on both the charge balancing and the size of tetrahedral cations.

[Received December 1, 1989; Accepted January 25, 1990]

Key-words: Fluorine mica, Al-substitution, Lattice constant, Solid solution, Infrared spectrum

1. Introduction

The isomorphic substitution of synthetic fluorine mica has been extensively studied, and micas with various compositions have been prepared.[1)] The authors previously reported on series of micas limited by end compositions of taeniolite $KMg_2Li(Si_4O_{10})F_2$[2)] and mica in which a part or all of the Si^{4+} was substituted with Ge^{4+}. The Si^{4+} and Ge^{4+} were further substituted with Ga^{3+} with a larger ionic radius to synthesize fluorine micas with various compositions, and the changes in infrared absorption spectra and lattice constants were investigated.[3)] In this study, as part of our research on the synthesis of isomorphic substituted analogues of such fluorine micas and their properties, the synthesis of Al-substituted fluorine micas with various compositions corresponding to the Ga-substituted fluorine micas in the previous report, infrared spectroscopy and powder X-ray diffraction of these materials were carried out. The changes in the infrared spectra and lattice constants of Al-substituted fluorine micas, and a comparison with Ga-substituted analogues are discussed. Such a comparison between compounds substituted with Al^{3+} and Ga^{3+}, which have different electronegativities and ionic radii, though in the same 3B family, is expected to provide useful information for defining the structure and characteristics of fluorine mica.

2. Experimental

2-1. Synthesis of Fluorine Mica

Special-grade reagents, SiO_2, MgO, MgF_2, LiF, KF, GeO_2 and Al_2O_3, were mixed to achieve the compositions of 8 series of compounds with the general formulas of $KMg_{2+x}Li_{1-x}(Al_xSi_{4-x-y}DGe_yO_{10})F_2$ and $KMg_{2+x}Li_{1-x}(Al_xGe_{4-x-y}SiMVyO_{10})F_2$ (x=0.0, 0.2, 0.4, 0.6, 0.8, 1.0) with y being 0, 1, 2, or 3. Each mixture (2g) was sealed in a platinum container (9×9×40mm) and melted at 1400°C for a sample with high SiO_2 content or at 1300°C with a high GeO_2 content for 2 hours. They were cooled gradually at a rate of 2-3°C/min. down to 800°C, and then removed from the furnace for cooling to obtain crystallized products. These were observed with a microscope to examine the size of the precipitated mica crystals as well as the presence of different minerals.The compositions of the 8 series of Al-substituted micas are expressed by the tetrahedral composition of mica, e.g. a $KMg_{2+x}Li_{1-x}(Al_xSi_{3-x}GeO_10)F_2$ series as the Al_xSi_{3-x} Ge series.

2-2. Infrared Absorption and X-ray Diffraction Analysis

Synthesized crystals were ground in an agate mortar, and sieved through a 325 mesh screen to prepare powder samples for infrared absorption spectrometry by the KBr disk method (Shimadzu, IR-430). The wavenumber of the absorption band was corrected using a polystyrene standard. For powder X-ray diffraction, CuKα radiation was used to identify any minerals other than mica. 12-16 diffraction lines were measured in the range of $24°\leq 2\theta \leq 74°$ at room temperature in order to determine the lattice constants by the least square method. Diffraction angles were corrected with silicon as standard.

3. Results and Discussion

3-1. Synthesis of Mica

Higher Al substitution and higher Ge content caused larger crystal sizes in the synthesized mica, and in the case

of $AlGe_3$ mica, crystals of good quality were obtained with a maximum size of 6-7mm, with a colorless and transparent appearance, and cleavability. Observed by a polarizing microscope and powder X-ray diffraction, no crystal phases or glass phases were detected except for fluorine mica. Therefore, the entire starting material was changed into mica with a constant composition, almost equal to the theoretical composition calculated from the starting material mixing ratios.

3-2. Infrared Absorption Spectra

Figure 1 shows the infrared absorption spectra of samples of the Al_xSi_{4-x}, Al_xGe_{4-x}, $Al_xSi_{3-x}Ge$, and $Al_xGe_{3-x}Si$ series. The absorption bands at 1115, 962, and 706cm^{-1} of mica with x=0.0 composition (equivalent to taeniolite) in the Al_xSi_{4-x} system in Fig. 1 (1) are due to the stretching vibration of Si-O, and according to the lattice vibrations of $(Si_2O_5)_n$ of talc[4] and mica,[5] the absorption bands are considered to be attributable to a^1_1, e^1_1, and a^2_1 modes, respectively. Further, the absorption band at 462cm^{-1} is caused by the deformation vibration of Si-O, and is attributable to an e^2_1 mode. Absorption bands at 1115 and 962cm^{-1} are distinctly separated from each other at x=0.0 and shifted toward each other with an increase in the X value. Moreover, at x=0.4, an absorption band appeared at 1020cm^{-1}, and at x=1.0, it changed into a single broad absorption band with shoulders on both sides. At the same time, as the x value increased, a new absorption band appeared near 810cm^{-1} and the absorption intensity showed a large increase. This absorption band is considered to be caused by the vibration of Al_{iv}-O from the results of infrared absorption spectra of conventional Al-substituted mica.[6] Additionally, with an increase in the x value, shoulders appeared on each side of the absorption band at 706cm^{-1}.

Samples with composition x=0.0 in the Al_xGe_{4-x} system in Fig. 1 (2) correspond to the Ge-isomorphic substitution analogue of taeniolite. The absorption bands at 880 and 800cm^{-1} in this spectrum are considered to be due to the stretching vibration of Ge-O, and that at 405cm^{-1} to the deformation vibration of Ge-O.[3] In this substitution system also, the absorption bands at 880 and 800cm^{-1} shifted closer to each other with an increase in the x value, and further at x=0.4 a new absorption band appeared in the vicinity of 840cm^{-1}, changing at x=1.0 into a single broad band with shoulders on both sides. In addition, an absorption band near 600cm^{-1} overlapped the one at 620cm^{-1} which appeared with an increase in the x value, forming a single broad band at x=1.0. In the case of the $Al_xSi_{3-x}Ge$ system in Fig. 1 (3) and $Al_xGe_{3-x}Si$ system in Fig. 1(4), major absorption bands appeared as in the Al_xSi_{4-x} and Al_xGe_{4-x} systems. When the x value increased, the spectrum of each system changed continuously in similar ways to those of the systems in Figs. 1 (1) and (2) above. Moreover, the intensity ratio of the absorption bands of Si-O and Ge-O appearing in the region 800-1100cm^{-1} varied with the Si-Ge content ratio. All the $Al_xSi_{2-x}Ge_2$, $Al_xSi_{1-x}Ge_3$, $Al_xGe_{2-x}Si_2$, and $Al_xGe_{1-x}Si_3$ systems had similar spectra to those in Figs. 1 (3) and (4).

When the spectral changes of these Al-substituted micas are compared with those of Ga-substituted mica, the following similarities occurred with an increase in the substitution:

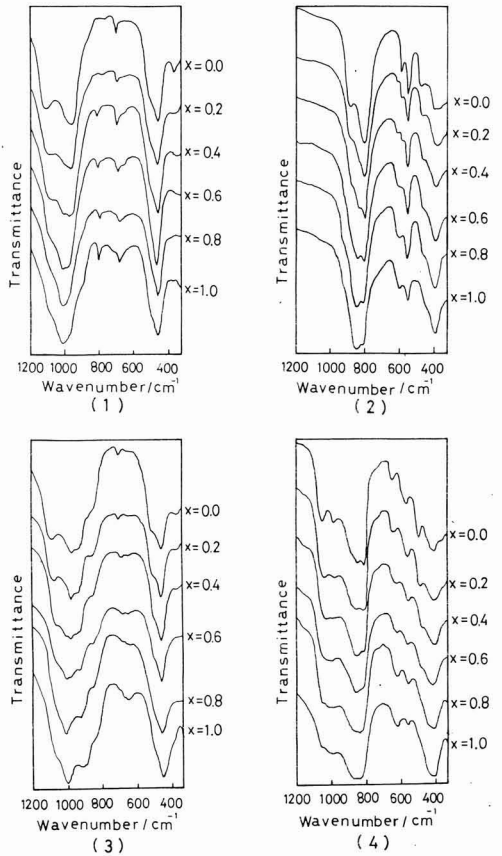

Fig. 1. Infrared spectra of Al-substituted fluorine micas.
(1) $KMg_{2+x}Li_{1-x}(Al_xSi_{4-x}O_{10})F_2$
(2) $KMg_{2+x}Li_{1-x}(Al_xGe_{4-x}O_{10})F_2$
(3) $KMg_{2+x}Li_{1-x}(Al_xSi_{3-x}GeO_{10})F_2$
(4) $KMg_{2+x}Li_{1-x}(Al_xGe_{3-x}SiO_{10})F_2$

i) absorption bands of a^1_1 and e^1_1 modes of Si-O and Ge-O shifted close to each other, and ii) a new absorption band appeared with an increase in the x value. However, the extent of the shift of the absorption bands was different as well as their locations. The absorption band of Al_{iv}-O was characteristic of Al_{iv} substitution, but was not detected in systems other than Al_xSi_{4-x} and $Al_xSi_3Ge_{1-x}$ because of the overlapping stretching vibration of Ge-O. As stated above, the infrared absorption spectra of fluorine mica proved to change sensitively in response to the chemical composition of mica. This indicates, therefore, that the composition of the synthesized mica varies according to the x value.

3-3. Lattice Constants

Figures 2 and **3** show the relationship between the x value and lattice constants for the mica of each substitution system, separated into two groups: a $KMg_{2+x}Li_{1-x}(Al_xSi_{4-x-y}Ge_yOMV10)F_2$ series with successive Si^{4+} substitution by Al^{3+} with a constant Ge content of the tetrahedral layer; and a $KMg_{2+x}Li_{1-x}(Al_xGe_{4-x-y}D\ Si_yO_{10})F_2$ series with suc-

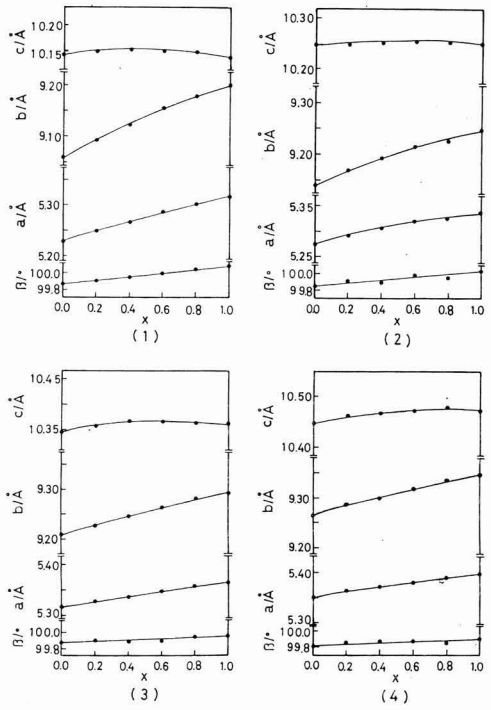

Fig. 2. Lattice constants of $KMg_{2+x}Li_{1-x}(Al_xSi_{4-x-y}Ge_yO_{10})F_2$ series fluorine micas.
(1) y=0; Al_xSi_{4-x} (2) y=1; $Al_xSi_{3-x}Ge$
(3) y=2: $Al_xSi_{2-x}Ge_2$ (4) y=3; $Al_xSi_{1-x}Ge_3$

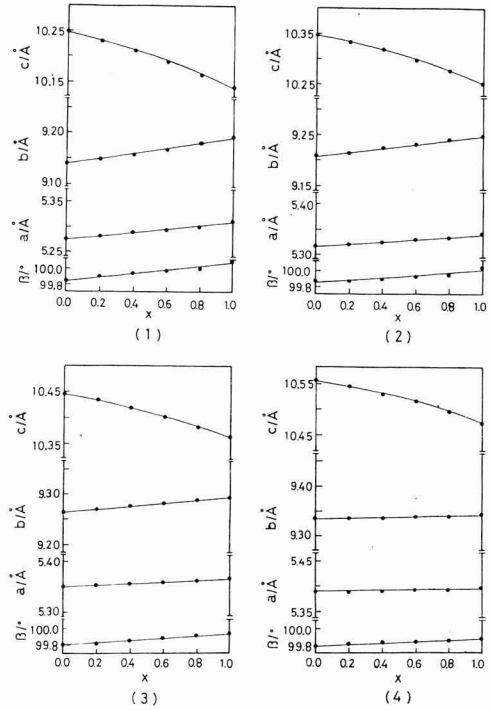

Fig. 3. Lattice constants of $KMg_{2+x}Li_{1-x}(Al_xGe_{4-x-y}Si_yO_{10})F_2$ series fluorine micas.
(1) y=3, $Al_xGe_{1-x}Si_3$ (2) y=2; $Al_xGe_{2-x}Si_2$
(3) y=1; $Al_xGe_{3-x}Si$ (4) y=0; Al_xGe_{4-x}

cessive Ge^{4+} substitution by Al^{3+} with a constant Si content in the tetrahedral layer. Moreover, the lattice constants measured for typical end member micas, as well as related reference data for mica are listed in **Table 1**. The standard deviation is given in parentheses. **Table 2** shows the data of powder x-ray diffraction for typical Al-substituted end member micas.

The measurement of the lattice constants of mica with x=0.0 composition (taeniolite) and with x=1.0 composition (fluorine phlogopite) of the Al_xSi_{4-x} system in Fig. 2 (1) were in good agreement with the reference values in Table 1. The lattice constants a and b of mica of the Al_xSi_{4-x} system in Fig. 2 (1), $Al_xSi_{3-x}Ge$ system in Fig. 2 (2), $Al_xSi_{2-x}Ge_2$ system in Fig. 2 (3), and $Al_xSi_{1-x}Ge_3$ system in Fig. 2 (4) increased almost linearly according to Vegard's rule with an increase in the x value. Nevertheless, the lattice constant c showed little change and tended to reach a maximum at a certain x value.

In contrast, in systems where Ge^{4+} was substituted by Al^{3+}, the lattice constants a, b, and β increased linearly with the x value as in Fig. 3, (1) to (4), while the lattice constant c decreased almost linearly. In the case of substitution systems with high Ge content, the axial angle β exhibited a low increase rate. As has been described above, the lattice constants of both the $Si^{4+}Al^{3+}$ substitution system in Fig. 2 and the Ge^{4+} Al^{3+} substitution system in Fig. 3 changed continuously with the x value, proving that they are complete solid solution systems.

Table 1.Lattice constants[1] for various fluorine micas.

Composition of micas	a(Å)	b(Å)	c(Å)	β(°)
$KMg_2Li(Si_4O_{10})F_2$	5.227(1)	9.057(2)	10.141(1)	99.86(2)
$KMg_2Li(Si_4O_{10})F_2$[2]	5.231(1)	9.065(2)	10.140(1)	99.86(2)
$KMg_2(AlSi_3O_{10})F_2$	5.315(1)	9.202(1)	10.137(1)	100.08(1)
$KMg_2(AlSi_3O_{10})F_2$[3]	5.307(1)	9.195(2)	10.134(1)	100.08(1)
$KMg_2Li(GeSi_3O_{10})F_2$	5.272(1)	9.139(1)	10.247(1)	99.84(1)
$KMg_2(AlGeSi_2O_{10})F_2$	5.335(3)	9.245(3)	10.249(3)	100.03(3)
$KMg_2Li(Ge_2Si_2O_{10})F_2$	5.315(1)	9.207(1)	10.345(1)	99.86(1)
$KMg_2(AlGe_2SiO_{10})F_2$	5.364(2)	9.292(2)	10.361(1)	99.94(2)
$KMg_2Li(Ge_3SiO_{10})F_2$	5.349(1)	9.263(1)	10.446(1)	99.80(2)
$KMg_2(AlGe_3O_{10})F_2$	5.396(2)	9.344(2)	10.471(2)	99.90(2)
$KMg_2(AlGe_3O_{10})F_2$[2]	5.417(6)	9.345(5)	10.468(1)	100.03(3)
$KMg_2Li(Ge_4O_{10})F_2$	5.388(1)	9.334(1)	10.556(1)	99.78(1)
$KMg_2Li(Ge_4O_{10})F_2$[2]	5.395(1)	9.341(1)	10.547(1)	99.87(2)

1) Standard deviations are in parentheses.
2) After Toraya et al.(1977),(1978).
3) After Takeda et al.(1975).

However, notable anisotropy was detected in "chemical expansion"[8] of lattices by such isomorphic substitution. Consequently, in order to study this anisotropic expansion and contraction behavior, the relationship between the b-axis value, a typical direction to indicate the size of a mica structure, and the basal spacing value (c·sinβ) in 8 series of synthesized mica was examined, as in **Fig. 4**. The major

compositions of end member micas of each series are given in the figure.

In the $Si^{4+}Al^{3+}$ substitution system in Fig. 4 (1), the relationship between the b-axis value and basal spacing is nonlinear, and the b-axis value greatly increases with an increase in the amount of Al substitution in each system while the basal spacing changes little or decreases after a slight increase. Such nonlinearity in the relationship between b and c·sinβ was not seen in the $Si^{4+}Ga^{4+}$ substitution of the Ga substitution system in the previous report.[3] Moreover, when the difference (Δb) of the b-axis values of both end member micas is compared as well as that of the basal spacing (Δc·sinβ), Δb decreases in substitution systems with high Ge content, while Δc·sinβ becomes negative in Al_xSi_{4-x} and $Al_xSi_{3-x}Ge$ systems, and positive in $Al_xSi_{2-x}Ge_2$ and $Al_xSi_{1-x}Ge_3$ systems, thus proving that the sign of Δc·sinβ is reversed with higher Ge content.

Table 2.X-ray powder diffraction data of Al-substituted fluorine micas.

$KMg_3(AlSi_3GeO_{10})F_2$			$KMg_3(AlSiGe_3O_{10})F_2$		
d /Å	I/I₀	hkl	d /Å	I/I₀	hkl
10.09	90	001	10.20	80	001
5.046	38	002	5.103	78	002
4.623	2	020	4.646	1	020
4.567	2	110	4.593	1	110
4.402	1<	$11\bar{1}$	4.445	1<	$11\bar{1}$
3.943	1	111	3.971	1	111
3.675	4	$11\bar{2}$	3.701	3	$11\bar{2}$
	sh	022		sh	022
3.364	100	003	3.402	100	003
3.157	8	112	3.184	6	112
2.929	6	$11\bar{3}$	2.954	5	$11\bar{3}$
2.720	3	023	2.745	3	023
2.658	3	$130,20\bar{1}$	2.672	3	$130,20\bar{1}$
2.627	5	$200,13\bar{1}$	2.642	4	$200,13\bar{1}$
2.523	16	004	2.551	21	004
2.441	4	$201,13\bar{2}$	2.457	3	$201,13\bar{2}$
2.271	1	$20\bar{3},132$	2.286	1	$20\bar{3},132$
2.180	2	$202,13\bar{3}$	2.196	1<	$202,13\bar{3}$
2.019	30	005	2.041	28	005
	sh	$20\bar{4},133$	2.018	1	$20\bar{4},133$
1.755	1	$134,20\bar{5}$	1.770	2	$134,20\bar{5}$
1.682	8	006,	1.701	5	006
	sh	$204,13\bar{5}$		sh	$204,13\bar{5}$
	sh	$20\bar{6},135$	1.558	2	$135,20\bar{6}$
1.541	6	$060,33\bar{1}$	1.549	2	$060,33\bar{1}$
1.442	3	007	1.522	1<	116
1.376	1	027	1.458	3	007
1.368	4	$136,20\bar{7}$	1.391	1	027
			1.381	3	$136,20\bar{7}$

1M mica-type structure.
Intesities probably affected by preferred orientation which inhances 001 reflections.
The sign sh shows the shoulder reflection.

On the other hand, in the case of the $Ge^{4+}Al^{3+}$ substitution system in Fig. 4 (2), the Al substitution slightly increased the b-axis value but decreased basal spacing greatly, but there was a linear relationship between the b-axis value and basal spacing. Especially, it was observed that as the Ge content increased the negative gradient became greater while Δb was lower. In the $Ge^{4+}Ga^{3+}$ substitution of the Ga substitution system reported earlier, a nonlinear relationship was detected between b and c·sinβ.[3]

Although the proportion of Mg^{2+} and Li^{+} at the octahedral site of mica of each substitution system is different depending on the x value, their ionic radii[7] are close (0.72 and 0.76 respectively) so that the influence of the size of positive ions at the octahedral site on changes in the b-axis value and basal spacing is considered to be small. In contrast, the ionic radii of Si^{4+}, Ge^{4+}, and Al^{3+} at the tetrahedral site are 0.26, 0.39, and 0.39 respectively.[7] Consequently, an increase in the b-axis value of the $Si^{4+}Al^{3+}$ substitution system is supposed to be caused mainly by the size of ions at the tetrahedral site, whereas an increase in the b-axis value and a decrease in basal spacing of the $Ge^{4+}Al^{3+}$ substitution system cannot be explained by the ion size. Then, the relationship between b and c·sinβ in Fig. 4 was investigated using the structural distortion of coordinated polyhedra in the mica structure.

It is known that the mica structure has structural distortion in each sheet to accommodate dimensional misfitting

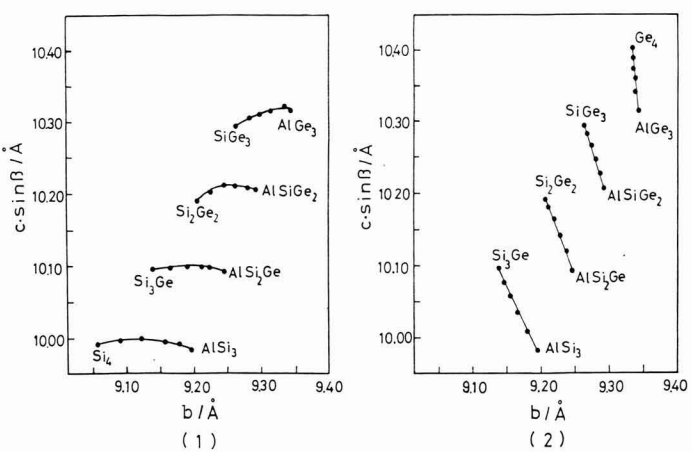

Fig. 4. A plot of c·sinβ vs. b-dimension for the Al-substituted fluorine micas. (1) $KMg_{2+x}Li_{1-x}(Al_xSi_{4-x-y}Ge_yO_{10})F_2$ series, (2) $KMg_{2+x}Li_{1-x}(Al_xGe_{4-x-y}Si_yO_{10})F_2$ series
The tetrahedral composition is expressed in the figure as abbreviated symbols for the end member fluorine micas.

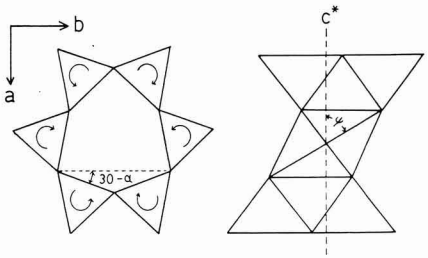

Fig. 5. Schematic illustration of tetrahedral rotation angle (a) and octahedral flattening angle (y).

between tetrahedral and octahedral sheets. As shown in **Fig. 5**, the distortion of the tetrahedral sheet is expressed by a tetrahedral rotation angle α and that of the octahedral sheet by an octahedral flattening angle ψ.[8,9] That is, with an increase in α the tetrahedral sheet contracts in the b-axis direction, and with an increase in ψ the octahedral sheet expands in the a-and b-axis direction and contracts in the $c\cdot\sin\beta(c^*)$ direction. Moreover, α and ψ are related to the b-axis value by the following equations (1) and (2)[8,9]:

$$\alpha = \cos^{-1}(b/2\sqrt{3}\cdot e_b) \quad \ldots\ldots (1)$$

$$\psi = \sin^{-1}(b/3\sqrt{3}\cdot d_o) \quad \ldots\ldots (2)$$

where e_b is the distance between basal oxygen and d_o is that between the positive and negative ions of the octahedron. Here, e_b and d_o values of four kinds of fluorine mica samples after structural analysis were used: taeniolite, fluorine phlogopite,[8] and their isomorphic substituted analogues.[10,11] In the case of the mica series governed by the same way of charge balancing that indicates whether interlayer cations in the mica structure compensate for positive charge deficiencies caused in the octahedral sheet or tetrahedral sheet, a linearity was assumed between the mean ionic radius (Rm) of a tetrahedral cation and e_b as well as the b-axis value and d_o in order to estimate e_b and d_o values of each end member micas. **Table 3** lists the above e_b and d_o values, α and ψ values obtained from these values along with the measured b-axis value using equations (1) and (2), and related reference values. From the table it is clear that the higher the Al substitution or the Ge content, the greater the α and ψ values, that is, the distortion of the mica structure in these samples. As stated above, Ge substitution causes great structural distortion and the rotation of the tetrahedra considerably relieved an increase in the b-axis value, so that in Fig. 4 (1) and (2) higher Ge content is considered to have resulted in lower Δb. In $Ge^{4+}Al^{3+}$ substitution in Fig. 4 (2), the b value increased even with the same size of Ge^{4+} and Al^{3+} ions; probably because as the charge balancing transforms an octahedral to a tetrahedral sheet, the negative charge localizes rather in basal oxygen than in apical oxygen, thus increasing the repulsion between basal oxygens as well as raising the e_b value as in Table 3.

The basal spacing ($c\cdot\sin\beta$) can be expressed by equation (3) using the thickness of an interlayer region (IL), that of a tetrahedral sheet (TL), and that of an octahedral sheet (OL).

$$c\cdot\sin\beta = IL + 2TL + OL \quad \ldots\ldots (3)$$

Table 3. Predicted values of a[1] and ψ[2] for some fluorine micas and estimated e_b[3] and d_o[4] values used for calculation.

Composition of micas	α (°)	ψ (°)	e_b (Å)	d_o (Å)
$KMg_2Li(Si_4O_{10})F_2$	2.5	57.7	2.617	2.061
$KMg_2Li(Si_4O_{10})F_2$[5]	1.08	57.9[6]	2.617	2.061
$KMg_3(AlSi_3O_{10})F_2$	6.7	59.1	2.671	2.061
$KMg_3(AlSi_3O_{10})F_2$[7]	6.5	59.4	2.671	2.061
$KMg_2Li(GeSi_3O_{10})F_2$	6.6	58.2	2.656	2.070
$KMg_3(AlGeSi_2O_{10})F_2$	10.8	59.5	2.717	2.065
$KMg_2Li(Ge_2Si_2O_{10})F_2$	9.4	58.5	2.694	2.078
$KMg_3(AlGe_2SiO_{10})F_2$	14.2	59.7	2.767	2.070
$KMg_2Li(Ge_3SiO_{10})F_2$	11.9	58.8	2.733	2.085
$KMg_3(AlGe_3O_{10})F_2$	16.3	60.0	2.811	2.076
$KMg_3(AlGe_3O_{10})F_2$[5]	15.9	60.2	2.811	2.076
$KMg_2Li(Ge_4O_{10})F_2$	13.7	59.2	2.773	2.092
$KMg_2Li(Ge_4O_{10})F_2$[5]	13.5	59.3[6]	2.773	2.092

1) α : tetrahedral rotation angle
2) ψ : octahedral flattening angle
3) e_b : the basal O-O distance
4) d_o : the average octahedral cation to anion distance
5) After Toraya et al.(1977),(1978).
6) shown for M(2) site
7) After Takeda et al.(1975).

Despite the same size of Ge^{4+} and Al^{3+} ions, the $c\cdot\sin\beta$ value of $AlGe_3$ mica is much lower than that of Ge_4 mica, which is due to the fact that the expansion and contraction of the lattice is affected by the charge balancing, thus leading to substantial flattening of the octahedral sheet and the OL value decreasing as in Table 3. The same reasoning applies to the case where $\Delta c\cdot\sin\beta$ in each substitution system in Fig. 4 (2) has a negative value. Moreover, $\Delta c\cdot\sin\beta$ has a negative value in substitution systems with high Si content in Fig. 4 (1), resulting in the conclusion that the decrease in OL exceeded the increase in TL.

In the above discussion, the thickness IL was approximated as constant, but in the substitution system with high Ge content, with high Al substitution and large α, IL is considered to increase as α increases,[3,8] so that it is necessary to consider an IL increase. Consequently, the conversion of $\Delta c\cdot\sin\beta$ to a positive value in the substitution system with high Ge content in Fig. 4 (1) is believed to be caused by the large contribution of this increase in IL. Additionally, $c\cdot\sin\beta$ reaching a local maximum at a certain x value can be shown to be due to the effect of an OL decrease due to Al substitution balancing that of a (TL+IL) increase. Further, higher Ge content in Fig. 4 (2) leads to a slight decrease in $\Delta c\cdot\sin\beta$; the reason may be that an (IL) increase because of an increase in the α value cancels the (OL) contraction because of an increase in the distortion of octahedrons. The above discussion taking changes in the thickness of each coordinated polyhedron into consideration, can explain complicated changes in basal spacing although in a qualitative manner.

The relationship between $c\cdot\sin\beta$ and the mean ionic radius (Rm) of tetrahedral cations is shown in **Fig. 6** for each end-member mica of the Al-substituted system and the corresponding Ga-substituted system,[3] as well as the major compositions of micas. Different straight lines are plotted

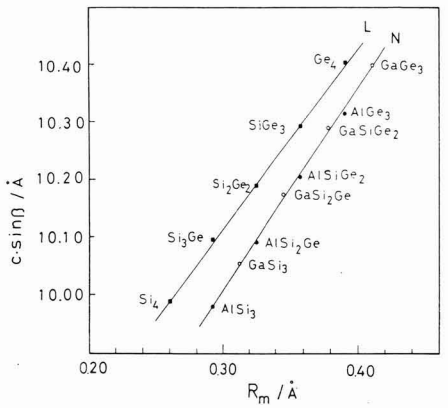

Fig. 6. The relationships between c·sinβ and average radius of tetrahedral cations for typical end member micas having general formulas KMg3 (ZSi3-yGeyO10)F2 [Z=Al, Ga; y=0, 1, 2, 3] and KMg2Li (Si4-yGeyO10)F2 [y=0,1,2,3,4]. Mica composition is shown as abbreviated symbols for composition of tetrahedral layers.

for mica series based on different charge balancing, but good linearity is established between c·sinβ and Rm. This indicates that the size of lattices and the distortion of coordinated polyhedrons is basically determined by the factors of ionic radius and charge balancing. In the figure the straight line N is located lower than the straight line L and has a greater gradient than the latter, suggesting that the charge balancing with a trivalent ion on the tetrahedral site allows a greater decrease in OL and a greater increase in IL (ΔIL). In this substitution system, both factors of Rm and the charge balancing vary with an increase in the x value, so that in the case of a $Ge^{4+}Ga^{3+}$ substitution system (Δr=0.08) and $Si^{4+}Al^{3+}$ substitution system (Δr=0.13) having a small difference (Δr) in the size of substitute ions, the b-c·sinβ relationship is considered to show a nonlinear change by the balance of the effect of both factors. Especially, in the case where either Rm or the way of charge balancing plays a greater role, it is expected to be a linear b-c·sinβ relationship.

4. Conclusions

A series of Al-substituted micas of $KMg_{2+x}Li_{1-x}(Al_xSi_{4-x-y}Ge_yO_{10})F_2$ and $KMg_{2+x}Li_{1-x}(Al_xGe_{4-x-y}Si_yO_{10})F_2$ [x=0.0 to 1.0, y = 0, 1, 2, 3] was synthesized using taeniolite, $KMg_2Li(Si_4O_{10})F_2$, and its Ge isomorphic analogues as end-member micas, in order to investigate changes in infrared absorption spectra and lattice constants due to isomorphic substitution. The results were compared with those of a Ga substitution system reported earlier,[3] to obtain the following results.

1) The infrared absorption spectra of mica varied continuously with changes in the amount of isomorphic substitution, and a new absorption band due to Al substitution in the high Si-content systems as well as the shift of Si-O and Ge-O absorption bands was observed.

2) Lattice constants changed continuously with the amount of Al substitution, showing a formation of complete solid solution system.

3) The lattice constants a and b increased monotonously with the amount of Al substitution. Basal spacing (c·sinβ) showed little change by the replacement of Si^{4+} with Al^{3+}, while it decreased monotonously by replacing Ge^{4+} with Al^{3+}.

4) A higher percentage of Al substitution and Ge content resulted in greater structural distortion (α, ψ) of tetrahedral and octahedral sheets.

5) The change of lattice constants by Al substitution could be explained by a b-c·sinβ diagram, structural distortion (α, ψ) and a change in the structures of interlayer regions.

6) Plotting c·sinβ value of each end member mica including the corresponding Ga substitution mica against the mean ionic radius (Rm) of tetrahedral cations showed a linear relationship for each mica series with the same charge balancing, which indicated that the lattice size and the distortion of coordinated polyhedrons depend on both the ion size and the way of charge balancing.

Acknowledgments:

The authors are grateful to Prof. Emeritus Nobutoshi Daimon of Shinshu University for his assistance and Mr. Koki Tachiuchi for his cooperation in experiments.

References:

1) a) H.R. Shell and K.H. Ivey, "Fluorine Mica", U.S. Bur. Mines., Bulletin 647, 110-22 (1969).
b) T. Matsushita, and S. Shikauchi, Kogyo Kagaku Zasshi, 74, 839-44 (1971).
c) K. Kitajima, R. Kondo and N. Daimon, Clay Miner., 13, 167-75 (1978).
2) H. Toraya, S. Iwai, F. Marumo and M. Hirao, Z. Kristallogr., 146, 73-83 (1977).
3) K. Kitajima, T. Inada, and N. Takusagawa, Seramikkusu Ronbun-Shi, 97, 649-55 (1989).
4) J.D. Russell, V.C. Farmer and B. Velde, Miner. Mag., 37, 869-79 (1970).
5) a) N. Ishi, Kobutsugaku Zasshi, 9, 193-206 (1969).
b) M. Ishi, T. Shimanouchi and M. Nakahira, Inorg. Chim. Acta, 1, 387-92 (1967).
6) a) V.C. Farmer and J.D. Russell, Spectrochim. Acta, 20, 1149-73(1964).
b) V.C. Farmer, "The Infrared Spectra of Minerals," Mineralogical Society, London, 345-46 (1974).
7) R.D. Shannon, Acta Crystallogr., A32, 751-67 (1976).
8) H. Takeda and B. Morosin, Acta Crystallogr., B31, 2444-52 (1975).
9) G. Donnay, J. D. H. Donnay and H. Takeda, Acta Crystallogr., 17, 1374-81 (1964).
10) H. Toraya, S. Iwai, F. Marumo and M. Hirao, Z. Kristallogr., 148, 65-81 (1978).
11) H. Toraya, S. Iwai, F. Marumo and M. Hirao, Mineral. J., 9, 221-30 (1978).

This article is a full translation of the article which appeared in Nippon Seramikkusu Kyokai Gakujutsu Ronbunshi (Japanese version), Vol.98, No.5, 1990.

Decrease of the Solubility of Gypsum by Incorporation of Phosphate Ion

Tamotsu Yasue, Yoshiyuki Kojima, Hiroaki Inoue and Yasuo Arai

Department of Industrial Chemistry, Faculty of Science and Engineering, Nihon University
1-8, Kanda-Surugadai, Chiyoda-ku, Tokyo 101, Japan

The conditions for direct preparation of fibrous II-gypsum anhydride having the lowest solubility in gypsum modifications by the reaction in $CaCl_2$-H_2SO_4-CH_3OH system were reported in a previous paper.Studies were made to investigate the relationship between the incorporation of phosphate ion and the decrease of both solubilities of acicular form (produced by the reaction of $CaCl_2$-Na_2SO_4-Na_2HPO_4 system) and fibrous form (produced by the reaction of $CaSO_4$-Na_2HPO_4-CH_3OH system) of gypsum hemihydrate.

Phosphate ion was incorporated into the acicular hemihydrate by adding a $CaCl_2$ solution to a mixed solution (pH8) of Na_2SO_4 and Na_2HPO_4 at 100°C.Changes in lattice constants caused by the substitution of SO_4^{2-} HPO_4^{2-} in gypsum hemihydrate crystal were found by X-ray diffraction.The upper limit of the incorporation was 7 percent (HPO_4^{2-}/SO_4^{2-} mol ratio 0.07).This finding was also supported from data of TG-DTA, IR spectra and scanning electron microscopic observation.However, the upper limit was raised up to 15 per cent ($HPO4^{2-}/SO_4^{2-}$ mol ratio 0.15), if pH of the mixed solution was adjusted to 9 from 8 by adding NaOH solution.

On the other hand, the fibrous hemihydrate was incorporated with phosphate ion by the reaction between Na_2HPO_4 solution and gypsum organogel which was produced by adding methanol to a saturated solution of gypsum dihydrate at 65°C.The upper limit of the incorporation of phosphate ion was also 15 per cent.This fibrous solid solution had a very high water-resistivity as 0.4×10^{-3} Ca^{2+} mol dm^{-3} after dipping in water for 1h retaining the original fibrous form.Moreover, fibrous II-anhydride produced by heating this fibrous solid solution showed a good water-resistivity, decreasing to about 1/50 against that of gypsum dihydrate (1.52×10^{-2} Ca^{2+} mol dm^{-3} after dipping in water for 1h).

[Received December 11, 1989; Accepted January 25, 1990]

Key-words: Incorporation of phosphate ion in gypsum, Water-resistivity of fibrous gypsum hemihydrate, $HPO_4^{2-} \leftrightarrow SO_4^{2-}$ substitution, Inorganic filler

1. Introduction

Gypsum, which is in wide use as a nonflammable lightweight architectural material, has such a relatively high solubility (0.202g $CaSO_4$/100cm^3 H_2O, 20°C) among the slow-dissolving salts that it is not suitable for applications involved with water.

Through a series of studies on making calcium compounds fibrous, we have already proved that gypsum hemihydrate, particularly when highly c-axis oriented in hexagonal crystals, is ready to be turned fibrous, and we have also reported that such gypsum, if kept fibrous by heating, can be turned into slow-dissolving II-gypsum anhydrite.[1)]However, it is inevitable that the fibers are weakened by heating and rearrangement.We also have reported on the decrease of solubility obtained by synthesizing fibrous II-gypsum anhydride directly from gypsum gel.[2)]

If the solubility of gypsum can be sufficiently decreased, gypsum can be applied as an exterior architectural material and if fibrous gypsum also can be made less soluble it will have prospects as a filler for paper and plastics.Thus, noticing that unstable-structured gypsum hemihydrate with the highest solubility was ready during its settling to allow other ions to coprecipitate and incorporate, we tried to decrease its solubility by allowing phosphate ions to incorporate in fibrous gypsum hemihydrate during synthesis.There are various reports on the incorporation of phosphate ions (HPO_4^{2-}) in gypsum dihydrate and double salts.[3-9)]Phosphate ions slow down the crystal growth of gypsum dihydrate and thus greatly retard the condensation of calcined gypsum made from gypsum dihydrate.This is a major difficulty in the manufacture of gypsum phosphate as a byproduct in the phosphate fertilizer industry.On the other hands, there are no reports on the incorporation of phosphate ions in gypsum hemihydrate.

We proved that the solubility of gypsum hemihydrate could be decreased to about 1/40 of that of gypsum dihydrate by investigating the synthesizing conditions and the properties of the synthesized products: acicular gypsum hemihydrate containing incorporation of phosphate ions produced in the presence of an Na_2HPO_4 solution in the $CaCl_2$-Na_2SO_4 reaction, fibrous gypsum hemihydrate containing incorporation of phosphate ions demethanolized and crystallized in the presence of an Na_2HPO_4 solution and gypsum organogel crystallized by adding methanol to a gypsum-saturated solution.This report describes our investigation.

2. Samples and Test Method

2-1. Samples

The acicular and the fibrous gypsum hemihydrate samples, both with incorporation of phosphate ions, were synthesized from a $CaCl_2$-Na_2SO_4-Na_2HPO_4 solution and from a $CaSO_4$-Na_2HPO_4-CH_3OH solution respectively.The reagents used here were guaranteed grades, made by Kanto

Kagaku, at purity levels of sodium sulfate anhydride 99%, sodium hydrogen phosphate anhydride 99%, calcium chloride anhydride 95%, calcium sulfate dihydrate 98% and methanol 99.6%. To fixate and wash phosphate ion incorporated gypsum hemihydrate, guaranteed reagents of methanol and acetone were used.

2-2. Test Method

For reactions of a $CaCl_2$-Na_2SO_4-Na_2HPO_4 solution, a 0.20mol/dm^3 Na_2SO_4 solution was mixed with a 0.20mol/dm^3 Na_2HPO_4 solution in a certain ratio (Na_2HPO_4-/Na_2SO_4 *mol ratio: 0.042 to 1.50) and 100cm^3 of the* product was held at 100°C in a 300cm^3 three-neckflaskwith acirculation tube. 50cm^3 of a 0.40mol/dm^{-3} $CaCl_2$ solution was added to this mixed solution.The product was cured for 5 min and then filtered.As a result, acicular gypsum hemihydrate with incorporation of phosphate ions was obtained.

In reactions of a $CaSO_4$-Na_2HPO_4-CH_3OH solution, phosphate ions were incorporated in the fibrous gypsum hemihydrate as follows.150cm^3 of methanol was added to 100cm^3 of a gypsumdihydrate solution (0.202g $CaSO_4$/100cm^3 H_2O, 20°C) at 65°C to produce gypsum organogel.30cm^3 of a Na_2HPO_4 solution conditioned from 1×10^{-5} to 3×10^{-1} mol/dm^3 was added to it and crystals were obtained by quickly sucking up and filtering the mixed solution.For characterization, the gypsum hemihydrate samples prepared with phosphate ions incorporated by the two methods mentioned above were submitted to X-ray diffraction, thermal analysis (TG-DTA), infrared absorption spectrum and chemical analysis as well as SEM observation.To determine phosphate and sulfate ions in sediments ICP analysis and an ammonium molybdate method were used for phosphate ions and a weight method was employed for sulfate ions by precipitating barium sulfate out of a 1/10N barium chloride solution.

To investigate the hydration stability of gypsum hemihydrate and II-gypsum anhydride with incorporation of phosphate ions, the levels of their solution were obtained.0.25g of each sample was dipped in 50cm^3 of pure water at 20°C for a certain period and, using a 93-20 calcium electrode made by Orion Research submerged in an Expandomatics SS-2 pH meter made by Toshiba-Beckmann, the level of Ca^{2+} was obtained from the variation in calcium concentration.[1,2]The amounts of phosphate and sulfate ions dissolved were determined by the same method.

3. Results and Review

3-1. Decrease of Solubility of Acicular Gypsum Hemihydrate by Incorporating Phosphate Ions ($CaCl_2$-Na_2SO_4-Na_2HPO_4 System)

In studies on solid solutions of the $CaSO_4{\cdot}2H_2O$-$CaHPO_4{\cdot}2H_2O$ system, a coprecipitation method with a $CaCl_2$ solution added to a mixed solution of Na_2SO_4 and Na_2HPO_4 is generally used.[3,6]From the relation between the solubility and temperature of gypsum variants in pure water, it is also known that gypsum hemihydrate is stable at temperatures above 100°C.[10-12]Thus, the present test was conducted at 100°C, within the range of gypsum hemihydrate production, by reactions in a $CaCl_2$-Na_2SO_4-Na_2HPO_4 solution.In fact, it was proved that in the synthesis of this system, gypsum hemihydrate was produced favorably at 100°C.

Figure 1 shows the relation between the initial reacting solution and HPO_4^{2-}/SO_4^{2-} mol ratios in precipitates generated when phosphate ion containing acicular gypsum hemihydrate is produced by adding a $CaCl_2$ solution to a mixed solution of Na_2SO_4 and Na_2HPO_4.As the HPO_4^{2-} mol ratio in the initial reacting solution is increased, the mol ratios in the precipitatesalsoriselinearly,butwhenthe HPO_4^{2-}/SO_4^{2-} *mol ratio exceeds* 1.0, they level off at around 0.55.This suggests that when the HPO_4^{2-}/SO_4^{2-}mol ratios are lower than 0.55, both precipitates and solid solutions are occasionally mixed with calcium phosphate.

Figure 2 shows the X-ray diffraction patterns of the precipitates obtained; (a) for a single phase of gypsum hemihydrate, (b) through (d) for precipitates with different HPO_4^{2-}/SO_4^{2-} mol ratios.As the HPO_4^{2-} mol ratio increases, the diffraction peaks of gypsum hemihydrate become less intense and broader.With HPO_4^{2-}/SO_4^{2-} mol ratios above 0.10, faint peaks of calcium hydrogen phosphate anhydride and dihydrate appear in addition to gypsum hemihydrate.Also, as the HPO_4^{2-}/SO_4^{2-} mol ratio increases, the peak of gypsum hemihydrate shifts toward the low angle side.Referring to the X-ray diffraction data, we studied variations in the lattice constants of gypsum hemihydrate with the HPO_4^{2-}/SO_4^{2-} ratios of the precipitates up to 0.10.

Figure 3 shows changes in the lattice constants a and c due to incorporation of phosphate ions into hexagonal gypsum hemihydrate.The lattice constants increase linearly in the precipitate HPO_4^{2-}/SO_4^{2-} mol ratio range below around 0.07 and stay constant in higher HPO_4^{2-}/SO_4^{2-} mol ratio ranges.This shows that the limit of solid solution under the present test conditions is 7 mol%.The ion radii of HPO_4^{2-} and SO_4^{2-} are nearly the same: 2.36 and 2.30 respective-

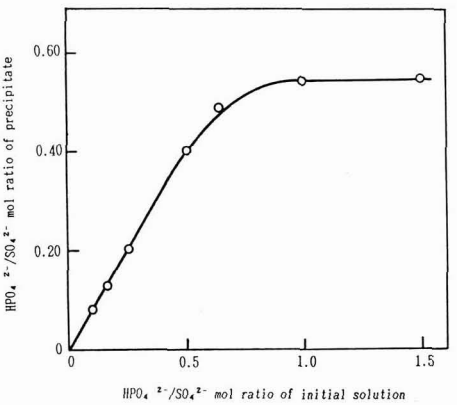

Fig. 1. Amount of phosphate ion in acicular gypsum hemihydrate. Temperature: 100°C, Aging time: 5 min. Na_2SO_4-Na_2HPO_4 solution (HPO_4^{2-}/SO_4^{2-} mol ratio 0.042 to 1.50): 0.200 mol/dm^3 (A), $CaCl_2$ solution: 0.400 mol/dm^3 (B), A/B volume ratio: 2/1.

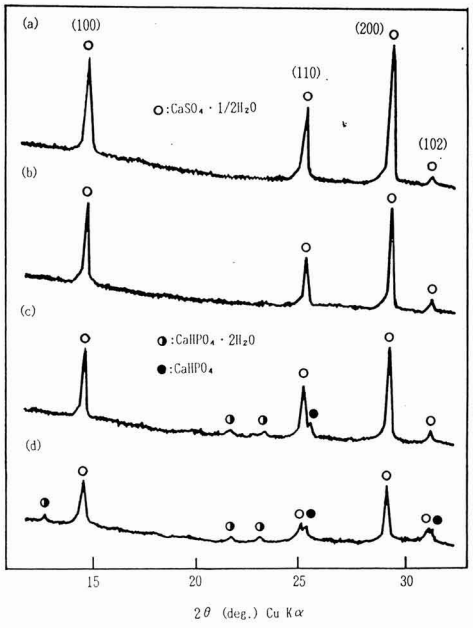

Fig. 2. X-ray diffraction pattern of acicular gypsum hemihydrate incorporating phosphate ions.
(a) Gypsum hemihydrate, (b) 0.05, (c) 0.10,
(d) 0.15 (HPO_4^{2-}/SO_4^{2-} mol ratio).

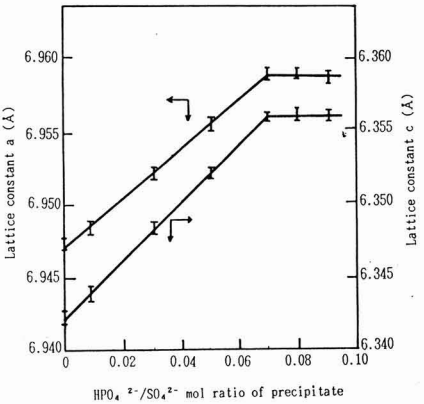

Fig. 3. Change in lattice constant of acicular gypsum hemihydrate incorporating phosphate ions.

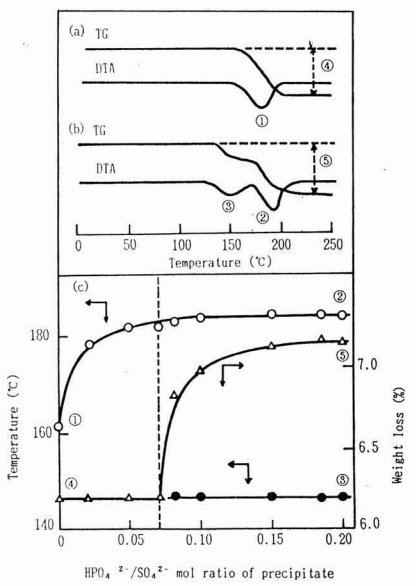

Fig. 4. TG-DTA curve of acicular gypsum hemihydrate incorporating phosphate ions.
(a) Gypsum hemihydrate, (b) HPO_4^{2-}/SO_4^{2-} mol ratio 0.20 (mixture of solid solution and calcium phosphate), (c) Top temperature of endothermic peak and weight loss of TG-DTA curve.

ly.This suggests that the incorporation of phosphate ions into gypsum hemihydrate is probably by a replacement; $HPO_4^{2-} \leftrightarrow SO_4^{2-}$.[5]

In fact, from the infrared absorption spectra of solid solutions of the $CaSO_4 \cdot 2H_2O$-$CaHPO_4 \cdot 2H_2O$ system, it is known that incorporation of phosphate ions into gypsum dihydrate causes a new absorption to appear at around $837cm^{-1}$.[6] Also the infrared absorption spectra obtained with the solid solutions in this study showed absorptions due to incorporation by $HPO_4^{2-} \leftrightarrow SO_4^{2-}$ replacement at around $837cm^{-1}$ with HPO_4^{2-}/SO_4^{2-} mol ratios up to 0.07, which proved the existence of solid solutions.

Figure 4 shows TG-DTA curve variations due to incorporation of phosphate ions into gypsum hemihy-drate. (a) is for a single phase of gypsum hemihydrate, (b) is for a precipitate (HPO_4^{2-}/SO_4^{2-} mol ratio 0.20) and (c) shows the relation between HPO_4^{2-}/SO_4^{2-} mol ratio variations due to incorporation of phosphate ions, maximum temperatures and weight decreases at endothermic peaks on the TG-DTA curves. (1) represents the maximum temperature of an endothermic peak due to dehydration in the change from gypsum hemihydrate to III-gypsum anhydride.With gypsum hemihydrate alone, this temperature is about 160°C.As the solid solution of phosphate ions increases, the dehydration temperature rises nearly to a mol ratio of 0.07 and becomes constant at around 180°C.At a mol ratio of 0.20, for example, in the range above 0.07 shown by a dotted line, a new endothermic peak (3) appeared at 145°C due to the dehydration of calcium hydrogen phosphate dihydrate ($CaHPO_4 \cdot 2H_2O$), which stayed constant irrespective of mol ratios. (4) represents a weight decrease due to dehydration of gypsum hemihy-drate into III-gypsum anhydride.It is about 6.2%, almost in agreement with the theoretical value for gypsum hemihydrate.With mol ratios above 0.07, in which calcium hydrogen phosphate dihydrate is produced in addition to solid solutions, the weight decrease at a mol ratio of 0.20 increases further by about 1.5% as shown by (5).Thus, the endothermic peak (2) is due to the incorporation dissolution of phosphate ions and this proves that gypsum hemihydrate with incorporation of phosphate ions shifts the dehydration temperature of the crystallization water up-

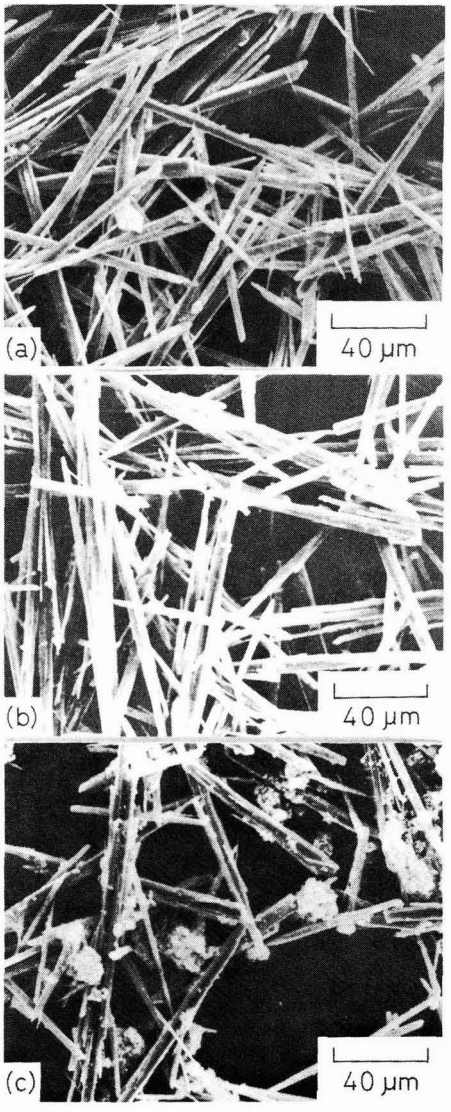

Fig. 5. Change in crystal shape of acicular gypsum hemihydrate incorporating phosphate ions.
(a) Gypsum hemihydrate, (b) HPO_4^{2-} mol ratio 0.07 (solid solution), (c) 0.15 (mixture of solidsolution and calcium phosphate).

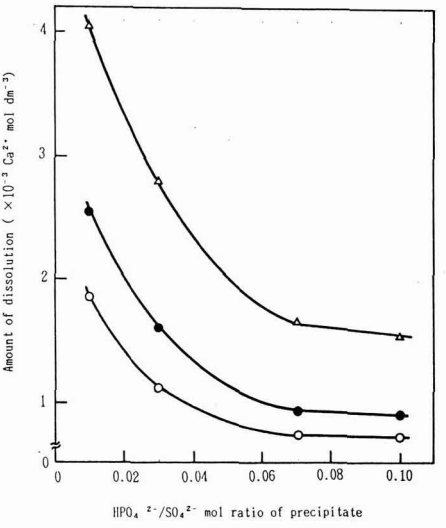

Fig. 6. Dissolution velocity of acicular gypsum hemihydrate incorporating phosphate ions.
Dipping time (min): ○ 30, ● 60, △ 180,
Temperature: 20°C.

ward and thermally stabilizes.Also, the level of the solid solution in precipitates with HPO_4^{2-}/SO_4^{2-} mol ratio of 0.20 is 0.07.If it is above 0.07, there is a mixture with calcium phosphate.

Figure 5 shows SEM graphs of acicular gypsum hemihydrate with incorporation of phosphate.In the single phase of gypsum hemihydrate (a), the products are acicular crystals about 140μm long and 4μm in diameter.In solid solution (b) at a HPO_4^{2-}/SO_4^{2-} mol ratio of 0.07, there is no change in shape from the original samples, either.At 0.15 (c), fine calcium phosphate is precipitated over the surfaces of acicular crystals of gypsum hemihydrate.Therefore, the results of TG-DTA curve analysis and SEM observation proved that phosphate ions incorporated by nearly 7mol% in acicular gypsum hemihydrate.

Figure 6 shows the relation between the level (HPO_4^{2-}/SO_4^{2-} mol ratio) of phosphate ions incorporated in acicular gypsum hemihydrate and the solubility in water.The solubility of gypsum hemihydrate in water is so much higher than that of gypsum dihydrate that the solution is oversaturated with gypsum dihydrate, causing gypsum dihydrate to be precipitated during dissolution.Thus, the ultimate result is the level of dissolution of gypsum dihydrate (0.202g $CaSO_4/100cm^3$ H_2O, 1.52×10^{-2} Ca^{2+} mol/dm^3, 20°C).As the solid solution of phosphate ions increases, the level of dissolution decreases.The level of dissolution of acicular gypsum hemihydrate with phosphate ions incorporated to a maximum at a HPO_4^{2-}/SO_4^{2-} mol ratio of 0.07 is particularly low, about 1/20 of that of gypsum dihydrate after 1h of immersion.However, it is constant with mol ratios about 0.07.The levels of SO_4^{2-} and HPO_4^{2-} ions in the eluate after immersion of the solid solutions with HPO_4^{2-}/SO_4^{2-} mol ratios below 0.07 were obtained and the results showed that these ions were dissolved at the same HPO_4^{2-}/SO_4^{2-} ratio before dissolution.

3-2. Decrease of Solubility of Fibrous Gypsum Hemihy-drate by Incorporating Phosphate Ions ($CaSO_4$-Na_2HPO_4-CH_3OH system)

Using the basic knowledge about the incorporation of phosphate ions in acicular gypsum hemihydrate produced in reactions of a $CaCl_2$-Na_2SO_4-Na_2HPO_4 solution, we tried to incorporate phosphate ions during the synthesis of fibrous gypsum hemihydrate by reactions of a $CaSO_4$-CH_3OH solu-

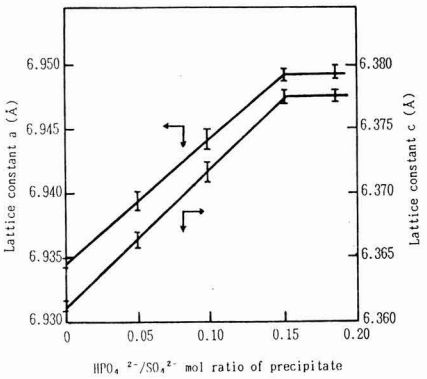

Fig. 7. Change in lattice constant of fibrous gypsum hemihydrate incorporating phosphate ions.

tion.[1)]

Adding methanol to a solution saturated with gypsum dihydrate causes gypsum organogel to be produced.We obtained fibrous gypsum hemihydrate with incorporation of phosphate ions by adding an Na_2HPO_4 solution to the gypsum organogel mentioned above and sucking up and filtering methanol quickly.It could also be done by adding methanol after mixing the gypsum dihydrate saturated solution with an Na_2HPO_4 solution with this method, the reactions started already during mixing, producing calcium phosphate precipitates, and so fibrous gypsum hemihydrate could not be synthesized.

Figure 7 shows changes in the lattice constants of fibrous gypsum hemihydrate due to incorporation of phosphate ions.As the HPO_4^{2-}/SO_4^{2-} mol ratio in the precipitates increases to 0.15, lattice constants a and c of gypsum hemihydrate rise linearly, and in higher mol ratio ranges they stay constant.While the maximum level of phosphate ions incorporated in the acicular gypsum hemihydrate produced in reactions of a $CaCl_2$-Na_2SO_4-Na_2HPO_4solutionis0.01intermsof HPO_4^{2-}/SO_4^{2-} mol ratio, that with the fibrous gypsum hemihydrate produce in reactions of a $CaSO_4$-Na_2HPO_4-CH_3OH solution is about double: 0.15.

The difference in the level of incorporation ofphosphate ions between acicular and fibrous gypsum hemihydrate can be ascribed to the stability of HPO_4^{2-} in the reacting solutions.While HPO_4^{2-} ions are stable in the pH range from 9.0 to 9.5, $H_2PO_4^-$ ions are stable in the acid side beyond this range.[13)]Thus, gypsum hemihydrate must be precipitated in the pH range of stable HPO_4^{2-} ions.In reactions of a $CaSO_4$-Na_2HPO_4-CH_3OH solution, a pH range of 9.0 to 9.5 can be attained by adding a Na_2HPO_4 solution to the gypsum organogel.It is assumed that as methanol is removed from this gel, gypsum nuclei grow explosively and the $HPO_4^{2-} \leftrightarrow SO_4^{2-}$ replacement is promoted, causing fibrous gypsum hemihydrate incorporated phosphate ions to be produced.

Under the test conditions for reactions of the $CaCl_2$-Na_2SO_4-Na_2HPO_4 mentioned earlier, the pH level of the mixed Na_2SO_4-Na_2HPO_4 solution is about 8, at which it is assumed that HPO_4^{2-} and $H_2PO_4^-$ ions coexist, causing the

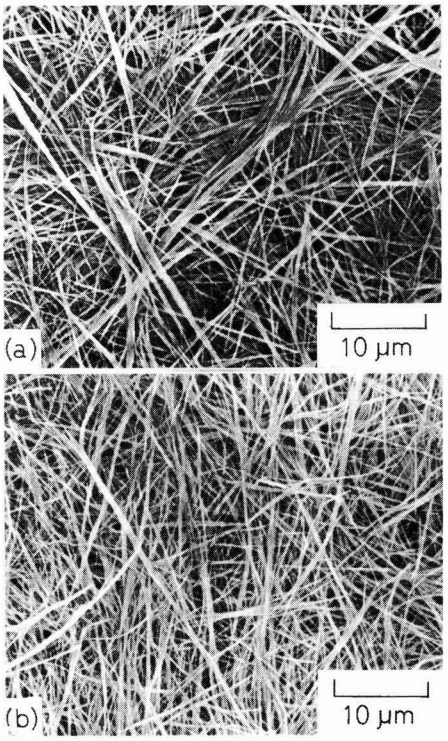

Fig. 8. Change in crystal shape of fibrous gypsum hemihydrate incorporating phosphate ions.
(a) Gypsum hemihydrate,
(b) HPO_4^{2-}/SO_4^{2-} mol ratio 0.15 (solid solution).

limit of solid solution to decrease.In fact, the limit of solid solution could be raised to 15 mol% by first conditioning the pH8 of the Na_2SO_4-Na_2HPO_4 mixed solution to the pH range 9.0 to 9.5 and then adding a $CaCl_2$ solution to the mixed solution above.When an NaH_2PO_4 solution was used instead of the Na_2HPO_4 solution, no production of solid solutions was confirmed with any system.Thus it was proved again that the upper limit of solid solution of phosphate ions in gypsum hemihydrate was about 15mol% with any system and that solid solution was by $HPO_4^{2-} \leftrightarrow SO_4^{2-}$ replacement.

Figure 8 shows a change in the fiber shape of gypsum hemihydrate with phosphate ions incorporated.(a) shows fibers of gypsum hemihydrate in the single-phase, 50μm long, 0.5μm in diameter and about 100 in aspect ratio. (b) shows the fibers of phosphate ion incorporated fibrous gypsum hemihydrate (HPO_4^{2-}/SO_4^{2-}mol ratio 0.15), 35μm long, 0.25μm in diameter and about 140 in aspect ratio, generally thinner than the fibers in (a).Both products here can be made into sheets with entangled fibers of gypsum hemihydrate.

Figure 9 shows variations in the level of dissolution of fibrous gypsum hemihydrate with phosphate ions incorporated.As the level of solid solution of phosphate ions rises, the level of Ca^{2+} dissolution in submerged state decreases and becomes constant at around the maximum

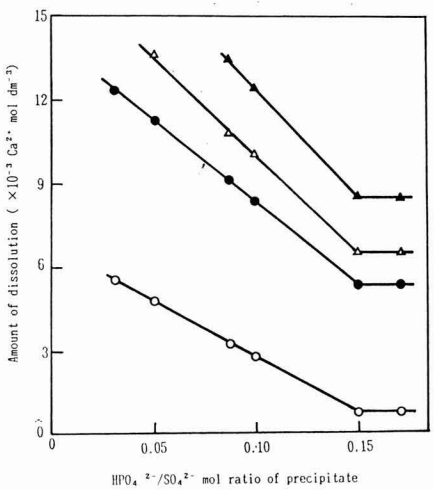

Fig. 9. Dissolution velocity of fibrous gypsum hemihy-drate incorporating phosphate ions.
Dipping time: ○1h, ●1d, △ 7d, ▲ 30d,
Temperature: 20°C.

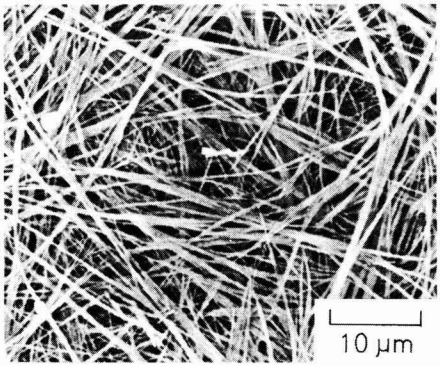

Fig. 10. Change in crystal shape of fibrous gypsum hemihydrate incorporating phosphate ions after dipping in water for 30 days.
HPO_4^{2-}/SO_4^{2-} mol ratio: 0.15 (solid solution),
Temperature: 20°C.

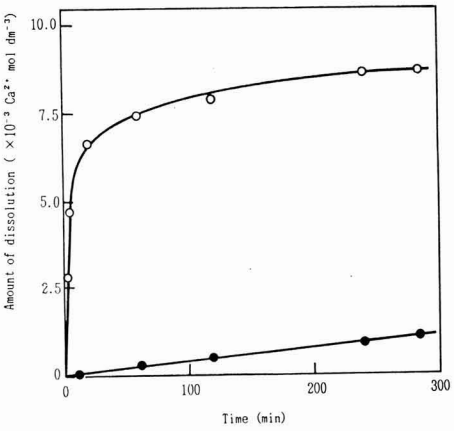

Fig. 11. Dissolution velocity of fibrous II-gypsum anhydride incorporating phosphate ions during dipping in water.
Temperature: 20°C
○ : Fibrous II-gypsum anhydride prepared by heating fibrous gypsum hemihydrate at 800°Cfor 2h.
● : Fibrous II-gypsum anhydride prepared by heating fibrous solid solution (HPO_4^{2-}/SO_4^{2-} mol ratio 0.08)at 500°C for 2h.

level of solid solution, or an HPO_4^{2-}/SO_4^{2-} mol ratio of 0.15, at which the level of dissolution after 1h of submergence is 0.4×10^{-3} Ca^{2+} mol/dm^3, about 1/40 of that of gypsum dihydrate.After 30 days, the level was about 7×10^{-3} Ca^{2+} mol/dm^3, about 1/2 of that of gypsum dihydrate.Also, from the results of X-ray diffraction and TG-DTA curve analyses of immersed samples after 30 days, it was proved that the fibrous gypsum hemihydrate still contained incorporated phosphate ions and remained completely fibrous (**Fig. 10**).

3-3. Decrease of Solubility of Fibrous II-Gypsum Anhydride by Incorporating Phosphate Ions

It is known that II-gypsum anhydride has stable rhombic lattices with a high symmetricity and a high ion chargeability, that it is chemically very stable and particularly slow to dissolve in water.[14,15] We have already reported that the solubility of fibrous gypsum hemihydrate in water can be decreased by heating this gypsum into fibrous II-gypsum hemihydrate.[1,2] While fibrous gypsum hemihydrate without phosphate ions is broken down when heated to 1000°C, II-gypsum anhydride obtained by heating to 800°C remains fibrous.[1] However, when fibrous gypsum hemihydrate, heavy with incorporation of phosphate ions, is heated, the II-gypsum anhydride produced cannot remain fibrous.This is because at a high content of incorporated phosphate ions, the solid solution is decomposed by dehydration and condensation of HPO_4^{2-} at around 500° to 550°C.[16] If the content of incorporated phosphate ions is below 8 mol%, the dehydration and condensation of HPO_4^{2-} is controlled, even when fibrous gypsum hemihydrate with incorporation of phosphate ions is heated to 500°C, and this allows gypsum to remain fibrous.Also, it was found from lattice constant variations that the limit of solid solution of phosphate ions in rhombic II-gypsum anhydride was about 8 mol%.

Figure 11 shows variations in the level of dissolution of fibrousII-gypsumanhydride containing incorporation of phosphate ions. After 1h of submergence of this gypsum, the level of Ca^{2+}dissolution is 0.3×10^{-3} Ca^{2}+mol/dm^3,which is 1/25 of the $7.5\times10^{-3}Ca^{2+}$ mol /dm^3 found with nonfibrous II-gypsum anhydride.

As described above, the solid solution of phosphate ions in acicular and fibrous gypsum hemihydrate was by the $HPO_4^{2-}\leftrightarrow SO_4^{2-}$ replacement because of nearly equal ion radii of HPO_4^{2-} and SO_4^{2-} and the limit of solid solution was about 15mol%.Also, it was proved that the solid solution of phosphate ions contributed to a decrease in solubility, while raising the stability, of gypsum hemihydrate.The solubility of fibrous gypsum hemihydrate with phosphate

ions incorporated to 15mol% in particular, after 1h or immersion, is about 1/40 of that of gypsum dihydrate.Furthermore, if the same gypsum is turned into fibrous II-gypsum anhydride with incorporated phosphate ions by heating, the solubility of this modified gypsum is about 1/50 of that of gypsum dihydrate.Thus, the rather high solubility of gypsum in water, conventionally the greatest limitation on the use of gypsum, could be reduced by incorporating phosphate ions, making the gypsum stable.The fibrous gypsum produced here could be widely applied as a nonorganic filler intended to increase strength, heat insulation and fire-resistance and to reduce the weight of composite materials.In particular, it can be manufactured as a slurry and is expected to find application as a nonorganic filler for paper.

Acknowledgment

We express our thanks to S. Tanabe and Y. Adachi, students at the Science and Engineering Dept., Nihon University, who helped us very much with testing.

References:

1) T. Yasue, Y. Kojima, Y. Arai, Nippon Kagaku, 1988, 1556-64.
2) T. Yasue, Y. Kojima, Y. Arai, Ceramics Journal, 97, 729-34 (1989).
3) T. Yasue, H. Takehisa, Y. Arai, Gypsum and Lime, No. 143, 23-32 (1976).
4) W.L. Hill, S.B. Hendricks, Ind. Eng. Chem., 28, 440-47 (1936).
5) S.V.D. Sluis, G.J. Witkamp, G.M. Vanrosmalen, J. Cryst. Growth, 79, 620-29 (1986).
6) I. Maki, R. Suzukawa, Ceramics Ass., 71, 54-59 (1963).
7) S.E. Dahlgren, Brit. Chem. Eng., 10, 776-77 (1965).
8) Y. Arai, T. Yasue, Gypsum and Lime, NO. 161, 13-28 (1979).
9) T. Sakae, H. Nagata, T. Sudo, Amer. Mineral., 63, 520-27 (1978).
10) H.R Corit, R. Fernandez-Prini, Can. J. Chem., 62, 484-88 (1984).
11) M. Adachi, A. Tanimoto, Gypsum and Lime, No. 135, 4-10 (1975).
12) M. Adachi, A. Tanimoto, Gypsum and Lime, No. 135, 17-26 (1975).
13) R.A. Day, J.A.L. Underwood, "Quantitative Analytical Chemistry", Baifukan, (1987) p. 168.
14) Y. Arai, T. Yasue, Kogyo Kagaku, 73, 2603-09 (1970).
15) Y. Arai, T. Yasue, S. Kikuchi, Nippon Kagaku, 1973, 1425-32.
16) T. Yasue, T. Suzuki, Y. Arai, Nippon Kagaku, 1983, 494-500.

This article is a full translation of the article which appeared in Nippon Seramikkusu Kyokai Gakujutsu Ronbunshi (Japanese version), Vol.98, No.5, 1990.

The Relationship between Cyclic Fatigue Properties and Microstructures of Sintered Silicon Nitride Ceramics

Manabu Takatsu, Kanji Ohya* and Masashi Ando

Nagoya Institute of Technology ,Gokiso-cho, Showa-ku, Nagoya 466, Japan
*R/D NTK Technical Ceramics Div. of NGK Spark Plug Co., Ltd., 14-18, Takatsuji-cho, Mizuho-ku, Nagoya 467, Japan

The present study deals with the relationship between the microstructures and the fatigue failure mechanisms in five different kinds of sintered silicon nitride ceramics. Static fatigue test and cyclic fatigue test were conducted with a stress ratio (R) condition of 0.1 using flex specimens at room temperature, as a means to determine the effects of microstructures on crack propagation. Also, the accelerative effects upon the propagation velocity of fatigue cracking in cyclic loading conditions were discussed quantitatively using the estimation method applied to the empirical equation for subcritical crack growth.

The results indicated that the accelerative effects on propagation velocity under cyclic fatigue conditions were observable in samples in which the matrix was composed of microcrystalline grains of the sintered silicon nitride ceramics, but not in those with a matrix composed of amorphous materials. Thus, under cyclic loading, the fatigue crack propagation was found to be governed by the microstructure of the sample, in particular by the matrix filling the gaps between the coarse grains.

[Received December 14, 1989; Accepted January 25, 1990]

Key-words: Sintered silicon nitride, Cyclic fatigue, Static fatigue, Microstructure, Crack propagation

1. Introduction

Ceramic materials are brittle, and improvements in strength and fracture toughness sometimes cause reduced fatigue-related characteristics. Silicon nitride ceramics are no exception. Some mechanical properties, such as critical stress intensity factor K_{IC} and strength, of sintered silicon nitride have been markedly improved recently, but fatigue-related properties under cyclic stresses[1-8] have not been improved as much as other properties. The authors have demonstrated that acceleration effects under cyclic stress conditions and the cyclic characteristics of sintered silicon nitride are correlated with the microstructure, based on the results of cyclic fatigue tests conducted at a higher frequency (100 to 500Hz) than those employed in previous studies (1 to 10Hz).[9-12] The g-function, proposed by Evans et al.,[13] was used to draw the master curves, in order to compare the results under cyclic stress conditions with those under static stress conditions.

In this study, the authors conducted cyclic fatigue tests, in which 5 sintered silicon nitride samples with different microstructures were subjected to cyclic load stresses, to investigate the effects of the microstructures on the fatigue properties of the samples. As a result, it was found that some materials, although having high K_{IC}, had poor fatigue properties, and were affected by the acceleration effects under cyclic stresses at a working-stress/strength ratio as low as about 0.6, and other materials, though lacking high K_{IC}, had the desired fatigue properties. These results are considered useful for the design of ceramic structures and examination of structures for specific purposes.

2. Experimental Procedure and Analytical Methods

2-1. Experimental Procedure

Five types of sintered silicon nitride samples were used in this study; each was pressurelessly sintered in the presence of a different sintering aid. **Table 1** summarizes these samples. The Al/Si intensity ratios were determined by X-ray fluorescence analysis, and were named A, B, C and D in ascending order of the intensity ratio. Sample E was Sample B thermally treated at 1573K for 20h in a N_2 gas atmosphere, to slightly change the constituent phases of the latter sample. The critical stress intensity factor was determined by the IF method.[14] Each sinter was cut into 3*4*40mm samples (as specified by JIS R1601), and each sample was mirror-polished (0.8S) on the face to be subjected to the tensile stress, and chamfered (C0.2 to 0.3).

The test apparatus was provided with a piezoelectric bimorph to generate cyclic loads, details of which are described elsewhere.[15] The static and cyclic fatigue tests were conducted. The conditions of the cyclic tests were as follows. Frequency, 250 and 550Hz, load stress amplitude ratio (R, ratio of maximum loading stress σ_{max} to minimum

Table 1. Properties and behaviors of sintered silicon nitride ceramics used in this experiments.

Sample	ρ [g/cm³]	S_f [MPa]	m [-]	E [GPa]	ν [-]	Hv [GPa]	K_{IC} [MNm$^{-1.5}$]	mean grain size short[μm]	long[μm]
(A)	3.18	762	22	278	0.30	11.6	6.6	0.75	2.6
(B)	3.26	921	11	308	0.29	14.2	7.4	0.67	1.9
(C)	3.24	991	19	313	0.30	14.9	8.0	0.69	1.8
(D)	3.27	551	12	288	0.30	12.1	5.0	0.66	1.5
(E)	3.26	857	14	306	0.29	13.6	6.2	0.74	1.9

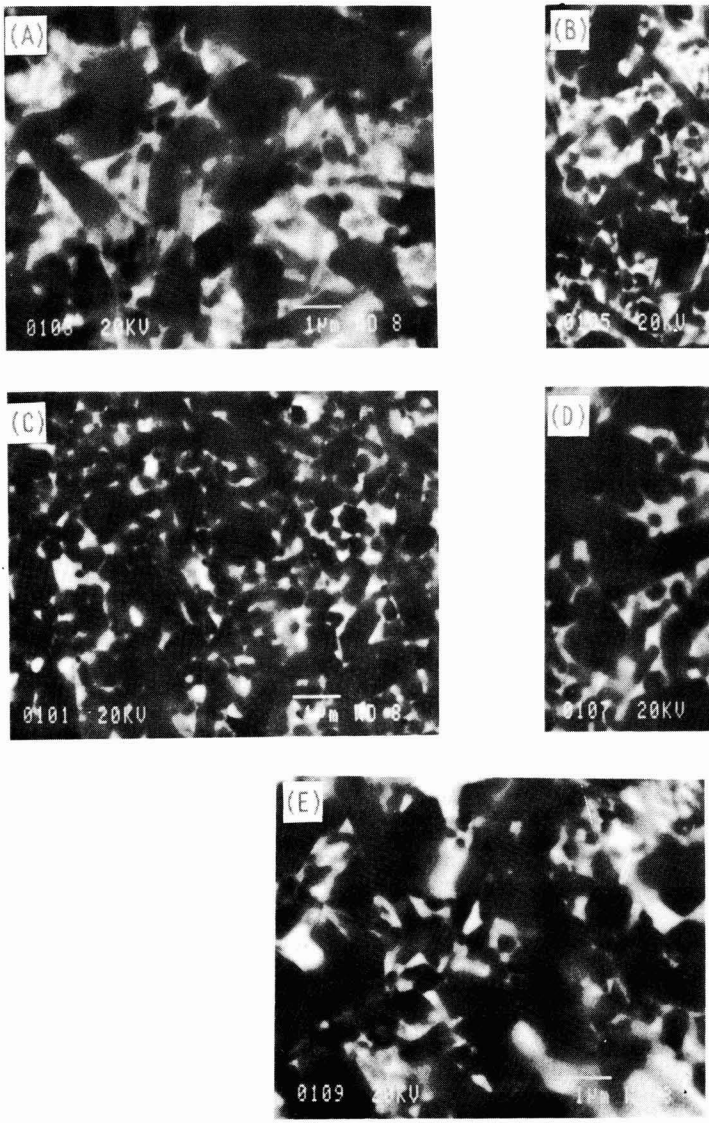

Fig. 1. Microstructures of each sample by backscattered electron images.

loading stress σ_{min}), 0.1 and 0.7 (pulsating cyclic fatigue conditions), room temperature and 50% RH or less. Each cyclic fatigue run lasted for 10^5 sec, and the samples which were not fractured during the test period were analyzed to determine their bending strengths.

The fracture surfaces were analyzed by a scanning electron microscope (SEM), for which 3mm square pieces were cut from the fracture surface. The portion to be clamped by the holder was ground and washed in acetone with ultrasonic agitation. A scanning electron microscope equipped with an energy dispersion type X-ray analyzer (EDAX: PV9800, Philips) was used to observe the microstructures. The constituent phases were identified by X-ray diffractometry.

2-2. Analysis of Fatigue Test Results

The fatigue test results were analyzed by the method briefly described below.Details are given elsewhere.[9] The following σ_{max}-$t_{fi} \cdot g_i^{-1}$ relationship is derived from the empirical equation $V=AK_I^n$ for SCG, represented by crack propagation speed (V) and stress intensity factor (K_I), by estimating the initial crack length in each fatigue test specimen from the bending strength distribution at stress loading rate σ:

$$\log(\sigma_{maxi}/S_{fi}) = -(1/n+1)\log(t_{fi} \cdot g_i^{-1}) - \log B_i \quad (1)$$

Table 2.Detected materials by XRD and values of relative intensity of diffraction peaks for silicon of fluorescent X-ray diffraction method.

	Relative intensity of diffraction peaks for silicon by FXRD								Detected matrials by XRD *1
	Al/Si	Y/Si	Dy/Si	Ce/Si	Zr/Si	Ti/Si	Sr/Si	Mg/Si	Fe/Si	
(A)	0.001	-----	-----	0.015	0.016	-----	0.008	0.007	-----	β, am
(B)	0.041	0.031	0.078	-----	-----	-----	-----	-----	-----	β, (DY)O, (DY)O·SO, am
(C)	0.065	0.038	-----	-----	-----	0.008	-----	-----	-----	β, SN·YO
(D)	0.108	0.074	-----	-----	-----	-----	-----	-----	0.001	β, am
(E)	0.039	0.046	0.074	-----	-----	-----	-----	-----	-----	β, (DY)O, (DY)SON

*1 β=β-Si_3N_4, (DY)O=Si_3N_4·(Dy,Y)$_2O_3$, (DY)O·SO=Si_3N_4·10(Dy,Y)$_2O_3$·9SiO_2, SN·YO=Si_3N_4·Y_2O_3 (DY)SON=(Dy,Y)SiO_2N, am=amorphous

where, subscript i stands for i-th data arbitrarily selected from the fatigue test data (total data number: N), S_{fi} is estimated bending strength, and t_{fi} is fatigue life. g_i^{-1} is the term with respect to load stress waveform, given by:

$$g_i^{-1}=\int_0^{\lambda}\left\{\frac{\sigma(t)}{\sigma_{max}}\right\}^n/\lambda dt \qquad \ldots (2)$$

where, λ is the time span of one wavelength, and B_i is defined by $B_i = \{(n+1)\sigma/\sigma_{maxi}\}^{1/(n+1)}$, but regarded as a constant for equation (1), because $n > 1$. Equation (1) indicates that the term $t_{fi}\cdot g_i^{-1}$ represents the effective life under a given cyclic stress. Plotting σ_{maxi}/S_{fi} against $t_{fi}\cdot g_i^{-1}$ on log-log paper will give fatigue parameter n from the slope of the estimated straight line, thus enabling the correlation of fatigue behavior with the static fatigue characteristics (master curve) in which the effects of load stress waveform are considered.

Bending strength was estimated by assuming that immediate fracture strength is represented by the 2-parameter Weibull distribution, and the $\sigma_{max}{}^n t_{fg}{}^{-1}$ value for each fatigue fracture data set was calculated as an ordered statistical quantity, from which bending strength was estimated using the cumulative fracture probability P_i for each order.

3. Results

3-1. Microstructures and Compositions

Figure 1 shows the back-scattered electron images of the microstructures of the sintered silicon nitride samples, and Fig.2 the X-ray fluorescence results. The phases detected by X-ray diffractometry are also presented in **Table 2**. The microstructure of each sample consisted of columnar β-Si_3N_4 grains (0.5 to 1μm along the minor axis and several μm along the major axis) and the white matrix phase. No heavy elements, such as Y, were detected in the β-Si_3N_4 grains by the EDAX analysis, from which it was considered that materials other than β-Si_3N_4, detected by X-ray diffractometry, were the matrix phase components. Al was detected in each microstructure section, and was considered to be dissolved in the system.

No Al was added to Sample A, and the Al found was an impurity. No Ce or Zr was detected by X-ray diffractometry, though they were detected by X-ray fluorescence analysis, indicating that the matrix phase was amorphous. The matrix phase of Sample B was considered to consist of microcrystals, because Si_3N_4·$(Dy,Y)_2O_3$ and Si_3N_4·10$(Dy,Y)_2O_3$·9SiO_2 were detected. The X-ray diffraction peaks were broad, suggesting that the matrix contained some residual amorphous phase.It was also observed that it extended more widely in the ceramic system than those of the other samples. Sample C had well densified structures of β-Si_3N_4 grains, and the matrix containing Si_3N_4·Y_2O_3 was completely microcrystalline. Sample D had a larger quantity of Al and Y than any other sample prepared in this study. However, no matrix phase was identified, indicating that it was amorphous. The matrix extended throughout the ceramic system, and some β-Si_3N_4 grains were large and columnar. Hayashi et al. suggested that sintered Si_3N_4-Y_2O_3-Al_2O_3 has an amorphous matrix, when Al_2O_3 content is high,[16] and the results observed in this study are in agreement. Sample E was Sample B which was thermally treated to change the matrix phase composition and microcrystalline structures greatly. Si_3N_4·(Dy,Y)-SiO_2N was detected in the matrix, though Si_3N_4·10$(Dy,Y)_2O_3$·9SiO_2 found in Sample B was not detected.Oda et al. reported that a glass system of Y_2O_3-Al_2O_3-Si_3N_4 has a glass transition temperature of around 900°C.[17] The matrix was completely microcrystalline, judging from the temperature at which it was treated.

3-2. Fatigue Test Results

Figure 2 plots the maximum loading stress σ_{max} against

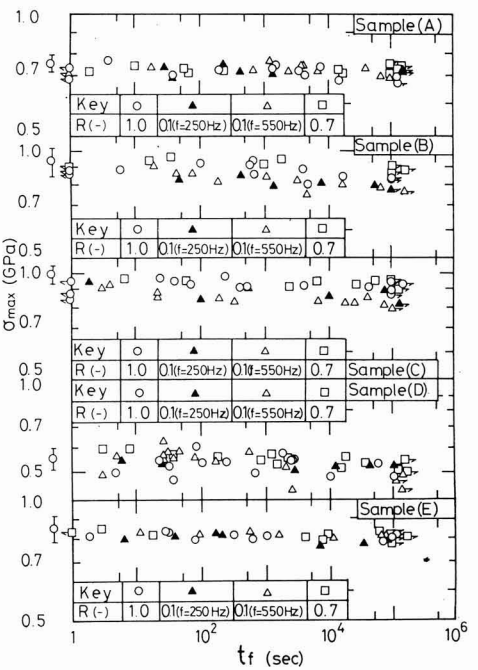

Fig. 2. Real data of relations between maximum loading stress and fatigue life as the parameter of stress ratio (R).

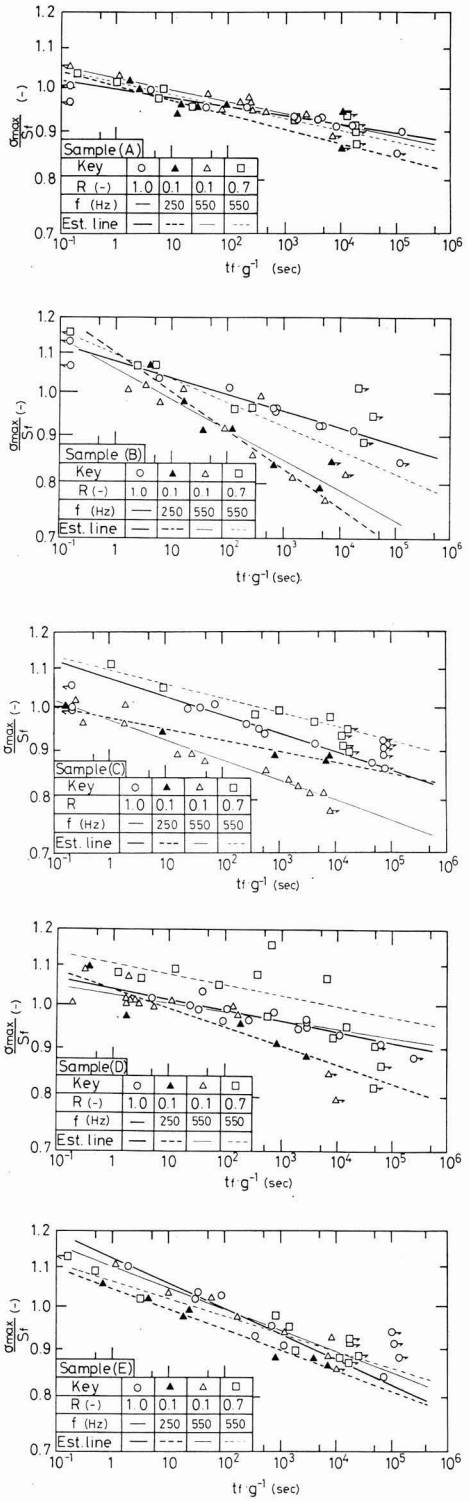

Fig. 3. Analytical expression of the data of cyclic fatigue properties expressed in Figs.2 by use of empirical equation (1).

Table 3.Parameter n by cyclic and static fatigue tests for sintered silicon nitride ceramics.

Sample	Static (R=1.0)	Cyclic (R=0.1) (f=550Hz)	Cyclic (R=0.1) (f=250Hz)	Cyclic (R=0.7)
(A)	105	80.5	65.0	82.6
(B)	54.7	29.2	23.3	38.7
(C)	49.2	45.7	83.9	65.6
(D)	87.1	112	49.9	84.2
(E)	36.1	43.2	43.9	52.8

fatigue life t_f, a time span extending from the initiation of loading to failure of the sample, on a log-log graph, to show the relationship between applied stress and fatigue life. **Figure 3** shows the relationship between σ_{max}/S_f and $t_f \cdot g^{-1}$ for each sample, where the fatigue test results were analyzed by the method discussed previously using equation (1).[9] The abscissa represents effective life $t_f \cdot g^{-1}$ in which stress loading waveform and loading stress amplitude were considered, and the ordinate represents the ratio of maximum loading stress σ_{max} to strength S_f estimated by the Weibull distribution.[9] Each straight line in Fig.3 was determined by the least squares method.

The results of the fatigue test at a low loading stress amplitude (R=0.7), which was conducted for confirmation, gave a straight line very close to the estimated line for the static fatigue data or slightly deviating to a longer life time, indicating that the cyclic fatigue behavior was similar to the static fatigue behavior at a small loading stress amplitude.

At a high loading stress amplitude of R=0.1, however, each sample had clearly distinguishable specific fatigue behavior. The σ_{max}/S_f–$t_f \cdot g^{-1}$ relationships of samples B and C, which had a high strength close to 1GPa, deviated considerably from the static fatigue lines to shorter life times, irrespective of the frequency of cyclic stress to which they were exposed, indicating that their strength decreased faster under cyclic fatigue conditions. On the other hand, no significant acceleration of strength decrease was observed under cyclic conditions with samples A, D and E, which had bending strengths in the range from 500 to 800MPa. **Table 3** shows the fatigue parameter n values, determined by substituting the fatigue data into equation (1) and analyzing by the least squares method, for each loading stress ratio. The n values, widely ranging from 30 to 100, tended to decrease as the strength of the sintered sample increased. The n value was insensitive to loading stress conditions, whether they were static or cyclic, for all the samples except sample B, where the value under cyclic stresses ranged from 1/2 to 2/3 that under static stress. Kobayashi et al. reported that the n value under a static stress is at least twice that under cyclic stresses for those ceramic materials which are fatigued faster under cyclic stresses.[18] A similar trend was observed with sample B, which exhibited the acceleration effect.

Figure 4 shows an SEM photograph of a typical fracture

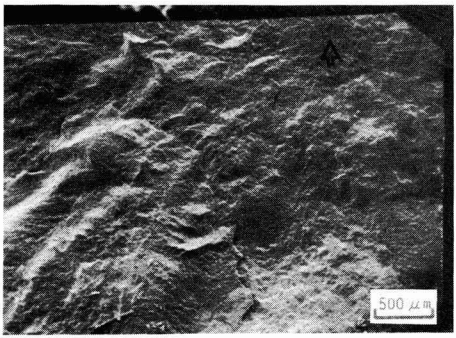

Fig. 4. Example of SEM fractograph for sintered silicon nitride.

face of a sample fractured under cyclic stress. The fracture origin, indicated by the arrow, was either a vacant pore, impurity or coarse grain on or near the surface exposed to tensile stress. The region of the fatigue-induced crack propagation was observed in a sample exposed to a relatively low stress, and tended to disappear as stress was increased. **Figure 5** shows a high-magnification SEM photograph of the fatigue-induced crack propagation regions, and **Fig.6** the region of the immediate fracture. The crack propagated mainly through the grain boundaries, but there were some grains in which cracks propagated to cause intragranular fracture, as indicated by the arrows shown in Fig.5. The intragranular fracture was observed more frequently in the immediate fractured region, due to the more rapid fracture occurring in the system, as indicated by the arrows shown in Fig.6.

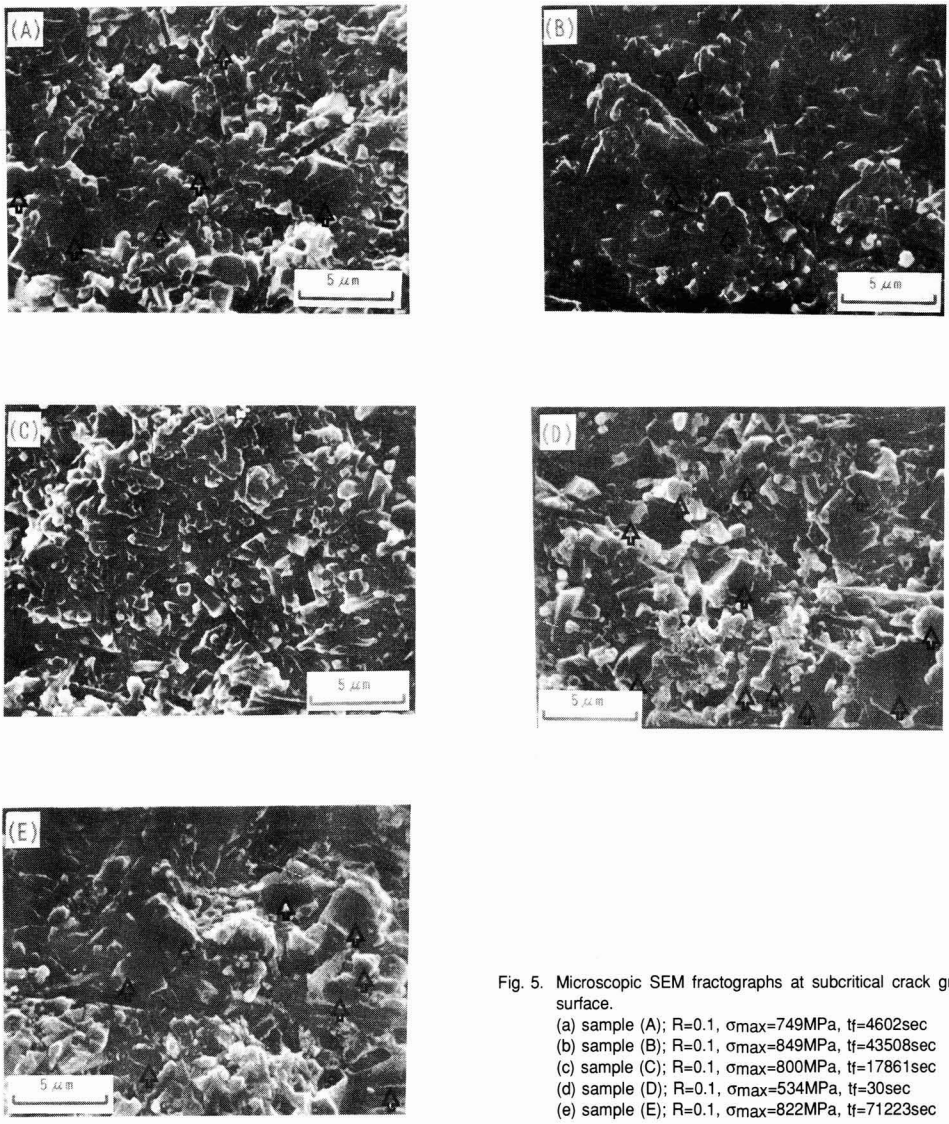

Fig. 5. Microscopic SEM fractographs at subcritical crack growth surface.
(a) sample (A); R=0.1, σ_{max}=749MPa, t_f=4602sec
(b) sample (B); R=0.1, σ_{max}=849MPa, t_f=43508sec
(c) sample (C); R=0.1, σ_{max}=800MPa, t_f=17861sec
(d) sample (D); R=0.1, σ_{max}=534MPa, t_f=30sec
(e) sample (E); R=0.1, σ_{max}=822MPa, t_f=71223sec

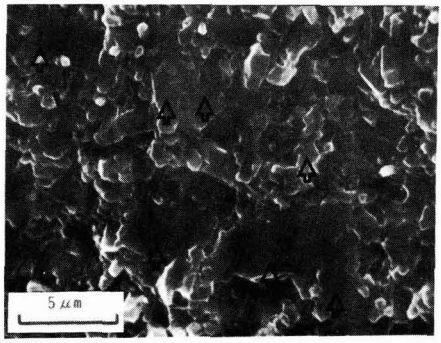

Fig. 6. Example of microscopic SEM fractograph at fractured surface instantaneously.

4. Discussion

The microstructures consisted of the β-Si_3N_4 grains and the white-colored matrix, with great variations in the matrix microcrystalline size, depending on the type and quantity of sintering aid used. The β-Si_3N_4 grains, on the other hand, were entwined with each other to form complex structures in a similar manner in all the sintered samples prepared in this study. It is therefore considered that the fatigue behavior of each sample was determined mainly by the white-colored matrix phase.

For example, samples B and C, with microcrystalline matrix phases, were both fatigued faster under cyclic stress at R=0.1, although in different ways. As shown in Fig.2(b), the cyclic fatigue data of sample B generally had a steeper slope than the static fatigue data, but coincided as the cyclic stress increased. In addition, no significant effects of cyclic stress amplitude were observed. The microcrystals and the amorphous phase were mixed in the microstructure in an extended area within the matrix phase. The fracture mainly occurred in the grain boundaries, as shown in Fig.5(b), although partly observed within the grains. The intragranular fracture occurred more frequently in the sintered silicon nitride samples with amorphous matrix phases, as discussed later. It is therefore considered that, in sintered silicon nitride systems with matrix phases consisting of microcrystals and an amorphous phase, cracks propagate to cause intragranular fracture of grains around the amorphous phase and deflection through the grain boundaries in the vicinity of the microcrystalline grains.

Sample C, on the other hand, was fractured in such a way as to cause the $\sigma_{max}/S_f - t_f \cdot g^{-1}$ relationship to move parallel to the static fatigue line towards shorter lifetimes. It was also observed that decreasing the frequency shifted the relationship to the longer lifetimes. Mai et al. and Kawakubo et al. investigated crack bridgings behind the crack tips for sintered Al_2O_3 and Si_3N_4, respectively.[19,3] The authors believe that the fatigue results obtained in this study are also represented by the R-curve behavior, for reasons now under examination. Microcrystals, although present, accounted for only a limited area of the matrix. The β-Si_3N_4 grains had a minor axis of 0.5 to 1μm and a major axis of 3 to 4μm. The fracture occurred mainly in the grain boundaries, and little intragranular fracture was observed, suggesting that fatigue-induced cracks would propagate deflecting through the grain boundaries.

The accelerated fatigue might be caused by residual stresses resulting from the difference in thermal intensity factor or anisotropy formed in the matrix when it was microcrystallized during the sintering process, or by the microflows formed at the triple points in the grain boundaries, or at the interfaces between the β-Si_3N_4 grains and the matrix, as a result of the volumetric shrinkage. Kobayashi et al. discussed the possibility of the formation of a local stress field in the system exposed to an external force, formed by the difference in modulus of elasticity between the grains and the matrix phase or anisotropy in the matrix phase, and different to the field of applied stress.[18] A similar phenomenon might occur in the samples prepared in this study; the formation of local stress fields in the interfaces between the grains and matrix, in addition to the field of the applied stress, would accelerate the fatigue.

Okada et al. reported that microflows are connected to each other to accelerate the growth of cracks in sintered alumina.[20] This may be applicable to sintered silicon nitride where the matrix phase is microcrystalline. **Figure 7** shows a proposed model for the accelerated fatigue. The crack moving from the fracture origin is temporarily stopped by a barrier, such as the triple point in the grain boundary of β-Si_3N_4 (Fig.8(a)). At the same time, the microflows are activated at the fronts by the local stress fields formed in the vicinity of the interfaces, growing mainly in a form like single-swing doors, but are also stopped by the triple points (Fig.7(b)). Both crack and microflows are reactivated while their fronts are repeatedly opened and closed under cyclic stresses.The microflows start to propagate in a mixed mode, and are connected selectively to each other at the fronts, extending their lengths (Fig.7(c)). Okada et al. considered that cracks are connected to each other in a line.[20] Microflows in the sintered silicon nitride samples prepared in this study, however, might run in zigzags, to form more irregularities on the fracture faces, with the result that the K_I value at the crack fronts would be made larger by the indent effects[21] produced by the projections on the fracture faces. This might cause the cracks to grow faster under cyclic stress than under static stress, to accelerate the fatigue.

In samples A and D, with amorphous matrix phases, no accelerated fatigue or effect of frequency or loading stress amplitude was observed under cyclic stress, as shown in Fig.3. The strength of these samples was less degraded than the others. It was also observed, as shown in Fig.5, that the

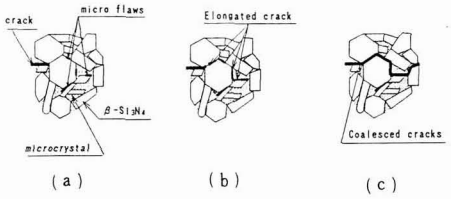

Fig. 7. Patterns of fatigue fracture of the samples in which gaps of coarse grains are filled by microcrystals.

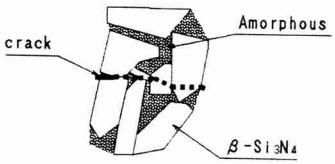

Fig. 8. A pattern of fatigue fracture of the samples in which matrix between the coarse grains comp

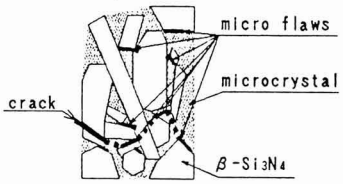

Fig. 9. A pattern of fatigue fracture of the sample (E), which sample (B) was heat treated.

Table 4.Comparative table of the state of fatigue properties with microstructures for each sample.
(a) Microstructure., (b) Fatigue properties., (b-1) Micro fatigue properties., (b-2) Macro fatigue properties.

(a) Microstructures.

Sample.	(A)	(B)	(C)	(D)	(E)
Structure.	β-Si_3N_4 and matrix	←	←	←	←
Detected material of matrix. (By XRD*)	None	$Si_3N_4 \cdot (Dy,Y)_2O_3$ $Si_3N_4 \cdot 10(Dy,Y)_2O_3 \cdot 9SiO_2$	$Si_3N_4 \cdot Y_2O_3$	None	$Si_3N_4 \cdot (Dy,Y)_2O_3$ $(Dy,Y)SiO_2N$
(By FXRD**)	Mg, Si, Sr, Zr, Ce	Al, Si, Y, Dy	Al, Si, Ti, Y	Al, Si, Fe, Y	Al, Si, Y, Dy
Crystal structure of matrix	Amorphous	Microcrystal (and amorphous)	Microcrystal	Amorphous (and microcrystal)	Microcrysatal
Region of matrix	Middle	Large	Small	Large	Middle

(b) Fatigue Properties.
(b-1) Micro fatigue properties.

Fracture origin.	Pores, etc.	←	←	←	←
Micro flows at matrix.	None	They were generated at sintering.	←	None	They were generated by decreased matrix volume for heat treatment.
Residual stress at matrix	None	It was generated at sintering.	←	None	It was generated at sintering and heat treatment.
Effects of amorphous	Large	Little	None	Large	None
Crack propagation within SCG.	Intergranular and Transgranular	Intergranular (Transgranular)	Intergranular	Intergranular and Transgranular	Intergranular (Transgranular)
Schematic illustration for fatigue crack growth path	Fig. 8.	Figs. 7.	Figs. 7.	Fig. 8.	Fig. 9.

(b-2) Macro fatigue properties.

Accelearated effect under cyclic fatigue condition	Little	Large	Large	Little	Little
Fatigue parameter n valie.	Cyclic lower than static fatigue. R=0.1: 80.5 R=1.0: 105	Cyclic much lower than static fatigue R=0.1: 29.2 R=1.0: 54.7	Cyclic as high as static fatigue. R=0.1: 45.7 R=1.0: 49.2	Cyclic higher than static fatigue. R=0.1: 112 R=1.0: 87.1	Cyclic higher than static fatigue. R=0.1: 112 R=1.0: 87.1

*: X-ray diffraction method. **: Fluorescent X-ray diffraction method.

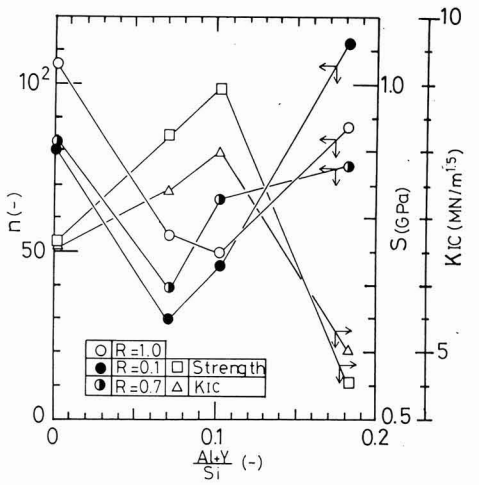

Fig. 10. Mutual relationships between relative intensity of (Al+Y)/Si and fatigue properties, mean bending strength, and critical intensity factor.

intragranular fracture occurred in a number of grains. These results suggested that the cracks ran straighter in sintered silicon nitride when the matrix was amorphous than when it was crystalline.

With respect to the fatigue behavior of these compositions, the cracks generally run faster in the crystalline or amorphous phase than in the microcrystalline phase. It is also considered that whether the cracks run straight or zigzag depends greatly on the wettability between the crystals and the matrix phase. In these samples, irrespective of their microstructures, cracks will propagate relatively easily throughout the crystals, running straight, when they collide against the crystals. The barriers that prevent propagation of the cracks, therefore, exist only in the interfaces between the crystals and the matrix phase in these samples. The increased K_I at the crack fronts, resulting from the indent effects, is rarely observed, because the cracks are likely to run straight. This may account for the absence of accelerated fatigue in these samples under cyclic stress. This concept is illustrated in **Fig.8**.

Sample E was thermally treated and also showed no accelerated fatigue under cyclic stress (Fig.3), and intragranular fractures occurred in many grains (Fig.5). The matrix phase was microcrystalline, like those of samples B and C. It was anticipated that the thermal treatment would produce residual stresses throughout the microstructures and a number of microflows in the matrix phase, as a result of the associated volumetric shrinkage.

In sample E, the cracks might propagate from the fracture origins along the grain boundaries, but their opening-closing movements would be less active than in sample B, due to the residual stresses present throughout the microstructures. The indent effects would be smaller in this sample than in sample B, where the cracks were deflected to a larger extent to produce more projections on the fracture faces. The K_I level would increase little at the crack fronts, and hence the acceleration effects would be little observed under cyclic stress of larger amplitude.This concept is illustrated in **Fig.9**.The residual stresses formed throughout the microstructures would activate the local stress fields, decreasing strength, K_{Ic} and the fatigue parameter n, to lower levels than those of sample B.

Table 4 summarizes the above results. Kawakubo et al. reported that cyclic stresses reactivate the cracks stopped at the triple points in the grain boundaries.[2,3,18]Similar results were obtained in this study. Furthermore, it was suggested that the propagation behavior of the fatigue cracks was largely determined by the matrix phase conditions.

Lastly, the effects of the matrix phase components on fatigue, strength and critical stress intensity factor are discussed. **Figure 10** plots the fatigue parameter n, strength S and critical stress intensity factor K_{IC} against relative intensity (Al+Y)/Si, shown in Table 2. Samples B and C, with microcrystalline matrix phases, and high strengths and critical stress intensity factors, but low fatigue parameters. On the other hand, samples A and D with amorphous matrix phases showed the opposite trends to samples B and C. This means that increasing strength and critical stress intensity factor are incompatible with improved fatigue properties. It is therefore necessary to take the critical stress intensity factor, strength and fatigue properties of these materials into consideration, when looking for applications for these materials.

5. Conclusions

Five different types of pressureless sintered silicon nitride samples were prepared, to investigate the relationship between their fatigue characteristics and the microstructures.

(1) It is suggested that the behavior of the cracks propagating through the fatigued samples is largely determined by the microstructures, in particular by the matrix conditions.

(2) The sintered silicon nitride sample with a microcrystalline matrix phase, was fatigued faster under the cyclic stresses, presumably because the fronts of the cracks and the microflows present in the matrix phase are activated under these stresses, to create the indent effects that increase K_I levels at the crack fronts and act to connect them selectively.

(3) The sample with amorphous matrix phase, on the other hand, is less affected by cyclic stress, because the cracks tend to propagate straighter, creating few indent effects that increase K_I levels.

(4) The thermally treated sample has lower K_{IC} and S levels than the other samples, because of the presence of residual stresses or microflows throughout the microstructures. Its fatigue, however, is little accelerated, due to the absence of the increased indent effects on the fracture faces.

(5) Increasing strength and toughness of the silicon nitride sinters is contrary to improved fatigue characteristics. It is therefore necessary to design microstructures taking into consideration the fatigue characteristics as well as strength and toughness.

(Presented to the annual meeting of the Ceramic Society

of Japan, May 1989)

Acknowledgments:
The authors thank Messrs. M. Sato and M. Nakagaki of NGK Spark Plug Co., Ltd. for their cooperation in the SEM analysis.

References:

1) T. Yamada, T. Hoshiide and H. Furuya, Zairyo, 33, 28-33 (1988).
2) T. Kawakubo and K. Yoneya, ibid., 34, 1460-65 (1985).
3) T. Kawakubo and K. Komeya, J. Am. Ceram. Soc., 70, 400-05 (1987).
4) M. Masuda, T. Sohma, M. Matsui and I. Oda, J. of Ceramic Society of Japan, 96, 277-33 (1988).
5) M. Masuda, N. Yamada, T. Sohma, M. Matsui and I. Oda, ibid., 97, 520-24 (1989).
6) Y. Matsuo, Y. Hattori, Y. Katayama and I. Fukuura, "Progress in Nitrogen Ceramics", edited by F.L. Riley, Martinus Nijhoff Publishers, The Netherlands, (1983), pp.515-22.
7) J. Chang, P.K. Khandelwal and P.W. Heitman, Ceram. Eng. Sci. Proc., 8, 766-77 (1987).
8) M.H. Rawlins, T.A. Nolan, L.F. Allard, V.J. Tennery, J. Am. Ceram. Soc., 72, 1338-42 (1989).
9) M. Takatsu, H. Kamiya, K. Ohya, Y. Ogura and T. Kinoshita, J. of Ceramic Society of Japan, 96, 990-96 (1988).
10) K. Ohya, Y. Ogura, M. Takatsu and H. Kamiya, Zairyo, 38, 144-48 (1989).
11) K. Ohya, K. Ogura, M. Takatsu, H. Kamiya, "Proceeding of '88 MRS International Meeting on Advanced Materials", Vol.5; edited by Y. Hamano, O. Kamigaito, T. Kishi and M. Sakai, Materials Research Society, Pittsburgh, PA, (1989).
12) H. Kamiya, M. Takatsu, K. Ohya, M. Ando and A. Hattori, Seramikkusu Kyokai Gakujutsu Ronbunshi, 98, 456-63 (1990).
13) A.G. Evans and E.R. Fuller, Met. Trans., 5, 27-33 (1974).
14) K. Niihara, R. Morena, D.P.H. Hasselman, J. Am. Ceram. Soc., 65, C116 (1982).
15) K. Ohya and Y. Ogura, Zairyo, 38, 44-48 (1989).
16) H. Hayashi and M. Osakai, J. of the Japan Society of Powder and Powder Metallurgy, 33, 210-15 (1986).
17) K. Oda and T. Yoshio, Seramikkusu Kyokai Gakujutsu Ronbunshi, 97, 1493-97 (1989).
18) H. Kobayashi and T. Kawakubo, J. of the Japan Institute of Metals, 27, 757-65 (1988).
19) Y.W. Mai, B.W. Lawn, J. Am. Ceram. Soc., 70, 289-94 (1987).
20) T. Okada, G. Sines, J. Am. Ceram. Soc., 66, 719-25 (1983).
21) A.G. Evans, Int. J. Fracture, 16, 485-498 (1980).

This article is a full translation of the article which appeared in Nippon Seramikkusu Kyokai Gakujutsu Ronbunshi (Japanese version), Vol.98, No.5, 1990.

Preparation of TiB_2-TiN Double Layer Coated Iron Powder by Rotary Powder Bed CVD

Hideaki Itoh, Kenji Hattori, Makoto Oya and Shigeharu Naka

Synthetic Crystal Research Laboratory, Faculty of Engineering, Nagoya University
Furo-cho, Chikusa-ku, Nagoya-shi 464-01, Japan

A composite iron powder coated with TiB_2 and TiN double layers was prepared by continuous rotary powder bed chemical vapor deposition in the reactant systems of $TiCl_4$-B_2H_6-H_2 and $TiCl_4$-N_2-H_2. TiN was coated on to spherical iron powder with a particle diameter of 70-120μm under the following deposition conditions; temperature: 1000°C, reaction time: 0-120 min, flow rate: $TiCl_4$ 3ml/min, N_2 200ml/min, H_2 300ml/min, Ar 20ml/min, and the rotation speed of specimen cell: 90 rpm. Crystalline or amorphous TiB_2 was subsequently coated on to TiN coated iron powder under the conditions: temperature: 600-850°C, reaction time: 60-240min, flow rate ratio of B_2H_6 to $TiCl_4$, R=0.16, H_2 300ml/min, Ar 140-300ml/min. The composite iron powder covered with uniform and adherent double layers of TiB_2 and TiN was oxidation-resistant up to 700°C in air.

[Received December 20, 1989; Accepted January 25, 1990]

Key-words: Titanium diboride, Titanium nitride, Rotary powder bed chemical vapor deposition, Composite powder, Double layer coating

1. Introduction

This is a study on preparing powders coated with other materials. Using a rotary powder bed CVD system we showed that graphite, titanium and iron powders could be coated with titanium nitride (TiN).[1,2] In the CVD of TiN on spherical carbonyl iron particles using a reactant $TiCl_4$-N_2-H_2 gas, the dispersion of the iron powder was improved and uniform TiN coating was obtained by surface adsorption of the reactant CVD gas when heating the iron powder.[2,3] To acquire basic knowledge about preparing multi layer coated powders by the same technique, we aimed to prepare an iron powder with a double layer coating of titanium boride (TiB_2) and titanium nitride (TiN). We investigated the possibility of preparing double layer coated powders by performing CVD of $TiCl_4$-N_2-H_2 and $TiCl_4$-B_2H_6-H_2 systems in succession and we observed the coated TiB_2-TiN-Fe powder and identified the phases produced.

2. Experimental Method

Figure 1 shows the structure of the rotary powder bed CVD system. It is basically the same as was shown in the previous reports.[1-3] B_2H_6+Ar gas was fed in through the port in the manifold on the gas feed side. Spherical carbonyl iron powder (150-200 mesh) was used as starting powder. The rotary specimen cell, charged with 2g of the sample powder, was rotated at a rate of 90rpm to degas the sample in a vacuum under conditions of 300°C, and 1×10^{-5} torr for 20 minutes. Subsequently, during heating to CVD temperature, a $TiCl_4$-N_2-H_2 or $TiCl_4$-B_2H_6-H_2 mixed gas was adsorbed on the surfaces of the iron particles. The CVD treatment temperatures and times with TiN and TiB_2 respectively were 1000°C, 0 to 120min and 550° to 1000°C, 60 to 240min. It is assumed that CVD reactions take place as follows:

$$TiCl_4 + 1/2N_2 + 2H_2 \rightarrow TiN + 4HCl \quad \ldots\ldots\ldots (1)$$

$$TiCl_4 + B_2H_6 \rightarrow TiB_2 + 4HCl + H_2 \quad \ldots\ldots\ldots (2)$$

After the treatment, the sample was cooled at a rate of 80°C/min in an argon flow. The sample was then submitted to X-ray diffraction analysis for identification of the formed phases, SEM observation on surfaces and cross sections and analysis with an X-ray microanalyzer (EDX). Also, the sample was subjected to a corrosion test in an HCl solution and an oxidation resistance test by thermogravimetric analysis (TGA) in air.

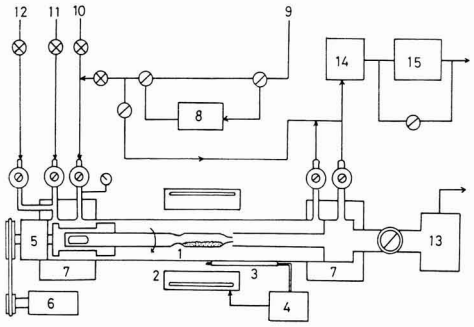

Fig. 1. Schematic diagram of equipment for rotary powder bed CVD.
1. rotary specimen cell, 2. infrared radiation furnace, 3. thermocouple, 4. temperature controller, 5. seal, 6. motor drive, 7. manifold, 8. $TiCl_4$ evaporator, 9. H_2, 10. N_2, 11. B_2H_6 + Ar, 12. Ar, 13. diffusion pump, 14. liquid nitrogen trap, 15. rotary pump.

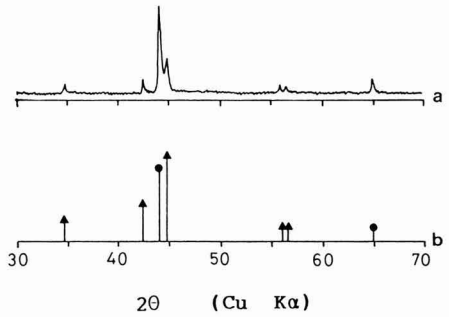

Fig. 2. X-ray diffraction pattern of the iron powder treated in the $TiCl_4$-B_2H_6-H_2 reactant stream.
(a) Deposition conditions; temperature: 800°C, reaction time: 80 min, flow rate: $TiCl_4$ 3ml/min, B_2H_6 3.2ml/min, H_2 300ml/min,
(b) diffraction lines in JCPDS cards; ●Fe, ▲ Fe_2B.

3. Results and Discussion

3-1. Conditions for Preparing TiB_2-TiN Double Layer Coated Powder

Iron particles start to coagulate and condense at around 600°C during heating. To obtain a highly dispersible powder, treated with either gas mixture, $TiCl_4$-N_2-H_2[2] or $TiCl_4$-B_2H_6-H_2, it was necessary to feed the reactant gas for adsorption on the particle surfaces starting at a relatively low temperature (300°C) with heating at a rather low rate (150°C/min) with the powder rotating. Using the $TiCl_4$-B_2H_6-H_2 reacting gas, we tried to coat iron particles with TiB_2. After adsorption with the reacting gas, CVD coating was carried out under the following conditions. Treatment temperature, 800° to 900°C; treatment time, 80min; gas flow rates: $TiCl_4$ 1.5 to 3ml/min, B_2H_6 0.8 to 3.2ml/min, H_2 300 to 500ml/min and Ar 140 to 300ml/min. Figure 2 shows a typical powder X-ray diffraction pattern of the treated powder. In all results Fe and Fe_2B were identified but the existence of TiB_2 could not be proved. On the surface of particles of the powder treated at 900°C for 120 min with gas flow rates of $TiCl_4$ 3ml/ min, B_2H_6 3.2ml/min and H_2 300ml/min, deposits looking like islands were observed as shown by the reflection electron image in **Fig.3**a and titanium was slightly detected in the TiKα image (see Fig.3b) of a particle surface taken by the EDX. TiKα line analysis of particle cross sections did not detect any titanium inside particles. On the other hand, with an iron plate charged in the sample cell, CVD was done under the same conditions as in Fig.3. The sample thus treated showed the existence of TiB_2 in addition to a trace of Fe_2B. These results suggest that in the CVD of the $TiCl_4$-B_2H_6-H_2 system on iron powder, the surface area of iron particles is so large, making the adsorption of the reacting gas on each particle so small, that Fe_2B is formed by the reactions between Ti-B deposits on iron particles and ions, causing only titanium to remain on the surfaces. Thus, it was proved that in the present CVD system, iron reacted with titanium so actively as to produce iron boride, which prevented iron particles from being directly coated with TiB_2.

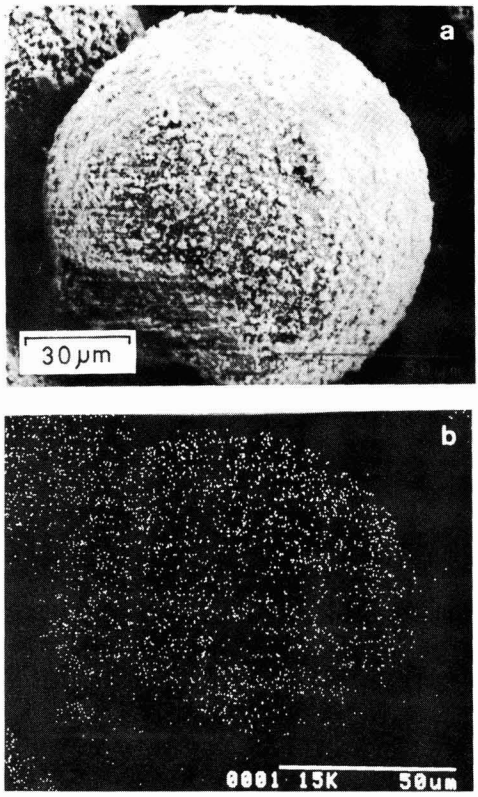

Fig. 3. EDX surface analysis of the same specimen as in Fig.2. (a) reflection electron image, (b) Ti Ka image.

In a previous report, we proved that iron particles can be coated with TiN by a reacting gas $TiCl_4$-N_2-H_2.[2] Now, using a $TiCl_4$-B_2H_6-H_2 gas, we tried to coat TiN-clad iron particles with TiB_2.The conditions for preliminary TiN coating were a treatment temperature of 1000°C, a treatment time of 60 min and the gas flow rates were constant: $TiCl_4$ 3, N_2 200, H_2 300 and Ar 20ml/min. TiN coating was followed by titanium boride CVD under conditions of treatment temperature 550° to 1000°C, treatment time 120min and gas flow rates of $TiCl_4$ 3.0 to 5.0, B_2H_6 0.4 to 3.2, H_2 300 to 500 and Ar 140 to 300ml/min. **Figure 4** shows the phases produced under various coating conditions. The horizontal and vertical axes represent titanium boride CVD temperature and B_2H_6-$TiCl_4$ mol ratio R=[B_2H_6]/[$TiCl_4$] respectively and the plots of the phases produced are discriminated by symbols. At high temperatures, since $TiCl_4$ is stabler than B_2H_6, less $TiCl_4$ than B_2H_6 is used for TiB_2 deposition. Thus, with R=1.0, which corresponds to the stoichiometrical composition of TiB_2, boron is excess in causing titanium boride (TiB_2) to be produced in the range of R. Around R=0.6, or with the B_2H_6 relatively high, although TiB_2 deposited, boron also co-deposited by the decomposition of B_2H_6, making the particle surfaces black.

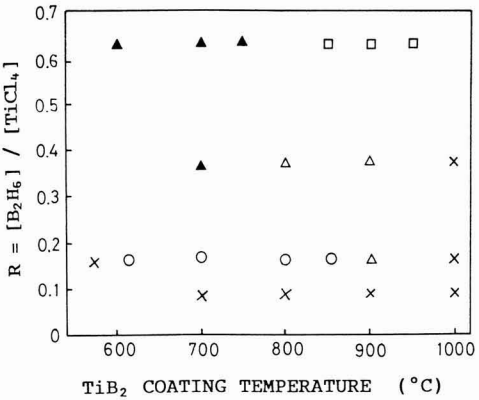

Fig. 4. Influence of the reactant gas mole ratio R=[B2H6]/[TiCl4] and TiB2 coating temperature on the product phases.
○TiB2, ▲ TiB2 + a-B, △ TiB2 or none,
❑ (TiB2 + a-B) or none, * none.

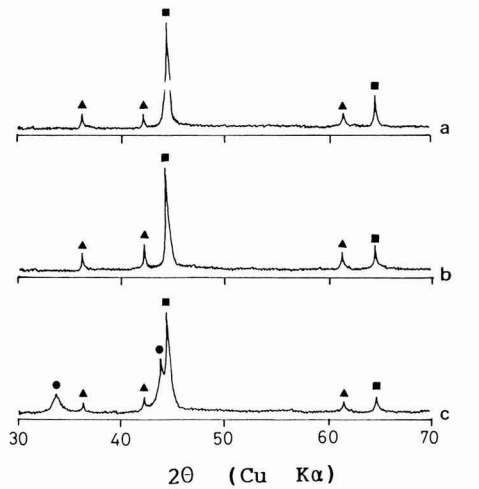

Fig. 5. X-ray diffraction patterns of the treated powder.
TiN precoating: 1000°C, 60 min;
TiB2 coating: (a) 650°C, (b) 700°C, (c) 800°C, 120 min.
●TiB2, ▲ TiN, ■Fe.

At temperatures of 600° to 700°C, boron deposited so heavily among particles that the powder bed became massive, preventing powder rotation. At high treatment temperatures (900° to 1000°C), boron was produced from the decomposition of B_2H_6 in the upper stream of the reaction tube but there was no deposition of titanium boride on the powder. As the flow rate ratio decreased, the deposition of decomposed boron also decreased and silver colored powder coated with titanium boride was observed. With conditions of R=0.16 and treatment temperature 600° to 850°C, the surfaces of the treated powders were consistently silver colored. At a low flow rate ratio R=0.08, there was no TiB_2 production but the surface of the powder was golden yellow, characteristic of titanium nitride.

Figure 5 shows the X-ray powder diffraction patterns of the samples obtained under conditions of R=0.16 and a treatment time of 120min. At treatment temperatures of 650° and 700°C (Fig.5, a and b), the samples were silver colored as mentioned earlier but only the diffraction lines of iron in the starting powder and TiN of the preliminary coating are shown. At 800°C, a broad but weak diffraction line of TiB_2 is observed. EDX analysis of the cross-sections of double layer coated particles detected the coexistence of Ti and B in the outer shell and that of Ti and N in the inner shell. This suggests that amorphous TiB_2 is produced on the TiN coated surfaces in the low-temperature range of 600° to 700°C and slightly crystalline TiB_2 is produced at a high temperature of 800°C. Such temperature dependency of the crystallinity of vapor growth titanium boride has also been observed in the CVD of $TiCl_4$-B_2H_6[4] and $TiCl_4$-BCl_3-H_2[5,6] systems and there is a report on the amorphous structure of TiB_2.[7]

The above results show that double layer coated TiB_2--TiN-Fe powder can be prepared by carrying out CVD of $TiCl_4$-N_2-H_2 and $TiCl_4$-B_2H_6-H_2 systems successively on iron powder.

3-2. Properties of Double Layer TiB_2-TiN Coated Iron Powder

Double layer coated TiB_2-TiN-Fe iron powders were obtained by TiN coating for 60 min under the same deposition conditions as in Fig.4 and subsequently by TiB_2 coating for 120 min at 700°C. Figure 6, (a) and (b) are SEM photographs of the surface appearance. The sample obtained with R=0.64 (Fig.6a) shows a rough surface due to the codeposition of boron. The sample treated with R=0.16 (B_2H_6: 0.8 and $TiCl_4$: 5.0ml/min) (Fig.6b) shows a smooth surface with a uniform coating. Neither cracks in double layer coated surfaces nor any separation of the coating from the iron particles were observed. The titanium boride surface reflected the patterns of the TiN undercoatings.

A double layer coated powder obtained by TiB_2 coating for 60 min at 700°C with R=0.16 after TiN coating for 120 min was embedded in epoxy resin and cross sections of particles were polished. Then, the polished sample was etched in a 1N-HCl solution at 100°C for 10 min to make the TiB_2-TiN boundaries clear. **Figure 7**a is the SEM photograph of a cross-section of the sample. Fig.7b is a magnified photograph of a double layer coated part in Fig.7a. It is evident that an outer shell consisting of a double TiB_2-TiN coating remains when the iron is corroded away by the acid treatment. Also, the double layer coating covers an iron particle uniformly and the two layers are adhesive closely together. From Fig.7b, the growth rates of the TiB_2 and TiN coatings are about 0.5 and 1μm/h respectively. It was proved that when the TiN coating time was reduced to 5 to 20 min (TiN coating thicknesses equivalent to 0.08 to 0.32μm), Fe_2B was not formed but the diffusion of boron into the iron particles was obstructed, permitting the thickness of the double layer coating to be controlled.

Figure 8 shows the results of oxidation resistance tests by TGA in air using (a) a single-coated powder sample without preliminary TiN coating (Fe_2B-Fe powder in Fig.2) and (b) a double layer coated powder sample (TiB_2-TiN-Fe

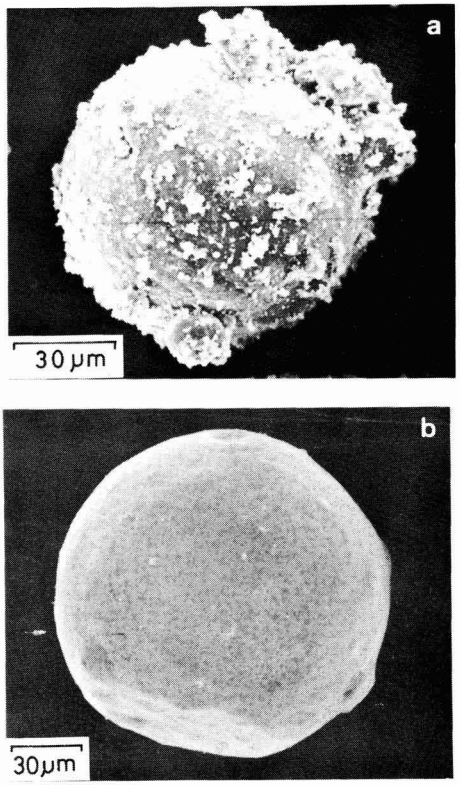

Fig. 6. SEM photographs of the treated particles.
TiN precoating: 1000°C, 60 min;
TiB_2 coating: 700°C, 120 min,
(a) R=0.64, (b) R=0.16.

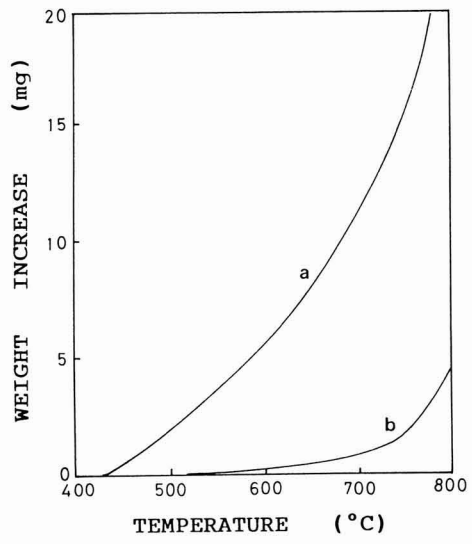

Fig. 8. Oxidation resistance test of the treated powder in air.
(a) Fe_2B/Fe powder, (b) TiB_2/TiN/Fe powder.

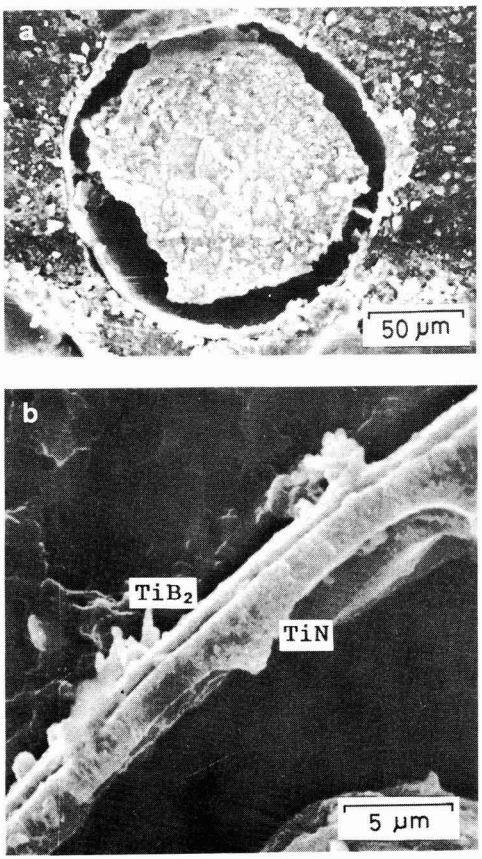

Fig. 7. SEM photographs of the cross sections after the acid treatment in 1N-NCl aqueous solution at 100°C for 10 min;
(a) TiB_2/TiN/Fe particle,
(b) double layer of TiB_2/TiN.

powder). While the Fe_2B-Fe powder in (a) is rapidly oxidized in temperature ranges above 450°C, the double layer coated powder in (b) has oxidation resistance improved by about 200 to 250°C in terms of temperature. Also, while the oxidation starting temperature of the TiN-Fe powder is about 650°C, that of the double layer coated TiB_2-TiN-Fe powder is about 700°C, showing some contribution of the double layer coating to improving oxidation resistance.

4. Conclusions

Using rotary powder bed CVD of $TiCl_4$-B_2H_6-H_2 and $TiCl_4$-N_2-H_2 systems in succession, we prepared iron powder samples with a double layer coating composed of titanium boride and titanium nitride. The following conclusions are obtained.

1)Boron diffuses so easily into iron particles, producing Fe_2B, that it is difficult to coat iron particles directly with

titanium boride.

2)TiN-coated powder can be coated uniformly with adhesive amorphous and crystalline TiB_2 at treating temperatures of 600 to 850°C with R=0.16.

3)A double layer coated TiB_2-TiN-Fe powder can be prepared by varying the flows of the starting gases and treatment temperature.

4)The adherence between the two layers of the double coating of the TiB_3-TiN-Fe powder is high. The oxidation starting temperature in air was about 700°C.

References:

1) H. Itoh, N. Watanabe and S. Naka, J. Mater, Sci., 23 43-47 (1988).
2) H. Itoh, H. Hattori and S. Naka, J. Mater, Sci., 24 3643-3646 (1989).
3) H. Ito, Boundary, 4, 32-34 (1988).
4) H.O. Pierson and A.W. Mullendore, Thin Solid Films, 72 511-516 (1980).
5) T.M. Besmann and K.E. Spear, J. Crystal Growth, 31 60-65 (1975).
6) T. Takahashi and H. Itoh, J. Crystal Growth, 49 445-450 (1980).
7) A.K. Kaloyeros, W.S. Williams, R.B. Rizk, F.C. Brown and A.E. Greene, J. Am. Ceram. Soc., 71 948-955 (1988).

This article is a full translation of the article which appeared in Nippon Seramikkusu Kyokai Gakujutsu Ronbunshi (Japanese version), Vol.98, No.5, 1990.

Effect of Glaze on Bending Strength of High Strength Whiteware Bodies

Yuichi Kobayashi, Osamu Ohira, Yasuo Ohashi and Etsuro Kato*

Toki Municipal Institute of Ceramics 1556-2, Dachi-cho, Toki, Gifu 509-54, Japan
*Aichi Institute of Technology Yakusa-cho, Toyota, Aichi 470-03, Japan

The effect of glaze on the bending strength of high strength whiteware bodies containing 30% alumina was investigated.The significant increase of the bending strength by the applied glaze is due to the reduced size of fracture origin at the surface of body. Compressive stress in the glaze is necessary to avoid fracture initiation within glaze. Coarse quartz grains in the glaze act as the fracture origin and reduce the bending strength. Raw materials for glaze must be milled well not to create fracture origins in the glaze. By glazing, bending strength could be raised by about 1.4 times of that of unglazed bodies; bending strength of unglazed and glazed test bars were 24.0kg/mm^2 and 33.5kg/mm^2 respectively.

[Received December 25, 1989, Accepted February 13, 1990]

Key-words: Whiteware bodies, Glaze, Stress in glaze, Alumina addition, Elastic modulus, Bending strength

1. Introduction

Previously we reported that high-strength whiteware bodies with 24kg/mm^2 or higher bending strength could be manufactured with Weibull modulus of 20 or above by using a material with 30% alumina.[1] The glazed bending strength is important in products. With conventional porcelains, products of a silica-feldspar-clay system, there are many reports on the glazed bending strength and it is known that quite high bending strengths can be obtained by preparing suitable glaze.[2,3]

In contrast, there are few reports on the glazed bending strength of alumina-containing high-strength whiteware bodies and to our knowledge, the highest glazed bending strength ever reported is 18.5kg/mm^2.[4] W.D. Kingery et al.[5] explained that stresses in glaze, compressive stresses in particular, due to thermal expansion differences between the body and glaze made a considerable contribution to increased strength but did not give any further discussion with actual data.

Through tests with various compositions and grain sizes of glaze, we discovered that the glazed bending strength could be increased to 1.3 to 1.4 times the unglazed bending strength, a glazed bending strength of 33.5kg/mm^2 being achieved with a unglazed bending strength of 24kg/mm^2. We report our results here.

2. Experimental Method

2-1. Preparation of Samples

(1) Body

The raw materials were the same as used in the previous report.[1] Alumina 30%, feldspar 30% and kaolin plus clay 40% were wet ball milled for a certain period in an alumina pot with a capacity of 5.0l. Three wet ball milling times, 8, 18 and 24h, were used. The material milled for 8h was passed through a 350 mesh sieve and then dehydrated and cast into test bars 10 × 5 × 80mm, the same size as in the previous report. The bending strength of these test bars,

Table 1.Chemical composition of raw materials for glaze.

	Ohira feldspar ss150	Ohira feldspar 2-60	Fukusima quartz	Wollastonite	Calcined talc	N.Z.China clay
SiO_2	66.56	75.80	99.78	53.50	62.61	49.78
Al_2O_3	18.21	14.27	0.08	0.52	0.26	35.72
Fe_2O_3	0.06	0.10	0.04	0.10	0.14	0.26
TiO_2	0.01	0.00	0.09	0.00	0.01	0.12
CaO	1.10	1.35	0.04	42.80	0.95	0.00
MgO	0.01	0.02	0.00	0.60	34.93	0.00
K_2O	10.37	4.76	0.00	0.09	0.00	0.00
Na_2O	3.50	3.74	0.03	0.03	0.19	0.06
Ig.loss	0.22	0.01	0.01	1.72	1.17	14.05
Total	100.04	100.15	100.07	99.36	99.86	99.99

Table 2.Composition of glaze expressed in Seger equation.

$$\left.\begin{matrix} X\ KNaO \\ Y\ \ MgO \\ Z\ \ CaO \end{matrix}\right\} 0.600Al_2O_3\ \ 5.600SiO_2$$

$X+Y+Z=1.00 \quad K_2O/Na_2O=1.00$

	G-1	G-2	G-3	G-4	G-5
X	0.45	0.40	0.35	0.30	0.25
Y	0.30	0.30	0.30	0.30	0.30
Z	0.25	0.30	0.35	0.40	0.45

fired at 1350°C for 1h without glazing, were 17.0, 21.9 and 24.0kg/mm^2 respectively. They were named K17, K22 and K24, respectively.

Before glazing, all test bars were fired at 700°C for 30min in an electric furnace.

(2) Glaze

Five glaze compositions, G1 to G5, were prepared using the raw materials shown in **Table 1**. They are represented by the Seger equation in **Table 2**. 2.5kg of raw materials were wet ball milled for a specified time in a 5.0l alumina pot and then passed through a 250 mesh sieve. Before glazing, the moisture contents of the glaze slip were adjusted to about 34 to 38 Baume degrees.

To measure the bending strengths of the fired test bars, the sample surfaces other than the top surface to be subjected to tensile stress were coated with water repellant. Then the samples were dipped in glaze slip for 2 to 3s and the surfaces except the top wiped with a water sponge to remove the glaze. The glaze thickness on the tensile surface of each fired sample was about 120 to 200μm.

(3) Firing

An electric furnace designed for atmosphere control was used. The temperature was raised at a rate of 400℃/h from room temperature to 1000°C. Then it was held for 30min while the furnace gas was discharged with a vacuum pump. Then, a reducing atmosphere was obtained by feeding nitrogen, carbon monoxide and carbon dioxide gases in at rates of 4.0, 0.5 and 0.5l/min respectively. Above 1000°C the temperature was raised at a rate of 200°C/h. At 1350°C, it was held for 1h and then the furnace was left to cool down.

If bubbles are present in the glaze, the elastic modulus cannot be measured accurately. Therefore, for the samples to be used for measuring the glaze modulus of elasticity only, the furnace was exhausted with a vacuum pump at 1100°C and then heated. Subsequently at 1350°C the furnace was charged again with a reducing atmosphere and the samples fired.

2-2. Measurement of Properties

(1) Thermal expansion

A thermal expansion test equipment TMA made by Rigaku Denki was used. The samples for measuring the thermal expansion of the body were prepared by firing test bars under the same conditions as for the bending strength test bars and then cutting out cylinders about 5mm in dia. and 20mm long with a diamond cutter and polishing.

The samples for measuring the thermal expansion of glaze were prepared by compacting dried glaze into blocks of about 100g and fired and melted under the same conditions for the bending strength test bars. Then cylinders 5mm in dia. and 20mm long were cut out with a diamond cutter and polished.

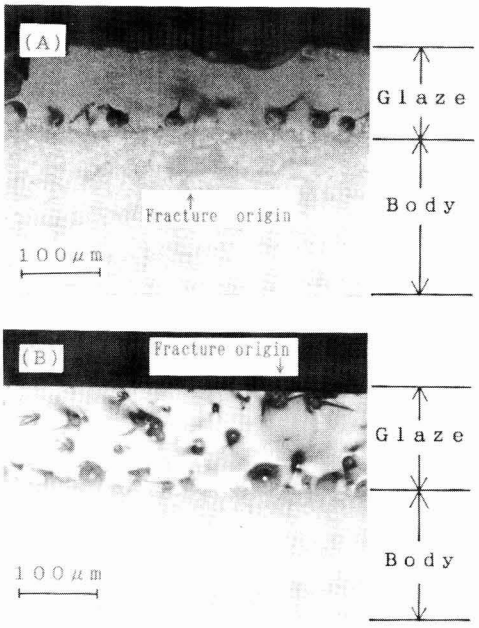

Fig. 1. Photograph showing linear feature at fracture surface in glaze.
(A)Fracture origin in body.
(B)Fracture origin in glaze.

(2) Modulus of elasticity

Modulus of elasticity was measured by using an electronic universal tester made by Yonekura Seisakusho together with jigs for accurately measuring the displacement of the center of each test bars with a differential transformer. The test samples were about 8mm wide and about 1.4mm thick and supported by a roller-to-roller span of 30mm in accordance with JIS R-1602. The crosshead speed was 0.05mm/min.

(3) Bending strengths

The bending strengths of fired test bars were measured by using rubber plates, a method employed in our previous report.[1] The samples were positioned so that tension acted on the glazed surface. The mean bending strength was obtained from about 16 measurements.

(4) Fracture surface observations

To study glazed bending strengths, it is necessary to know whether the fractures originate in the glaze or body. Thus, after measurement of the bending strengths, the fracture surface were observed under a reflection microscope to detect the fracture origins.

If a fracture passed through bubbles in the glaze in a bending strength test, linear features were observed in the microscope at the tips of bubbles as shown in **Fig.1**. Such features surround the fracture radiantly. So, the origin of a fracture can be roughly located by tracing successive fea-

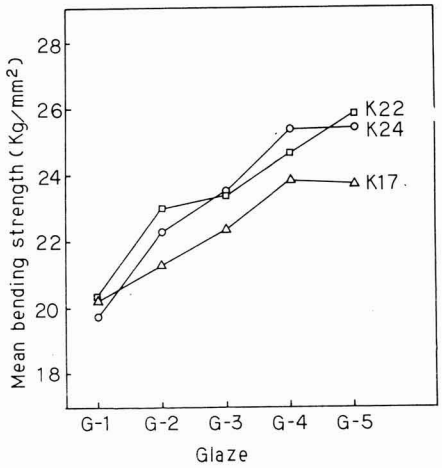

Fig. 2. Effect of glaze composition on bending strength.

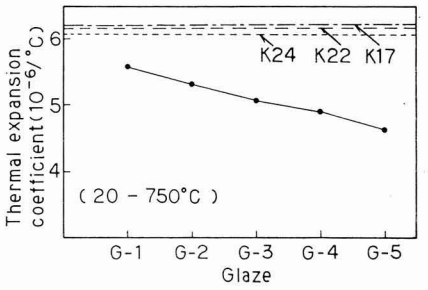

Fig. 3. Effect of glaze composition on thermal expansion coefficient.

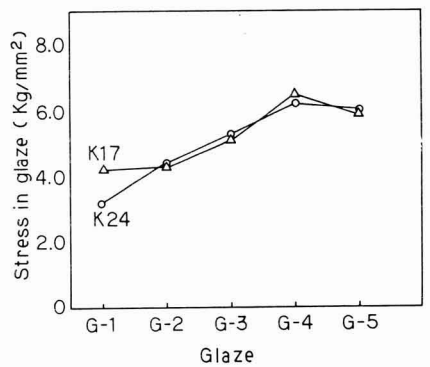

Fig. 4. Effect of glaze composition on internal stress in glaze.

tures at bubbles.

(5) Stress in glaze

Samples for measuring stress in glaze were cut out of the samples used for strength measurement with a diamond cutter. The cut surfaces were polished successively with #500, #1000 and #2000 abrasives and the glaze stresses measured by Inada's method[6] using a polarizing microscope.

3. Results

3-1. Effect of Glaze Composition

3 types of unfired bodies, K17, K22, K24, were coated with glazes G1 to G5, fired and the bending strengths were measured. The results are shown in **Fig.2**. **Figure 3** shows the measured coefficients of thermal expansion of the glazes and the bodies. In the glaze compositions, the content of feldspar decreased from G1 to G5 and the coefficients of glaze thermal expansion followed the same trend.The bending strengths of the samples showed the reverse trend; they increased as the content of feldspar and the coefficient of thermal expansion decreased. Glaze stresses in K17 and K24 were measured and the results are shown in **Fig.4**. Here, the thicknesses of the glazes were about 110 to 200μm. As expected from the coefficients of thermal expansion, the compressive stresses in the glazes increased as the content of feldspar decreased. Also, it is evident that as the compressive stresses in the glazes increased, the bending strengths increased. Again, as glaze stresses rose, the bending strengths also rose. However, the difference between the two glazed bending strengths is smaller than the difference between the two unglazed bending strengths. For example, the difference was 7.0kg/mm^2 between K17 and K24. Furthermore, with K17, as the glaze stresses increased, the glazed bending strength rose by about 1.4 times to 23.8kg/mm^2 but this was the limit. With K22 and K24, on the other hand, the maximum was about 25.7kg/mm^2, showing no considerable improvement. To investigate these phenomena further, the fracture faces of all the samples from bending strength testing were observed with a reflection microscope to identify fracture origins. The discrimination of fracture origins between glaze and body is shown in **Table 3**. With K17, the unglazed bending strengths were relatively low and the ratio of fracture origins in the body high. In K22 and K24 with high unglazed bending strengths, the fracture origins were mostly in the glaze. This may be because the glazed bending strengths of K22 and K24 were not very high in Fig.2. In other words, fractures start in the glaze before fractures start in the body. Thus, if compressive stresses in the glaze are higher or if fracture origins in the glaze are smaller, the glaze bending strengths will be larger, causing fractures to start in the body.

Table 3.Effect of glaze composition on location of fracture origin (glaze: body).

Body	Glaze G-1	G-2	G-3	G-4	G-5
K17	6:10	1:13	7: 8	5:11	3:12
K22	16: 0	11: 0	14: 0	12: 1	17: 0
K24	15: 0	16: 0	13: 0	14: 0	16: 0

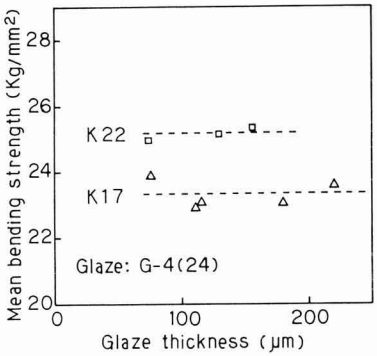

Fig. 5. Effect of glaze thickness on bending strength.

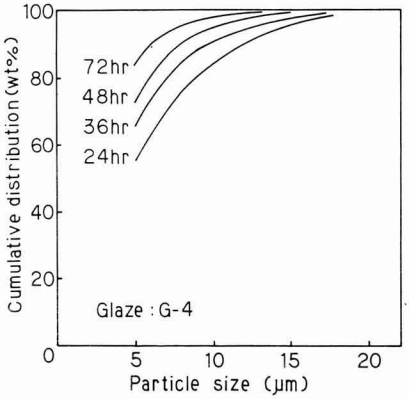

Fig. 6. Relationship between particle size distribution of glaze and milling time.

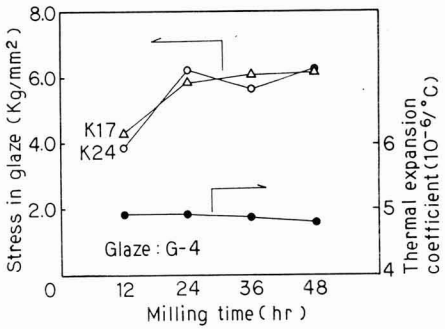

Fig. 7. Effect of glaze milling time on internal stress in glaze and thermal expansion coefficient of glaze.

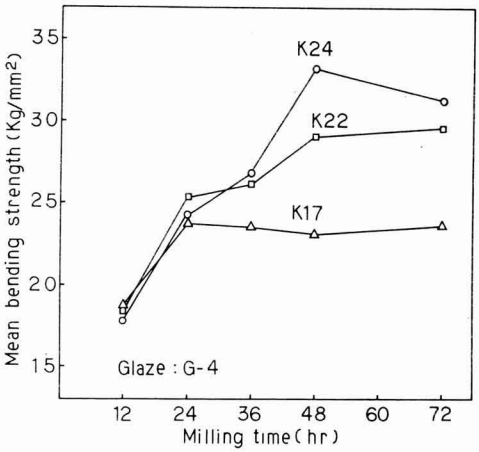

Fig. 8. Effect of glaze milling time on bending strength.

3-2. Effect of Glaze Thickness

To investigate the effect of glaze thickness on the bending strength, samples K17 and K22 were coated with glaze of several thicknesses from 70μm to 220μm varying the concentration of G-4 glaze and the dipping time in the glaze slip.

The results of measuring bending strengths are shown in **Fig.5**. With either sample, there was little variation in strength with variations in glaze thickness. However, if the graph is extrapolated to glaze thickness zero, the bending strengths are 23kg/mm^2 with K17 and 25kg/mm^2 with K22, which do not agree with the bending strengths of the body only. This may be because the surfaces of the body and glaze differed. Some surface roughness features depending on the size of grains or fine cracks which may act as fracture origins are distributed on the body surface. On the other hand, the glazed surface is covered with a uniform vitreous layer with cracks not open outwards and thus the bending strength is higher.

3-3. Effect of Glaze Milling Time

With K17, the fracture origins were in the body and the glazed bending strengths were higher by up to about 1.4 times. With K22 and K24, on the other hand, fractures often started in the glaze. This may be because there were some fracture origins in the glaze, causing the glaze strength to decrease.

Thus, samples with several G-4 glaze milling times were prepared and the effect of these times on the glazed bending strengths and stresses in glaze examined. The glaze materials milled for 12h and over 24h were passed through 250 mesh and 350 mesh sieves, respectively. **Figure 6** shows the relationship between the glaze milling time and grain size, **Fig.7** shows the relationship between glaze milling times and coefficients of thermal expansion, and stress in glaze. **Figure 8** shows the relationship between glaze milling time and glazed bending strength and **Table 4** shows the discrimination of fracture origins in the body or glaze.

With a milling time of 12h, it was observed under the microscope that the glaze grains were still coarse with unmelted quartz remaining. The stress in the glaze was as low as 4.0kg/mm^2. The coefficients of thermal expansion showed little variation. With all bodies, the bending strengths were about 19kg/mm and all fracture origins were

Table 4.Effect of glaze milling time on location of fracture origin (glaze: body).

Body	Milling time of glaze(hr)				
	12	24	36	48	72
K17	16: 0	1:12	0:15	0:16	0:18
K22	16: 0	7: 4	16: 0	7: 5	9: 9
K24	16: 0	14: 0	13: 2	11: 4	–

in the glaze. This may be because the quartz remaining in the glaze formed the fracture origins.

With the glaze milled for over 24h, few unmelted grains were observed microscopically. The compressive stresses in the glaze were constant at 6.0kg/mm^2. With K17 and K24, fracture origins in the body were also observed. With a milling time of over 36h, the fracture origins of K17 were all in the base. The glazed bending strength for K17, however, did not exceed 24kg/mm^2, about 1.4 times the bending strength without glaze.

With K22, the glazed bending strength rose and reached a peak of 29.5kg/mm^2 with no further rise in the first 48h of milling time. This value of 29.5kg/mm^2 is about 1.34 times the bending strength without glaze.

With milling times over 24h, the stress in the glaze was constant at about 6.0kg/mm^2. Increases in strength here can thus be ascribed to the absence of quartz fracture origins. With K24, the strength in the first 48h of pulverizing time rose, reaching a peak of 33.5kg/mm^2, which is about 1.38 times the bending strength of the body without glaze.

Thus, it was proved that if the glaze was milled very finely, fracture sources in it were reduced, allowing the glazed bending strength to increase.

4. Discussion

The results obtained show that if the grain size and the coefficient of thermal expansion of the glaze material are suitably controlled, with high-strength whiteware body containing 30% alumina, a glazed bending strength of about 1.4 times the unglazed bending strength can be obtained. This increase in strength may be due to the following two reasons.

First, as described earlier for the effect of glaze thickness, without glaze there is some surface roughness, depending on the grain size of the raw material, or fine cracks as possible fracture origins.Glazing makes such cracks closed inside, not open outward, causing their effect on fractures to decrease.Secondly, compressive stresses in glaze may contribute to the bending strength, which will be studied in more detail.

Glazed bending strength can be raised to over 30kg/mm^2 by using carefully controlled glazing. If the compressive stress in glaze of 6.0kg/mm^2 is deducted, the value above is 24.0kg/mm^2. Compared with the fracture strength of glass, as a strength for glaze this seems too high. A further study is made here using actual examples with such factors as stresses in glaze taken into account.

First, we consider the measured bending strength 30kg/mm^2 of the K22 body coated with glaze G-4 milled for 48h (Fig.8).

Suppose that the test bar 84mm wide and 4.2mm thick was fractured in a 3-point bending test with load P: 98.8kg and span L: 30mm. Maximum stress σ_B caused in the body here is given by the equation for bending strength as

$$\sigma_B=\frac{3\times L\times P}{2\times w\times t^2} \quad \cdots\cdots\cdots\cdots\cdots (1)$$

$$=\frac{3\times 30\times 9}{2\times 8.4\times 4.2^2}=30 \text{ kg/mm}^2 \quad \cdots\cdots\cdots\cdots (2)$$

In other words, a tensile stress of 30.0kg/mm^2 is generated directly below the load. With the elastic modulus of body written as E_B, distortion ε_B in the region in which the maximum tensile stress is acting is given by

$$\sigma_B = E_B \times \varepsilon_B \quad \cdots\cdots\cdots (3)$$

Table 5 shows the results of measurement of the modulus of elasticity of bodies and glazes. The glaze thickness is only about 150μm, only about 3.5% of the entire test bars. Assuming that the modulus of elasticity of the sample is E_B of the body, we have

$$\varepsilon_B = \sigma_B/E_B = (30/1.3 \times 10^4) = 0.0023. \cdots\cdots (4)$$

The modulus of elasticity E_{GL} of the glaze is about 0.78×10^4kg/mm^2, which is much lower than that of the body.The stress generated when distortion $\varepsilon_{GL}(=\varepsilon_B)$ =0-.0023 is caused in the glaze is given by

$$\sigma_{GL}=E_{GL}\times\varepsilon_{GL}$$
$$=0.78\times10^4\times0.0023$$
$$=17.9\text{kg/mm}^2 \quad \cdots\cdots (5)$$

This implies that a tensile stress of 17.9kg/mm^2 is caused at fracture. In practice, there is already a compressive stress of about 6kg/mm^2 in the glaze. If this is deducted, the test bar fractures under a tensile stress of about 12(=17.9–6.0)kg/mm^2 acting in the glaze.

This value can be considered as the fracture stress in the glaze itself rather than the 24.0kg/mm^2 resulting from the bending strength 30kg/mm^2 minus the compressive stress in glaze of 6.0kg/mm^2. This value is closer to the ordinary

Table 5.Modulus of elasticity of glaze and unglazed body.

Specimens		Elastic modulus (10^4kg/mm^2)
Body	K17	1.29
	K22	1.28
Glaze	G-4(12)	0.80
	G-4(24)	0.78
	G-4(72)	0.78
	G-1(24)	0.74

Number in ( ) : milling time(hr)

strength of glass.

Consider another case. A K22 body is coated with glaze G-2 milled for 12h and the glazed bending strength measured as 17.0kg/mm^2. From equation (3), the distortion of the body is given by

$$\varepsilon_B=\sigma_B/E_B=\frac{1700}{1.31\times10^4}$$
$$= 0.0013 \quad \ldots\ldots\ldots (6)$$

With this distortion, stress σ_{GL} in the glaze is given by equation (5)

$$\sigma_{GL}=E_{GL} \times \varepsilon_{GL}$$
$$=0.78 \times 104 \times 0.0013$$
$$=10.0 \quad \ldots\ldots\ldots (7)$$

The compressive stress in the glaze being 4.0kg/mm^2, the strength of the glaze is about 6(=10–4)kg/mm^2. This value is considered reasonable because there is some unmelted quartz remaining in the glaze. Here, if the difference in the modulus of elasticity is not taken into account, the fracture strength of the glaze is 17.0 –4.0=13.0kg/mm^2, which can hardly be considered the actual strength. Therefore, because the modulus of elasticity of the body is larger than that of the glaze, the measured bending strength is overestimated.

With all bodies K17, K22 and K24, the glazed bending strengths were limited to 24, 30 and 33.5kg/mm^2 respectively, all about 1.4 times the unglazed bending strength. No bending strength can be greater than 1.4 times because with a longer glaze milling time, there will be no fracture sources left in the glaze. Therefore fractures do not start in the glaze but in the body. Thus, the strengths of high-strength whiteware bodies can be raised to 1.4 times by glazing but this is the limit and even if the strength of the glaze is increased or the compressive stresses in the glaze are increased, fractures start in the body, so glazed bending strengths cannot be increased further.

5. Conclusions

The effects of the composition and thickness of glaze, glaze milling conditions, etc., on the glazed bending strength of 30% alumina-containing high-strength whiteware bodies were investigated. The position of the fracture origin, in the body or glaze, was carefully assessed in the samples. As a result, we discovered that increases in bending strengths caused by glazing were due to the size of the fracture origins in the surface of the body being reduced by glazing. Thus, it was proved that to raise glazed bending strengths, stresses must be applied to prevent fractures from starting in the glaze and the glaze must previously be crushed well to eliminate fracture origins.

1)If coarse quartz grains remain in the glaze, they will become fracture sources, causing the strength to decrease.

2)If a suitable glaze composition has been selected, compressive stresses will act in the glaze and if the glaze has been milled finely, fractures will start not in the glaze but in the body. Under such conditions, the glazed bending strengths can be raised to 1.4 times the bending strengths of body. If the bending strength of a body is 24kg/mm^2, a maximum bending strength of 33.5kg/mm^2 can be obtained from the glazed body.

3)With a glaze thickness of about 150μm, the glaze stress must be above 6.0kg/mm^2.

4)The fact that higher glazed bending strengths can be obtained is explained by the modulus of elasticity of the body being about 1.7 times higher than that of the glaze and size reduction of cracks in the body by glazing.

References:

1) Y. Kobayashi, O. Ohira, Y. Ohashi and E. Kato, Yogyo-Kyokai-Shi, 95 (9) 887-92 (1987).
2) C. Bettany and H.W. Webb, Trans. Brit. Ceram. Soc., 39 (11), 312-335 (1940).
3) L.E. Thiess, Jour. Amer. Ceram. Soc., 19 (3) 70-73 (1936).
4) Fine Ceramics Handbook, ed. K. Hamano, p.526 (Asakura Shoten, 1984).
5) W.D. Kingery, H.K. Bowen and D.R. Uhlmann, Introduction to Ceramics Second Edition p.812.
6) H. Inada, Yogyo-Kyokai-Shi, 85 (10) 487-95 (1977).

This article is a full translation of the article which appeared in Nippon Seramikkusu Kyokai Gakujutsu Ronbunshi (Japanese version), Vol.98, No.5, 1990.

Oxygen Diffusion in $BaTiO_3$-PTC

Toshiki Saburi, Makoto Hori, Mitsuru Asano, Hajime Haneda*, Junzo Tanaka* and Shinichi Shirasaki*

Nippondenso Co., Ltd. 1-1 Showa-cho, Kariya, Aichi 448, Japan

* National Institute for Research in Inorganic Materials 1-1, Namiki Tsukuba, Ibaragi 305, Japan

A relation between PTC (Positive Temperature Coefficient) characteristics and oxygen diffusion coefficients in $BaTiO_3$-PTC thermistors was studied. As a result, PTC behavior was not obtained unless the annealing temperature exceeded 900°C. Both coefficients of oxygen volume diffusion with and without PTC behavior were equal to each other and of $2\times10^{-14}cm^2/s$ at 850°C. But, the coefficient of oxygen boundary diffusion with PTC behavior was much larger than that without PTC behavior.

[Received January 6, 1990; Accepted February 13, 1990]

Key-words: $BaTiO_3$, PTC, Oxygen boundary diffusion, Oxygen volume diffusion

1. Introduction

The characteristics of $BaTiO_3$-PTC thermistors with added rare earth elements or Nb ions change remarkably with annealing temperature and atmospheric conditions. If a thermistor showing PTC characteristics is annealed at about 1000°C in a reducing atmosphere, the change in resistance at the Curie point decreases with annealing time, and finally PTC characteristics become uninvestigatable. By contrast, if a thermistor without PTC behavior is annealed in an oxygen atmosphere, it again shows PTC characteristics.[1-4]

From this phenomenon, it may be presumed that there is a close relation between the PTC characteristics of $BaTiO_3$ thermistors and their reduction and oxidation. In this paper, the relation between PTC behavior and oxygen diffusion characteristics was investigated by annealing, in air or oxygen atmosphere, specimens that had lost PTC behavior by reduction.

Results showed that the coefficients of oxygen volume diffusion both with and without PTC behavior were equal to each other. But the coefficient of oxygen boundary diffusion with PTC behavior was much larger than that without PTC behavior.

2. Experimental Procedures

2-1. Preparation of Specimens and Measurement of Electrical Properties

$BaTiO_3$-PTC was prepared by compounding $BaCO_3$ and TiO_2 (extra pure reagent, manufactured by Wako Pure Chemical Industries, Ltd.) to a Ba/Ti ratio of 0.99, and 0.2mol% of Y_2O_3 (extra pure reagent, manufactured by Wako Pure Chemical) was added to the mixture, which was wet-blended with a pot mill for 24hrs. The resulting material was dried and calcined at 1100°C for 2hrs, and the powder thus obtained was granulated with a binder, molded under pressure of 49MPa into a shape 20mm in diameter and 2mm in thickness, which was reduced by firing at 1300°C for 1hr (with a temperature-changing rate of 300°C/h) in N_2-H_2 (7% H_2). The reduced specimens were annealed at 500°, 800°, 900° and 1100°C for 1hr in (300°C/h) in air. At 1100°C, they were also annealed in oxygen gas.

To measure the PTC characteristics of the reduced specimen and the specimens annealed in oxygen as mentioned above, their surfaces were polished and coated with ohmic silver electrodes and fired at 500°C for 10min, to prepare electrodes. Resistance at room temperature R_{20} and variation in resistance change at around Curie point and $R=\log(R_{max}/R_{min})$ were measured.

2-2. Quantitative Analysis of Oxygen

Of the specimens prepared in (1), a reduced specimen and specimens annealed at 800°C in air and at 1100°C in oxygen were ground and quantitatively analyzed with a nitrogen-oxygen analyzer (EMGA-2800, manufactured by Horiba Seisakusho) to measure the change of oxygen quantity.

2-3. Measurement of Coefficient of Oxygen Diffusion

Oxygen diffusion characteristics of the reduced specimen and the specimens annealed at 500°, 800°, 900° and 1100°C in air and oxygen were measured by the gas-solid phase exchange method.[5] **Figure 1** shows the measurement method of oxygen diffusion coefficients. A platinum-crucible containing powdered specimen (for measurement, powders prepared by crushing specimens to ranges of 14 to 16 mesh and 200 to 300 mesh were used) was set in a quartz glass container which was evacuated to below 10^{-3}mmHg

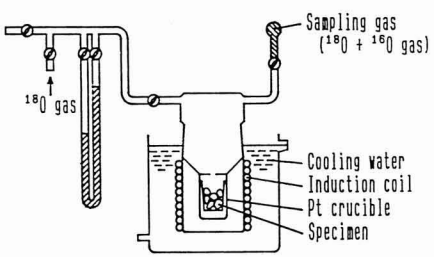

Fig. 1. Measurement method of oxygen diffusion coefficients.

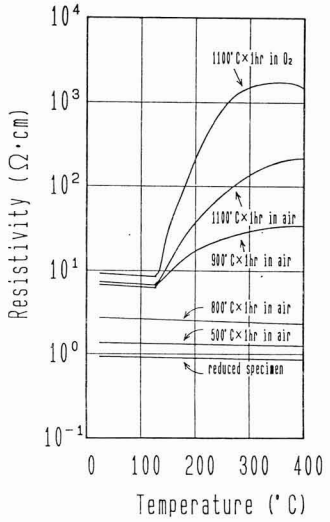

Fig. 2. Resistivity versus temperature of $BaTiO_3$-PTC specimens annealed in different conditions.

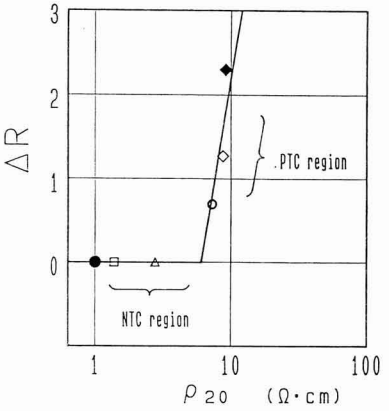

Fig. 3. R=log (R_{max}/R_{min}) versus resistivity at room temperature ρ_{20} annealed in different conditions.
(●) reduced specimen, (❑) 500°C in air,
(△) 800°C in air, (○) 900°C in air,
(❑) 1100°C in air, (■) 1100°C in O_2.

(0.133Pa) and oxygen containing 20% of ^{18}O isotope was admitted to an oxygen gas pressure of 40mmHg (5.33kPa). Setting the temperature of the specimen powder at a test temperature (850° and 1100°C) after preheating it at 800°C for 10min with an induction coil, the compositional change of $^{18}O + {}^{16}O$ gas with time was quantitatively analyzed with a double-focussing mass-spectrometer (Hitachi, B-80). The measurement method for the diffusion coefficient utilized changing gas composition with time due to the exchange reaction between ^{16}O in the specimen solid and ^{18}O in gas. In calculating diffusion coefficients, the specimen was assumed to be a sphere, and the following equation was used.[6]

$$M_t/M_\infty = 1 - \sum_{n=1}^{\infty} \frac{6\alpha(\alpha+1)\exp(-Dq_n^2 t/a^2)}{9+9\alpha+q_n^2\alpha^2} \quad \cdots\cdots (1)$$

Where q_n is the non-zero root of $\tan q_n = (3q_n/3 + \alpha q_n^2)$, a is the radius of the specimen sphere, α is the ratio between the number of oxygen atoms in the gas and solid and $Mt/M\infty$ is the ratio of diffusion amount at time t and after infinite time.

3. Experimental Results and Discussion

3-1. Annealing and PTC Characteristics

Figure 2 shows the change in resistance temperature of specimens annealed under different conditions. The porosity of the specimens after reduction by firing was 9% and the particle radius was about 40μm. The resistivity at room temperature (ρ_{20}) was about 1.0 Ω·cm and showed NTC (Negative Temperature Coefficient) behavior. When the reduced specimen was annealed for 1hr at 800°C in air, the resistivity ρ_{20} increased to 2.7Ω·cm, while PTC behavior was not observed. PTC behavior was remarkable for specimens annealed at above 900°C, particularly at 1100°C. The temperature at which resistance started rising was 120°C. The difference in resistance change was 1.2 for a specimen annealed for 1hr at 1100°C and 2.2 for a specimen annealed in an oxygen atmosphere. Thus, it follows that the higher the oxygen partial pressure, the larger is the value of R.

Figure 3 shows the plotted relation between resistivity at room temperature ρ_{20} and difference in resistance change R. The figure shows two regions resulting from annealing a reduced specimen in air or oxygen. One is the region without PTC behavior and with zero R (NTC region), and the other is the one with PTC behavior and with non-zero R (PTC region).

Based on Heywang's barrier model[7], resistance is

$$\rho = \rho_v \exp(e\phi/kT) \quad \cdots\cdots (2)$$

where is the height of the barrier and is given by

$$\phi \propto N_s^2/N_D \quad \cdots\cdots (3)$$

where N_s is the acceptor density of the grain boundary and N_D is the donor density. Based on the result of this study, no acceptor level seems to be formed in the grain boundary because Equation (2) gives 0 for since R is 0 in the NTC region. The increase of ρ_{20} with increasing annealing temperature is attributable to the increase of bulk resistance ρ_v with decreasing donor density resulting from oxidation.

When ρ_{20} becomes 6 to 7Ω·cm, R is no longer 0, as shown by Equation (2). Accordingly Equation (3) gives Ns = 0, and it is expected that an acceptor level was formed.

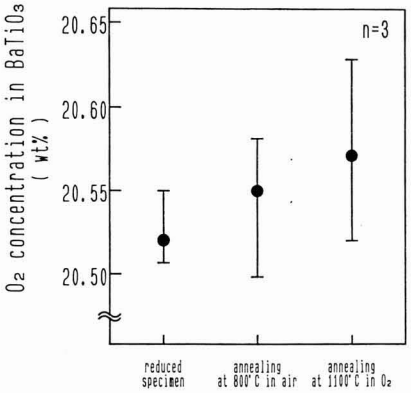

Fig. 4. O_2 concentration in $BaTiO_3$ specimens annealed in different conditions.

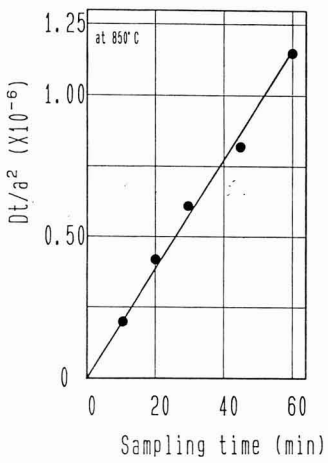

Fig. 5. Typical plot of Dt/a^2 against time for a specimen thermally-treated at 1100°C in O_2.

Increasing R with ρ_{20} in the PTC region seems to be attributable to either decreasing N_D in Equation (3) or gradually increasing N_s as in NTC region, or both.

The above shows that the appearance of PTC behavior has a critical point in the annealing temperature range of 800° to 900°C at which ρ_{20} is 6 to 7Ω·cm and that N_s is almost 0 at temperatures below that temperature and takes a finite value above that temperature.

3-2. Quantitative Analysis of Oxygen

Figure 4 shows the oxygen concentration in reduced specimens and those annealed at 800°C in air and at 1100°C in oxygen. Measurements were conducted three times, and the average oxygen concentration was 20.57wt% for specimens annealed at 1100°C and 20.52wt% for reduced specimens. The oxygen concentration in $BaTiO_3$ without oxygen defects was given as 20.58wt%, almost equal to the value for the specimen annealed at 1100°C in oxygen. Calculation based on oxygen concentration in reduced specimens gave the oxygen defects as $4.1 \times 10^{20}/cm^3$, almost equal to the data obtained by Daniels et al.[8] at 1310°C under O_2 partial pressure of 10^{-14} to 10^{-15}atm. These results show that the oxygen defect number decreases with an increase in annealing temperature and oxygen partial pressure when the reduced specimen is oxidized by annealing.

Compared with Fig.3, it is revealed that is not 0 when the oxidation makes progress to a certain degree with the increasing in ρ_v with decreasing oxygen defect number.

3-3. Oxygen Diffusion Coefficient

Figure 5 shows the results of experiments on oxygen diffusion at 850°C in specimens of 14 to 16 mesh annealed at 1100°C in oxygen. The figure shows the relation between Dt/a^2 and sampling time t, which is a straight line, revealing that the rate of exchange reaction is being determined by oxygen diffusion.

From the slope, the value of D/a^2 is obtained as $3.2 \times 10^{-10}(sec^{-1})$ and since a=0.0548cm, D is 9.6×10^{-13} $(cm^2 \cdot sec^{-1})$.

D is the apparent diffusion coefficient including the contribution of boundary diffusion.[9]

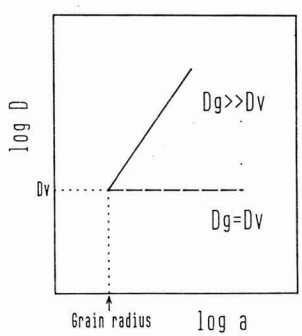

Fig. 6. Schematic illustration of the relations between log D (oxygen diffusion coefficient) against log a (particle radius) for the two extreme cases: (– –) $Dg \gg Dv$ and (- -) $Dg=Dv$, where Dv is a volume diffusion coefficient and Dg is a grain boundary diffusion coefficient.

Here, the relation between apparent diffusion coefficient and particle radius of the powder specimen will be mentioned. For specimens prepared by grinding reduced specimens to a certain particle radius, when grain boundary contribution to apparent diffusion coefficient is large because of increasing effective surface area, the larger the grain size of the specimen is, the larger is the apparent diffusion coefficient. In this case, as shown in **Fig.6**, the apparent diffusion coefficient has positive dependence on specimen particle radius. When the coefficients of boundary diffusion and volume diffusion are approximately equal to each other, the specimen can be considered to be composed of grains with no grain boundary, and so the apparent diffusion coefficient for any specimen radius is equal to the coefficient of volume diffusion. As stated above, the coef-

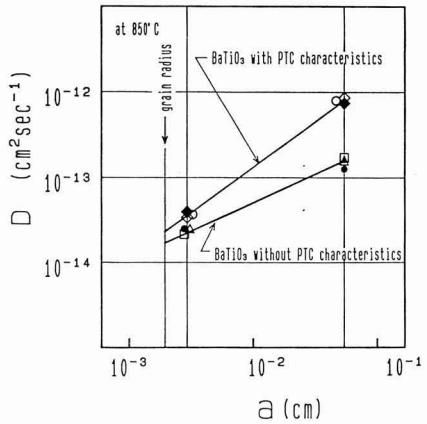

Fig. 7. Plot of oxygen diffusion coefficients against particle radius under different annealing conditions.
(●) reduced specimen, (❑) 500°C in air, (Δ) 800°C in air, (○) 900°C in air, (✧) 1100°C in air, (✦) 1100°C in O_2.

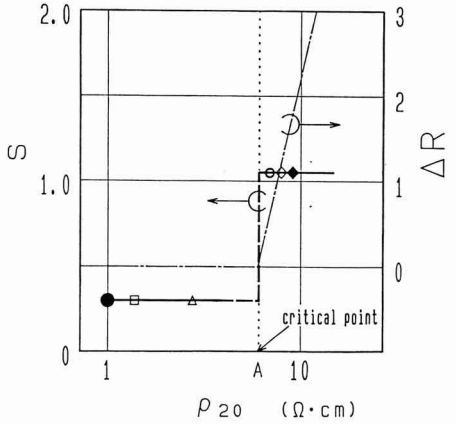

Fig. 8. Plot of slope (S) in Fig.7 and R against p20 with different annealing conditions.
(●) reduced specimen, (❑) 500°C in air, (Δ) 800°C in air, (○) 900°C in air, (✧) 1100°C in air, (✦) 1100°C in O_2.

ficient of volume diffusion can be obtained from the value of the apparent diffusion coefficient for each particle radius extrapolated to primary particle radius. The mathematical treatment of this volume diffusion coefficient calculation is difficult at present, but its experimental pertinence is shown in the study of Shirasaki et al.[9] When this dependence on specimen size has a positive value, for specimens having the same value of volume diffusion coefficient, the larger the slope S is, the larger the boundary diffusion coefficient is.

Figure 7 shows the apparent coefficient of oxygen volume diffusion D measured at 850°C for reduced thermistors and specimens obtained by annealing the thermistors at 500°, 800°, 900° and 1100°C, using the above method. As shown in the figure, every specimen showed the same value of coefficient of oxygen volume diffusion, that is, 2×10^{-14} cm^2/sec.

The value of the coefficient of oxygen volume diffusion for this bulk was about the same as the oxygen volume diffusion data obtained by SIMS in the study of Hasegawa et al.[10]

When specimens with PTC behavior (those annealed at 900° and 1100°C) and those without PTC behavior (reduced thermistors and specimens annealed at 500° and 800°C) are compared, if the rate of change in particle radius against that of oxygen diffusion coefficient with particle radius is slope S, for the specimen with PTC behavior, S=1.08, and for that without PTC behavior, S=0.29, showing a great difference between the two. This wide difference in slope shows that for specimens with PTC behavior, the contribution by grain boundary diffusion to apparent diffusion coefficient is greater than for specimens without PTC behavior.

Haneda et al.[11] observed the same tendency, showing a higher rate of change in the coefficient of boundary diffusion for specimens with PTC behavior, based on the evaluation of oxygen boundary diffusion characteristics obtained by SIMS.

In the results from measuring the coefficient of oxygen diffusion at 1100°C, the coefficient of oxygen diffusion of bulk showed the value of about 3×19^{-13} cm^2/sec for all the specimens, with a slope of 1.0, showing no difference. In other words, the difference in grain boundary diffusion between specimens with and without PTC behavior as shown in the measurement at 850°C was not observed. This might be because 1100°C is the temperature range where PTC behavior tends to occur, and reduced specimens which showed no PTC behavior and specimens annealed at 500° and 800°C in air changed to show PTC behavior during the measuring process.

3-4. PTC Characteristics and Oxygen Diffusion

It was clarified that there was a close relation between PTC characteristics and annealing temperature and partial oxygen pressure and that, in particular, PTC behavior appeared when annealing temperature rose above around 800° to 900°C, where NTC and PTC ranges were divided, as shown in Fig.3. Although in both ranges the same cation compositions exist, the state of oxygen diffusion differs, with the ratio of boundary diffusion to intragranular diffusion becoming larger during transition from NTC to PTC range.

Figure 8 shows the relation between these characteristics. It is notable that boundary diffusion behavior starts to change sharply at the point where PTC behavior occurs as shown by the slope S which is the index of the coefficient of boundary diffusion, with the critical points being identical with each other.

As the mechanism of PTC behavior, it is essential for a double Schottky barrier to be formed in the grain boundary, as shown by Heywang's barrier model. In this case, the formation of an acceptor level is necessary for the barrier height () to occur, as in Equation (3). However, as shown by the results of this study the formation of an acceptor level does not always occur until annealing is done to the PTC region as shown in Fig.3. In other words, the formation of an acceptor level is strongly affected by annealing temperature and partial oxygen pressure.

Although it is considered possible that the appearance of defect V_{Ba} (V_BƏ$_a$ or $V_B\forall_a$) of Ba site or the disappearance of oxygen defect V_0 (V_o or Vö) may accompany oxidization of PTC thermistors, Daniels[3] et al. explained that the formation of an acceptor level was attributable to the formation of defect V_{Ba} of Ba site in the vicinity of the grain boundary.

In this experiment, it was clarified that the ratio of grain boundary diffusion of specimens with PTC behavior was higher, which showed that oxygen concentration in the bulk was higher in the vicinity of the grain boundary while there was a relation of $[V_{Ba}] \propto Po_2^n$ (n0), and thus it seems that the formation of V_{Ba} becomes concentrated in the vicinity of the grain boundary due to the increasing oxygen in the bulk in the vicinity of the grain boundary resulting from a larger ratio of boundary diffusion. On the other hand, since the results of this study in Fig.4 also confirm that oxygen concentration in the bulk increases with annealing temperature and partial oxygen pressure, the disappearance of oxygen defect V_0 becomes concentrated in the vicinity of the grain boundary, which could contribute to the formation of an acceptor level. In either case, this oxygen is supplied from the grain boundary.

As shown by Figs.3 and 8 of this study, there is a critical point between NTC and PTC regions where the coefficient of oxygen diffusion and electrical characteristics change sharply. In particular, the ratio of boundary diffusion shows a sharp change during the transition from NTC region to PTC region as shown in Fig.8. The coefficient of grain boundary diffusion D_{GB}, if the amount of oxygen defect is N_{GB} and moving rate of oxygen defect is Dv_{GB}, is given by

$$D_{GB} \propto N_{GB} \times Dv_{GB} \quad \ldots\ldots\ldots (4)$$

Here, regarding the change of oxygen concentration in the bulk with the change of annealing temperature from NTC region to PTC region, the quantity of oxygen defect N in the bulk is presumed to gradually change with annealing temperature, based on the change of resistance (ρ_{20}) in Fig.3 and the results of oxygen analysis in Fig.4.

If the quantity of the oxygen defect N_{GB} related to boundary diffusion is affected by annealing as the oxygen defect N is related to bulk oxygen diffusion, N_{GB} will be in proportion to N. In this case, the ratio S in Fig.8 at the boundary is expected to change gradually. However, in actuality, S starts sharply increasing in its behavior at the point A where PTC appears. This suggests that N_{GB} or Dv_{GB} in Equation (4) should start to change sharply at the point A. In any case, the results shown in Fig.8 suggests that such a critical phenomenon as phase transformation should start occurring at the point A in the grain boundary, as it is formed in the grain boundary. It is thought, not that the acceptor level in Heywang's model gradually increases, but that it suddenly starts appearing at the point A.

4. Conclusions

By evaluating the dependence of PTC characteristics on annealing conditions and oxygen diffusion state in $BaTiO_3$-PTC thermistors, the following information was obtained.

1)Reduced $BaTiO_3$ thermistors showed PTC characteristics at annealing temperature above 900°C, with NTC and PTC regions existing bordering at the critical point in the temperature range of 800° to 900°C.

2)The coefficient of volume diffusion in both regions was $2 \times 10^{-14} cm^2/sec$. However, the slope S in PTC region was 1.08, being larger than 0.29 of that in NTC region, while there existed a critical point where the ratio of boundary diffusion to apparent diffusion coefficient started sharply increasing.

This critical point agreed with the bordering of NTC with PTC regions related to the appearance of PTC behavior.

References:

1) I. Ueda and S. Ikegami, "Oxidation Phenomena in Semiconducting $BaTiO_3$".
2) Hmal-Allak, G.J. Russell and J. Woods, "The Effect of Annealing on the Characteristics of Semiconducting $BaTiO_3$ PTC of Resistance Devices", J. Phys. D, Appl, Phys, 20, 1645-1651 (1987).
3) J. Daniels and R. Wernicke, 'Part 5, New Aspects of an Improved PTC Model", Philips Res. Reports, 31, 544-559 (1976).
4) M. Kuwabara, "PTC Mechanism and Stabilization of Characteristics", Erekutoroniku Seramikkusu, Vol.19, 15-21 (1988).
5) Y. Oishi and W.D. Kingery, J. Chem. Phys., 33, 480 (1960).
6) J. Crank, "The Mathematics of Diffusion" (Oxford University Press, London, 1957) p.88.
7) W. Heywang, "Resistivity Anomaly in Doped Barium Titanate", J. American Ceramic Society 47, 484-490 (1964).
8) J. Daniels and K.H. Hardtl, Part 1, Philips Res. Reports, 31, 544-559 (1976).
9) S. Shirasaki and H. Haneda, "Electrical Property and Defect Structure of Lanthanum-doped Polycrystalline Barium Titanate", J. Materials, Science, 22, 4439-4445 (1987).
10) A. Hasegawa and S. Fujizu, "Boundary Diffusion and PTC Effects of Barium Titanate", Nippon Seramikkusu Kyokai Nenkai, Yokoshu, p.476, 1989.
11) H. Haneda, submitted to J. Materials Science.

This article is a full translation of the article which appeared in Nippon Seramikkusu Kyokai Gakujutsu Ronbunshi (Japanese version), Vol.98, No.5, 1990.

Direct Observation Method for Internal Structure of Ceramic Green Body
-- Alumina Green Body as an Example --

Keizo Uematsu, Jin-Yung Kim, Zenji Kato, Nozomu Uchida and Katsuichi Saito

Department of Chemistry, Nagaoka University of Technology, 1603-1, Kamitomioka, Nagaoka 940-21, Japan

An alumina green body was made transparent by immersing in a liquid which has a refractive index close to that of alumina. Its internal structure was examined directly with an optical microscope.
[Received Nov. 30, 1989; Accepted Feb. 13, 1990]

Key-words: Green body, Structure, Alumina, Powder compaction, Transparency, Refractivity, Processing

1. Introduction

The nonuniformity of powder particle packing and inclusions in a green body often remain in the final sintered body,[1] diminishing the various characteristics of the ceramic. It is a starting point in the preparation of high performance ceramics to obtain a green body with minimum defects. If the internal structure of a green body could be understood an ideal green body might become reality by feeding back the results to the forming process. However, it was difficult to make this feedback in the past because the characterization of small defects in a green body was not easy.

Noting that no light scattering occurs at an interface of mediums which have the same refractive indexes,[2] we developed a method for closely characterizing the internal structure of a ceramic green body. In the method, a body was made transparent by immersing it in a liquid with a refractive index close to that of the green body and it was observed with an optical microscope. Using this method, the microstructure at optical microscope level can be observed over the whole range of the volume of the specimen and detailed information can be obtained on the entire structure of the green body. Compared to the observation of specimens flaked with a microtome,[3] this experimental method is very easy, not requiring any particular apparatus and capable of preparing a specimen within a short time. The method is thought to be a very important step in advancing the science of green body formation, compared with the conventional method by which only two-dimensional information could be obtained on an incidental fracture or a ground surface, or very large defects only could be estimated with an ultrasonic microscope.[4] The method is as follows. An isotropic-pressed alumina green body is used as a model, and it is made transparent by immersing in a liquid which has a refractive index close to that of alumina, (alumina: 1.77, liquid: 1.69-1.79),[5] and its internal structure is directly observed with an optical microscope.

2. Experimental Procedures

Commercial alumina powder granules (TM-DS manufactured by Taimei Kagaku), were monoaxial-press- formed into pellets (13mm in diameter, 2mm in thickness) at 10Mpa, and these were hydrostatic-pressed at 20MPa to prepare a specimen green body. To remove binder, the specimen was heated to 600°C at a temperature increase rate of 2°C/min in air, kept for 1h and cooled to room temperature. As immersion liquids, 1-bromonaphthalene (refractive index: 1.69), iodomethane (refractive index: 1.749) and in addition, a solution saturated with sulphur (refraction index: 1.79) and a solution with dissolved sulphur of about one-third of saturated volume (estimated refractive index: 1.76) were used. The green body was put into the liquid and deaeration was conducted for 10min in a vacuum desiccator using a water-jet pump to make the immersion liquid permeate sufficiently inside the green body. Although the internal structure could be observed as it was, a flake specimen was ground to a thickness of about 0.2mm with sandpaper and similarly permeated with the immersion liquid to observe in more detail. The internal structure of the flake specimen was observed with a transmission optical microscope by moving its focus position stepwise from the upper to the lower surface of the specimen.

3. Results and Discussion

Figure 1 shows photographs of alumina green body

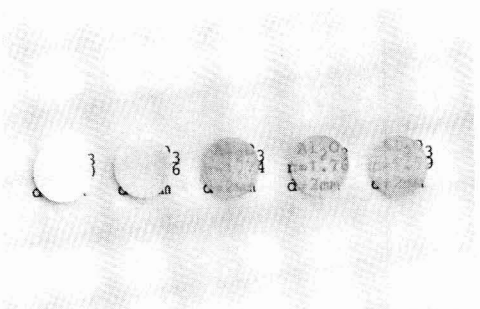

Fig. 1. Alumina green body specimens with immersion liquid having various refractive indexes; from left to right: n=1.0, 1.69, 1.75, 1.76, 1.79.

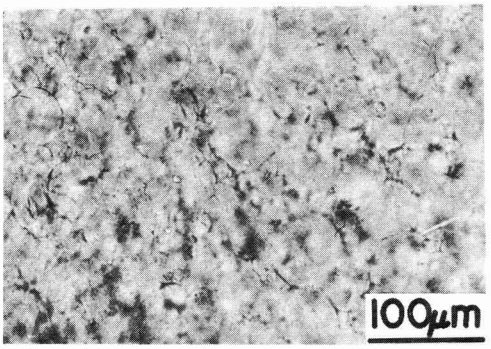

Fig. 2. Transmission optical micrograph of alumina green body specimen showing internal structures.

specimens with immersion liquids. For a green body with this thickness, a very good transparency is obtained with refractive index in the range of 1.749 to 1.79. In case of 1-bromo-naphthalene with a refractive index of 1.69, letters written on the foundation cannot be read. However, as the difference in tone of the photographs shows, transparency is considerably improved also with this liquid.

Figure 2 shows an optical micrograph of the green body specimen showing internal structures about 20μm below the surface. For this observation, 1-bromonaphthalene, which is easy to handle, was used. As shown in the figure, granules tens of μm in diameter were seen piled up on each other with cavities definitely existing among them. As the focus of the microscope was moved, such structures appear and disappear one after another at various depths. For a 0.3mm-thick specimen, there was little change in the sharpness of the image as the focus was moved from the upper to the lower surface, and so the internal structures could be closely investigated by this method. For a specimen permeated with liquid without the removal of binder similar results were obtained.

The defect images observed in the microscope were not much influenced by the kind of immersion liquid, and in all cases defects were clearly seen. For example, when iodomethane which has a refractive index close to that of alumina is used, the whole image becomes clearer though the contrast of the defect images somehow decreases due to improved transparency. The results up to now generally show that the closer the refractive indexes of the liquid approaches to that of the grains, the easier the observation of defects becomes. The reason for such results may be as follows. For defects to be seen by a microscope, scattering of light has to take place at the interface between grains and liquid, and theoretically when the refractive indexes of both completely coincide the scattering should become zero and the internal structure of the specimen ought to be invisible. Practically, however, since the refractive index of a material changes with wavelength, and the wavelength dependence differs from one material to another, light with a wavelength susceptible to scattering is always present in an observation that uses white light, as in this study, so the existence of defects is inevitably observed.

The reason for observing internal structures with many granules being piled up is that the granules were not completely crushed, because forming pressure during the preparation of the green body was low. In fact intergranular cavities decreased in number with increasing pressure. However, those cavities did not entirely disappear even when the formation pressure was 600MPa.

We previously conducted another direct observation of internal defects in high-density HIP ceramics using a transmission-type optical microscope,[6] and reported that many defects of about 20μm size existed in the high-density transparent ceramic prepared from the same powder used in this study and that the ceramic had a strength of 700Mpa. One of the causes for the formation of those defects might be that the cavities which existed in the green body remain even after sintering HIP. Although the alumina granule used in this study was one of the highest-level commercial products of this kind at present, its properties will be further improved by enhancing granular characteristics.

References:

1) J. Zheng and J.S. Reed, J. Am. Ceram. Soc., 72, 810-17 (1989).
2) W.D. Kingery, H.K. Bowen, D.R. Uhlmann, K. Komatsu, T. Sata, Y. Moriyoshi, K. Kitazawa and K. Uematsu, "Seramikkusu-Zairyokagaku-Nyumon, Oyohen", Uchida-Oizuru-Ho (1981), p. 625-677.
3) M. Arakawa, K. Hirota and M. Yamano, Nippon Seramikkusu Kyokai Gakujutsu Ronbunshi, 96, 942-45 (1988).
4) W.D. Friedman, R.D. Harris, P. Engler, P.K. Hunt and M. Srinivasan, "Proceedings of Non-destructive Testing of High-Performance Ceramics," Am. Ceram. Soc., 128-147 (1987).
5) Nihon Kagakukai Hen, "Kagaku Binran, Kisohen II", Maruzen (1984), p. II-556-7.
6) M. Sekiguchi, J. Kim, Z. Kato, N. Uchida, K. Uematsu and K. Saito, Jpn. Ceram. Soc. Tohoku Hokkaido Shibu Kenkyu Happyokai, Koenyoshishu, 7-8 (1989).

This article is a full translation of the article which appeared in Nippon Seramikkusu Kyokai Gakujutsu Ronbunshi (Japanese version), Vol.98, No.5, 1990.

A Model for Two-Dimensional Compaction of Cylinders

Takayasu Ikegami

National Institute for Research in Inorganic Materials ,1-1, Namiki, Tsukuba-shi, Ibaraki 305, Japan

A model for two-dimensional compaction of cylinders is proposed. The equation $\ln(P_2/P_1) = k_l k_s N_t (1/Z_{s2} - 1/Z_{s1})$ based on the model well described an experimental relation between the applied pressure P_a and the number of propagation sources of rearrangement, Z_s, where k_l is a constant, k_s is a coefficient of friction, N_t is the total number of contacts among cylinders, Z_{s1} and P_1 are the initial value of Z_s and that of P_a, and Z_{s2} and P_2 are the final ones, respectively. The equation indicates that $\ln(P_2/P_1)$ is roughly proportional to $1/Z_{s2}$ under the condition $P_1 \ll P_2$ because of $Z_{s2} \ll Z_{s1}$, which means that a feature in the initial packing structure vanishes on compaction. The k_s value, on the other hand, has appreciable influence on the Z_{s2} value, i.e., the final packing structure.

[Received December 18, 1989; Accepted April 13, 1990]

Key-words: Theory f compaction, Two-dimensional compaction, Compaction of cylinders, Compaction apparatus

1. Introduction

There is an essential difference between a regular array of particles in a sintering model and a random one in an actual powder compact. This causes severe questions[1-3] for application of theoretical equations of sintering to practical data of usual powder. If one can elucidate packing structure of particles in a usual powder compact, a sintering theory must be effectively developed.

Successive studies[4-10] about compaction have been made in various fields such as ceramics,[4] powder metallurgy,[5] soil,[6,7] pharmacy[8] and applied physics.[9,10] Compaction phenomena of a powder are so complicated that most of the studies have derived only empirical equations relating an applied pressure to the volume of a powder compact. Mathematical studies,[9,10] on the other hand, have been made under an assumption that the powder compact can be treated as a continuum medium. This assumption is reasonable for macroscopic behaviors[11] of a powder. It is, however, well-known that properties of ceramics critically subject not only to macroscopic inhomogeneity[12] in packing of particles but also to packing defects[13] of particles in microscopic regions. The present study was made to obtain information about microscopic packing structure of particles. Since it is very difficult to analyze and describe a three-dimensional packing structure of particles, a two-dimensional one was examined through analysis of compaction process of cylinders located in the flat box of a compaction apparatus.[14]

2. A Compaction Model

2-1. Typical Arrays of Cylinders

Figure 1 shows two typical examples of packing of cylinders, from which one can find some statistical relation between a number of cylinders C_p and the shape of a polygon linked with their centers. **Figure 2** shows four examples of the polygons, in which polygons with $C_p \leq 5$ are inevitably convex. If a concave polygon is defined as the polygon having one concave site at least, a number fraction, R_c, of the total number of concave polygons for a given C_p abruptly increases with increasing the C_p value from 6. Most of polygons of $C_p \geq 8$ are accordingly concave. Figure 2 shows that when cylinder a or b at a convex site shrinks toward the center of the polygon, cylinders c, d,near it in-

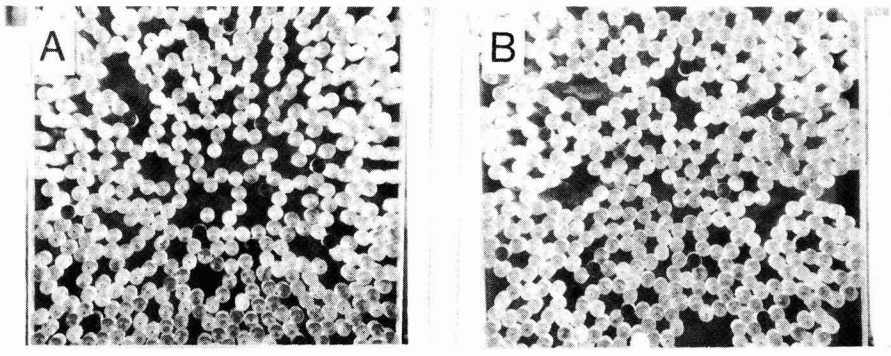

Fig. 1. Two typical arrays of adhesive cylinders. (a) random, (b) granules.

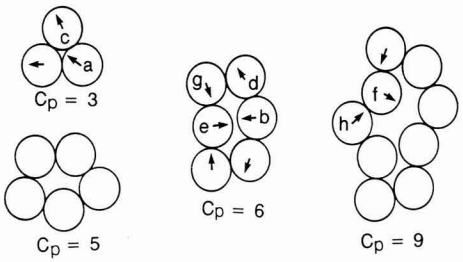

Fig. 2. Four examples of polygons linked with Cp cylinders.

evitably move toward outer side. The applied pressure restricts such movement in general. The polygons, therefore, are considered to be hard in the sense that the restriction force prevents them from breaking down. It is, on the other hand, probable that cylinder e or f at a concave site in Fig. 2 shrinks toward the center of the polygon together with cylinders g, h,near it. The concurrent shrinkages indicate no operation of the restriction force stated above, and hence the polygon is considered to be soft in the sense that its collapse can easily occur. Furthermore, most concave sites in a polygon can play the role of propagation sources, PS's, at the rearrangement of cylinders.

2-2. Rearrangement of Cylinders in A Sub-Region

We consider a slide at a contact between two cylinders. Such a slide occurs when an applied force, F_a, increases by Δf_a. Physics[6,7,9] lead an equation

$$\Delta f_a = k_s F_a \quad \ldots\ldots\ldots (1)$$

where k_s is a coefficient of friction. A sub-region is defined as a region where the rearrangement of cylinders is directly induced by that at one or several PS's. If simultaneous slides occur at Z_r contacts in the sub-region, $Zr\Delta f_a$ is equal to the least increment of F_a which just causes the rearrangement. There is a relation,

$$P_a = n_a F_a. \quad \ldots\ldots\ldots (2)$$

among F_a, an applied pressure, P_a, and a number of cylinders per a unit length for the planar packing, n_a. n_a is statistically equal to $1/(\sqrt{\rho_r} \times d_c)$, where ρ_r is an area fraction of occupation of cylinders to the total area of the compaction field and d_c is the radius of a cylinder. The previous study,[14] on the other hand, showed the practically slight change of the ρ_r value from 60% to 80%. This inappreciable change as compared with the former one roughly means that n_a is constant during compaction. Consequently, Eq. (2) indicates that F_a is proportional to P_a. It is natural that $Z_r\Delta f_a$ is induced by increase, ΔP_r, of P_a. From these relations and Eq. (1),

$$\Delta P_r = k_s Z_r P_a \quad \ldots\ldots\ldots (3)$$

is obtained.

2-3. Decrease of PS in Number

To derive an equation which relates a number of sub-regions to an applied pressure, the following are assumed:

(1) An applied pressure, P_a, results in some balanced array of cylinders. At this time, force F_a, which is proportional to P_a, acts at a contact between cylinders.

(2) The rearrangement of cylinders at PS has directly influence on directions of movement of other cylinders in the same sub-region, but has indirectly influence on those in the other sub-regions.

(3) A number, Z_r, of sliding contacts in a sub-region is proportional to the total number of contacts Z_m in it.

Compaction induces translations or rotations of cylinders and their clusters with slides at contacts among cylinders as well as those without such slides. Z_r, therefore, is smaller than Z_m. It is very difficult exactly to estimate the Z_r value. If, however, rearrangement of cylinders is fully random, a constant ratio is statistically evaluated between sliding cylinders and the other ones. This situation is in accord with assumption (3).

From the definition, every sub-region has a PS or more PS's. PS's which exist closely must belong to the same sub-region, and co-operatively induce the rearrangement of cylinders in it. The existence of such sub-regions means that the total number, Z_s, of sub-regions is not more than that, Z_p, of PS's. Eq. (3), however, indicates that the ΔP_r value decreases with decreasing the Z_r value. This tendency means that rearrangement of cylinders easily occurs in a compaction field with small (many) sub-regions in comparison with that with larger (fewer) ones. This condition suggests that sub-regions with one PS are much more than the other with several PS's in general, and Z_s is roughly estimated as Z_p. The compaction field is, thus, divided into Z_p sub-regions from PS to PS.

Assumption (1) indicates that the increase of P_a to $P_a+\Delta P_r$ results in a new balanced array of cylinders with PS's of Z_s-1 from the old one with Z_s. Rearrangement from (Z_s-1) to (Z_s-2) occurs if the applied pressure increases from $P_a+\Delta P_r$ to $P_a+2\Delta P_r+\Delta 55MV1$' further one from (Z_s-2) to (Z_s-3), also, proceeds after increase of the applied pressure from $P_a+2\Delta P_r+\Delta 55MV1$ to $P_a+3\Delta P_r+\Delta 552$ and so on. If $dZ_s\text{-}1 \ll Z_s$, $\Delta_q \ll \Delta P_r$ (q=1, 2, - -). dP_a is defined as the increment of the applied pressure during which the value of Z_s decreases by dZ_s. $dP_a = \Delta P_r dZ_s$. Very difficult estimation of the ΔP_r value results in that of the dP_a value. A relation that ΔP_r is proportional to Δp_r, however, may hold because of slight structural change of array of cylinders from Z_s to Z_s-1. Both the values of Z_s and dZ_s are proportional to the area of the compaction field, which, on the other hand, has inconsiderable influence on the value of dZ_s/Z_s. dP_a is hence related to dZ_s/Z_s to eliminate the effect of the area of the compaction field on the relation, and dP_a is found to be proportional to the product of ΔP_r and dZ_s/Z_s. N_t denotes the total number of contacts in the compaction field, and Z_s is equal to N_t/Z_m. From the aforesaid relations, $dP_a \alpha \Delta P_r \times dZ_s/Z_s$, $Z_r \alpha Z_m$ and $Z_s = N_t/Z_m$

$$dP_a = -k_1 k_s \frac{N_t}{Z_s} P_a \frac{dZ_s}{Z_s} \quad \ldots\ldots (4)$$

is derived from Eq. (3), where k_1 is a constant. If N_t is

Table 1.Applied pressures, P_a, ratios of occupation, ρ_r, and numbers of polygons linked with Cp cylinders for a random array.

P_a	ρ_r	C_p										
		3	4	5	6	7	8	9	10	11	12	13
.9	0.674	81	38	14	24	11	12	6	7	3	0	1
2.5	0.698	89	39	17	27	14	15	5	4	2		
5.8	0.730	104	45	24	32	17	8	3	3	1		
7.7	0.739	112	62	26	32	18	5	2	2			
14.2	0.760	131	70	34	32	12	3	3	1			
20.4	0.770	153	71	36	24	15	2	3				
22.6	0.780	177	66	38	21	14	2	2				
24.0	0.793	189	74	35	21	14	1	2				
37.2	0.796	189	78	40	23	11	1	1				
55.0	0.807	196	64	49	23	10	1	1				
87.0	0.807	206	71	47	20	9	1	1				
122.0	0.808	215	82	42	19	7	1	1				
135.0	0.809	204	84	46	17	7	1	1				
156.0	0.810	209	84	46	17	6	1	1				

a constant, integrating Eq. (4) results in

$$\ln(P_2/P_1) = k_1 k_s N_t (1/Z_{\sigma 2} - 1/Z_{s1}). \quad \ldots\ldots (5)$$

where P_1 and Z_{s1} are the initial values of P_a and Z_s, P_2 and Z_{s2} are the final ones, respectively.

3. Experimental

The apparatus, CA,[14] was fabricated to observed compacting process of something like 500 acrylic resin cylinders with 10mm in diameter by 16mm in high. The cylinders were compacted with the four movable walls which slide on the flat plate of the apparatus. The purchased cylinders are slippery, and their sides were covered with a pressure sensitive adhere double coated tape to give adhesiveness to the cylinders. Analysis was carried both on a packing process of the randomly arranged cylinders and on that of granules consisting with about 25 cylinders. Packing structure was taken with a camera located above CA. An applied pressure was measured with a strain gauge. ρ_r was estimated as the ratio of the total basal area of cylinders to the area of the square encircling them.

4. Results and Discussion

Table 1 shows ρ_r, P_a and distributions of numbers of polygons. From the Table, increase of P_a occurred slightly from ρ_r=68%, and appreciably from ρ_r=78%. It was, however, very difficult to obtain a larger ρ_r value than 81%.

If there is a direct interdependence among all the slides at contacts in the compaction field (this corresponds with the compaction field having one sub-region), it is very difficult to explain the reason why densification at a relatively low ρ_r (D%) easily occurs even at an insignificantly applied pressure. This perplexed situation induces the conception, that is, "sub-regions". This conception, also, well explains

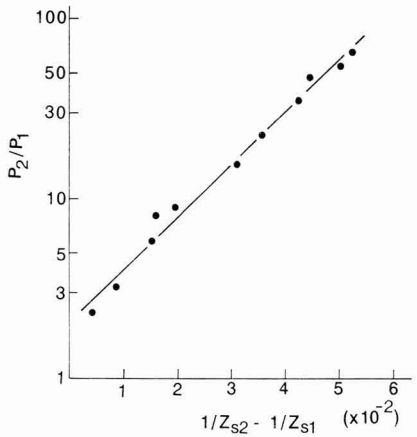

Fig. 3. A relation between P_2/P_1 and $1/Z_{s2} - 1/Z_{s1}$.

one of origins for the abrupt increase of P_a from 78%<F128p_r because of appreciable decrease of PS in number.

Numbers of polygons of C_p = 3 to 5 notably increased, but those of $C_p \geq 8$ decreased on compaction. These different tendencies in change of the number may be attributed to the shapes of polygons. That is, the polygons of C_p=3 to 5 are inevitably convex, but R_c for a given C_p value increased with increasing C_p, and most of polygons of $C_p \geq 8$ are concave.

The value of Z_s has to be evaluated to test the reasonability of Eq. (5), but not only this evaluation but also that of Z_p is very difficult. The major part of concave sites, on the other hand, was identified as propagation sources of rearrangement of cylinders, and Z_s may be substituted with a number of all the concave sites in the compaction field. We, then, enumerated such sites to calculate Eq. (5). The solid line in **Fig. 3** shows the result obtained from Eq. (5)

under an assumption that the k_l value is constant. The close fit of the theoretical values to the experimental data supports the reasonability of this assumption.

Eq. (5) indicates that the value of $1/Z_{s2}-1/Z_{sl}$ approaches to that of $1/Z_{s2}$ with increasing P_2. This means that if an applied pressure is appreciably high, Z_{sl}, an initial array of cylinders, has slight influence on the Z_{s2} value, the final array of cylinders. Our previous paper[14] has shown that the initial array of cylinders has strong influence on packing structure in the early stage of compaction. This feature vanished on compaction as suggested from Eq. (5). The data, also, roughly support that the k_l value is constant. It was, however, very difficult completely to eliminate the trace of the packing feature in the initial array in spite of applying a very high pressure. Further development of the present compaction model is required to specify the trace.

It is well-known that a coefficient of friction[11] has appreciable influence on packing structure. Eq. (5), also, theoretically confirms this influence irrespective of a degree of compaction. This result suggests that it is very desirable to fabricate a powder with a very small k_s for achievement of a very small Z_{s2} value, effective elimination of relatively large pores.

5. Conclusions

The presently derived equation describes a two-dimensional compacting process, where the initial feature in a packing array vanishes on compaction. The equation, also, indicates that a final structure by compaction statistically depends both on a friction coefficient among particles and a final compression pressure.

References:

1) D.L. Johnson, and T.M. Clarke, Acta Metall., 12, 1173-79 (1964).
2) K. Asaga, and K. Hamano, Yogyo-Kyokai-Shi, 83, 136-42 (1975).
3) C. Greskovich, and K.W. Lay, J. Amer. Ceram. Soc., 55 142-46 (1972).
4) A.R. Cooper, Jr., and L.E. Eaton, J. Amer. Ceram. Soc., 45 97-101 (1962).
5) G.C. Kuczynski, and I. Zaplatynskj, J. Metals, 8, 215 (1956); Trans. AIME, 206, 215 (1956).
6) P.T. Shield, J. Mechanics Phys. Solids, 4, 10-16 (1955).
7) K. Kawakita, and Y. Tsutsumi, Bull. Chem. Soc. Japan, 39, 1364-68 (1966).
8) M. Nakagaki, and K. Sunada, Japan J. Pharmacy, 83, 73-78 (1963).
9) T. Wakabayashi, Oyo Butsuri, 31, 556-71 (1962).
10) S. Hayakawa, Report Sci. Technol. of Tokyo Univ., 4, 87-92 (1950).
11) T. Nagao, Ceramics Japan, 18, 804-09 (1983).
12) T. Ikegami, and Y. Moriyoshi, J. Amer. Ceram. Soc., 67, 174-78 (1984).
13) T. Ikegami, M. Tsutsumi, S. Matsuda, S. Shirasaki, and H. Suzuki, J. Appl. Phys., 49, 4238-41 (1978).
14) T. Ikegami, S. Matsuda, S. Shirasaki and K. Eguchi, "Sintering 87", Proc. Int'l Institute for the Science of Sintering (IISS) Symposium, edited by S. Somiya, M. Shimada, M. Yoshimura and R. Watanabe, Elsevier Appl. Sci., Tokyo (1987) p.285-90.

This article is a full translation of the article which appeared in Nippon Seramikkusu Kyokai Gakujutsu Ronbunshi (Japanese version), Vol.98, No.5, 1990.

Information & communications

News

Domestically-produced Special Glass Available

Nippon Electric Glass has demonstrated the quality of special glasses developed by its own technology as the materials to be used for maintaining the solar battery of a scientific satellite.

The company has developed borosilicate glass "BDX" for a space satellite under the guidance of the Space Science Research Laboratory of the Ministry of Education, and performance tests were conducted by the Laboratory on "Akebono", an Aurora observation satellite which was launched on February 22 last year.

Two kinds of the product are cover glass (500μm in thickness) and heat controlling mirror (200μm in thickness) for a solar battery, for which the standard product of 4cm in length and 2cm in width in a total of 4200 sheets was mainly used. This product, a boronsilicate glass containing cerium oxide and titanium oxide, is also superior in its heat controlling function, with a high heat radiation rate.

When exposed to ultraviolet rays in space, the output of a satellite battery declines because its protective glass deteriorates. This product was designed to retain 330 W at launching and not less than 270 W after one year, but the experimental results were so favorable that it retained 365 W after 6 months, even exceeding the standard level after one year.

LBO Single Crystal Developed

Mitsui Petrochemical Industries, Ltd. has developed LBO (lithium tetraborate) single crystal to be used for SAW (surface acoustic wave) elements. This product is more favorable in its high frequency characteristic than rock crystal and other single crystals. SAW elements are used for filters capable of selecting frequencies, as well as for resonator and delay line elements. It is also used for automobile telephones, cordless telephones, pocket pagers, etc. A research group of the company's functional materials research laboratory has successfully grown a LBO single crystal of 2 inches in diameter and 3 inches in length using the CZ method. However, since it is actually required to produce a crystal larger than 3 inches in diameter for SAW elements, the company is intending to improve both the size and growth speed for crystals. Toshiba and Nippon Mining Co., Ltd. are the only companies which are manufacturing LBO single crystals. Thus, the company is planning to produce a crystal in a larger diameter so as to put it to practical use within this year.

Porous Ceramics with Eluted Glass Phase

The ceramic test station of Nagasaki prefecture has developed mullite porous ceramics by eluting a glass phase. After cobalt oxide or copper oxide is mixed with New Zealand kaolin, the mixture is molded and calcined to obtain a mass mainly consisting of mullite phase in the neighborhood of 1400°C. Then, glass phase immersed in soda lye is eluted to obtain a mullite porous mass. The size of pore diameters can be adjusted by the mixture ratio of oxides and calcination temperature. The basic property is a uniform pore diameter within a scope of 1 to 0.05μm with a pore ratio of 50 to 60%. A specimen with a smaller diameter showed a specific surface area of $50m^2/g$. In the evaluation experiment, this product was proved to be a favorable filter medium of methane fermentation liquid. The porous surface can be improved by organic silane compounds. The company is planning to enlarge its usage as a filter for drainage, bioreactors, and IC plants as well as chromatography fillers for the isolation of various kinds of chemical elements.

Potassium Hexathionate Fiber

Kubota Iron Works Co., Ltd. has started the mass-production of potassium hexathionate fiber. This fiber is more favorable than asbestos in its heat resistance and heat-insulating resistance. The company has invited the manufacturing technology based on the melt method from the National Institute for Researches in Inorganic Materials of the Science and Technology Agency, and is now developing the mass-production technology at its Technology Development Research Laboratory. Flat fiber crystal of potassium titanate is 10 to 30μm in diameter and 80 to 350μm in length. This material is an excellent friction material because of its wear resistance and high temperature stability. Thus, it is suitable for automobile disc brake pats, and is now being tested on a vehicle of a leading automobile manufacturer. Needle fiber of potassium titanate is 0.2 to 0.5μm in diameter and 5 to 20μm in length. It is a larger needle shape with high mechanical strength, and is rich in dispersion. Thus, it is an ideal stabilizing member for plastic and ceramics, metallic product, etc. Since this product is also usable as grinding parts, frictional parts, precision parts and others, the company is scheduled to increase the monthly production to a maximum level of 50 t as the non-asbestos mass production can be expected.

High Temperature Phase of Molybdenum Silicide Synthesized Under Normal Temperatures

A study group led by Shinya Iwamoto, head of Welding Engineering Research Laboratory of Osaka University, has succeeded in synthesizing a powder of β-molybdenum silicide (high temperature phase of molybdenum silicate) using the mechanical alloying method (MA), which consists of kneading a powder of molybdenum and silicon under normal temperatures for a long period of time.

Molybdenum is often used as molybdenum silicide with an addition of more than 60 to 70% atomic units for improving such properties as mechanical strength, anticorrosion and antioxidation. In most cases, alpha-molybdenum silicide is processed by the press plastic method, and sintered before it is used for heat-resistant and antioxidation coating materials or turbine wings, rocket nozzle, antiexothermic agent and electrode materials.

Molybdenum has two different phases of its temperature crystal structures in that it is β-molybdenum silicide in hexagonal crystal between 2,020-1,900°C and α-molybdenum silicide in tetragonal crystal below these temperature levels. When molybdenum and silicone are reacted at high temperatures by the melting method, β-phase is created, but it is soon decomposed or shows phase changes, becoming α-phase alone which is stable at low

temperatures.

In the current experiment, Iwamoto et al. discovered that there exists only α-phase for about 10 hrs when a fine powder of molybdenum and silicon was kneaded in a ball mill, but β-phase appeared 1.5 hrs thereafter, leaving almost β-phase alone after more than 30 hrs had passed. It was also confirmed that the synthesized powder was of hexagonal crystal in an X-ray diffraction image. The reason why β-phase was created has yet to be clarified. The MA method which has been attracting an attention as a method of manufacturing amorphous alloys without depending on superquenching has thus proved to be effective in the silicide formation.

Industrial Association of Ceramics-Lined Fume Tubes Established

An Industrial Association of Cerafume Pipe aiming at the popularization of excellent ceramics-lined-fume tubes was established. The members of this Association include Teikoku Fume Tube, who developed Cerafume Pipe, Noritake Co., Ltd., Nippon Fume Tube, Nippon Kohatsu Concrete, Daido Concrete and others, in total 17 companies. Cerafume pipe is a centrifugally molded fresh concrete tube lined with a mixture of ceramics and resin. Unlike coated tubes, this product is excellent in its anticorrosion and non-abrasive properties as it is impregnated in the concrete in centrifugal molding.

Although the product has been sold since 4 years ago, the Association has currently decided to provide its members with technical know-how for a consideration, and is planning to propagate the use of this product for the pipe conduits of corrosive drains at sewage disposal plants, etc.

Collaboration on Effective Utilization of Coal Ash

The Electric Power Development Co., Ltd. has started a collaboration with Ozawa Concrete Co., Ltd and two other companies for promotion of the effective utilization of coal ash discharged from coal thermal power plants. The company aims to develop and commercialize construction materials with high added value, such as ceramic paving material and hollow ceramic blocks. Power companies retaining coal thermal power have so far effectively utilized fly ash for cement admixtures and artificial lightweight aggregate concrete. However, a large quantity of coal ash is still thrown away for disposal, creating environmental problems. Encouraged by the building boom, power companies are gearing up for the development of construction materials for the future. Electric Power Development has decided on a collaboration with the above specialized manufacturers in the belief that there is an excellent market for construction materials.

Titanium Nitride Films on a Zirconia Substrate

Hitachi, Ltd. have succeeded in forming nitride films on a zirconia substrate by ion-beam mixing. The film forming operation which used to take about a week by conventional methods such as ion implantation can be completed in about 15 min, with higher adhesion. It is also possible to form metallic thin films of aluminum or copper on a zirconia substrate. Films thus obtained are expected to find their applications in the fields of heat sinks for electronic parts and sensor-mounted ceramic cutters for IC automatic mounting.

Using a bucket-type ion source, such as is used for nuclear fusion, with a capacity 100 times greater than that used for ion implantation, Hitachi's ion beam mixing method provides high film-forming speeds and film thicknesses from 60 to 70μ. The method also features high adhesion resulting from a mixed layer formed on the substrate. The ion source voltage and output current are 20kV and 0.15amp, respectively.

Hot-cut Pellet Manufacturing Apparatus for Material Tests

Union Plastic Co., Ltd. has developed an extruder for manufacturing 30mm hot-cut pellets. Material tests of composite plastics and ceramics including other composite substances have been essential requirements in recent years. It is also required in various fields to utilize the feature of machineries in meeting such requirements in the preparation of pellets. Thus, this is an ideal equipment with less cost and no worries for draining and drying for the preparation of hot-cut pellets.

Marketing O_2 HIP

A high volume of orders for the Atmospheric Oxygen Hot Isostatic Press (O_2 HIP) system, which Mitsubishi Heavy Industries and Toray have jointly developed, has encouraged these manufacturers to further promote the marketing of the system.

The main feature of this O_2HIP is in the development of a heat-resistant inner cylinder. Made by laminating two kinds of unique ceramics, this has overcome the previously inevitable drawbacks of the conventional inner cylinder of a heating furnace, i.e., such defects as that the cylinder tends to break during temperature rise and fall. This prolongs the life of heating units due to not overloading them, and furthermore temperature rise or fall time can be shortened with speeds of more than 500°C per hour, resulting in making its cycle time less than one half that of other maker's HIP.

This HIP has such advantages as that a single unit can be converted for use with several different furnaces, enabling processes in different conditions of atmosphere and temperature.

Abstracts of Articles on Ceramics from the Selected Journals of the Learned Societies

4680
Japanese Journal of Applied Physics
Vol.29, No.1, Jan. 1990
pp. 131-137

Molecular Orientational Structures in Ferroelectric, Ferrielectric and Antiferroelectric Smectic Liquid Crystal Phases as Studied by Conoscope Observation

Ewa GORECKA*, A. D. L. CHANDANI, Yukio OUCHI, Hideo TAKEZOE and Atsuo FUKUDA

Tokyo Institute of Technology, Department of Organic and Polymeric Materials, O-okayama, Meguro-ku, Tokyo 152

Molecular orientational structures in MHPOBC were studied by means of conoscope observation. Contrary to a ferroelectric response of the conoscope to an electric field in the smectic C^* phase, the conoscopic figure in the antiferroelectric smectic C_A^* phase does not shift its center and is biaxial with its optic plane perpendicular to the field direction. This conoscope change is only due to a dielectric contribution, indicating the existence of the inherent threshold in the electric field induced transition to the ferroelectric phase. In between the ferroelectric and antiferroelectric phases, a kind of ferrielectric phase was clearly distinguished in the field response of the conoscopic figure; the shift of the conoscope center perpendicular to the applied field and the biaxial optic plane parallel to the field suggest a novel molecular orientational structure.

KEYWORDS: ferroelectric liquid crystal, antiferroelectric, ferrielectric, smectic liquid crystal, conoscope, biaxiality

4708
Japanese Journal of Applied Physics
Vol.29, No.1, Jan. 1990
pp. L30-L32

Preparation of Bicrystal in a Bi-Sr-Ca-Cu-O Superconductor

Naruaki TOMITA, Yutaka TAKAHASHI† and Yoichi ISHIDA

Institute of Industrial Science, University of Tokyo, Tokyo 106
†Department of Precision Machinery Engineering, Faculty of Engineering, University of Tokyo, Tokyo 113

A [001]-twist bicrystal was prepared by sintering single crystal sheets of an 80 K Bi-Sr-Ca-Cu-O superconductor Resistivity measurement showed that the transition temperature of the bicrystal agreed with that of the single crystal. However, a large shoulder was observed in the current-voltage measurement suggesting weak coupling of the grain boundary.

KEYWORDS: Bi-Sr-Ca-Cu-O superconductor, critical current, grain boundary, weak coupling, twist boundary, bicrystal

4709
Japanese Journal of Applied Physics
Vol.29, No.1, Jan. 1990
pp. L33-L35

Preparation of $YBa_2Cu_3O_x$ Thin Film by Flame Pyrolysis

Makoto KOGUCHI, Yoshikazu MATSUDA, Eiji KINOSHITA and Kazuto HIRABAYASHI

The Furukawa Electric Co., Ltd., No. 6 Yawata-kaigandori, Ichihara, Chiba 290

$YBa_2Cu_3O_x$ thin films were prepared by flame pyrolysis. The X-ray diffraction analysis showed that as-prepared films had a strong preferred orientation with the c-axis perpendicular to the film plane. Film resistivities showed a sharp transition at temperatures below 90 K. After thermal annealing in the O_2 atmosphere, films showed zero resistivity at about 90 K.

KEYWORDS: flame pyrolysis, $YBa_2Cu_3O_x$, film

4710
Japanese Journal of Applied Physics
Vol.29, No.1, Jan. 1990
pp. L36-L39

Effects of Oxygen-Potential-Controlled Annealing on the Superconducting Properties of $(Bi, Pb)_2Sr_2Ca_2Cu_3O_y$ Thin Films

Hisao HATTORI†, Keikichi NAKAMURA and Keiichi OGAWA

National Research Institute for Metals, 1-2-1 Sengen, Tsukuba, Ibaraki 305
†Itami Research Laboratories, Sumitomo Electric Industries, LTD., 1-1 Koyakita 1-Chome, Itami, Hyogo 664

The oxygen potential of thin films consisting of monophasic $(Bi, Pb)_2Sr_2Ca_2Cu_3O_y$ was controlled by annealing them under various oxygen partial pressures. The T_c of $(Bi, Pb)_2Sr_2Ca_2Cu_3O_y$ was found to decrease monotonously with

decreasing oxygen potential. However, T_c did not change when annealed under higher oxygen pressure up to 2.9×10^1 torr. The carrier concentration was found to change with oxygen partial pressure, implying that oxygen supplies the carrier. An optimum range of the carrier concentration exists for attaining the highest T_c. This finding is consistent with those of other high T_c hole-type superconductors.

KEYWORDS: (Bi, Pb)$_2$Sr$_2$Ca$_2$Cu$_3$O$_y$, monophase, film, oxygen concentration, resistivity, Hall coefficient

4711
Japanese Journal of Applied Physics
Vol.29, No.1, Jan. 1990
pp. L40-L42

Preparation of Superconducting Bi-Sr-Ca-Cu-O Films with Preferred Orientation through a Metal Alkoxide Route

Shin-ichi HIRANO, Takashi HAYASHI and Hiroyuki TOMONAGA

Department of Applied Chemistry, School of Engineering, Nagoya University, Furocho, Chikusaku, Nagoya 464-01

Superconducting Bi-Sr-Ca-Cu-O films were prepared through a metal alkoxide route. The superconducting thin films composed of high T_c and low T_c phases with (00*l*) preferred orientation were successfully prepared at 850°C for 30 min on MgO(100) single-crystal substrates by a dip-coating method using partially hydrolyzed metal alkoxide solutions with 2-dimethylaminoethanol. The high T_c $Bi_2Sr_2Ca_2Cu_3O_y$ phase was found to form from the $Bi_2Sr_2CuO_y$ phase through the low T_c $Bi_2Sr_2CaCu_2O_y$ phase in the Bi-Sr-Ca-Cu-O system. The preferentially orientated thin films prepared at 850°C exhibited the superconducting transition with an onset of 114 K and an offset of 65 K.

KEYWORDS: chemical processing, high T_c superconducting oxides, Bi-Sr-Ca-Cu-O system, metal alkoxide route, high T_c and low T_c phases

4712
Japanese Journal of Applied Physics
Vol.29, No.1, Jan. 1990
pp. L43-L45

Magnetic Properties of 40 K Class Oxide Superconductor $(Gd, Ce)_4(La, Ba, Sr)_4Cu_6O_{18.8}$

Takahiro WADA, Tetsuyuki KANEKO, Ataru ICHINOSE, Yuji YAEGASHI, Sumio IKEGAWA, Hisao YAMAUCHI* and Shoji TANAKA

Superconductivity Research Laboratory, International Superconductivity Technology Center, 10-13 Shinonome 1-Chome, Koto-Ku, Tokyo 135

The superconducting properties of a 40 K class superconductor, $(Gd_{0.667}Ce_{0.333})_4(La_{0.133}Ba_{0.133}Sr_{0.133})_4Cu_6O_{18.8}$, were investigated by transport and magnetization measurements. The lower critical field, $H_{c1}(0)$, estimated from the field dependence of magnetization was 110 Oe. Adopting the 80% points of the resistive superconducting transition as T_c's in magnetic fields, the upper critical field, $H_{c2}(0)$, was determined to be 72.7 T. The superconducting material parameters were derived using these values for $H_{c1}(0)$ and $H_{c2}(0)$: $\kappa_{GL} = 126$, $\xi_{GL}(0) = 21$ Å, $\lambda_{GL}(0) = 2680$ Å and $H_c(0) = 4.1$ kOe.

KEYWORDS: oxide superconductor, magnetic property, superconducting materials parameter, coherence length, penetration depth, GL parameter

4713
Japanese Journal of Applied Physics
Vol.29, No.1, Jan. 1990
pp. L46-L49

ESR Absorption in a High-T_c Bi(Pb)-Sr-Ca-Cu-O Superconductor

Akihiko NISHIDA and Kazumi HORAI

Department of Applied Physics, Faculty of Science, Fukuoka University, Fukuoka 814-01

ESR absorption at 22.9 GHz of the high-T_c phase of a Bi(Pb)-Sr-Ca-Cu-O ceramic superconductor has been studied under two different spectrometer modes: a conventional field-modulation mode and a direct reflection-amplitude mode. Owing to the effect of hysteresis in the microwave response, the field modulation did not provide the proper field derivative of ESR absorption. By employing the direct mode, we were able to obtain more reliable data for the temperature dependence of the *g* value, linewidth and integral intensity. The spin susceptibility followed the Curie-Weiss behavior with the negative Weiss temperature around −4 K.

KEYWORDS: high-T_c superconductor, Bi system, ESR absorption, hysteresis, integral intensity, Curie-Weiss

4714
Japanese Journal of Applied Physics
Vol.29, No.1, Jan. 1990
pp. L50-L52

Site-Dependent ^{18}O Substitution in $YBa_2Cu_3O_7$ Studied by Raman Scattering Measurements

Ryusuke NISHITANI, Naoki YOSHIDA, Yoshiro SASAKI, Yuichiro NISHINA, Hiroshi YOSHIDA-KATAYAMA†, Yutaka OKABE† and Takashi TAKAHASHI†

Institute for Materials Research, Tohoku University, Sendai 980
†Department of Physics, Tohoku University, Sendai 980

The site-dependent replacement of ^{16}O with ^{18}O in $YBa_2Cu_4{}^{16}O_8$ has been identified by Raman scattering measurements of different vibrational modes in the CuO_2 and BaO planes. The Raman shifts due to isotope substitution for different

modes in inequivalent oxygen positions show different temperature dependences. The activation energy of oxygen replacement in the BaO plane is lower than that in the CuO_2 plane. The results show that the degree of oxygen substitution is site-dependent.

KEYWORDS: Raman scattering, superconducting oxide, $YBa_2Cu_3O_y$, isotope effect, phonon, site-selective substitution

4716
Japanese Journal of Applied Physics
Vol.29, No.1, Jan. 1990
pp. L57-L59

Rietveld Refinement of the Structure of $TlSr_2CaCu_2O_7$ by X-Ray Powder Diffraction Data

Toshiya DOI, Katsuhisa USAMI and Tomoichi KAMO

Hitachi Research Laboratory, Hitachi Ltd. Hitachi, Ibaraki 319-12

Single phase $TlSr_2CaCu_2O_7$ was synthesized, and the crystal structure was refined from X-ray powder diffraction data using Rietveld analysis. The structure has single Tl-O sheets and tetragonal symmetry ($a=3.7859$ Å, $c=12.104$ Å) with space group $P4/mmm$, and is similar to $TlBa_2CaCu_2O_7$ and $Tl_{0.5}Pb_{0.5}Sr_2CaCu_2O_7$ (1212 type). Possible substitution of about 14% of Ca-sites with Tl ions was suggested.

KEYWORDS: Tl-Sr-Ca-Cu-O system, superconductor, crystal structure, X-ray diffraction, Rietveld refinement, $TlSr_2CaCu_2O_7$

4717
Japanese Journal of Applied Physics
Vol.29, No.1, Jan. 1990
pp. L60-L63

Preparation of Single Phase $(Bi_{0.8}Pb_{0.2})_2Sr_2Ca_2Cu_3O_y$ Films with Preferential Orientation of *C*-Axis by Laser Ablation Method

Ahmed A. A. YOUSSEF, Takeshi FUKAMI, Takashi YAMAMOTO and Shoichi MASE

Department of Physics, Kyushu University, Fukuoka 812

By a laser ablation method using an Ar-F excimer pulsed laser, $(Bi_{0.8}Pb_{0.2})_2Sr_2Ca_2Cu_3O_y$ (H-BSCC) films have been prepared in almost single phase on MgO(100) substrates. As-deposited films on substrates at room temperatures did not show any diffraction peaks of X-ray powder analysis. As-deposited films were treated thermally and the optimum conditions to obtain H-BSCC films in almost single phase were confirmed. Essential conditions were the temperature just below the melting point of H-BSCC, and heating for a prolonged duration together with a bulk sample of the same composition as that of the target.

KEYWORDS: $(Bi_{0.8}Pb_{0.2})_2Sr_2Ca_2Cu_3O_y$, laser ablation, single-phase film, thermal treatment

4718
Japanese Journal of Applied Physics
Vol.29, No.1, Jan. 1990
pp. L64-L66

Bi-Pb-Sr-Ca-Cu-O Superconducting Fibers Drawn from Melt-Quenched Glass Preforms

Masashi ONISHI, Takashi KOHGO, Yoshiki CHIGUSA, Kazuo WATANABE, Michihisa KYOTO and Minoru WATANABE

Yokohama Research Laboratories, Sumitomo Electric Industries, Ltd., 1, Taya-cho, Sakaeku, Yokohama 244

Bi-Pb-Sr-Ca-Cu-O glass fibers were drawn from melt-quenched glass preforms by the method that is ordinarily applied to optical fiber fabrication. The drawn fibers were very flexible, and their surfaces were smooth. The glass fibers were crystallized by annealing and had superconducting properties. The annealed (1133 K, 240 hour) $Bi_{1.6}Pb_{0.4}Sr_2Ca_2Cu_3O_y$ fiber exhibited superconductivity with a T_c(zero) of 68 K and a critical current density (30 K, zero magnetic field) of 22 A/cm^2.

KEYWORDS: high-T_c superconductor, Bi-Pb-Sr-Ca-Cu-O system, melt-quenching method, superconducting fiber

4719
Japanese Journal of Applied Physics
Vol.29, No.1, Jan. 1990
pp. L67-L69

A Simple Method of Fabricating Preferentially Oriented $YBa_2Cu_3O_{7-x}$ Film on Silver Substrates

Mitsuru SUZUKI, Shinji KONDOH, Eiji YANAGISAWA, Jun-ichi SHIMOYAMA, Naoshi IRISAWA and Takeshi MORIMOTO

Research Center, Asahi Glass Co., LTD. Hazawa-cho, Kanagawa-ku, Yokohama 221

Porous $YBa_2Cu_3O_{7-x}$ film stuck to a flexible silver substrate was easily fabricated by sintering a doctor-blade-cast green sheet of $YBa_2Cu_3O_{7-x}$ placed on the silver substrate. Furthermore, preferentially oriented dense $YBa_2Cu_3O_{7-x}$ film was also fabricated by adopting a copper plated silver substrate and then sintered below the melting temperature of silver. A possible mechanism for the appearance of the preferentially oriented dense $YBa_2Cu_3O_{7-x}$ is discussed based on the liquid-phase sintering in the $YBa_2Cu_3O_{7-x}$-CuO-Ag system.

KEYWORDS: superconducting tape, green sheet, doctor blade, *c*-axis orientation, differential thermal analysis

4720
Japanese Journal of Applied Physics
Vol.29, No.1, Jan. 1990
pp. L70-L72

Oxygen Control in $Bi_2Sr_2Ca_1Cu_2O_x$ Superconducting Thin Films by Activated Oxygens

Kou TAKEUCHI, Masashi KAWASAKI, Mamoru YOSHIMOTO, Yasutoshi SAITO and Hideomi KOINUMA

Research Laboratory of Engineering Materials, Tokyo Institute of Technology, Nagatsuta 4259, Midori-ku, Yokohama 227

Activated oxygens were generated by various methods to compare their effect on the control of oxygen stoichiometry in $Bi_2Sr_2Ca_1Cu_2O_x$ superconducting thin films. The treatment of a film with an oxygen plasma or ozone at 400°C decreased the T_c onset of the film by as much as 20 K from untreated film as it was in the case of film treatment in atmospheric oxygen under UV light irradiation. On the other hand, films exposed to UV light irradiation in the presence of N_2O (400 Torr) increased their T_c onset to 100 K by about 20 K. These T_c changes accompanied the change in the c-axis lattice constant. The lattice of the specimens with T_c onset of 60 K was smaller than that of the untreated films, while the specimens with T_c onset of about 100 K had a stretched c-lattice. Thus, the oxygen content or hole concentration in $Bi_2Sr_2Ca_1Cu_2O_x$ films can be controlled at a relatively low temperature and its effect is reflected in the changes of lattice constant and T_c.

KEYWORDS: superconducting film, Bi-Sr-Ca-Cu-O, oxygen control, activated oxygen, N_2O

4723
Japanese Journal of Applied Physics
Vol.29, No.1, Jan. 1990
pp. L81-L82

80 K Superconductivity in Bi-Sr-Cu-O Thin Films

Hideaki ADACHI, Yo ICHIKAWA, Kumiko HIROCHI, Tomoaki MATSUSHIMA, Kentaro SETSUNE and Kiyotaka WASA

Central Research Laboratories, Matsushita Electric Industrial Co., Ltd., Moriguchi, Osaka 570

High-T_c superconductivity near 80 K has been obtained in Bi-Sr-Cu-O thin films. Films were prepared by rf-magnetron sputtering onto heated MgO substrates and heat-treated. It was found that the Bi-based crystal structure with a c-axis length of 3.12 nm was formed in thin film. This film exhibited the superconducting transition with the onset temperature of about 80 K. The present superconducting phase in the Bi-Sr-Cu-O system is considered to be the isostructure with the conventional 80 K $Bi_2Sr_2CaCu_2O_x$ (2-2-1-2) phase.

KEYWORDS: oxide superconductor, high-T_c Bi-Sr-Cu-O, thin film, sputtering

4738
Japanese Journal of Applied Physics
Vol.29, No.1, Jan. 1990
pp. L129-L132

Growth Kinetics of Microscopic Silicon Rods Grown on Silicon Substrates by the Pyrolytic Laser-Induced Chemical Vapor Deposition Process

Se Il PARK and Sang Soo LEE

Department of Physics, Korea Advanced Institute of Science and Technology, P.O. Box 150, Cheongryang, Seoul, Korea

By using a cw Ar^+ ion laser beam, microscopic crystalline silicon rods $\approx 10^2$ μm in diameter and $\approx 10^1$ μm in height have been grown on a silicon substrate by pyrolytic dissociation of SiH_4. The kinetics of lateral growth of the silicon rods is derived from the time integration of the Arrhenius equation using a reasonable assumption that the temperature on the edge of the deposit saturates inversely to the substrate temperature with illumination time. For the axial growth, excluding the initial transient growth, the same result as Bäuerle and his collaborators is derived. The influences of laser power and illumination time on the deposited diameter and height are found experimentally, and it is found that the derived theory agrees well with the experimental results.

KEYWORDS: pyrolytic LCVD, growth kinetics, microscopic silicon rods, lateral growth, axial growth, time dependence of temperature

4739
Japanese Journal of Applied Physics
Vol.29, No.1, Jan. 1990
pp. L133-L136

Preparation of $Pb(Zn_{0.52}Ti_{0.48})O_3$ Films by Laser Ablation

Shigeru OTSUBO*, Toshihiro MAEDA, Toshiharu MINAMIKAWA†, Yasuto YONEZAWA†, Akiharu MORIMOTO and Tatsuo SHIMIZU

Department of Electronics, Faculty of Technology, Kanazawa University, Kanazawa 920
†Industrial Research Institute of Ishikawa Prefecture, Kanazawa 920-02

$Pb(Zr_{0.52}Ti_{0.48})O_3$ films were prepared on an *r*-plane sapphire substrate by laser ablation using the ArF excimer laser. This is the first report on the preparation of $Pb(Zr_{0.52}Ti_{0.48})O_3$ films by laser ablation. The composition of the deposited films was found to be fairly close to the composition of the target material for a wide range of the substrate temperature, 400-750°C. The substrate temperature greatly influences the crystal structure; a low substrate temperature produces a pyrochlore phase and a high substrate temperature (750°C) a perovskite phase.

KEYWORDS: $Pb(Zr_{1-x}Ti_x)O_3$ thin film, laser ablation, no deviation of composition, pyrochlore, perovskite, XRD, EPMA, SEM

4768
Denki Kagaku
58, No.2 (1990)
p. 172-177

Development of a Zinc-Chlorine Battery for Load Leveling II.
Development of a Carbon Chlorine Eletrode Activated by RuO2 Catalyst

Koichi ASHIZAWA*, Toshio HORIE and Yuichi WATAKABE†

A carbon electrode activated by RuO_2 catalyst was developed as the chlorine electrode of the zinc-chlorine battery for energy storage. The chlorine electrode was obtained by dipping the carbon substrate in $RuCl_3 \cdot nH_2O$ solution and pyrolyzing it in air. From the kinetic analysis of thermogravimetric (TG) results, the optimum burning conditions, such as decomposing time and temperature, were determined. The polarization tests of a chlorine electrode reaction on this electrode revealed that the overpotential is small not only on charge but also on discharge at a low chlorine concentration. Further, charge-discharge cycling tests of a small-size single cell proved the voltage efficiency of 88% at a current density of about 30mAcm^{-2} and the performance of the chlorine electrode turned out quite efficient.

4852
Chemistry Letters
pp.247-248, 1990

Preparation of Silica Fibers from Sodium Silicate Solution

Akio TADA,* Hiromi YAGINUMA, Hidenobu ITOH,
Tamotu HIROTA,*† and Toshiyuki MAEDA†
Department of Environmental Engineering, Kitami Institute
of Technology, Kitami 090
† Research & Development Center, Osaka Gas Co. Ltd.,
Konohana-ku, Osaka 554

Silica fibers were prepared from sodium silicate solution. A spinnable sol was obtained by the reaction of a sodium silicate solution with ethyl acetate, and gel fibers obtained by dry spinning of this sol were converted to silica fibers by treating in an acid bath followed by drying at 100 °C and heating at 600 °C.

5715
Yu-Kagaku
Vol.39, No.2 (1990)
p. 71-76

Application of Hydrous Zirconium Oxide to Catalyst

Hajime MATSUSHITA, Makoto SHIBAGAKI, and Kyoko TAKAHASHI
Life Science Research Laboratory, Japan Tobacco, Inc.
(6-2 Umegaoka, Midori-ku, Yokohama-shi, 〒227)

Zirconium oxide is stable and has been rarely used as a material for catalyst except for a carrier. Recently, some high catalytic activities of the hydrous zirconium oxide have been found.

It catalyzes esterification, amidation, and acetalyzation. It also catalyzes a reduction of carboxylic acids to aldehydes with hydrogen gas. Ketones, aldehydes, carboxylic acids, esters, and nitriles are readily reduced to the corresponding alcohols with 2-propanol. It is worthy of remark because it implies an extension of the so-called Meerwein-Ponndorf-Verley reduction. The surface acidity of the oxide is weak and the reaction is applicable to acid-sensitive compounds.

5719
Yu-Kagaku
Vol.39, No.2 (1990)
p. 95-99

Inclusive Reactions by Swellable Clay Minerals. I
Inclusion of Nonionic Surfactants by Sodium-Montmollironite and Its Gelation in Oil

Michihiro YAMAGUCHI

An oil gel was formed in a ternary system of sodium-montomollironite (Na-Mon), nonionic surfactant (SAA) and oil. Formation of the oil gel was caused by formation of an inclusion compound functioning as an SAA/Na-Mon binary system. The SAA having about 8 for an HLB value was easily taken in by the interlayer (silicate layer) of Na-Mon. From X-ray diffraction measurement, basal spacings of Na-Mon increased with the amount of SAA. The basal spacings of inclusion compounds were constant at an SAA/Na-Mon weight ratio of 1/1. Inclusion compound formation was completed when the adsorption of SAA in the interlayer of Na-Mon was saturated with a monomolecular layer at a 1/1 weight ratio.

The inclusion compound swelled on adding an oil such as liquid paraffin (LP). with subse-

quent formation of the oil gel. X-ray diffraction indicated regular diffraction peaks in the stable and rigid oil gels. The structure of the swollen compound was lamellar with basal spacing ranging from 50~60 Å. This interlayer swelling occurred with the inclusion of about 26 wt% of LP in the interlayer of the inclusion compound (SAA/Na-Mon).

5720
Yu-Kagaku
Vol.39, No.2 (1990)
p. 100-104

Inclusive Reactions by Swellable Clay Minerals. II

Inclusion of Nonionic Surfactants by Organophylic-Montmollironite and Its Gelation in Oil

Michihiro YAMAGUCHI
Shiseido Basic Research Laboratories
(1050, Nippa-cho, Kohoku-ku, Yokohama-shi, 〒223)

An organophilic-montmollironite (Or-Mon) was prepared by a cation-exchange reaction between sodium-montmollironite (Na-Mon) and dioctadecyldimethylammonium chloride (DODAC). The cation exchange amount of DO-DAC in the Or-Mon was 80 meq/100 g-Na-Mon. This corresponds to the cation exchange capacity (CEC) of Na-Mon. The basal spacing of the Or-Mon was 26.75 Å, which could be explained by the formation of a single layer complex with the alkyl chain lying parallel to the silicate surface of Na-Mon.

The Or-Mon easily adsorbed a nonionic surfactant (SAA) with an HLB value of about 8. The inclusion ratio of SAA to Or-Mon was 0.2/1.0 in weight, and the inclusion compound (SAA/Or-Mon) had 36.78 Å for the basal spacing indicating monolayer adsorption of DODAC into the silicate layer of the Na-Mon interface. SAA/Or-Mon swelled in an oil such as liquid paraffin, resulting in the formation of a gel. The swelling of SAA/Or-Mon may possibly have been induced by entrance of the oil into the interlayer of the SAA/Or-Mon.

5816
Chemistry Letters
pp. 331-334, 1990

Ionic Conductivity of $LiTi_2(PO_4)_3$ Mixed with Lithium Salts

Hiromichi AONO, Eisuke SUGIMOTO, Yoshihiko SADAOKA†
Nobuhito IMANAKA,†† and Gin-ya ADACHI*††
Department of Industrial Chemistry, Niihama National College of Technology, Yagumo-cho 7-1, Niihama, Ehime 792
†Department of Industrial Chemistry, Faculty of Engineering, Ehime University, Bunkyo-cho 3, Matsuyama, Ehime 790
††Department of Applied Chemistry, Faculty of Engineering, Osaka University, Yamadaoka 2-1, Suita, Osaka 565

$LiTi_2(PO_4)_3$-lithium salt systems have been investigated in order to obtain a high lithium ion conductor. The salts acted as binder for sintering. The porosity decreased considerably and the conductivity of the pellets increased by the binder utilization. The maximum conductivity was 3×10^{-4} S·cm^{-1} for the $LiTi_2(PO_4)_3$ - $0.2Li_3BO_3$ system. The mixed binder was found to exist as a glassy or a thin coating second phase.

5817
Chemistry Letters
pp. 335-338, 1990

Liquid Phase Carbonylation with Solid Catalyst. Carboxy Methylation of Dihalo Methane with Group VIII Metals Supported on Active Carbon

Hiroshi YAGITA, Hiroyuki KUWAHARA, Kohji OMATA, and Kaoru FUJIMOTO
Department of Synthetic Chemistry, Faculty of Engineering,
The University of Tokyo,
Hongo 7-3-1, Bunkyo-ku, Tokyo 113

It was found that cobalt supported on active carbon showed an excellent catalytic activity for the carbonylation of dibromo methane in the liquid phase. For example, when the reaction was conducted under the conditions of 140 °C, P(CO)=31 atm, the yields of dimethyl malonate and bromomethyl acetate were 34.4% and 22.2%, respectively. Pd and Rh also showed catalytic activities.

5818
Chemistry Letters
pp. 339-342, 1990

p-Methoxybenzyl as a New N^3-Imide Protecting Group of 5-Fluorouridine and Its Application to the Synthesis of 5'-O-Acryloyl-5-fluorouridine[1)]

Takahiko AKIYAMA, Masahiro KUMEGAWA, Yasuhiro TAKESUE,
Hiroyuki NISHIMOTO, and Shoichiro OZAKI*
Department of Resources Chemistry, Faculty of Engineering,
Ehime University, Matsuyama, Ehime 790

5'-O-Acryloyl-5-fluorouridine was prepared by use of p-methoxybenzyl(PMB) group as a new N^3-imide protecting group of 5-fluorouridine. A chemoselective method for protection has been developed by use of ethyldiisopropylamine as a base and deprotection was effected by $AlCl_3$-anisole system.

5843
Chemistry Letters
pp. 429-432, 1990

An Improved Coprecipitation Method for Preparation of Superconducting Bi,Pb-Sr-Ca-Cu-O Material

Hidenobu ITOH,* Kazuhiro OKADA, Tatsuya FUJISAWA,
Noriyasu OKAZAKI, and Akio TADA*
Department of Environmental Engineering, Kitami Institute
of Technology, Kitami 090

Superconducting Bi,Pb-Sr-Ca-Cu-O material has been prepared by an improved coprecipitation method; mixed metal oxalates as the precursor were precipitated from a homogeneous acetic acid solution of the constituent metal acetates and dimethyl oxalate. This method permits easier fabrication of the superconducting material which is almost free from low-Tc phase.

5845
Chemistry Letters
pp. 437-440, 1990

A Mössbauer Study on Behaviors of Tin Deposited on the α-Fe_2O_3 Surface

Sumio ICHIBA,* Hiroyuki OSHITA, and Hiroshi SAKAI
Department of Chemistry, Faculty of Science, Hiroshima University,
Higashisenda-machi, Naka-ku, Hiroshima 730

The doping process of metallic tin into the α-Fe_2O_3 crystal lattice was studied by using ^{119}Sn Mössbauer spectroscopy. The spectra of the heat-treated samples at 300 °C for 10 h show the existence of Sn_2O_3, remaining β-Sn, and α_2-Sn. The α_2-Sn species is characteristic with the unusually large value of the isomer shift (I.S.=4.5 ± 0.2 mm s^{-1}).

5846
Chemistry Letters
pp. 441-444, 1990

Correlation between Gas Sensitivity and Crystallite Size in Porous SnO_2-Based Sensors

Chaonan XU, Jun TAMAKI, Norio MIURA, and Noboru YAMAZOE*
Department of Materials Science and Technology, Graduate School of Engineering Sciences, Kyushu University, Kasuga, Fukuoka 816

The gas sensing properties of SnO_2-based sensors in which the size of SnO_2 crystallites was controlled by various dopants were investigated. It was found that the gas sensitivity to H_2, CO or $i\text{-}C_4H_{10}$ increased as the SnO_2 crystallite size decreased in the range below 10 nm. Quite high gas sensitivity was achieved at a crystallite size of ca. 5 nm.

5886
Kei-Kinzoku
Vol.40, No.2 (1990)
p. 75-81

Joining of ceramics to aluminum using Al-Mg and Al-Si alloys as fusible insert*

Seijiro MAKI** and Masao NAKAMURA**

Joining of aluminum (A1100) and four kinds of ceramics, Si_3N_4, SiC, Al_2O_3 and PS ZrO_2 (partially stabilized), was attempted by using Al-Mg and Al-Si alloys as fusible insert. Effects of insert composition and joining parameters, such as temperature, time, pressure, cooling rate and amount of insert, on the bond strength were investigated. The results obtained are as follows: (1) Both aluminum alloys worked successfully on the joining, and relatively high bond strength was obtained at the compositions, 5-20 wt%Mg and 5-10 wt%Si. (2) Joining at temperatures below 878 K using the Al-Mg alloy insert, however, gave rise to high thermal stress, which decreased the bond strengths of Al_2O_3 and SiC remarkably. (3) A use of Al-Si alloy insert can be recommended when thermal stress becomes a serious problem. (4) Al-10 wt%Mg alloy can be recommended as suitable insert for Si_3N_4 and SiC, and Al-5 wt%Si alloy for PS-ZrO_2 and Al_2O_3. (5) The following measures are effective to reduce the thermal stress in use of the Al-Mg alloy insert; i) to minimize the amount of the insert, ii) to increase joining temperature and/or time, and iii) to decrease the rate of cooling after joining.

Keywords: joining, ceramics, insert, aluminum alloys, reactive element

5893
Kei-Kinzoku
Vol.40, No.2 (1990)
p. 123-130

Mechanical properties of alumina short fiber reinforced Mg–Nd alloys

Harumichi HINO*, Mikiya KOMATSU* and Hirotaro MORI**

In order to improve the high temperature properties of an alumina short fiber reinforced magnesium alloy for automotive component application, an alumina short fiber reinforced Mg–Nd alloy, referred here to FRMg, has been developed by squeeze casting. The relation between its properties and metallurgical structure has been examined with the following experimental results. (1) The high temperature strength of FRMg with a sound metallugical structure is superior to that of the matrix. (2) Mg_2Si precipitate produced by the reaction between the molten magnesium metal and silica binder in the fiber preform is preferentially present in the area where the molten magnesium metal finally infiltrates. (3) In the deformation of FRMg containing Mg_2Si precipitates, the fracture of Mg_2Si precipitates in contact with the fiber is observed in the heavily deformed matrix. (4) The properties of FRMg containing Mg_2Si precipitates scatter considerably, with some of them being inferior to those of the matrix. Examination of the metallurgical structure reveals, in the FRMg containing Mg_2Si precipitates, that Mg_2Si fractures at the beginning stage of plastic deformation because of the stress concentration induced at the precipitate/matrix interface and that this degrades the properties of FRMg.

Keywords: fiber reinforced magnesium alloy, reaction products, silica binder, stress concentration, fracture

DAILY RECORD

*The joint academic-industrial research group sponsored by the NTT and the Ministry of Education's High-Energy Physical Research Laboratory have developed a diffraction grating for heat-resistant optical devices which is capable of producing spectra from radiation 100 to 1000 times stronger than an ordinary SOR. The SiC substrate is coated with an Au film, which is provided with very fine grooves.

*The Science and Technology Agency's National Institute for Research in Inorganic Materials has developed, jointly with Shinagawa Refractories, partially stabilized α-Sialon ceramic material of high-temperature strength, with a bending strength of 90 to 100km/ml^2 at 1200°C. The HIP-prepared ceramic material consists of α-Sialon mixed with acicular crystals of Si_3N_4, and features uniform and pore-free structures.

*Matsushita Electric Works has started selling 2 types of driers for domestic purposes. Each is a high-efficiency device (heat efficiency: 70% at molecular level), emitting infrared rays from the specially designed ceramic heater element.

*Dai-ichi Kogyo Seiyaku has developed and started selling a water-soluble binder capable of forming ceramic materials into highly densified shapes. Use of the binder allows increases in the density and tensile strength of the articles formed by 12% and 100%, respectively, compared with untreated materials. Being water-soluble, it is easier to handle.

*The Science and Technology Agency's National Institute for Research in Inorganic Materials has prepared a thick film of PGO, 50 to 200μm in thickness, using an ultraquenching method, and have developed a pyroelectric infrared sensor incorporating this thick film.

*A.M. Technology (0559-67-5166) has developed a melting/forging process for aluminum composite materials, in which Al_2O_3 fibers or SiC whiskers are preformed and set in a mold into which molten aluminum is poured, and the aluminum-impregnated reinforcing material is then pressed. This aluminum composite material is comparable with iron in strength and heat resistance.

*Sante has started selling a water purifier, in which water is electrolyzed by the aid of a granular ceramic material and treated by far-infrared rays.

*Oki Electric Industry has developed a full-color EL element display, with a luminescent film which uses SrS with traces of Ce and Eu as the luminous material.

*Mitsui Petrochemical Industries has developed a single LBO crystal, 2in. in diameter and 2in. long, for SAW elements, using the CZ method.

*K. Torii of the Agency of Industrial Science and Technology's Government Industrial Research Institute, Tohoku, has developed a porous body with a mesopore of 46.4Å. Silicate-containing smectite, synthesized by the hydrothermal process using Si and Mg, is combined with an organic compound and heat-treated.

*The Nagasaki Prefecture's Institute for Ceramic Materials has developed a new mullite-base porous ceramic material. A mixture of New Zealand kaolin and Co_2O_3 or CuO is formed and sintered, and the glassy phase is eluted out from the sintered body. It is characterized by its uniformly sized pores. Porosity is 50 to 60%.

*Takenaka Komuten has found that granular cement paste (water content: 18 to 23%), which shows no fluidity, is in flux instantaneously when vibrated ultrasonically. It can be solidified and highly densified to have a compressive strength of 1302kg/cm^2, when mixed with pure mortar.

*N. Inoue of the Agency of Industrial Science and Technology's Government Industrial Research Institute, Kyushu, has synthesized pure TSH in long-fiber crystals (max. length: 1mm), using SiO_2 and $CaCO_3$ as the starting materials and treating them hydrothermally.

*Hitachi, Ltd. has succeeded in forming a Ti_3N_4 film over a ZrO_2 substrate in 15min by the ion beam mixing method, in which a bucket-type ion source developed for nuclear fusion is applied. The film is reaction-bonded fast to the substrate.

*Shiseido has developed an inorganic photochromism-type pigment, in which TiO_2 is mixed with a special agent.

*Mitsui Mining and Smelting has developed a chemically stable composite ceramic material of high strength and high thermal conductivity, consisting of SiC sandwiched by Al_2O_3.

*Kanthal Artcore has developed a ZrO_2-base heating element, capable of heating an oven up to 2300°C.

*Wing (03-862-0531) has developed a polarizing tile coated with specially prepared particles, which exhibits various colors, depending on angles of light which fall on it.

*H. Yamada of the Agency of Industrial Science and Technology's Government Industrial Research Institute, Kyushu, has developed a process for producing large (10μm in size) plate-shape crystals of basic $CaCO_3$ at around room temperature. Weathered quicklime microparticles are treated in a low-concentration aqueous solution of saccharose to grow the nuclei while hydration is controlled.

*Takenari UF Institute (0899-76-8835) has developed a white ceramic powder bleached with an enzyme extracted from pineapple juice.

TAIKABUTSU OVERSEAS

TAIKABUTSU OVERSEAS

Quarterly English Journal of
The Technical Association of Refractories, Japan

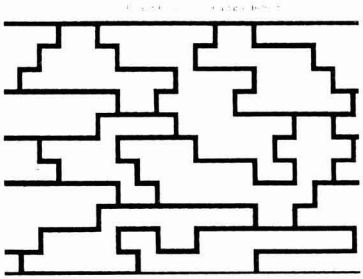

TAIKABUTSU OVERSEAS is a worldwide distributed quarterly magazine about refractories. It has a coverage of various countries in five continents. In each of these countries, it is read by engineers and technicians, as well as executives engaged in refractories related industries.

In TAIKABUTSU OVERSEAS, you find articles on new technology, reviews, professional opinions, and general information, aside from current events, and up-to-date activities of the Technical Association of Refractories, Japan (TARJ).

ORDER FORM

To: Circulation Div., The Technical Association of Refractories, Japan
c/o Fuji Technology Press Ltd.
Daini Bunsei Bldg., 1-11-7 Toranomon,
Minato-ku, Tokyo 105, Japan

Date: _____

Please enter my annual subscription to **TAIKABUTSU OVERSEAS**
(for _____ copy/lies) quarterly

Name: _____
Position: _____
Address: _____
Signature: _____

□ Payment enclosed □ Bill me
(Payment enclosed is preferred)

□ Surface mail	¥40,000
□ Airmail	¥41,500 (Asia & Oceania)
	¥42,000 (North & Central America)
	¥42,500 (Europe and other areas)